Synthesis and Characterisation of Layered Double Hydroxides (LDHs) Using Red Mud and their Environmental Applications

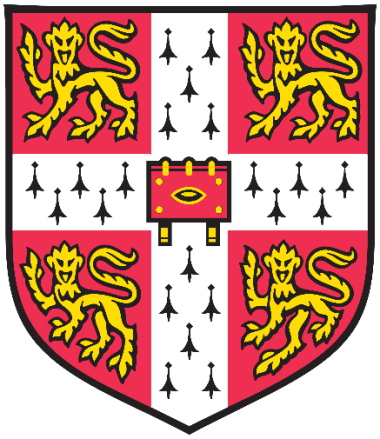

Yiyun Zhang

Department of Engineering

University of Cambridge

This dissertation is submitted for the degree of

Doctor of Philosophy

Christ's College **January 2020**

Declaration

I hereby declare that this dissertation is the result of my own work and includes nothing which is the outcome of work done in collaboration except where specifically indicated in the text. I further state that no substantial part of my thesis has already been submitted, or, is being concurrently submitted for any such degree, diploma or other qualification at the University of Cambridge or any other University or similar institution except as declared in the Preface and specified in the text.

In accordance with the Department of Engineering guidelines, this dissertation does not exceed 65,000 words, inclusive of appendices, references, footnotes, tables and equations, and it does not contain more than 150 figures.

_____

Yiyun Zhang
December 2019

Synthesis and Characterisation of Layered Double Hydroxides (LDHs) Using Red Mud and their Environmental Applications

Yiyun Zhang

Abstract

The disposal of industrial waste has posed many environmental challenges. Recently, transition to low-carbon economy has gained increasing awareness and is calling for new practices of waste reduction. Utilisation of waste materials therefore present twofold merits: (1) minimise waste disposal, (2) serve as alternative resources. Bauxite residue, also known as red mud (RM), the aluminium industry's largest solid waste stream, is the by-product from the Bayer process of bauxite ore digestion. Worldwide, there are around 80 active Bauxite processing plants and over 150 million tonnes of red mud are generated every year, whereas the portion of RM having been reused is still negligible. This thesis explores the feasibility of using RM as a combined source of metal oxides for layered double hydroxides (LDHs) synthesis and evaluates the characteristics of the as-synthesised products and their potential in practical applications. LDHs have received great attention recently for their unique structural properties and diverse applications, such as catalysts and catalyst precursors, anion exchangers, flame retardants, electroactive and photoactive materials etc. In particular, LDHs are excellent anion clay materials that often have high removal capacity for organic and inorganic water pollutants as adsorbents.

Two RM samples were sourced from Aluminium-Oxide Stade GmbH (AOS) in Germany and Aughinish Limerick plant in Ireland, respectively. In the first part of this thesis, a thorough characterisation of RM raw materials was performed. Based on the review of RM surface chemistry and the conventional ways for preparing LDH, four different synthetic scenarios were proposed. The key operating parameters include different pre-treatments (heat treatment, dry grinding and wet grinding) and process variables (dispersion, M^{II}/M^{III} ratio, liquid-to-solid ratio and aging condition). Subsequently, the physiochemical properties of the as-synthesised products were characterised to assess if they meet the 'golden rules', i.e., agree with a set of structure features of a typical LDH. The formation of LDH phases was most easily observed in Scenario III products, which were named as RM-LDHs and synthesised from Ireland RM and reactive MgO. The optimal experimental parameters were determined, which were CO_3^{2-} solution environment, L/S ratio = 20, M^{II}/M^{III} ratio = 3.0 and aging at 70°C

for 72 h. RM-LDHs were recognised to be carbonates intercalated Mg^{2+}/(Al^{3+}, Fe^{3+})-LDH, with a higher substitution of Fe^{+3} than Al^{3+} in the hydroxide sheet.

The 'role plays', i.e., chloride binding study and dye adsorption study, were carried out to further understand the anion removal capacity, thermal stability and 'memory effect' of the synthesised products. A material screening test was firstly conducted, suggesting RM-w-CLDH (calcined RM-LDH with wet grinding pre-treatment) was the optimal product for chloride removal. While the raw materials for synthesising RM-LDHs exhibited significantly lower sorption capacities, indicating the removal of chloride was mostly contributed by the CLDH phase in RM-w-CLDH. Batch sorption studies found the chloride sorption capacities of RM-w-CLDH and commercial CLDH were 53.3 mg/g and 17.3 mg/g. Microstructural characterisations revealed that ion exchange and reformation of the initial layered structure via 'memory effect' were the main sorption mechanisms for RM-w-CLDH. This agrees well with the literature and further confirms the existence of LDH structure in RM-w-LDH.

In the last section, the selected RM-LDHs were investigated for Remazol Brilliant Blue R dye (RBB) immobilisation. RBB is among the reactive dyes, widely used in textile industry and however, it is a harmful dye and can damage aquatic and vegetal life. The non-biodegradable and chemically stable characteristics of RBB make it difficult to be removed from effluents using conventional treatment process. Adsorption appears to be a viable way to control the dye pollutant in wastewater. In the present research, sorption studies were also performed for raw materials and the commercial Mg/Al LDH as comparisons. All adsorbents showed certain sorption for RBB and the calculated sorption capacities were in the order of RM-w-CLDH > RM-w-LDH > RM-d-LDH > Commercial LDH > RM > CRM (i.e., calcined red mud). The sorption mechanisms were determined through batch sorption tests and microstructure characterisations. Reconstruction of LDH structure and partial intercalation of RBB ions were suggested to be the main sorption mechanisms for RM-w-CLDH. Regeneration study indicated that the contaminated sorbent RM-w-CLDH-R could be cleaned up by calcination treatment and reused in dye sorption. After the 3rd adsorption cycle (and the 2nd regeneration cycle), the removal rate maintained at 87.2% of the original RM-w-CLDH. In terms of RM-LDHs, ion exchange and external surface adsorption were the dominant mechanisms. For the raw material IRM and Cal-IRM, however, the adsorption rate constants were much lower, and the equilibrium took longer to be achieved. Physical adsorption was the main sorption mechanism. The physicochemical characteristics of RM-LDHs, RM-w-

CLDH and commercial LDH, including the BET surface area, pore size, total pore volume and particle size, were not the controlling factors to the sorption performance.

In summary, this thesis proposed a novel strategy for RM reuse, working as a proof-of-concept. It confirmed that LDHs were successfully synthesised from RM, and RM-w-CLDH in particular has a great potential to serve as chloride inhibitor and dye amendment in wastewater. However, the effectiveness of this synthesis is sensitive to the origin of RM. Follow-up research is encouraged to consider more precise control of the M^{II}/M^{III} ratio and reaction pH. The predominant drawback of RM-LDH products is the impurities, some inherited from RM and some formed during the synthesis. Further study is expected to identify the effects of these impurities in environmental applications.

Acknowledgement

This work would not have been possible without the love and support of Cambridge around me. I can never repay the assistance (face-to-face or remotely) that I've received over the past few years nor fit the names of everyone that has guided me onto this small page.

First of all, huge thanks to my supervisor Professor Abir Al-Tabbaa for her continuous support and patience over the past few years. Sincere thanks go to my advisor Dr. Stuart Scott for your advice and comments during the review meetings. My gratitude also goes to Chris Knight, Dr. Rod Lynch, Anthony Dennis, Dr. Liwu Mo and Simon Griggs for their constant help in the labs.

Special thanks go to Dr. Fei Jin, Dr. Zhengtao Shen, Dr. Wenting Mao, Dr. Wai Yuk Lau and Dr. Livia Ribeiro De Souza for your incredible friendships and advices. And to everybody else in the GRO office during 2014-2019: thank you so much for making it a happy, warm and supporting place every day.

I would also like to thank Ms. Nicola Cavaleri at Language centre for reviewing the thesis drafts, and to Dr. Raffaele Vinai in Professor Marios Soutsos' research group and Dr. Albert Boehlke at Aluminium-Oxide Stade GmbH (AOS) company for supplying me with red muds to carry out this research.

I would not be here without the Schiff's Foundation and the Cambridge Trust Scholarships and would not have such unparalleled times in Cambridge without such a pure, intellectual and inclusive community. Thank you to Christ's College for being my home away from home and for always providing me friends, sports, great brunch and wines. Specially, big hugs to Louise Yirrell and Dee Kunze for always helping with dozens of requirements from me over the years.

Under the Covid-19 travel restriction policy in China, I am unable to attend the graduation ceremony. May I forever return to Christ's and to Senate House to find an old friend and have a small celebration.

Dedicated to my family, my hometown Hangzhou and the great town Cambridge, for always loving me, for no matter joyful and stressful times with me over the past seven year.

Table of Contents

List of Symbols and Abbreviations

Red mud & Synthesised products

AOS RM	*Aluminium-Oxid Stade GmbH red mud from Germany*
CRM	*calcined red mud*
Cal-IRM	*calcined IRM*
IRM	*Ireland red mud from Aughinish Limerick plant*
LDH	*layered double hydroxide*
CLDH	*calcined LDH*
RM	*red mud*
RM-I	*scenario I RM products*
RM-II	*scenario II RM products*
RM-III	*scenario III RM products*
RM-IV	*scenario IV RM products*
RM-CLDH	*RM-LDH after calcination*
RM-LDH	*RM-III products meet the 'golden rules' of typical LDHs*
RM-d-LDH	*RM-LDH from dry grinding synthesis route*
RM-w-LDH	*RM-LDH from wet grinding synthesis route*

Symbols

A	*absorbance*
A_{pHx}	*amount of acid needed to reach pH=x for sample weight M (ANC test)*
ANC_{pHx}	*acid neutralisation capacity (ANC test)*
b	*Langmuir isotherm constant*
C_{aq}	*final sorbate concentration*
C_i	*initial sorbate concentration*

C_e	*sorbate concentration at equilibrium*
C_{max}	*highest initial sorbate concentration*
C_s	*calculated concentration of sorbate adsorbed to adsorbent*
Ct	*sorbate concentration at time t*
d	*basal spacing*
D_{50}	*median diameter of particle size distribution*
Hc	*coercivity*
k_1	*pseudo-first-order rate constant*
k_2	*pseudo-second-order rate constant*
k_i	*intraparticle diffusion coefficient*
K_f	*Freundlich isotherm constant*
m	*mass of adsorbent*
M_{max}	*maximum applied magnetic field*
Mr	*remanence magnetization*
Ms	*saturation magnetisation*
n	*adsorption intensity*
N	*normality of standard acid*
N_{pHx}	*acid normality based on the buffer capacity around pH = x (ANC test)*
qe	*equilibrium adsorption capacity*
qt	*adsorbed amount at time t*
Qmax	*Langmuir adsorption capacity*
R^2	*correlation coefficient*
R_L	*separation factor*
S_{BET}	*BET specific surface area*
T	*temperature*
V	*volume of solution*
w	*moisture content in solid particle*

Abbreviations

AAS	*alkali-activated slag cement*
AEC	*anion exchange capacity*
AFm	*monosulfoaluminate*
ANC	*acid neutralisation capacity*
AO7	*Acid Orange 7*
ATH	*aluminium trihydroxide*
BANS	*boehmite-aluminium nitrate solution*
BET	*Brunauer–Emmett–Teller*
BFS	*Blast furnace slag*
BRDA	*bauxite residue disposal area*
CCD	*clarification and counter-current decantation*
CEC	*cation exchange capacity*
CH-1	*prepared concentrated Chloride solution*
CH-2	*prepared diluted Chloride solution*
C-S-H	*calcium-silicate-hydrate*
CR	*Congo red*
DTG	*derivative thermogravimetric analysis*
DSP	*desilication product*
EDX	*energy dispersive x-ray*
FT-IR	*Fourier-transformed infrared spectroscopy*
GGBFS	*ground granulated blast furnace slag*
IAI	*International Aluminium Institute*
IC	*ion chromatography*
ICP-OES	*inductively coupled plasma-optical emission spectrometry*
LOD	*limit of detection*

L/S	*liquid to solid ratio*
MC	*minocycline*
MO	*methyl orange*
pHpzc	*pH point of zero charge*
RBB	*Remazol Brilliant blue R*
REEs	*rare earth elements*
RSD	*relative standard deviation*
SEM	*scanning electron microscopy/microscope*
TGA	*thermogravimetric analysis*
UV-Vis	*ultraviolet–visible spectroscopy*
VSM	*vibrating sample magnetometer*
XRD	*powder x-ray diffraction crystallography*
XRF	*x-ray fluorescence analysis*

Chapter 1 Background and Introduction

In the face of climate change and increasing challenges in the supply of raw materials, the answer is to minimise emissions and waste, optimise the efficiency of resource utilisation, and exploit yet untapped alternative resources. Industries need to promote circular-economy practices. There has been much recent interest in seeking alternative feedstock for industrial processes, such as industrial waste and metallurgical by-products, to substitute raw materials. One key industrial waste that is currently either not or poorly valorised is bauxite residue from alumina refineries, more commonly known as Red Mud (RM). This thesis investigates the use of RM as starting materials to synthesise Layered Double Hydroxides (LDH) and apply them to environmental treatments. Chapter 1 gives an overview of waste management and some available technologies of synthesising valuable products from waste materials, as well as a brief introduction on how these products could be evaluated in adsorption studies.

1.1 Background of Waste Management

The increasing industrial and agricultural activities on a global scale, have resulted in the generation of various types of solid waste, which pose one of the most distressing problems to the society. In general, waste residues require physical and/or chemical treatment and then landfilled at specific sites such as tailing ponds. When wastes are disposed, it is crucial to ensure they remain physically, geographically, chemically and radiologically stable and inert, otherwise they must be isolated and avoided from interacting with the ecosystem (Bian *et al.*, 2012). The major waste treatment techniques are mechanical separation, residue washing, chemical stabilisation, solidification, vitrification, use of physical or engineered barriers and biological remediation (Amutha Rani *et al.*, 2008; Karaca, Cameselle and Reddy, 2018). In the long term, environmental monitoring or assessment studies should always be equipped in the disposal or reuse site.

However, conventional disposal routes have presented some drawbacks, such as occupation of land, high reagents and/or energy consumption, and generation of further toxic waste products. Recent studies have been actively seeking the alternative disposal methods and novel use of solid waste. Each kind of waste has its unique mineralogical and chemical characterisations, therefore has its own appropriate options for disposal or reuse. Among various industrial waste, red mud is a by-product occurred from the Bayer process during the production of alumina. The disposal of red mud leads to a long-term environmental burden

(Khairul, Zanganeh and Moghtaderi, 2019). The literature review will provide a detailed background of red mud management, with some of the up-to-date findings for red mud utilisation and recycling.

1.2 Utilisation of Waste-based Products

Over the last decades, much efforts have been made to pursue cost-effective and sustainable techniques to reuse waste materials or transform them to value-added products. Apart from reducing the volume for waste storage, waste utilisation can bring many additional benefits in environmental alleviation. In this context, a range of utilisation strategies have been developed, with varying degree of success, using various physical, chemical and biological methods to modify waste materials or derive some values. Some of the widely reported methods are mechanical activation, leaching, heat treatment, hydrothermal treatment or polymerisation, etc. (Blissett and Rowson, 2012; He *et al.*, 2013).

The potential utilisations of industrial waste include recovery of metals, synthesis of materials (e.g. zeolites, mullite, composite materials), preparation of construction materials, development of catalysts or catalyst supporters and, more recently, sink for CO_2 sequestration (Iyer and Scott, 2001; Raut, Ralegaonkar and Mandavgane, 2011; Chiang *et al.*, 2014; Gu *et al.*, 2014). To enhance the use of waste as raw materials has always been a core interest of our research group. Jin & Al-Tabbaa (2015) reported the production of more sustainable alkali-activated slag cements, which is based on ground granulated blast furnace slag. Shen et al. (2018) investigated biochars of different feedstocks for their performances in heavy metals remediation.

In practice, an interesting and versatile utilisation of solid wastes is to transform them into low-cost adsorbents for pollution control, including wastewater treatment, soil remediation and purification of flue gas. In recent years, a number of industrial wastes, such as fly ash, steel slag, red mud, rice husk ash, hazelnut shell, limestone and wood sawdust, have been studied and developed into functionalised adsorbents for either heavy metal or organic pollutants removal (Wang *et al.*, 2005; Ferrero, 2007; Blissett and Rowson, 2012). For instance, Kuwahara et al. (2010) reported on the conversion of blast furnace slag to Ca/Al hydrotalcite-like compounds and A/X-type zeolite by separated processes. Murayama et al. (2012) have employed aluminium dross leachates to synthesise different types of LDHs, which exhibited comparable anion exchange abilities with standard LDHs. In another study, Akin et al. (2012) took red mud to prepare magnetic Fe_3O_4 nanoparticles by using microwave

digestion and strong acid dissolution; and they found the product was effective in arsenic adsorption from aqueous medium. The mesoporous carbon nanocomposites, which was synthesised from a green biomass source, cotton fabric, demonstrated outstanding ability to remove organic dye and heavy metal ions from water (Chen et al. 2016).

Inspired by those works, this thesis attempts to take red muds as raw materials to prepare layered double hydroxides. LDHs have received great attention in recent years for their unique structural properties and tuneable compositions that allow their diverse applications, such as catalysts and catalyst supports, precursors for coatings, sorbent materials, anion exchangers, bioactive nanocomposites, electroactive and photoactive materials and flame retardant (Shanmuganathan and Ellison, 2014). Since very limited studies have considered using RM for LDH synthesis, the motivations behind the idea will be specifically explained in Chapter 2. And prior to a discussion on the possible synthetic strategy, the conventional techniques to produce LDHs will be briefly reviewed. Owing to the presence of interlayer spaces and exchangeable anions, LDHs show superior adsorption capacity for anionic ions (Yue *et al.*, 2017; Zubair *et al.*, 2017).

1.3 Basics of Adsorption Study

The contamination of water and groundwater is a widespread issue that can adversely impact human health and ecosystems. Adsorption, usually regarded as a powerful and sustainable technique to remediate these contaminations, has drawn extensive attentions. But the cost of the widely used adsorbent, for instance activated carbon, still remains expensive (Extremera *et al.*, 2012; Nasri *et al.*, 2014). For this reason, alternative adsorbents, derived from natural materials or industrial solid wastes, have been explored for their applications in water or soil to immobilise contaminants (De Gisi *et al.*, 2016). In the present thesis, RM-based products are examined for their potential in chloride binding and organic dye removal. The main adsorption mechanisms for chloride ions and organic dye will be introduced in Chapter 2.

The adsorption performance of sorbent agents is associated with their chemical, physical and structure properties. In this sense, adsorption studies can be carried out as the underpinning for the evaluation of the as-prepared materials. Batch sorption experiments are generally performed to determine sorption rate and sorption capacity. Meanwhile, the effects of solution pH, temperature and co-existing anions on the sorption process are usually investigated (Zhao et al., 2017). A better understanding of the sorbents and the sorption mechanisms helps to predict the strategy of desorption or the long-term stability of the

immobilisation. However, adsorption studies can only indicate the sorption mechanisms indirectly. In order to clearly identify the interactions between adsorbent and adsorbates, further microstructural characterisations are suggested (Cheng *et al.*, 2016). It is important to highlight the characterisation of mineral wastes is sometimes very challenging, due to their structurally disordered, chemically complex and multiphase nature (Castaldi *et al.*, 2010; Provis, Palomo and Shi, 2015).

1.4 Aims and Objectives

The main aims of this thesis are to investigate the feasibility of utilising red mud as the raw material for LDH synthesis and to assess how the as-synthesised RM-LDHs will perform in adsorption studies. The latter parts of the research focus on chloride binding and dye removal, which were intended to reflect the properties of RM-based products. This thesis mainly acts as a proof-of-concept, exploring an innovative recycling strategy of red mud. This will also contribute to expanding the knowledge of generating valuable products from other kinds of mineral wastes.

The primary objectives are:

- to examine if RM has the potency to be the starting material for LDH synthesis;
- to investigate the viable modification and/or synthesis methods, including feasible pre-treatments and process variables;
- to identify if the as-synthesised products meet the ‘golden rules’ of the LDH phase;
- to evaluate the chloride binding capacity of RM-LDHs;
- to understand the role of RM-LDHs for organic dye adsorption.

1.5 Thesis Structure

This thesis is comprised of seven chapters:

Chapter 1 Background and introduction

Chapter 1 provides a background to waste management, utilisation of waste-based products and basics of adsorption study. It also clarifies the objectives and structure of this thesis.

Chapter 2 Literature review

Chapter 2 provides a review of existing literature for the industrial management of RM, the conventional methodologies of synthesising LDH, the relevant considerations of employing RM in LDH synthesis, and finally the adsorption studies for chloride and organic dye. It

identifies the research gaps, limitations and interests for further research. The schematic framework of this thesis is outlined in this chapter.

Chapter 3 Materials and methods

Chapter 3 describes the materials involved, and the methodologies for all the laboratory experiments, characterisations and analyses.

Chapter 4 Synthesis routes of RM-LDHs using red mud

Chapter 4 investigates the LDH phase synthesis routes starting with RM and the influence of pre-treatments and process variables. This chapter also identifies the basic characteristics of as-synthesised RM-LDHs (if any).

Chapter 5 Synthesised RM-LDHs for chloride binding

Chapter 5 relates the RM-LDHs obtained in Chapter 4 and evaluates the relevant products as chloride inhibitors. It selects the materials from as-synthesised RM-LDHs that exhibit the optimum binding capacity. It then analyses the products obtained and links to further research in Chapter 6.

Chapter 6 Synthesised RM-LDHs for dye removal from wastewater

Chapter 6 investigates the performance of two types of RM-LDHs in the sorption tests of Remazol Brilliant Blue R dye (RBB). It conducts detailed comparisons with commercial LDH and calcined RM-LDHs. Characterisation results are presented, and a possible sorption mechanism is discussed.

Chapter 7 Conclusions and Recommendations

Chapter 7 summaries the key findings and generates recommendations for future work. The limitations of the present thesis are acknowledged, and follow-up research is suggested.

Chapter 2 Literature Review

This chapter provides a comprehensive review of the literature to date relevant to the synthesis of layered double hydroxides using red mud, as well as a detailed analysis of uncertainties and knowledge gaps. First, it introduces the background of industrial waste red mud and its current disposal and utilisation. This is followed by a review of how it has been modified for various environmental applications. The properties of layered double hydroxides (LDH) and conventional synthesis methodologies are then outlined, and innovative synthesis methods using red mud as the raw material are explored. The characterisations and applications of LDH products for chloride binding and the removal of acid dye contaminant are reviewed, and the comparisons between different sorbents and sorption outcomes are drawn based on the literature. Finally, this chapter identifies the major research gaps and how these will shape further study.

2.1 Bauxite Residue, its Production, Properties and Treatment

2.1.1 Aluminium Industry and Bauxite Residue Generation

Aluminium is a comparatively contemporary metal and has been in use for only about 150 years. More aluminium is produced currently than any other non-ferrous metal. It is one of the most widely used metals in the transport, construction, packaging and electrical sectors, and has the advantage of being light, strong, durable, flexible, impermeable, conductive and non-corrosive (International Aluminium Institute (IAI), Australian Aluminium Council and Brazilian Aluminium Association, 2018). A simplified flowsheet of aluminium industry is shown in Figure 2.1.

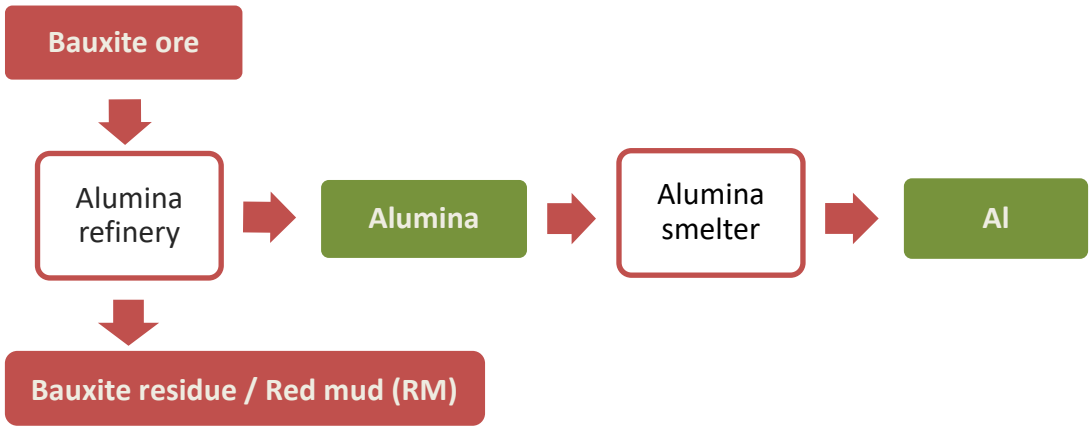

Figure 2.1 Aluminium industry flowsheet and its connection to Bauxite residue / Red mud.

Bauxite is the primary ore used to extract alumina and produce aluminium (see Figure 2.2 (a-d)). Bauxite residue, also named Red Mud (RM), is the aluminium industry's largest solid waste stream (see Figure 2.2 (e-f)), the by-product from the digestion of bauxite ore for alumina extraction in the caustic Bayer process at temperatures of between 150ºC–230ºC under pressure. Bauxite is a lateritic rock consisting of a mixture of oxides and aluminium hydroxides, such as diaspore, boehmite and gibbsite, with other materials of various consistencies, mainly silicon-bearing clay minerals, titanium oxides and carbonates (Si, Ma and Lin, 2013; Sutar *et al.*, 2014; Verma, Suri and Kant, 2017). From an economic perspective, bauxite with a high content of alumina (60% - 75%), deriving from syenites and feldspathoid syenites, is most desirable. Mineral reserves exist in many countries including Australia, Brazil, China, Greece, Guinea, Hungary, India, Vietnam and etc (IAI, 2013). The Bayer process dominates around 90% of alumina production, while the sintering process or a combination of these two constitute the other 10% (Sutar *et al.*, 2014; Ujaczki *et al.*, 2018).

In the Bayer process, bauxite undergoes the following phases which yield bauxite residue: milling, pre-desilication, digestion, clarification and counter-current decantation (CCD) washing (Power, Gräfe and Klauber, 2011). The bauxite residue is formed during digestion and then separated from the green liquor ($NaAl(OH)_4$ solution). The bauxite residue is successively transferred to the CCD washer trains, where it is repetitively washed and thickened in order to recover soda (NaOH) and alumina-bearing species ($NaAl(OH)_4$). After CCD washing, the bauxite residue is usually treated in a final thickener and conveyed into the bauxite residue disposal area (BRDA) (Power, Gräfe and Klauber, 2011; Sutar *et al.*, 2014).

(a) Bauxite

Reference: International Aluminium Institute

(b) Bauxite Stockpile

(c) Bauxite, Alumina, Aluminium

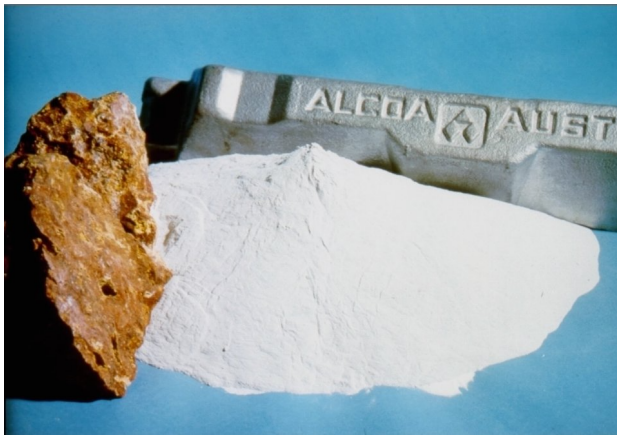

Reference: International Aluminium Institute

(d) Aluminium Foil

(e) Bauxite Residue / Red Mud

Reference: Hard Rain Project
http://www.hardrainproject.com/hrpl?n=3133

(f) Bauxite Residue Disposal Area–Aughinish Ireland

Reference: International Aluminium Institute

Figure 2.2 Bauxite, Aluminium products and Red mud

2.1.2 Global Demand and Production

Worldwide, there are around 80 active Bauxite processing plants, widely spread in Europe (22), Asia (18), Australia (7), South America (12), North America (11) and China (an increase from 7 in 2001 to 49 in 2011) (Dentoni, Grosso and Massacci, 2014; Wang *et al.*, 2018). Data from the International Aluminium Institute (IAI) statistical system revealed that global alumina production in the period of 1998 – 2018 aggregated to more than 1.6 billion metric tonnes. As plotted in Figure 2.3 (a) & (b), the trend demonstrates a continuous growth in global production, and also the establishment of new production regions like China, with a comparatively minor change in Europe. The aluminium demand is forecast to grow consistently at more than 4% until 2030 (International Aluminium Institute (IAI), Australian Aluminium Council and Brazilian Aluminium Association, 2018).

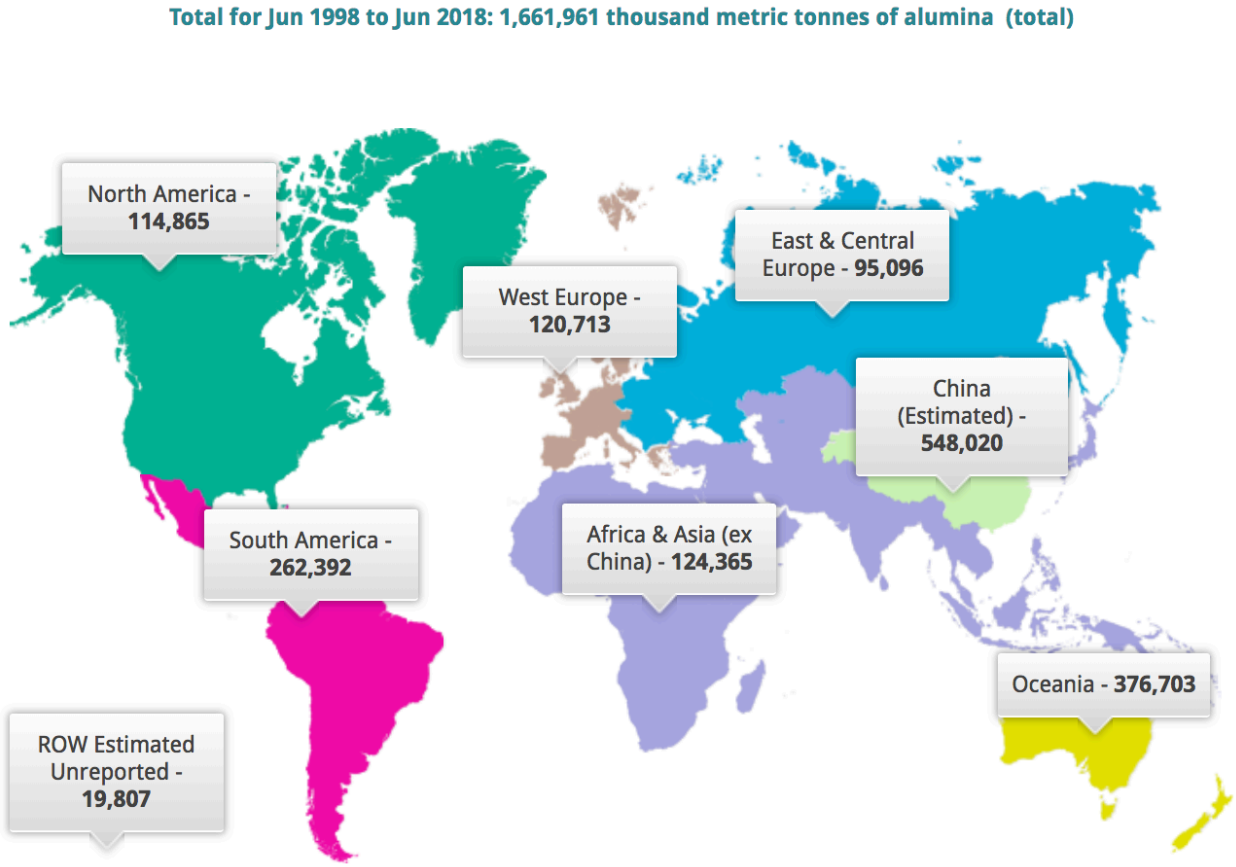

The data used to generate this graph have been derived exclusively from voluntary reports of International Aluminium Institute (IAI) member and non-member companies. China Estimated Unreported is not included.

Figure 2.3 ***(a)*** *Global alumina production trend for 1998-2018, map view exported from International Aluminium Institue (IAI) (2018).*

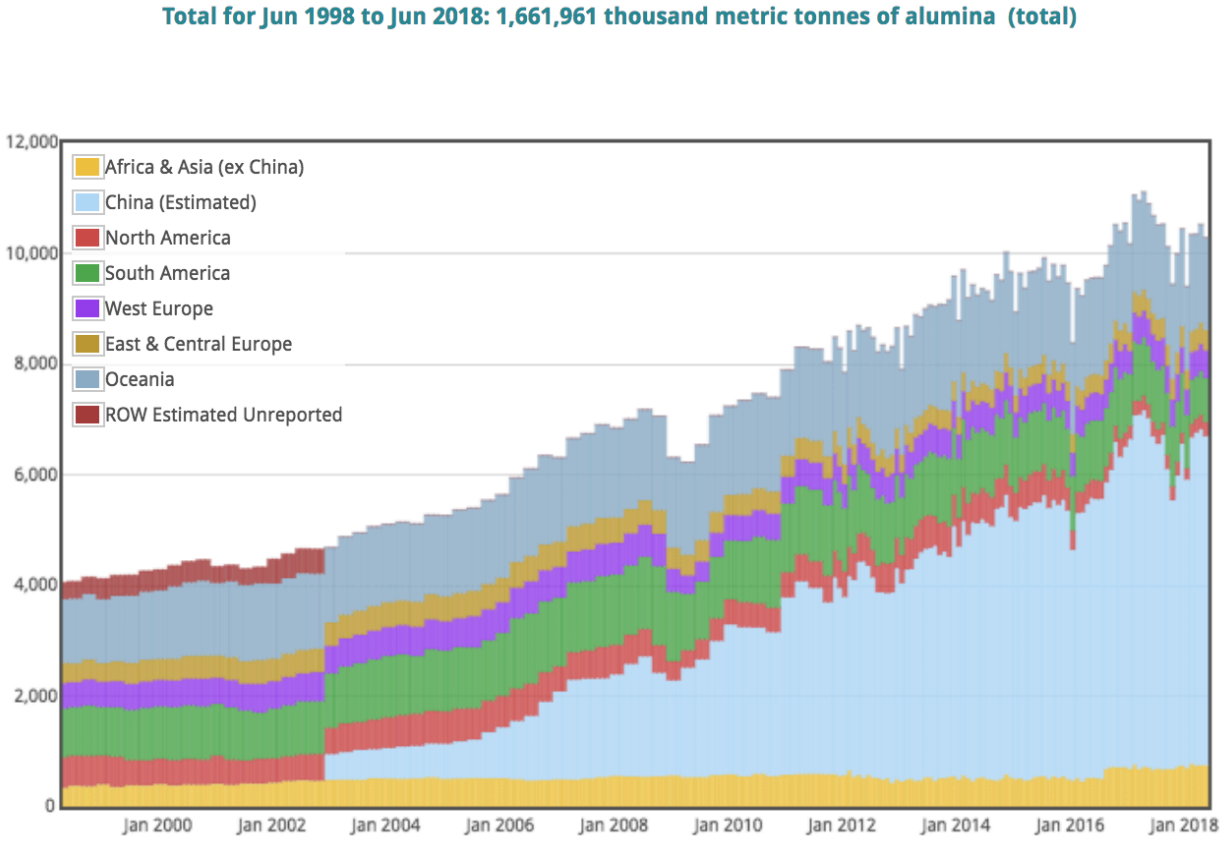

Figure 2.3 ***(b)*** *Global alumina production trend for June 1998-June 2018, histogram view exported from International Aluminium Institue (IAI) (2018).*

Generally, bauxite residue is generated at a rate of about 1.0–6.0 tonnes per tonne of alumina generation (International Aluminium Institute (IAI), Australian Aluminium Council and Brazilian Aluminium Association, 2018; Ujaczki *et al.*, 2018), depending on the initial bauxite-ore grade and the alumina's extraction efficiency. To sustain current and future demand, there has been and will continue to be an increase in alumina production, as well as in the amount of red mud. Amongst the over 150 million tonnes of RM generated annually, 6.8 million tonnes are in Europe alone, as shown in Table 2.1 (Balomenos, 2018; Ujaczki *et al.*, 2018). In addition, there are at least another 50 closed legacy sites. The combined stockpile of RM at active and legacy sites is estimated to be about 3.4 billion tonnes (Wang *et al.*, 2018).

Table 2.1 European Alumina and Red mud production

Country	Location	Total Alumina Annual Capacity (kt)	Estimated Red Mud (kt)
Greece (AoG)	Viotia	850	750
Ireland (AAL-RUSAL)	Aughinish	1,990	1,800
Romania (ALUM)	Tulcea	500	450
France (ALTEO)	Gardanne	635	570
Germany (AOS)	Stade	1,050	950
Spain (ALCOA)	San Ciprian	1,500	1,350
Turkey	Seydisehir	490	440
Bosnia & Herzegovina	Birac	600	540
	TOTAL	7,615	6,850

Source of Data: (Balomenos, 2018)

2.1.3 Properties of Red Mud

Red mud is produced as a red slurry, primarily composed of the insoluble fraction of bauxite ore. Differences in bauxite ore sources or refining processes generate RM's variety of physical, chemical, and mineralogical properties. RM possesses a complex mineral mixture, with approximately 30% of the mineralogy existing in the amorphous phases, and the remaining 70% in the crystalline phases (Wang, Ang and Tadé, 2008). RM contains more than 30 minerals, and the majority of these minerals originate from parent rock weathering (Grafe, Power and Klauber, 2009). A typical order of elemental abundance within the red mud is Fe > Al > Si ~ Ti > Ca > Na, present in the form of oxides Fe_2O_3 (30-60%), Al_2O_3 (10-20%), SiO_2 (3-50%), Na_2O (2-10%), CaO (2-8%) and TiO_2 (trace-10%), which is similar to raw bauxite (Wang, Ang and Tadé, 2008; Sahu, R. K. Patel and Ray, 2010). The alumina extraction process also initiates a number of secondary minerals, including desilication products, as well as carbonates, oxides and hydroxides (Evans, 2016). Amongst these minerals, hematite is the most ubiquitous component, together with goethite, magnetite, gibbsite, sodalite, perovskite, quartz and etc. The minerals' forms and chemical composition are listed in Table 2.2 (IAI, 2013; Collins, Clark and Payne, 2014; Sutar *et al.*, 2014; Verma, Suri and Kant, 2017).

Table 2.2 Common Mineral Composition and Contents of Bauxite Residue

Component	Typical Range (%)
Sodalite ($3Na_2O.3Al_2O_3.6SiO_2.Na_2SO_4$)	4-40
Goethite (FeOOH)	10-30
Hematite (Fe_2O_3)	10-30
Magnetite (Fe_3O_4)	0-8
Silica (SiO_2) crystalline and amorphous	3-20
Calcium aluminate ($3CaO.Al_2O_3.6H_2O$)	2-20
Boehmite (AlOOH)	0-20
Titanium Dioxide (TiO_2) anatase and rutile	2-15
Muscovite ($K_2O.3Al_2O_3.6SiO_2.2H_2O$)	0-15
Calcite ($CaCO_3$)	2-20
Gibbsite ($Al(OH)_3$)	0-5
Perovskite ($CaTiO_3$)	0-12

Trace metal elements

Additionally, a variety of trace elements or metal oxides may exist at trace levels, for instance arsenic (As), beryllium (Be), cadmium (Cd), chromium (Cr), copper (Cu), gallium (Ga), mercury (Hg), lead (Pb), manganese (Mn), nickel (Ni), potassium (K), thorium (Th), zinc (Zn), etc. (IAI, 2013; Khairul, Zanganeh and Moghtaderi, 2019). Many of the valuable elements are included in the 2017 list of Critical Raw Materials for the EU (Blengini *et al.*, 2017). The undissolved elements would be eliminated together with bauxite residue, whilst soluble elements in the Bayer process either build up in the Bayer liquor, or precipitate along with the aluminium hydroxide (IAI, 2013). It is noted that bauxites contain very low concentrations of naturally occurring radioactive materials (in the mg/kg range), which give rise to extremely low levels of radioactivity, at or below naturally occurring radioactivity found in granite rocks. Most of the radioactive species consequently remain in the bauxite residue. A considerable amount of studies indicated that there was no problem in leachability of radioactivity from the bauxite residue (IAI, 2013).

Alkalinity

The caustic nature of red mud (pH 10.5-12.5) is derived from the remaining caustic soda (after wash) and the soluble sodium content (NaAlOH, Na_2CO_3 and NaOH) in the liquor

(Kounalakis, Aravossis and Karayianni, 2016; Verma, Suri and Kant, 2017; Nikbin *et al.*, 2018). These alkaline anions in bauxite residue solution are OH^-, CO_3^{2-}/HCO_3^-, $Al(OH)_4^-/Al(OH)_{3(aq)}$ and $H_2SiO_4^{2-}/ H_3SiO_4^-$ (Gräfe, Power and Klauber, 2011). Alkalinity also links with the solid surfaces of the residues, such as tricalcium aluminate, and can also be formed with other anions such as phosphate, zincate and titanate, as well as with cations such as magnesium and potassium, which is normally equal to ~30g/kg as $CaCO_3$.

Particle size

Apart from chemical composition, other parameters that affect RM's applications are the residual sodium species, the particle size and the moisture content. Red mud contains various particles with different sizes and shapes. With reference to the grain size distribution, on which the physical properties of the red mud mainly depend, two classes are usually distinguished: sand (coarse grains >100 μm) and the majority of the mud (80% of grains with a size <100 μm). The average specific surface area of RM is 32.7±12.2 m^2g^{-1}, typically in the range of 15 to 58 m^2g^{-1} (Grafe, Power and Klauber, 2009; Ujaczki *et al.*, 2018), depending on the degree of grinding of bauxite.

Surface charge

Red mud particles carry a significant negative charge under basic conditions due to ionized OH groups on their surface. The surface charge property is usually defined as the point of zero charge (pH_{pzc}) – the pH at which the net charge on the surface is zero. Atun & Hisarli (2000) employed the potentiometric technique and reported that the pH_{pzc} of red mud was 8.3 in low concentrations of NaCl, CsCl and $SrCl_2$. Chvedov et al. (2001) presented slightly lower pH_{pzc} values at 6.5-7.7. Both results are close to the pH_{pzc} of Fe_2O_3, Al_2O_3 and TiO_2, which is around 7-8 (Parks, 1965).

Given the characteristics of fine particles, high alkalinity and trace metal content, a large quantity of RM in ponds or abandoned mines poses a massive disposal issue for the alumina industry worldwide (Rai *et al.*, 2012, 2013; Sutar *et al.*, 2014). According to EU Regulations, bauxite residue is classified as non-hazardous waste, with the identification code 01 03 09 (Dentoni, Grosso and Massacci, 2014), since its residual sodium hydroxide (0.2-0.6% typically) is below the 1% hazardous threshold. However, it still leaves serious landfill problems and the risk of leaching, which may pollute the soil and groundwater and have negative effects on living organisms.

2.1.4 Available Red Mud Disposal Methods

Refineries around the world have disposed of and still dispose of red mud in a variety of ways, depending on the location, the start-up time, the size of the refinery, the nature of the residue and the legislative requirements. The cost of bauxite residue disposal is high, accounting for about 2% of the alumina price (Sutar *et al.*, 2014). The most common disposal and storage methods are marine discharge, lagooning, dry stacking and dry disposal, as summarized and compared in Table 2.3.

Table 2.3 Summary of various disposal methods of red mud (Power, Gräfe and Klauber, 2011; Rai *et al.*, 2012; IAI, 2013)

	Methods	Disadvantages
Marine discharge	RM slurry after washing is directly pumped into the deep ocean (>3 km) via a pipeline.	1) Less recovery of caustic owing to no return of water; 2) Extensive pipeline requirement; 3) Direct contact to the marine environment, that poses the highest impact on the environment. It is pointed out as 'strongly discouraged by the 1981 UNEP/UNIDO workshop.
Lagooning	RM slurry is directly pumped into the tailing ponds at a low solid level, where allows the consolidation process to form a drier residue. The land-based ponds are fully fabricated structures with linings to achieve secure containment.	1) High risk of leakage and dam failure; 2) Considerable physical footprint required; 3) High evaporation climate required.
Dry stacking	RM slurry is thickened to 48-55 wt% solids, flows down to form layers of uniform thickness at an angle of 2º to 6º. The pastes are then air-dried or be facilitated with under-drainage before discharge of next layer, to achieve a final density of approximately 65-70% solid	1) Additional stage of filtration required; 2) Increase dust generation and requires funds for its long-term closure; 3) Hardly to achieve in locations of low net evaporation.
Dry cake disposal	RM slurry is thickened and filtered to a dry cake with a solid level >65 wt%. Then it is washed on the filter to recover soda. Since the dry cake is not pumpable, it is transported to the disposal area by convey or trucks.	1) Requires installation and operation of filtration plant; 2) Needs to overcome the pressure drop to obtain sufficiently 'dry' cake.

Table 2.4 provides an overview of the status of major alumina plants in Europe. At present, at the Aughinish plant in Ireland, every year 1.83 km^2 land is occupied, due to the production of 1.2 million tonnes of red mud (Balomenos, 2018). Furthermore, extensive labour and material resources are required to build and maintain RM disposal dams. However, there is still a risk of contamination for the surrounding environment. Catastrophic accidents of RM storage have occurred from time to time, such as in Ajka Hungary 2010, where a red mud dam collapsed, killing 10 people, and causing another 150 to suffer from severe chemical burns. In Luoyang (China) in 2016, a waste dam broke and swept down the mountainside releasing 2 million m^3 of RM and submerging the whole village (Novais *et al.*, 2018). The red mud also destroyed many farms, domestic animals and a nearby river, which triggered public fears regarding RM management. These accidents indicate the challenge of residue disposal, and the subsequent excessive environmental and economic impact.

Table 2.4 The main characteristics of the 8 alumina plants in the EU (Dentoni, Grosso and Massacci, 2014)

Refinery	Disposal Period	Percentage of Reuse	Disposal Method	Residue Production Rate (kt/year) *	Residue Disposal Area (ha)
Ludwigshafen	1976–2014	0%	Dry stacking	n.d.	6.5
Stade	1973	0%	Lagooning	1500	150
Gardanne	1893–2012	0%	Sea discharge	690	29.4
	2012–2014	30% **	Sea discharge/Dry stacking	n.d.	29.4
San Ciprian	1981–2014	0%	Dry stacking	2175	84
Aughinish	1983	0%	Dry stacking	3000	121
Mytilineos Group	1966–2012	0%	Sea discharge/ Dry stacking	1200 ***	
	2012–2014		Dry stacking	830	19
Eurallumina	1977–2009	0%	Lagooning	1200 ****	120
	From 2016	-	Dry disposal		

* Estimated as 1.5-times the alumina production rate [1]; ** bauxaline patent; *** in the last part of the indicated period, the amount of waste discharged into the sea was progressively reduced in favor of dry disposal; **** 2009 bauxite residue (BR) production.

2.1.5 Available Red Mud Neutralisation Methods

In light of the complex chemical and physical features of RM, neutralisation and a certain amount of dilution are essential for any long-term disposal solution. This is generally achieved through a pH-reduction processing step. Partial or complete neutralisation of the residues is sometimes implemented; this can be accomplished by the use of acids (normally sulphuric acid or hydrochloric acid), carbon dioxide, sulphur dioxide, seawater or concentrated reject brine (Ujaczki *et al.*, 2018). Although a variety of neutralisation methods have been investigated, the following three main techniques (I-III) provide the greatest potential.

I. Seawater neutralisation

Seawater neutralisation is generally only available to plants close to oceanic water, and up to 20 times the amount of seawater is required to process an equivalent amount of red mud (Couperthwaite *et al.*, 2014). Through the introduction of seawater, anionic ions like CO_3^{2-} and aluminate ions are precipitated out with Mg^{2+} and Ca^{2+} ions to form alkaline solids, in particular hydrotalcite ($Mg_6Al_2(CO_3)(OH)_{16}\cdot 4(H_2O)$) and calcite ($CaCO_3$) (Koumanova, Drame and Popangelova, 1997). This buffers the residue solution in the range of pH 8 to 9 and a total alkalinity < 200 mg/l (as $CaCO_3$ equivalent) can be achieved (Palmer, Frost and Nguyen, 2009; Sutar *et al.*, 2014), accompanied by additional benefits (Hanahan *et al.*, 2004):

(i) A decrease in the use of freshwater;
(ii) An increase in the settling rates of ponds due to agglomerate consolidation;
(iii) An increase in the acid neutralisation capacity;
(iv) The improvement of soil properties after rehabilitation.

However, seawater neutralisation does not eliminate OH^- from the system as it continues to exist in the form of less soluble, weakly alkaline solids $Ca(OH)_2$.

II. Mineral acid neutralisation

Since a large amount of acid is required for neutralising RM, mineral acid that is available at low cost is another option indicated by McConchie et al. (2002). However, mineral acid would remove all the (solid) alkalinity, leaving the RM as a useless starting material for a range of applications and not improving its physical properties (Mcconchie *et al.*, 2006). Compared to seawater neutralisation, mineral acid's performance in carrying off aluminate

from solution is drastically less effective because it merely relies on the precipitation of aluminate hydroxide instead of hydrotalcite (Klauber, Gräfe and Power, 2011).

III. CO_2 neutralisation

Gaseous CO_2 from either the atmosphere or industrial emissions is bubbled into the RM slurry prior to dry stacking and large-scale CO_2-neutralisation of bauxite residues. This process began in 2000 at Alcoa's Kwinana refinery in western Australia (Power, Gräfe and Klauber, 2011). Provided with sufficient drying time, the RM in an open pond can be stabilised at a pH of less than 10, with less dusty conditions (IAI, 2013). The carbonation process also facilitates the drying process, allowing faster deposition of the next layer of residue onto the storage area and thereby decreasing the area required for storage. In spite of the significant start-up cost, from a climate change perspective, CO_2 treatment offers the additional benefit of locking up carbon dioxide. CO_2 is normally available as a by-product from nearby plants and is otherwise released into the atmosphere (Grafe, Power and Klauber, 2009; Klauber, Gräfe and Power, 2011; Sutar *et al.*, 2014). For instance, Alcoa's Kwinana carbonation plant has the ability of locking up 70,000 tonnes of CO_2 a year, which is equivalent to eliminating over 17,500 cars from the road (IAI, 2013). In light of the current production rate of RM, it is possible for approximately 6 million tonnes CO_2 to be sequestered annually through atmospheric carbonation (Si, Ma and Lin, 2013). Proper amenders like gypsum and other organic wastes may be incorporated with CO_2 to mitigate the caustic bauxite residue (Rai *et al.*, 2012).

2.1.6 Available Red Mud Utilisations Methods

The ever-growing demand for bauxite residue disposal space, along with increasingly limited land availability, has the potential to ultimately threaten both the established alumina industry and the environment. There is a need to provide optimised means of storage and remediation, and to develop options for utilising large-quantities of RM as an industrial by-product. As discussed in Section 2.1.3, bauxite residues contain considerable amounts of valuable elements. On the World Economic Forum, Jones (2017) pointed out the huge potential and significance of 'enhanced landfill mining', where recoverable materials in the landfilled industrial waste are extracted and further transformed into products. A vast amount of research has been conducted to develop applications for bauxite residues. The utilisations of RM lie in almost all areas of inorganic material science, including (i) recovering specific

elements (e.g. iron, aluminium or rare earths); (ii) using RM as the source of a particular component (e.g. iron and alumina in cement); (iii) developing RM for specific uses (e.g. pigments and paints); (iv) preparing RM for catalysts; (v) or using RM as an impervious material for covering landfill (Sutar *et al.*, 2014; Verma, Suri and Kant, 2017), as demonstrated by the more than 700 patents for RM processing since 1964 in Figure 2.4.

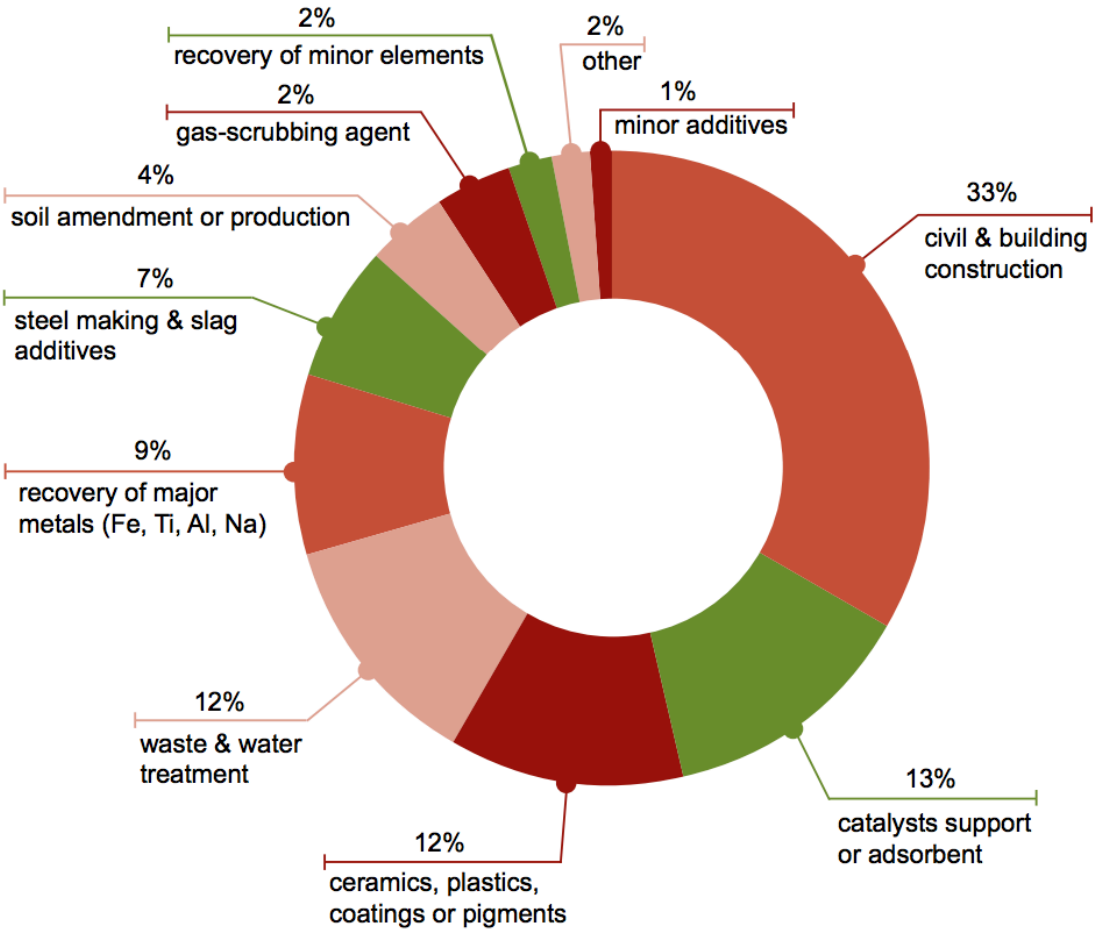

Figure 2.4 Patents on red mud processing – areas of intended usage

I. Construction materials

Producing different kinds of building materials with bauxite residue (e.g. binders, geopolymers, glass-ceramics and coating materials) is a direct, simple and quick way to expend the substance. Bauxite residue has been of interest to the Portland cement industry for over 75 years, attributing to its rich aluminium and iron content that provides cement with improved strength and setting characteristics (IAI, 2013). Moreover, the environmental performance of lightweight concrete benefits from using 25% RM replacement (Nikbin *et al.*, 2018). However, the presence of sodium ions (alkali content) as well as chromium content

could be of concern, if too high a proportion of bauxite residue (>1%) is used (Wang *et al.*, 2018). Dewatered, compacted RM could also be a good road building material when it is blended with an appropriate binder. For instance, the construction of the Perth to Bunbury Highway applied around 25,000 m^3 Red Sand® from Alcoa, Australia (IAI, 2013).

Geopolymers possess a number of potential uses as a replacement for Portland cement and for advanced high-tech composites and ceramic applications (Sutar *et al.*, 2014). The formation of geopolymers involves the chemical reaction between RM and alkali metal silicate solution and then the polymerisation of a –(-Si-O-Al-O-)n- polymer chain structure (Rai *et al.*, 2012). Furthermore, RM is also considered as a potential material by brick production, where it is mixed with clay, shale, sand and fly ash (Rai *et al.*, 2012). The high levels of sodium ions once again affect the long-term weathering resistance and durability of the bricks; therefore, the sodium should be replaced by calcium.

II. Metal recovery

The high percentage of iron oxides (mainly as hematite) in RM has attracted much interest in its recovery. Several methods have been proposed, such as roasting magnetic recovery, the reducing smelting method, the direct magnetic separation method and the leaching-extraction method (Sutar *et al.*, 2014). However, these methods are not that economically viable since iron in the red mud needs to first be converted into magnetite using reductants at temperatures as high as 400-1000°C prior to magnetic separation (Qiu *et al.*, 1995; Rai *et al.*, 2012). The later recovery of iron from the magnetic separation method still requires a higher temperature. The titanium recovery is of greatest interest as well (Agatzini-Leonardou *et al.*, 2008).

III. Wastewater treatment

Neutralised red mud as an inexpensive adsorbent is effective in water treatment for removing toxic heavy metals and metalloid ions, inorganic anions such as NO^{3-}, F^-, PO_4^{3-} and organics like dyes, phenolic compounds and bacteria (Huang *et al.*, 2008; Wang, Ang and Tadé, 2008; Bhatnagar *et al.*, 2011; Rai *et al.*, 2012). For example, at sewage treatment plants in the UK, Bauxsol® in pellet form has successfully decreased the phosphorus level to <0.06 mg/L in the final effluent that comfortably meets the EU Habitats Directive (IAI, 2013). Based on various studies focusing on different elements, the removal efficiency is sensitive to parameters including pH, ionic strength, adsorbent dosage, initial pollutant concentration and

source water composition. Entrapped metals are not easily exchangeable and removable. However, more investigation is encouraged to further explain the metal trapping mechanisms of red mud.

IV. Soil remediation

Soil amendment is an appealing way to utilize a great bulk of red mud. RM has a favourable environmental repair effect on acidic and sandy soils. Extensive laboratory, field and catchment-scale research has been conducted by the Department of Agriculture, Western Australia and Alcoa World Alumina Australia Ltd. (Rai *et al.*, 2012). The additions imparted to the soil promote its structure, porosity, water retention and nutrient utilisation ability (Hanahan *et al.*, 2004; Bhatnagar *et al.*, 2011; IAI, 2013). Red mud has been applied to increase the phosphorus^{-} retention (and also As, Cu, Ni) of sandy soil (Santona, Castakdi and Melis, 2006; Gadepalle *et al.*, 2007; Feigl *et al.*, 2012). These features are useful in the revegetation of bauxite residue areas, and for creating various reuse products (Rai *et al.*, 2012; Sutar *et al.*, 2014). Although doubts have been expressed about the leachability of heavy metals and radionuclides from red mud, quite a few research studies have demonstrated that there are no risks to date (Wang, Ang and Tadé, 2008; IAI, 2013).

2.2 Modification of Red Mud and its Environmental Benefits

Following the discussion from Section 2.1.6, extensive investigations have been performed to develop viable recycling and utilisation solutions for red mud. This section intends to expand further on the methodologies deployed to modify RM waste for different purposes and to demonstrate the feasibility of producing RM-based environmental materials. In particular, the aim is to present the logic underlying the synthesis methods proposed in this thesis and the precedents regarding how the synthesised products might be evaluated.

2.2.1 Recovery of Individual Metals in Red Mud

Fe_2O_3, Al_2O_3, and TiO_2 are the main constituents of red mud (Table 2.2), with an average iron oxide content of 40% and an average alumina content of 20%. Europe alone possesses an equivalent of 3.4 million tonnes of iron ore. A few researchers have proposed several complex processes to separate aluminium, iron, titanium and rare earth elements (REEs) from red mud, and their work is reviewed in this section (Erçağ and Apak, 1997; Borra *et al.*, 2016a; Verma, Suri and Kant, 2017).

Fe recovery

The recovery of iron conventionally involves two main approaches: (1) liquid-phase reductive smelting, where RM is sintered in the presence of a reducing agent and smelted at a high temperature (generally above 1500°C) to obtain pig iron and a slag (Erçağ and Apak, 1997; Borra *et al.*, 2016b, 2016a); (2) solid-state reduction, where RM is reduced with a solid or gaseous reductant. For instance, Liu et al. (2009) extracted iron by a carbon powder reduction roasting process (at 1300°C) followed by magnetic separation. In addition, direct magnetic separation was carried out by Liu & Naidu (2014) subject to a low recovery rate.

Al recovery

After iron extraction, Al_2O_3 can be recovered from the remaining solution. Most of the Al in RM exists in a sodalite form ($3Na_2O.3Al_2O_3.6SiO_2.Na_2SO_4$), referring to Section 2.1.3. In the hydrometallurgical process, RM leached in sulfuric and organic acid (citric, oxalic acids) is the common way to recover Al (Liu and Naidu, 2014). Wu et al. (2011) and Wang et al. (2018) investigated the calcification-carbonation process to convert sodalite to non-alkali and lean alumina states. In some cases, alumina is extracted before smelting to extract iron. The alkali roasting (sintering) process is applied, with the addition of Na_2CO_3. Vachon et al.

(1994) developed a biotechnological process using bacterial and fungal leaching under acidic conditions to enhance the solubilisation of Al from red mud.

TiO_2 recovery

There are two ways of managing RM for titanium recovery: pyrometallurgical and hydrometallurgical (Agatzini-Leonardou *et al.*, 2008). The pyrometallurgical process requires a series of complicated steps coordinated with Fe (III) and Fe (II) content in the mixture. Erçağ & Apak (1997) suggested a process, prior to the extraction of titanium, by which the leachate needs to be diluted and the acidity adjusted after separating the pig iron. The Na_2CO_3 solution is stripped in to precipitate titanium out as $TiO(OH)_2$ at 65-70°C. $TiO(OH)_2$ is then filtered, dried and calcined at 1000°C to become pigment-grade TiO_2. Hydrometallurgical processes offer an alternative, as long as iron dissolution is carefully controlled. Zimmer et al. (1978) proposed a RM digestion process, with concentrated sulfuric acid, that was heated at a pH =1 to precipitate $TiO(OH)_2$ by hydrolysis. Recently, Agatzini-Leonardou et al. (2008) reported that 64.5% of Ti was extracted from RM using diluted H_2SO_4 solution (6N) at 60°C under atmospheric pressure, and 46% iron was leached though less than 37% aluminium was leached out.

REEs recovery

RM contains several other critical metals including rare-earth elements (REEs) (Klauber, Gräfe and Power, 2011). REEs can be extracted by direct acid leaching, but due to the presence of alumina and iron, the extraction yield was rather low (Borra *et al.*, 2016a; Verma, Suri and Kant, 2017). To improve the REEs recovery rate, the extraction is usually carried out after iron and alumina recovery, via the hydrometallurgical process or combined pyrometallurgical and hydrometallurgical processes (Rai *et al.*, 2012; Borra *et al.*, 2016a). Amongst REEs, scandium (Sc) is the most abundant one and attracts the majority efforts (Balomenos, 2018). Extraction of Sc has been taken to the pilot plant stage by Ochsenkühn-Petropoulou et al. (2002), based on a nitric acid leach then ion exchange separation of the Sc.

To sum up, single recovery is not commercially viable. Simultaneous recoveries of valuable metals from red mud should be developed. Currently there is no simple and economical method for utilising these metals, which typically experience problems like high energy consumption, large volumes of acid by-product after the leaching process and the fine particle size of red mud. No process has to date been implemented on the large scale in industrial

extraction (Khairul, Zanganeh and Moghtaderi, 2019). RM recovery strives to find commercial value. Therefore, there is a great need to consider those valuable compositions of RM as a whole; in other words, to utilise RM as an integral source of resources.

2.2.2 Modification of Red Mud as a Whole

Instead of extracting individual metals from RM, modifications are generally in demand to upgrade or activate RM as a bulk raw material. On the basis of Section 2.1.6, modified red mud has great potential in environmental applications, like low-carbon construction materials, as a catalyst for fuel gas purification, as an adsorbent for wastewater treatment and soil remediation, etc. (Bhatnagar *et al.*, 2011; Collins, Clark and Payne, 2014). The major modification approaches of RM are summarised in Table 2.5. It can be seen that red mud presents a variety of capabilities depending on the source and the processing method by which it was generated. This research aims to further understand the properties and potential of RM.

Mechanical and heat treatment can alter the physiochemical properties of red mud. The BET surface area of activated RM by Tor & Cengeloglu (2006) was 20.7 m^2/g. Manfroi, Cheriaf & Rocha (2014) also discovered that the RM dried and calcined at 600, 700, 800 and 900°C presented significant higher (about 6-9 times) specific area than the Portland cement CPII-F (3200 cm^2/g).

Furthermore, the mineral composition of RM can be modified by thermal treatment and acid activation. Liu et al. (2016) observed that RM loses free and structural water, as well as undergoes the transformation of alumina and the reduction of hematite to magnetite during thermal treatment (200-600°C). Koumanova et al. (1997) increased the yield of usable ferric oxide, alumina and titanium dioxide from RM through treating it with concentrated H_2SO_4.

Table 2.5 Summary of research literatures investigating environmental applications of red mud after modifications

Properties & Influences on applications	Modification methods	References
As construction materials, additives		
As cement paste substitution up to 15%, RM shows suitable microstructure, mechanical and hygroscopic properties for construction, and fixation ability of contaminants, especially good retention of Cd. However, increasing the RM content reversely correlated with the compressive strength.	1) Optimum at up to 5% of Brazilian RM 2) RM was **calcined** at 600°C – 900°C for 1 h	(Manfroi, Cheriaf and Rocha, 2014)
Reduced chloride penetration in concrete due to its superfine particle-size distribution and its "filler" effect yielded a longer service life, reaching more than double that of the reference samples (16.5 versus 35 years).	Addition of RM in which cement was partially replaced by 10, 20, and 30% in weight	(Ribeiro, Labrincha and Morelli, 2011)
RM particles can capture aggressive ions. RM is therefore a good corrosion inhibitor against Cl^- attacks in alkaline media. As a corrosion inhibitor for carbon steel surfaces, RM captures Cl^- on the steel surface and depassivation takes place at lower Cl^-/OH^- ratios.	1) RM suspensions: 20 g RM was added to 1 L distilled water and left overnight. 2) The steel samples were immersed decanted suspension (pH=12)	(Collazo *et al.*, 2005)
Reduction in the environmental impact of lightweight concrete (LWC) incorporating 25% of RM, in terms of cumulative energy demand (CED) and major criteria air pollutants CO, NO_X, Pb and SO_2 by 31%, 32.5%, 31.8%,17.1% and 22.4% respectively.	Lightweight concrete mixed with RM addition by 25%	(Nikbin *et al.*, 2018)
A high surface area of fine RM particles mixed in mortars accounts for hydration of cement, resulting in an increased water absorption rate. 15%, 20% and 25% RM content as cement replacement, lead to 23%, 26% and 30% growth of water absorption.	RM as cement replacement	(Senff *et al.*, 2014; Nikbin *et al.*, 2018)
As lightweight aggregates and workable paste for mortars, e.g. RM replaced Portland cement. RM reduced the workability and increases the torque.	RM with 34-38 wt% water added, replaced up to 50 wt% Portland cement	(Senff, Hotza and Labrincha, 2011)

As geopolymers, glass-ceramics and flame retardant		
RM-based geopolymer spheres were synthesised for the first time, who exhibits a continuous and prolonged pH buffer capacity that allows its use in wastewater treatment, which can be used as pH regulator.	Suspension-solidification approach was adopted. 60 wt% RM mixed with fly ash wastes, along with alkaline activator.	(Novais *et al.*, 2018)
Cementitious material with RM shows more compression strength with an increased Si/Al and Na/Si molar ratio. For the studied range of compositions, the red mud geopolymers possess a compressive strength of 7 to 13 Mpa, comparable to certain types of Portland cement. Similarly, a new geopolymer composite was synthesised from RM and rice husk ash (RHA). Higher RHA/RM ratios generally lead to higher strength, stiffness and ductility, but excessive RHA may cause the opposite effect.	RM & fly ash: **dry-mixing** at selected weight ratio, add 1.5 M sodium trisilicate solution to the powder mixture, stirred for >15 min, forming the geopolymer precursor paste, followed by curing.	(Zhang, He and Gambrell, 2010) (He *et al.*, 2013)
Layered double hydroxides (LDHs) was synthesised using RM for flame-retardant ethylene-vinyl acetate (EVA).	1) Dried RM was **ground** by a Ball Machine into 300-mesh particles, **mixed with MgO**. 2) The mixture was **roasted** at 650°C for 4 h, **leached** in Na_2CO_3 solution. 3) The slurry was filtered, washed and dried to obtain Mg/Al/Fe-LDHs.	(Qian, Li and Chen, 2015)
RM is feasible to produce glass-ceramic (CaO-SiO_2-Al_2O_3) or glass, since the chemical structure of RM is similar to glass-ceramics. The glasses obtained contain nanocrystal phase, whose nucleation is facilitated by the impurities like TiO_2 in the RM.	1) Dried RM was ground with SiO_2, Al_2O_3-rich fly ash, **melted** in air at 1360°C. Then it was cast and annealed in the muffle. 2) RM was crushed in a mortar, **dehydrated and heated** at 800°C to remove decomposable components. It was then melted with additives (SiO_2 + Na_2O) at room temperature and annealed at 650°C for 1 h.	(Peng *et al.*, 2005; Yang *et al.*, 2008)

As catalyst alternatives		
Metal oxides are desirable constituents for catalysts. With minor treatments, RM-based catalysts can be cheap catalysts alternative on a commercial scale. Its iron content (Fe_2O_3), has a high surface area and is non-toxic in nature, which makes it a catalyst for many reactions.		(Wang, Ang and Tadé, 2008; Verma, Suri and Kant, 2017)
RM perform as an iron oxide and iron ceria catalysts in hydrogenation and liquefaction process for coal, biomass, oil shale and petroleum residues. For instance, RM was applied for tar conversion in a flow type double bed microreactor, getting 95-100% tar conversion at 600°C.	1) RM was activated by **boiling in aqueous HCl** for 2 h, precipitating by the addition of ammonia until pH=8. 2) The precipitate was filtered, washed, dried and **calcined** in air at 500°C for 2h	(Yokoyama *et al.*, 1989; Yanik *et al.*, 2008; Dulger Irdem *et al.*, 2014)
RM was used for combustion of methane. Deactivation of RM catalyst is due to the loss of surface area. Aluminium and titanium contents were observed to decrease the activation energies of RM.	RM was dissolved in a mixture of aqueous HCl and H_3PO_4, in order to get a 4 wt% P in the calcined catalyst.	(Pratt and Christoverson, 1982; Paredes *et al.*, 2004)
As adsorbents for wastewater treatment		
$MgCl_2$ /red mud system was employed to remove > 98% of the colouring material from 0.1 g/L dye solution at a dosage of 25 g RM/L dye solution and 1.5 mL $MgCl_2$/L dye solution in the decolorization process.	**Ground and sieved** RM (dried, particle size < 180 μm) was added to dye solution along with $MgCl_2$ solution	(Wang *et al.*, 2009)
Removal of congo red (CR) anionic dye from aqueous solution by acid activated RM. The effective pH for adsorption was 7.0, the monolayer sorption capacity (Q_0) is 7.08 mg/g.	1) RM was suspended in distilled water, L/S=2/1 (weight base) until pH=8.0-8.5 2) 10g Dried RM was boiled in 200 mL of 20 wt% HCl for 20 min, then filtered, washed and dried at 40°C.	(Tor and Cengeloglu, 2006)
Modified RM was employed for removal of methylene blue from wastewater. Both heat treatment and acid treatment reduce the adsorption capacity of RM.	- **Heat treatment** at 800°C overnight; - 10 g RM was treated in 20 mL **1N HNO_3** for 24 h at room temperature and dried	(Wang *et al.*, 2005)

Adsorption study implicated that phosphates removal by RM relies on ligand-exchange mechanism. Two RM activation methods were employed, heat treatment and acid treatment. Experiment showed that acid treatment presented a negative effect on phosphate removal, however, heating enhanced its capacity due to the increase in surface area.	- **Heat treatment** at (200, 400, 600 and 800 °C) for 4 h, then ground and sieved through a 200-mesh sieve - 50g dried RM suspended in 1L, 0.25-2.0 M HCl solution, stirred for 2 h, and filtrated and dried at 105°C	(Altundoğan and Tümen, 2002; Altundoğan and Tümen, 2003; Huang *et al.*, 2008)
Layered double hydroxide adsorbent (BR-LDH) was successfully prepared under alkali conditions using boron mud and red mud, when the mass ratio boron mud: RM: C_{NaOH} = 4:1 and 4 mol/L. BR-LDH was used to remove the phosphate from wastewater and reached 93% removal ratio at the dosage of 0.25 g/50 mL.	1) RM and Boron mud were mixed in distilled water, dried at 120°C, **calcined** at 600°C for 3 h (BR-600). 2) 60 g BR-600 were added to NaOH solution at 30°C for 6 h and **aged** at room temperature for 24 h.	(Hu *et al.*, 2016)
Arsenate (As(V)) and arsenite (As(III)), the most common soluble inorganic arsenic species in water. In general, alkaline aqueous media (pH 9.5) favoured the removal of As (III), whereas pH (1.1-3.2) was effective for As(V) removal.	RM as adsorbent for arsenic removal	(Soner Altundoğan *et al.*, 2000)
Activated seawater-neutralised RM was used for adsorbent of As from water, the optimal pH for As(V) adsorption is 4.5 with close to 100% removal. However, at an elevated pH of 11.5, only 60% removal was observed.	RM was neutralised by seawater to pH 8.6±0.2, then activated by the combined **acid and heat treatment** (i.e. reflux in HCl, add ammonia to precipitate, filter and **calcine** at 500°C for 2 h).	(Genç-Fuhrman, Tjell and McConchie, 2004)
Most As(V) (0.39–7.86 mmol kg−1) being adsorbed was associated with amorphous and crystalline Al and Fe oxides (24.1–43.8% and 24.7–59.0% of total adsorbed arsenic, respectively). Exchangeable As was the smallest fraction, 0.4–5.2% of the total adsorbed.		(Rubinos *et al.*, 2005)
The maximum capacity of RM for fluoride removal was 13.46 mg/g. Modified RM with $AlCl_3$ (MRNA) and by heat activation (MRMAH) advanced their capacities to 68.07 and 91.28 mg/g respectively.	RM was modified by $AlCl_3$ (MRNA) and by **heat activation** at 200°C (MRMAH)	(Ning *et al.*, 2009; Bhatnagar *et al.*, 2011)

The high contents of Fe^{3+} and Al^{3+} in RM make it a promising material for coagulant production, which is suitable for heavy metal and turbidity removal from wastewaters. The coagulant has a few advantages: (1) negligible pH variations during the purification; (2) one step removal of cationic and anionic species; (3) negligible leaching of heavy metals under normal conditions	Partial dissolution of RM with **diluted HCl** (30 wt%), separation of liquid from residual RM, and neutralization of acid RM (pH 0) with waste base to pH 8.	(Wang, Ang and Tadé, 2008)
Modified RM (MRM-PS) with a hierarchical microporous-mesoporous structure (surface area = 232 m^2 g^{-1}) was prepared by using polystyrene microspheres and red mud. The adsorption capacity for rhodamine B was 59.37 mg/g at pH 1.0 and the equilibrium was reached in 10 min.	1) 40 mL distilled water was added to 10 g RM, stirred then 60 mL **6M HCl** solution was added. 2) The mixture was digested at 85°C for 2h, cooled and 200 mL ethanol water of 6.4 g PS particles was added. 3) Ammonia adjusted pH to 7.5, the slurry was aged at 60°C for 30 min. 4) The precipitate was separated, dried and calcined in air at 350°C for 2h.	(Cao *et al.*, 2014)
As soil amendments		
RM is a strong amendment for metal /metalloid-contaminated soil, owning to Fe and Al oxide/oxyhydroxide content in immobilizing. With the presence of RM, the mobility of Cr, Ni, Pb and Zn (<0.6%) became very low. But the pH condition is critical on influencing the 'potentially mobile' metal fractions.	RM application rate of 1%-5% w/w to the soil.	(Rubinos and Barral, 2013; Hua, Heal and Friesl-Hanl, 2017)
RM was applied to increase the low pH of acidic sandy soil.	RM (pH 10.2) mixed into the sandy soil ranged between 0 and 50%.	(Summers, Bolland and Clarke, 2001; Ujaczki *et al.*, 2016, 2018)
The effect of RM amendment on soil carbon: Total organic carbon (TOC) after 2 years has decreased from 34.9 g kg^{-1} to 20.1 g kg^{-1} in parallel comparison. Whilst, dissolved organic carbon (DOC) saw a decline.	RM application rate of is 4% and 2% in respective.	(Lombi *et al.*, 2002; Garau *et al.*, 2011)

2.2.3 Incentives: Properties of Red Mud and Key Facts

Inspired by the diverse attempts to produce high added-value materials from red mud as illustrated in Table 2.5, this research aims to focus on a relatively unexplored niche. Looking back to Section 2.1, there are several prominent characteristics of RM that should be put to good use, as follows:

1) Metal contents

Crucially, red mud is rich in Al, Fe elements, which can be the main metal sources for layered double hydroxides (LDH). The host layers of LDHs are constructed from an array of divalent and trivalent metals, including but not limited to: Mg^{2+}, Ni^{2+}, Zn^{2+}, Al^{3+}, Cr^{3+} and Fe^{3+} (see Figure 2.6). Synthesis of LDH is usually economical due to the common and abundant metals in their structure. As reported by a number of researchers (Koumanova, Drame and Popangelova, 1997; Palmer, Frost and Nguyen, 2009; Palmer and Frost, 2011), hydrotalcite (e.g. $Mg_6Al_2(CO_3)(OH)_{16}{\cdot}4(H_2O)$), which is a layered double hydroxide type, has been observed during the seawater neutralization of RM. The similarities of employing RM and other salt-oxides as starting materials for LDH synthesis is reviewed in Section 2.3.2 and Section 2.3.3.

2) Alkalinity

Apart from the metal contents, the alkalinity nature of RM (pH 10.5-12.5) is also a desirable prerequisite for LDH formation. Hence, the addition of alkaline solution for controlling pH could be eliminated during LDH precipitation process. As illustrated by Paikaray & Hendry (2014), alkaline conditions (pH $\geq$ 9.0) are favoured in the formation mechanism of LDH in Mg^{2+}, Al^{3+} and Fe^{3+} media.

3) Particle size, surface area

The fine particles and relatively high surface area of RM are encouraging features for LDH formation. The particle size affects solubility and the contact opportunities between particles (Palmer, Frost and Nguyen, 2009). On the other hand, the accumulation of LDH precipitates effectively increases the particle size of the treated RM waste (Khairul, Zanganeh and Moghtaderi, 2019). The porous surface is another advantage, which not only facilitates the synthesis of LDH, but also provides the final LDH products with the potential to be more effective in the corresponding applications. The high surface area and porosity are considered to be the characteristics of successful sorbent materials.

4) Clay-like behavior

A number of researches have noted that RM exhibits clay-like behaviour, that includes high thermal stability (Hind, Bhargava and Grocott, 1999; Sutar *et al.*, 2014). LDHs are essentially layered clay-like materials with high anion exchange capacity (Rajamathi *et al.*, 2000). Therefore, the resemblance between RM and LDH might offer some merits during synthesis and upon application.

Apart from the characteristics of RM that favour LDH synthesis, the similarities between RM and LDHs are found in terms of modification and utilisation. The main incentives for using RM as raw materials are therefore summarised in Figure 2.5.

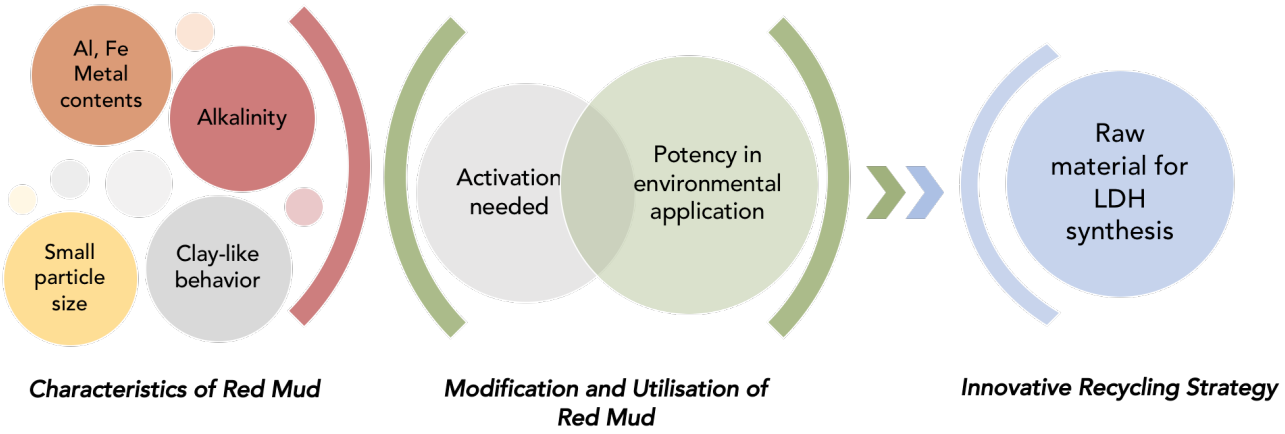

Figure 2.5 Schematic diagram of incentives lead to using RM for LDH synthesis.

1) Similarities in modification

Several researchers have notably started to explore the possibility of using red mud as the raw material for LDH synthesis (Palmer and Frost, 2011; Qian, Li and Chen, 2015; Hu *et al.*, 2016). Apart from the novelty of reusing RM in LDHs synthesis, this strategy is also expected to motivate investigation into the added-value of RM in applications after modification. As summarised in Table 2.5, various modifications have been considered to activate RM or enhance its performance. Analogous modifications have been observed when different LDHs are prepared, which are demonstrated in Section 2.3.

2) Similarities in environmental applications

As aforementioned, RM has attracted extensive attention and plays an active role in the field of environmental applications, such as construction additives, flame retardant, catalysts, adsorbents for wastewater treatment and soil amendments. This matches the value of LDH materials. LDHs possess versatile applications in environmental remediation and industrial

processes as adsorbents, catalyst, drug delivery carriers, anion exchangers or flame retardant etc. (Valente, Cantu and Figueras, 2008; Yanmin Yang *et al.*, 2012). In particular, LDHs are interesting clay-like materials with low toxicity, large interlayer spaces, high anion exchange capacity, tuneable structures, high thermal stability and memory effect, making them suitable sorbent materials (Johnston *et al.*, 2021). Besides, fast kinetics and remarkable regeneration ability in a short time for reuse are the advantages of LDH compared to other adsorbents (Goh, Lim and Dong, 2008).

2.3 Red Mud for Layered Double Hydroxides (LDH) Synthesis

Given the rich content of iron and alumina in RM, as well as its high alkalinity and an inherent clay-like behaviour, one interesting approach is to directly employ RM as a source of metal oxides to produce layered double hydroxides (LDHs). Notably, LDHs possess versatile applications in environmental remediation and industrial processes as adsorbents, catalysts, drug delivery carriers, anion exchangers or flame retardants, etc. (Valente, Cantu and Figueras, 2008; Othman *et al.*, 2009; Yanmin Yang *et al.*, 2012). Hence, this would be an innovative recycling strategy that may reduce the disposal of RM and equip it with exciting new functions and flexibility. This section aims to summarise the key synthesis methods to date for LDH production and link them to aforementioned modification methods for red mud utilisation. This is followed by a comparison of the similarities and differences when using red mud as a raw material. Finally, the various pre-treatment and operation factors that are likely to influence the synthesis outcomes are investigated.

2.3.1 Layered Double Hydroxides (LDHs)

Layered double hydroxides (LDHs), also known as anionic clays, are a group of minerals with an anionic exchange property (Rives, 2001; Paikaray *et al.*, 2014). The general formula for these structures is $[{M^{2+}}_{1-x}{M^{3+}}_{x}(OH)_2]^{X+}{A^{n-}}_{x/n} \cdot mH_2O$, which consists of positively charged brucite-like host layers $M(OH)_2$ that are partially substituted by trivalent cation M^{3+} (Valente, Cantu and Figueras, 2008; Paikaray and Hendry, 2012). M^{2+} are divalent cations such as Mg^{2+}, Zn^{2+}, Cu^{2+}, etc., whilst M^{3+} can be Al^{3+}, Cr^{3+}, Fe^{3+}, etc. The metal octahedra share edges to form two-dimensional infinite sheets (Figure 2.6). The positive charge is compensated by A^{n-} (F^-, Cl^-, CO_3^{2-}, SO_4^{2-}, oxy and polyoxy-metallates, anionic complexes and organic anions) in the interlayer regions, with the remaining free space occupied by H_2O (Rives, 2001; Guo *et al.*, 2013). Water molecules in the interlayer are connected via hydrogen bonding to the hydroxyl ions of the metal hydroxide layers and interlayer anions (Marcelin *et al.*, 1989). The constituents of the interlayer cations and anions can be altered for different purposes. A number of transition metal-bearing LDHs (such as Fe-Al, Co-Al, and Ni-Al) are active in technological applications due to their special catalytic, electronic, optical, and magnetic properties (Liu *et al.*, 2006; Othman *et al.*, 2009). Different divalent and trivalent cationic substitutions of Mg and Al can be used to obtain LDHs with varied and tuneable physicochemical properties, such as surface area, pore structure and reducibility (Chmielarz *et al.*, 2002). Likewise, the anion basicity has an impact on the reactivity of the LDH materials. For instance, the carbonate and hydroxide intercalated

materials are more active than the chloride derivative (Constantino and Pinnavaia, 1995). The calcination of LDH at moderate temperatures (400-550°C) could lead to the formation of metastable mixed oxides that cannot be achieved by mechanical means. Therefore, the potential of LDH and their hybrids lies in their plasticity and variability. These properties are considered in association with the synthetic strategy applied to their preparation.

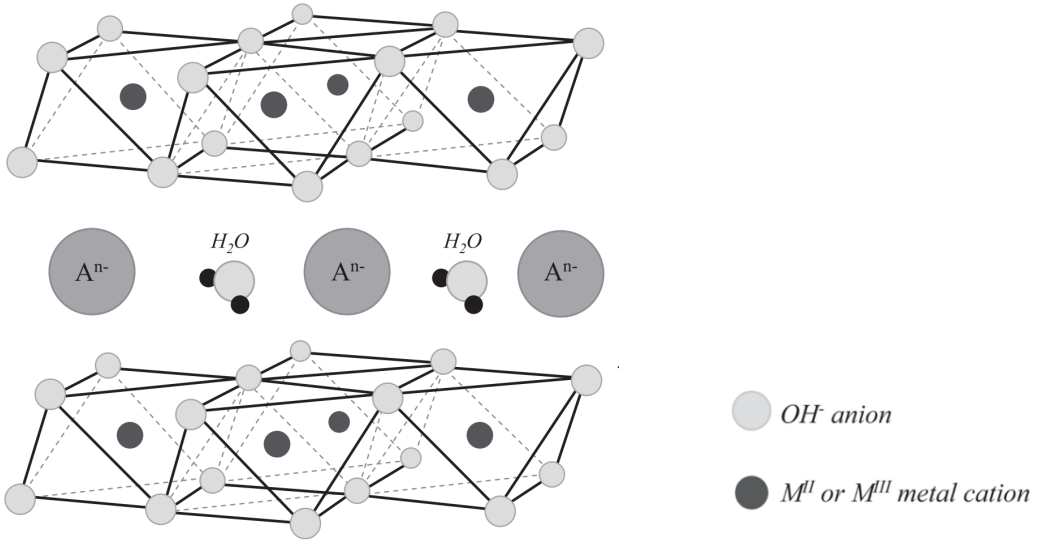

Figure 2.6 Structure representation of LDH (Tamura *et al.*, 2006; Salomão *et al.*, 2011; Yang *et al.*, 2016).

2.3.2 Conventional Methods for LDH Synthesis

Over the last decade, significant progress related to the synthesis of LDH with new compositions and morphologies has been made. There mainly exist five routes to synthesize LDHs, i.e. co-precipitation, urea-based method, salt-oxide method, ion-exchange (applicable when divalent or trivalent metal cations or the anions are unstable in mixed solution), and calcination-rehydration (reconstruction, based on the 'memory effect' property) (Rives, 2001; Qian, Li and Chen, 2015). Ion-exchange method usually aims at synthesising LDHs with poly anions or organic anions in the interlayer region, whereas, the other ways generally only support inorganic anions (Duan and Evans, 2006; He *et al.*, 2006; Qian, Li and Chen, 2015). Furthermore, other methods such as sol-gel synthesis using ethanol and acetone solutions (Aramendía *et al.*, 2002), electrochemical synthesis (Indira, Dixit and Kamath, 1994), and a fast nucleation process followed by a separate aging step (Yun Zhao *et al.*, 2002), have also been reported.

Figure 2.7 describes the relationship between different synthetic methods and the forms of LDH; Table 2.8 will compare different cation and anion sources, and the main operating parameters in the existing research.

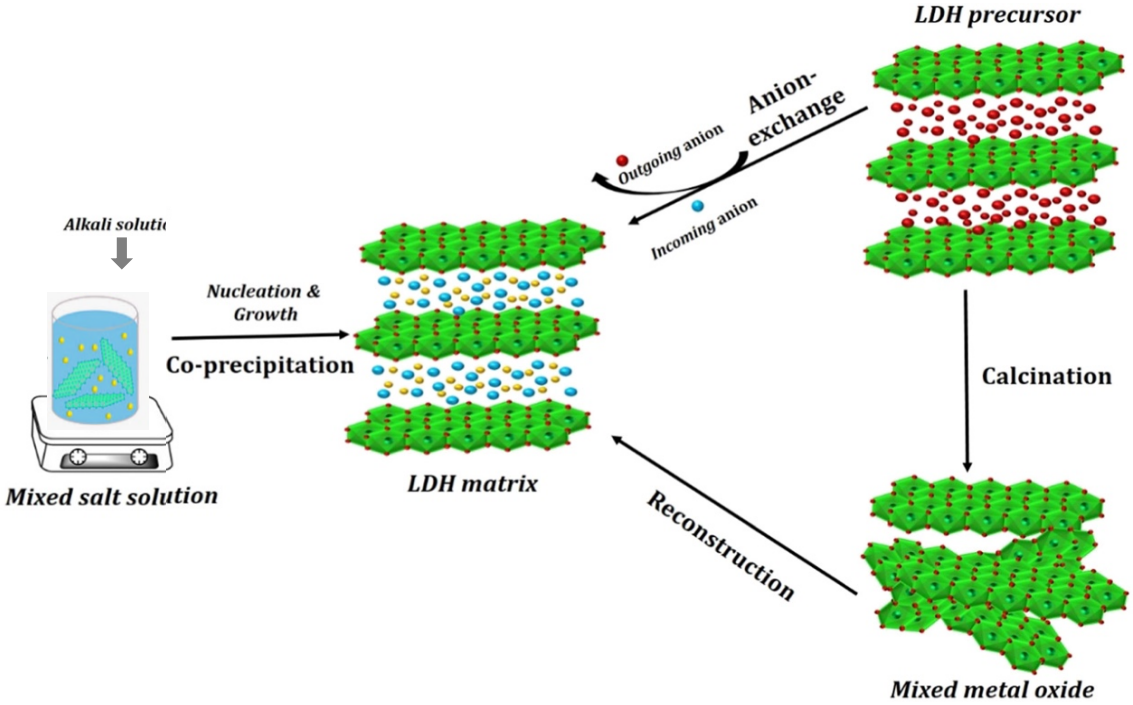

Figure 2.7 Schematic diagram of synthesis methods and post-synthesis modification of LDH (Mishra, Dash and Pandey, 2018).

I. Co-precipitation method

Among the variety of methods available, co-precipitation remains the most widely spread and simplest way of preparing LDH (Othman *et al.*, 2009; Palmer, Frost and Nguyen, 2009). In this 'one-pot' direct method, the aqueous solution of chosen M^{2+} and M^{3+} cations is mixed in alkaline solution that contains potential interlayer anions to generate LDH (He *et al.*, 2006; Liu *et al.*, 2006). The main steps are described in Table 2.6. To ensure the simultaneous precipitation of two or more cations, it is recommended that synthesis be conducted under supersaturation conditions (Cavani, Trifirò and Vaccari, 1991; Othman *et al.*, 2009). The supersaturation can be adjusted by controlling the pH or the M^{2+}/M^{3+}salt ratio in the reactor. In order to improve the crystallinity, an aging process at a higher temperature (over a few hours or several days) or a hydrothermal treatment is proposed (Miyata, 1975; Paikaray and Hendry, 2014). The subsequent drying temperature also affects the properties of the LDH formed (Kuwahara *et al.*, 2010).

Table 2.6 Most common route by co-precipitation process (Salomão *et al.*, 2011)

	Steps	Remarks
(1)	Solution of divalent cation salt (e.g. $MgCl_2$), Solution of trivalent cation salt (e.g. $AlCl_3$))	Mg:Al = (3-2):1, excess M^{2+} or M^{3+} results in $M(OH)_2$ or $M(OH)_3$ admixture
(2)	$6Mg^{2+} + 2Al^{3+} + 18Cl^- + xH_2O$ ↓	pH ≤ 7
(3)	Na_2CO_3 addition, pH increase ↓	${CO_3}^{2-}$ can be substituted by other anions, e.g. F^-, Cl^- or carboxylic organic anions
(4)	$6Mg^{2+} + 2Al^{3+} + 18Cl^- + nOH^- + n{CO_3}^{2-}$ ↓	pH = 10-12, metastable solution
(5)	$Mg_6Al_2(OH)_{16}CO_3 \cdot 4H_2O(precipitated) + 18Cl^-$ ↓	pH = 10-12, hydrotalcite suspension
(6)	Hydrothermal treatment (e.g. Autoclave) ↓	Improve crystallinity, narrow particle size distribution, prevents particles agglomeration
(7)	Purification (centrifugation, washing…) ↓	Discard not-aimed anions
(8)	Controlled drying, $Mg_6Al_2(OH)_{16}CO_3 \cdot 4H_2O$	Dried LDH hydrotalcite product

In a low supersaturation process, metal salts are slowly added into a reactor containing an aqueous solution of the desired interlayer anion (Qian, Li and Chen, 2015). Normally, metal nitrate and chloride salts are applied because of the low selectivity of LDH toward these anions (Cavani, Trifirò and Vaccari, 1991). The second alkali solution enters the reactor at a rate that maintains the reaction pH at a selected value. The principal advantage of this method is that it allows the precise control of the charge density (M^{2+}/M^{3+} ratio) of the hydroxide layers. The low supersaturation conditions usually provide the resulting LDH with higher crystallinity, as the rate of crystal growth is higher than the rate of nucleation (He *et al.*, 2006).

In a high supersaturation condition, a mixed M^{2+}/M^{3+} salt solution is added very quickly to an alkaline solution containing the desired interlayer anion, where the pH changes continuously. That triggers the formation of impurity $M(OH)_2$ and/or $M(OH)_3$ phases (Paikaray and Hendry, 2014), resulting in the LDH of an undesired M^{2+}/M^{3+} ratio and less crystalline state (Cavani, Trifirò and Vaccari, 1991). However, if the LDHs are to be employed as catalysts, poor crystalline materials with high surface areas, narrow pore size and the presence of structural or compositional defects are preferred (Othman *et al.*, 2009).

Mechanism of co-precipitation

The formation mechanism of LDHs has not yet been completely understood (Rives, 2001; Chubar *et al.*, 2017). According to the literature, co-precipitation is likely to be a two-stage process: firstly, aluminium hydroxide or hydrous oxide is formed in the presence of excess Al^{3+}, followed by the formation of LDH from aluminium hydroxide in the presence of excess Mg^{2+}. In the second stage, the crystallization of LDH starts with diffusing Al atoms into the $Mg(OH)_2$ structure or through incorporating surface-absorbed Mg^{2+} continuously into the lamellar Al-rich LDH-type phase. Yang et al. (2012) studied the LDH structure formation from $Mg(NO_3)_2$, $Al(NO_3)_3$ and urea, and deduced a detailed formation mechanism, as shown in Figure 2.8.

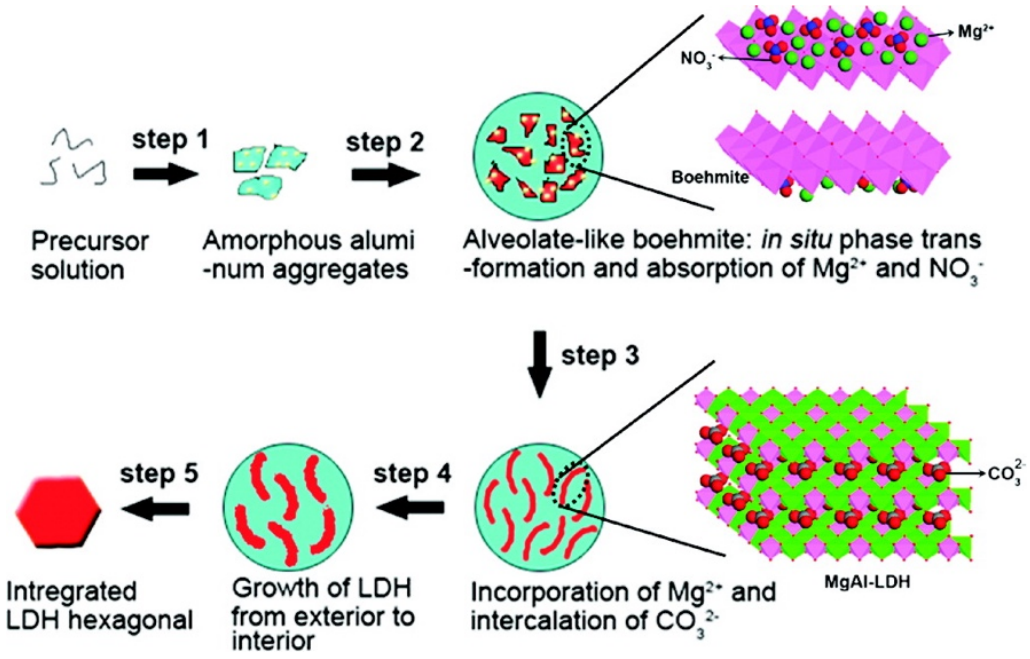

Figure 2.8 The formation mechanism of Mg–Al LDH is proposed by Yang et al. (2012) *with careful investigations using $Mg(NO_3)_2$, $Al(NO_3)_3$ and the urea precipitation method.*

Initially, amorphous aluminium hydroxide with featureless morphology starts to precipitate, meanwhile NO_3^- and a small amount of Mg^{2+} are absorbed on the surface (step 1). Along with the gathering of aluminium hydroxide particles into sphere-like aggregates, amorphous aluminium transforms to lamellar boehmite (γ-AlOOH), and then forms an alveolate-like structure (step 2). The surface absorbed Mg^{2+} then starts to incorporate into the sheet of the lamellar boehmite. This leads to an imbalance of charges on the sheet, and the hydrogen bonds existing between the sheets are destroyed. Therefore, CO_3^{2-} intercalates into the interlayer region through an electrostatic interaction, creating an initial LDH phase (step 3). The growth of LDH crystallites happens from the exterior to the interior of the aggregates (step 4). Finally, layers pile up to construct a 3-D network and integrate into a plate-like LDH structure (step 5).

II. Urea-based method

Although it has many similarities with co-precipitation method, urea method is generally classified as a separated technique (Theiss, Ayoko and Frost, 2016). Urea is a very weak Brønsted base (pKb = 13.8), which is highly soluble in water and its hydrolysis rate is highly sensitive to the temperature of the reaction (Rives, 2001; He *et al.*, 2006). Therefore, control of the pH could be achieved by adjusting the temperature. The chemical mechanism of urea hydrolysis to ammonia and hydrogen carbonate is explained by Shaw & Bordeaux (1955). The hydrolysis creates an environment of about pH 9, depending on the temperature. Urea decomposition enables hydroxide formation from metal cations to be a gentler and slower process (Chubar *et al.*, 2017):

$CO(NH_2)_2 \rightarrow NH_4CON$;

$NH_4CNO + 2H_2O \rightarrow (NH_4)_2CO_3$;

$NH_4^+ + H_2O \rightarrow NH_3 + H_3O^+$;

$CO_3^{2-} + H_2O \rightarrow HCO_3^- + OH^-$;

In theory, this process results in more chemical phases in the final LDH product. The exact experimental conditions can vary according to different research. Hydrothermal treatment has been adapted to improve the crystallinity of the LDH (Tao *et al.*, 2006; Budhysutanto *et al.*, 2010), which is generally performed in an autoclave in the presence of water vapour and under autogenous pressure. In addition, Benito et al. (2008) and Lonkar et al. (2015) optimised the synthesis process by incorporating a microwave hydrothermal step.

III. Salt-oxide method

Solid compounds of divalent and trivalent metals, such Mg and Al hydrous oxides, can result in the formation of LDHs. In 2004, Fogg et al. successfully produced a novel class of $[MAl_4(OH)_{12}](NO_3)_2 \cdot xH_2O$ (where M = Zn, Cu, Ni and Co) using grinding-activated gibbsite (γ-$Al(OH)_3$) and metal nitrates ($M(NO_3)_2$) solution. This method has been developed further to incorporate different M (II) and M (III) metals into the prepared LDHs. Chitrakar et al. (2011) conducted various studies on the synthesis of Mg-Al-Cl^- LDH by mixing crystalline gibbsite γ-$Al(OH)_3$ and solid $MgCl_2 \cdot 6H_2O$ with subsequent hydrothermal treatment. The author also illustrated that the calcined Mg-Al LDH and Mg-Fe LDH regained the layered structure through recovery in a low concentration Br^- solution. Salomão et al. (2011) reported a novel co-precipitation method to synthesise Mg-Al LDH using various Mg, Al precursors, including MgO, $Mg(OH)_2$, Al_2O_3 and $Al(OH)_3$. However, the transformation of LDH on a larger scale level could lead to the presence of admixture phases in the products (F. Zhang *et al.*, 2014). More relevant examples are presented in Table 2.8.

Mechanism of salt-oxide method

The salt-oxide method is a solid-liquid reaction system which requires the input of an anionic solution in the metal oxide suspension. A series of reactions are involved in the crystallisation pathways during LDH formation, such as the hydrolysis of MgO and Al_2O_3, as well as the dissociation of $Mg(OH)_2$ and $Al(OH)_3$. Xu & Lu (2005) proposed a 'dissociation-deposition-diffusion' mechanism. Figure 2.9 describes two main pathways of LDH formation, and Table 2.7 explains the core reactions in each.

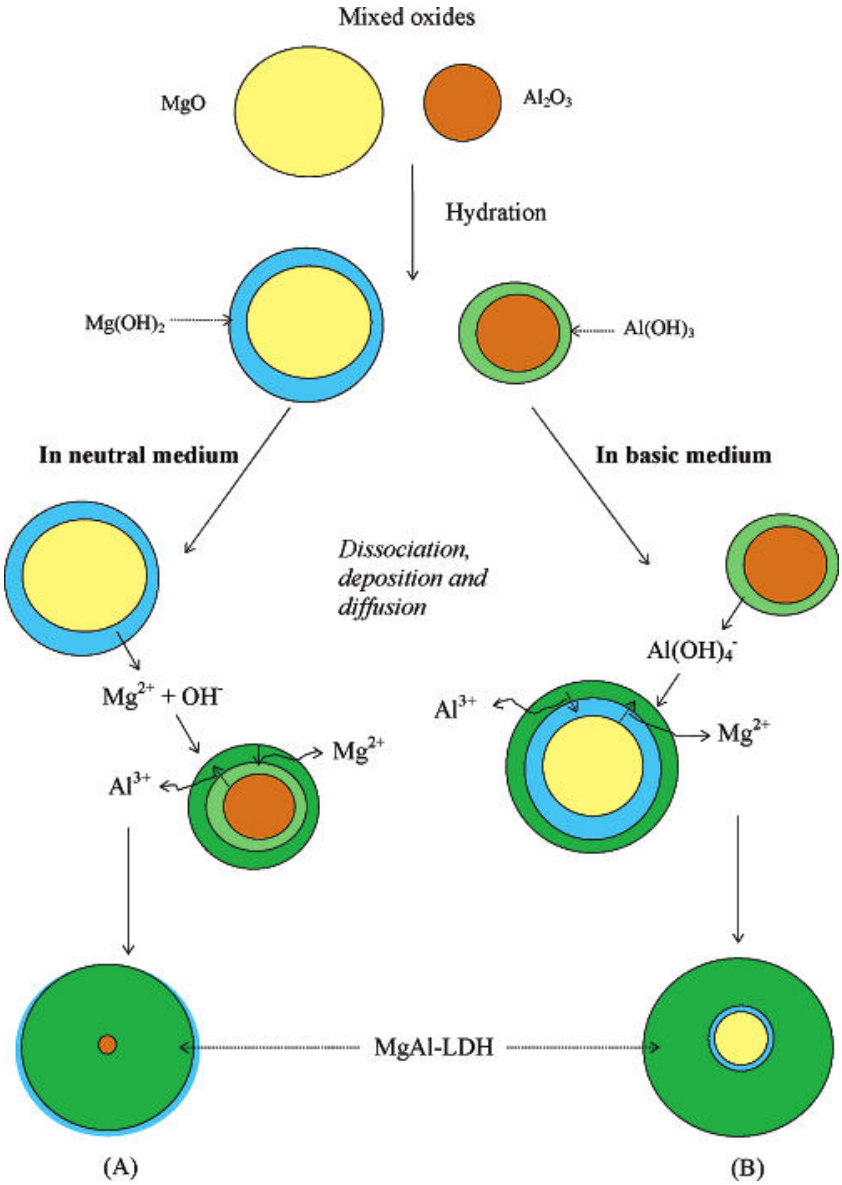

*Figure 2.9 Mechanism for LDH formation from mixed MgO and Al_2O_3 in a **(A)** neutral and **(B)** basic aqueous solution, suggested by Xu & Lu (2005).*

Table 2.7 Crystallisation pathways of LDH formation from metal oxides
(Xu and Lu, 2005; Valente *et al.*, 2009)

	Reactions	Remarks
(1)	$MgO + H_2O \rightleftarrows Mg(OH)_2 \rightleftarrows Mg^{2+} + 2OH^-$	The newly formed $Mg(OH)_2$, form thin layers on their own oxide particle surfaces. pH generally increases to 12.
(2)	$Al_2O_3 + 3H_2O \rightleftarrows 2Al(OH)_3 \rightleftarrows 2Al(OH)_2^+ + 2OH^- \rightleftarrows 2Al(OH)^{2+} + 4OH^- \rightleftarrows 2Al^{3+} + 6OH^-$	Several Al cationic species are likely to be generated. However, their total concentration is as low as 10^{-7} M, which can potentially be ignored at pH>7 (Oehman, 1988).
(3)	$Al(OH)_3 + OH^- \rightleftarrows Al(OH)_4^-$	**$Al(OH)_4^-$ is the predominant** Al species in the solution, and its concentration increases with $[OH^-]$
(4)	$aMg(OH)_2(s) + Al(OH)_3(s) + xH_2O + A^- \rightleftarrows Mg_2Al(OH)_{2+2a}A \cdot xH_2O(s) + OH^-$	**Can be neglected,** due to very limited contact between $Mg(OH)_2$ and $Al(OH)_3$
(5)	$aMg^{2+} + Al(OH)_4^- + (2a-2)OH^- + xH_2O + A^- \rightleftarrows Mg_aAl(OH)_{2+2a}A \cdot xH_2O(s)$	**Very limited,** due to the solubility of $Mg(OH)_2$ is low, hereby the calculated $[Mg^{2+}]$ is possibly 10^{-3}-10^{-4} M (Boclair and Braterman, 1999).
(6)	$aMg^{2+} + Al(OH)_3(s) + (2a-1)OH^- + xH_2O + A^- \rightleftarrows Mg_aAl(OH)_{2+2a}A \cdot xH_2O(s)$	***In the neutral condition* - Route (A)** in Figure 2.9, the dissociation of $Mg(OH)_2$ is the key step. **(6) directs** the formation of LDH
(7)	$aMg(OH)_2(s) + Al(OH)_4^- + xH_2O + A^- \rightleftarrows Mg_aAl(OH)_{2+2a}A \cdot xH_2O(s) + 2OH^-$	***In the basic condition* - Route (B)** the dissociation of $Mg(OH)_2$ is constrained, the deposition of $Al(OH)_4^-$ onto the $Mg(OH)_2$ lattice to form LDH **is favoured.**

*$Where\ A^-\ denotes\ OH^-, Cl^-, or\ 1/2\ CO_3^{2-}$.

Other key points from Figure 2.9 and Table 2.7, which are mainly provided by Xu & Lu (2005) are:

a) McLaughlin et al. (1994) also proposed that the nucleation and growth of LDH occurs directly on the $Mg(OH)_2$ surface while mixing magnesium hydroxide and aluminium hydroxycarbonate. They observed that the higher the initial pH in the suspension, the quicker the LDH forms, which agrees with Paikaray et al. (2014);

b) Long-time aging (or hydrothermal treatment) is preferred to aid bilateral diffusion and produce thermodynamically stable LDH;
c) In Route (B), the dissociation of $Mg(OH)_2$ is further inhibited, as a result of the continuous deposition of $Al(OH)_4^-$ onto the $Mg(OH)_2$/MgO surface;
d) When most of the $Mg(OH)_2$ and $Al(OH)_3$ are converted into less soluble Mg-Al LDH, the dissolution-recrystallisation process may be initiated to form bigger crystallites (Stanimirova and Kirov, 2003).

IV. Ion-exchange method

A key feature of LDH is their anionic exchange capacity, which allows the prepared LDH to be modified by introducing new species. This method can be classified as a 'post-synthesis' method. The LDH precursor (e.g. weak electrostatic interaction Cl^-, NO_3^-, ClO_4^- anions bearing) is suspended in an aqueous solution containing a large excess (10 to 20 times excess) of the anions to be intercalated (Rives, 2001). pH plays a determining role in the exchange process. At higher pH values (10-12), the intercalation of CO_3^{2-} is strongly encouraged. Therefore, to complete the exchange of CO_3^{2-}—LDH by other anions, the reaction must be performed under an acidic pH (4.5-6) (Rives, 2001). The chemical expression is as follows:

$$[M^{2+}\text{-}M^{3+}\text{-}X] + Y \rightarrow [M^{2+}\text{-}M^{3+}\text{-}Y] + X$$

Where X is the intercalated anion species,
Y is the ready-to-exchange anion

Thermodynamically, ion exchange in LDH mainly relies on the electrostatic interactions between positive-charged hydroxylated sheets and the ready-to-exchange anions. The selectivity for divalent anions is generally higher than that of monovalent anions. Based on the calculations of ion-exchange isotherms, Miyata (1983) put forward a sequence of ion selectivity for various anions: for monovalent $OH^- > F^- > Cl^- > Br^- > NO_3^- > I^-$ and for divalent $CO_3^{2-} > HPO_4^{2-} > SO_4^{2-}$, according to He et al. (2006) and Chitrakar et al. (2008). Miyata (1983) also pointed out that CO_3^{2-}-LDH has a theoretical anion exchange capacity of 3.6 meq./g, if all the CO_3^{2-} in the general formula is exchanged. Using the ion-exchange approach, organic anions with long chains (but dependent on the anion size) can directly replace the inorganic anions inside the LDH precursors (Meyn, Beneke and Lagaly, 1990). The composition of anions also influences the structure of the LDH produced, particularly on the crystallinity and layer spacing (Tsyganok, 2003; Aschenbrenner *et al.*, 2011).

V. Calcination-rehydration method

Reconstruction is another important method to prepare LDH intercalated with various desirable anions, such as inorganic, organic and biomedical anions (Xu and Lu, 2005; Palmer, Frost and Nguyen, 2009). The rehydrated materials have been applied as highly active solid base catalysts (Othman *et al.*, 2009; Nishimura, Takagaki and Ebitani, 2013). LDHs generally remain stable up to 400ºC, but at 200ºC, water molecules in the interlayer run away and anhydrous LDH is obtained (Lopez *et al.*, 1996). Along with increasing temperature, LDHs dehydroxylate and subsequently de-anionise to form mixed metal oxides that cannot be obtained by mechanical means. For example, with the most common Mg-Al LDH, $Mg_6Al_2(OH)_{16}CO_3{\cdot}4H_2O$, when it reaches around 500 ºC, CO_3^{2-} is lost and solids are partially hydroxylated, i.e. $Mg_6Al_2O_{8(}OH)_2$ is formed.

Although the periodic layer-layer structure collapses, the local cations remain evenly distributed in the mixed oxides (Xu and Lu, 2005). When back in contact with water and carbonate solution, the 2-D layer structure starts taking anions from the aqueous solution and the original layered structure is re-formed. Usually, 24 h is required for rehydration for the sample calcined at or below 550 ºC. This is the so called a 'structure memory effect'. The procedure is relatively more complicated than co-precipitation or the ion-exchange method. The generated phases are mostly amorphous (He *et al.*, 2006). There is no direct correlation between the degree of LDH crystallinity and the corresponding synthesis method. However, LDH produced via the calcination-rehydration method generally experiences a decrease in crystallinity (Lv *et al.*, 2006a).

It is important to note that both the chemical composition of LDH sheets and the calcination temperature have a considerable effect on the reconstruction process. 'Memory effect' decreases with an increase in the calcination temperature, since excessive calcination temperatures cause the solid-state diffusion of divalent cations into tetrahedral positions, which results in the formation of stable spinel. For instance, when the calcination temperature is above 450ºC, Mg-Al CLDH transforms to the spinel $MgAl_2O_4$ that does not possess a reconstruction ability (Lopez *et al.*, 1996); similarly, after calcination at 600ºC, Cu-Co-Zn-Al LDH loses its 'memory effect' (Marchi and Apesteguıa, 1998).

Table 2.8 Summary of possible methods to synthesis LDHs using different M^{2+}, M^{3+} sources

Reference	LDH Product	Source of M^{2+}, M^{3+}	Anionic condition	Methods	Parameters
(Wu *et al.*, 2011)	Mg-Al/CO_3^{2-} LDH	$Mg(NO_3)_2 \cdot 6H_2O$ (0.008 or 0.16 mol) $Al(NO_3)_3 \cdot 6H_2O$ (0.04 mol)	- In 180 mL solution - Add 140 mL solution containing (0.7 mol NaOH + 0.18 mol Na_2CO_3)	Co-precipitation	[Mixing]: 50°C, magnetic [Mg:Al] = 2:1 [Aging]: 60°C, 24 h [Drying]: 80°C, overnight
(Constantino and Pinnavaia, 1995)	Mg^{2+}/$A1^{3+}$/CI^--LDH	$MgC1_2 \cdot 6H_2O$ (20.0g, 0.100 mol) $AlC1_3 \cdot 6H_2O$ (11.87 g, 0.050 mol)	- In 200 mL deionized water - Add NaOH solution (100 mL, 2M) under N_2	Co-precipitation	[Mg:Al] = 2:1 or 4:1 [pH] = 10 [Aging]: 70°C, overnight [Drying]: 80°C, overnight
(Das *et al.*, 2009)	Mg/Al/Ti/CO_3^{2-}-LDH	$Mg(NO_3)_2$ Bauxite sample with Ti content (20 g, digested in 200 mL, 25 v% H_2SO_4 for 6 h)	NaOH (2.0 M) & Na_2CO_3 (0.05 M) were added dropwise to Na_2CO_3 solution (100 mL, 0.01 M)	Digestion Co-precipitation	[Mg: Al: Ti] = 3: 0.9: 0.1 [pH]: constant at 10 [Aging]: room T, overnight [Drying]: 80°C, 24h
(Ferreira *et al.*, 2004; Benselka-Hadj Abdelkader *et al.*, 2011)	Mg/Fe/CO_3^{2-}-LDH	$Mg(NO_3)_2 \cdot 6H_2O$ (0.10 mol) $Fe(NO_3)_3 \cdot 9H_2O$ (0.005 mol or 0.025 mol)	- Dissolved in 70 mL solution - Add to 150 mL solution of NaOH (2.0 M) & Na_2CO_3 (0.1 M)	Co-precipitation	[Mg: Fe] = 2:1 or 4:1 [pH]: 8-9 or 12-13 [Aging]: 85°C, 2 h [Drying]: 80°C, 24h
(Wang *et al.*, 2017)	Mg/Al/Fe-LDH	$Mg(NO_3)_2 \cdot 6H_2O$ $Al(NO_3)_3 \cdot 9H_2O$ $FeSO_4 \cdot 7H_2O$	- Dissolved in 250 mL distilled water - Add to 200 mL, 0.04 M Na_2CO_3	Co-precipitation	[Mg: Fe: Al] = 5:1:2 [pH]: 10, adjusted by 1M NaOH [Aging]: 80°C, 24 h [Drying]: 40°C, in vacuum

Reference	LDH Product	Source of M^{2+}, M^{3+}	Anionic condition	Methods	Parameters
(Huang *et al.*, 2015)	Hierarchical flower-like MgAl(Cl^-, CO_3^{2-})-LDH	$MgCl_2 \cdot 6H_2O$ $AlCl_3 \cdot 6H_2O$	- With Urea - In 60 mL anhydrous methanol solution	Urea-based hydrothermal	[Mg: Al: urea] = 2:1:7 [Aging]: 150°C, 6 h autoclave [Drying]: 80°C, overnight under N_2
(Abou-El-Sherbini *et al.*, 2015)	CO_3^{2-}/Cl^- bearing 3(Mg+Zn)/(Al+Fe) -LDH	Mg^{2+}, Zn^{2+}, Fe^{3+}, Al^{3+} chloride salts	Na_2CO_3 solution	Co-precipitation	[M^{2+}:M^{3+}] = 3:1 [pH]: 10 adjusted by NaOH [Aging]: 70-80°C, 7 days [Drying]: 70°C, 48 h
(Kuwahara *et al.*, 2010)	Ca-Al/Cl^- -LDH	Blast furnace slag (CaO, SiO_2, Al_2O_3, MgO) - 10 g, ball milled at 650 rpm for 10 min, leach with 200 mL, 3M HCl at 100°C for 2h	Add 2 M NaOH dropwise to the leachate until pH 11.5	Acid-leaching Co-precipitation	[Mg: Fe] = 2:1 or 4:1 [pH]: 8.5, 9.5, 10.5 and 11.5 [Aging]: 30, 65, 100°C, 18 h [Drying]: 100°C, overnight
(Costantino *et al.*, 1998; Benito *et al.*, 2008)	Ni/Al or Zn/Al (CO_3^{2-})-LDH	$NiCl_2 \cdot 6H_2O$ or $ZnCl_2$, 0.333 mol $AlCl_3 \cdot 6H_2O$, 0.165 mol	- As 1L solution (0.5 M) - With 1.65 mol Urea	Urea-based microwave-hydrothermal	[Ni/Zn: Al] = 2:1 [urea/(M^{2+} + M^{3+})] = 3.3 [Aging]: 100, 125, 150 or 175°C for 5-300 min in a microwave [Drying]: 40°C, in air
(Zhao *et al.*, 2017)	PDOPA-*f*-LDH	$MgCl_2 \cdot 6H_2O$, 15 mmol $AlCl_3 \cdot 6H_2O$, 5 mmol Levodopa (DOPA)	- Dissolved in 75 mL deionised water - Add 160 mmol urea - LDH re-disperse in water with DOPA solution	Hydrothermal Co-precipitation	[Mg: Al] = 3:1 [Aging]: 120°C in autoclave for 24 h [Drying]: 60°C, vacuum

Reference	LDH Product	Source of M^{2+}, M^{3+}	Anionic condition	Methods	Parameters
(Constantino and Pinnavaia, 1995)	$Mg^{2+}/A1^{3+}/OH^-$-LDH	Mixed metal oxide formed by the calcination (500°C, 4 h) of 6 g $Mg_{2.44}Al(OH)_{6.88}][CO_3]_{0.5}\bullet\ nH_2O$	- Suspend in 200 mL decarbonated water under N_2	Calcination & Restructuring	[Mg: Al] = 2.49:1 [L/S] ≈ 10 [Aging]: room T, 3 days [Drying]: 80°C, overnight, N_2
(Xu and Lu, 2005)	①Mg/Al/OH^- - ② Mg/Al/ CO_3^{2-} - ③ Mg/Al/Cl^- -LDH	MgO (0.162 g, 4.0 mmol) Al_2O_3 (0.102 g, 1.0 mmol) or MgO (0.243 g, 6.0 mmol) Al_2O_3 (0.102 g, 1.0 mmol)	① In 40 mL deionized water ② 2.0 mmol Na_2CO_3 ③ 2.0-2.3 mmol NaCl	Salt-oxide Hydrothermal (Dissociation Deposition Diffusion)	[Mixing]: thoroughly shaken [Mg: Al] = 4:1 or 6:1 [Aging]: 110°C in autoclave for 5 or 10 days [Drying]: 80°C, overnight
(Salomão *et al.*, 2011)	$Mg^{2+}/A1^{3+}/CO_3^{2-}$-LDH	Mg^{2+}: reactive MgO, $Mg(OH)_2$ Al^{3+}: calcined Al_2O_3 (α-Al_2O_3), $Al(OH)_3$ ➔ MgO - $Al(OH)_3$ presented the most promising results	- In 200 mL deionized water - Case into polymeric cylindrical non-adherent molds and sealed in flasks	Salt-oxide (Hydration Dissolution)	[Mixing]: paddler mixer, 5000 rpm, 300s [Mg: Al] = different ratios [Aging]: at (10, 30, 50 and 80°C) for 7 days [Drying]: 110°C, overnight
(Sánchez-Cantú *et al.*, 2014)	Mg/Al-LDH or Mg/Zn/Al-LDH	① MgO (58.03 g) Boehmite γ-AlO(OH) (25.33 g) $Al(NO_3)_3\cdot 9H_2O$ (43.45 g) ② MgO (13.05 g) Boehmite γ-AlO(OH) (25.33 g) $Al(NO_3)_3\cdot 9H_2O$ (10.72 g) $Zn(NO_3)_2\cdot 6H_2O$ (22.75 g)	e.g. in Scenario ① 1. MgO, dispersed in 290 mL deionised water (A) 2. $Al(NO_3)_3\cdot 9H_2O$, dissolved in 548 mL deionised water; 3. Boehmite, dispersed in the solution (B); 4. Add slurry (A) to (B);	Salt-oxide (Dispersion Dissolution Co-precipitation)	[Mixing]: 5000 rpm, 15 min dispersed at 8000 rpm, 30 min [M^{2+}:M^{3+}] = 3:1 [L/S] ≈ 5 for MgO, then 10 [Aging]: 80°C, 6 h [Drying]: 100°C, overnight

Reference	LDH Product	Source of M^{2+}, M^{3+}	Anionic condition	Methods	Parameters
(Chitrakar *et al.*, 2007, 2008)	①Mg/Al/ Cl^-- ②Mg/Fe/ Cl^-- ③Zn/Al/ Cl^- - LDH	MgO (1.0 g, 0.025 mol) ① $AlCl_3$ (0.06, 0.08, 0.12 M) ② $FeCl_3$ ③ ZnO (1.0 g, 0.012 mol), $AlCl_3$	①&②: Mixed with 100 mL M^{3+} solution ③: MgO, ZnO were mixed with 50 mL $AlCl_3$ solution	'New no-solvent no pH-control' Salt-oxide Co-precipitation	[Mixing]: at 30°C [Mg: Al] = 2:1 [Aging]: 30°C, 2 days [Drying]: room T
(Murayama *et al.*, 2012)	①Mg/Al/ Cl^-- ②Ca/Al/ Cl^-- ③Zn/Al/ Cl^- - LDH	Aluminum dross (leach with 100 mL HCl (2.0 M) or <u>NaOH</u> (2.0 M) for 5 h $M^{2+}Cl_2$ solution (0.5 M) $AlCl_3$ solution (0.2 M)	- In 200 mL M^{2+}-Al mixed solution - Add to 100 mL, 0.64 M NH_4Cl solution	Digestion Co-precipitation	[M^{2+}:M^{3+}] = 2.5:1 [pH] = 8, 11, 12, adjusted by NaOH or HCl [Aging]: 24 h [Drying]: 70°C
(Zhang *et al.*, 2013; F. Zhang *et al.*, 2014)	Mg/Al/Fe/NO_3^- LDHs	MgO $Mg(OH)_2$ (0.10 mol) $Al(OH)_3$ (0.017 mol) $Fe(NO_3)_3 \cdot 9H_2O$ or $Mg(NO_3)_2 \cdot 6H_2O$	1. $Mg(OH)_2$ and $Al(OH)_3$ was milled for 1 h by ball mill 2. With 30 mL, 0.078 M $Fe(NO_3)_3 \cdot 9H_2O$ solution	Salt-oxide Mechano-hydrothermal	[Pre-milling]: 450 rpm [Mg: Al+Fe] = 3:1 [pH] = initial 7.8, final 7.0 [Aging]: 80°C in autoclave for 3 or 6 h [Drying]: 60°C
(Hu *et al.*, 2016)	BR-LDH	Red mud (gibbsite $Al(OH)_3$, sodalite $Na_4Al_3Si_3O_{12}Cl$, hematite Fe_2O_3) Boron mud (forsterite Mg_2SiO_4, muscovite $KAl_2(AlSi_3O_{10})(OH)_2$, huntite $Mg_{0.92}Ca_{0.08}CO_3 \cdot 3H_2O$)	1. Dried mixture was calcined at 600°C for 3 h (BR-600, 60 g) 2. BR-600 was added to NaOH solution to react at 30°C for 6 h	Calcination Salt-oxide	[boron mud: red mud] = 1:1, 2:1, 3:1, <u>4:1,</u> 5:1 [pH] = 4-12 [Aging]: room T, 24 h [Drying]: 80°C, overnight

* → *indicates the system with the most promising result*

* *<u>Underlined</u> parameters represent the optimum reaction conditions*

**Conditions that are not recorded are either not reported or not controlled*

Summary of Table 2.8

A wide range of industrial wastes containing metal oxide or hydroxides are found to become the material sources for constructing LDH layer structure, such as bauxite, blast furnace slag, aluminum dross, red mud and boron mud (Das *et al.*, 2009; Kuwahara *et al.*, 2010; Hu *et al.*, 2016). The intercalated anions between the interlayers are determined by the anion supplied in the suspension solution. Table 2.8 illustrates that co-precipitation and salt-oxide method are most commonly employed. The key operating factors influencing the properties of the final products are presented in the above table, including pre-treatment, the M^{3+}/M^{2+} ratio, the liquid-to-solid ratio, pH, aging and drying conditions. To briefly sum up, the optimum $[M^{3+}/M^{2+}]$ ratio is generally in the range of 2-4:1; the aging temperature is around 70-80°C without hydrothermal treatment; drying is controlled at 60-80°C overnight. The common differences among the methods is the variation of pH during precipitation. Some researchers leave the pH unadjusted, while in some cases, pH is kept at a fixed value. For example, Mg-Al LDHs were prepared by Béres et al. (1999) at pH 8–9 and by Constantino & Pinnavaia (1995) and El Gaini et al. (2009) at pH = 10. Fe-Al LDHs were produced by Ferreira et al. (2004) at pH = 8-9 or 12-13 depending on $[M^{3+}/M^{2+}]$ ratio. Though not included in the table, it is worth noting that Ferna et al. (1998) also applied a pH of 10 for the synthesis of Mg-Al-Fe LDH.

2.3.3 Synthetic Strategy for Using RM as Metal Sources

2.3.3.1 Surface chemistry of the RM solid phases

In order to better understand the possible characteristics of employing RM to synthesise LDH, the surface chemistry of the RM solid phases is studied in this section. Chevedov et al. (2001) found that RM particles have acid/ base type properties in aqueous solutions, which result from the surface hydroxyl groups. In addition, RM solids exhibit a high acid neutralizing capacity (ANC) from 1 to 3.6 mol/kg given the endpoint pH=7 (Gräfe, Power and Klauber, 2011), due to the abundance of amorphous and finely crystalline phases (McConchie, Clark and Davies-McConchie, 2002). This property is retained after neutralization treatment as the existence of multiple major contributors like boehmite, calcite, sodium-aluminium-silicate that in turn form weak bases (Khaitan, Dzombak and Lowry, 2009; Palmer, Frost and Nguyen, 2009; Khaitan *et al.*, 2010).

As mentioned in Section 2.2.3, Al and Fe phases in RM are of particular interest for LDH synthesis. In Table 2.9, Khairul et al. (2019) stated the common Fe and Al minerals present in RM.

Table 2.9 Commmon mineral forms of the Fe and Al element in red mud, summarized by Khairul et al. (2019)

Element	Mineral	Chemical formula
Fe	Hematite	α-Fe_2O_3
	Goethite	α-FeOOH
	Magnetite	Fe_3O_4
	Ilmenite	$FeO{\cdot}TiO_2$
	Ferryhydrite	$Fe_2O_3{\cdot}0.5H_2O$
	Maghemite	γ-Fe_2O_3
Al	Gibbsite	α-$Al_2O_3{\cdot}3H_2O$
	Boehmite	α-$Al_2O_3{\cdot}H_2O$
	Diaspore	β-$Al_2O_3{\cdot}H_2O$

The Al-containing species in RM are usually in crystalline form with little soluble content in alkaline solutions (Hu *et al.*, 2019), so they cannot directly take part in LDH synthesis (also refer to Table 2.5). Thermal or mechanochemical pre-treatments could reduce the binding energies of Al-O, thus enhancing the activity of Al_2O_3 and releasing more soluble Al species in alkaline solutions (Ye *et al.*, 2017). The effects of calcination/ heat treatment on RM are discussed in Section 2.3.4.

With regard to the most abundant solid phase, Fe species in the RM exist in the form of hematite and octahedral Fe^{3+} in the aluminosilicates (Hu *et al.*, 2019). Iron oxides dissolve slowly over a wide pH range according to the solubility diagram (Figure 2.10). Between pH 4 to 10, the level of total Fe in solution is $<10^{-6}$ M. Generally, the solubility of Fe^{III} oxides is very low, while Fe^{II} oxides are sparingly-soluble. Basu (1983) pointed out that the solubility of goethite (FeO(OH)) in sodium aluminate solutions is close to zero at ambient temperatures. Iron oxides appear to have the minimum solubility around pH 7–8, which is around their pH_{pzc}. The solubility of solid is also affected by the particle size of the solid (Palmer, Frost and Nguyen, 2009).

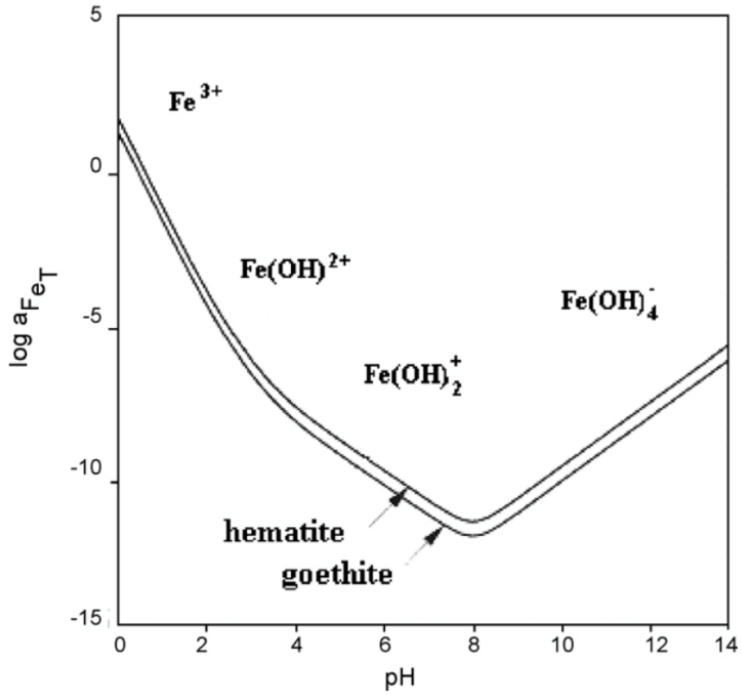

Figure 2.10. Solubility of goethite and hematite as a function of pH (Cornell and Schwertmann, 2003).

2.3.3.2 Impacts of Fe spinel and oxides

The inclusion of Fe^{III} in the LDH structure enhances the efficiency of the adsorbent (Abou-El-Sherbini *et al.*, 2015). The various possible Fe minerals in RM-LDH products (Pulford *et al.*, 2012; Heredia *et al.*, 2013), including spinel ferrite MFe_2O_4 (M = Mg, Zn, Co, Ni, etc), magnesium-ferrite aluminate, iron oxides (Fe_3O_4), maghemite (γ-Fe_2O_3) and α-Fe_2O_3 with various nanostructures are of great interest in displaying magnetic behaviour (Li *et al.*, 2004; Lu, Salabas and Schüth, 2007; Heredia *et al.*, 2013). Magnetic separation is a smart solution for water treatment as well as the recycling of adsorbents. The synthesis of magnetic nanoparticles also involves similar processes with LDH production (Table 2.10), such as the widely studied co-precipitation, thermal decomposition (Lu, Salabas and Schüth, 2007; Akin *et al.*, 2012).

Table 2.10 Comparison of the synthetic methods for magnetic nanoparticles (Lu, Salabas and Schüth, 2007)

Synthetic method	Synthesis	Reaction temp. [°C]	Reaction period	Solvent	Surface-capping agents	Size distribution	Shape control	Yield
co-precipitation	very simple, ambient conditions	20–90	minutes	water	needed, added during or after reaction	relatively narrow	not good	high/ scalable
thermal decomposition	complicated, inert atmosphere	100–320	hours–days	organic compound	needed, added during reaction	very narrow	very good	high/ scalable
microemulsion	complicated, ambient conditions	20–50	hours	organic compound	needed, added during reaction	relatively narrow	good	low
hydrothermal synthesis	simple, high pressure	220	hours ca. days	water-ethanol	needed, added during reaction	very narrow	very good	medium

A number of researchers have carried out experiments on the removal of dye pollutant using magnetic LDH (Yang *et al.*, 2016). For example, Abou-El-Sherbini et al. (2015) successfully synthesised a series of Fe-containing LDHs that exhibited magnetic behaviour and could be magnetically separated after being loaded with Isolan Dark Blue (IDB) or chromate. Core-shell Fe_3O_4@Mg_3Al-CO_3 LDH prepared by Yan et al. (2015) is another superior magnetic adsorbent for the anionic dye Acid Yellow 219 (AY219). It preserves the 'memory effect' feature of LDHs, whose structure collapses at 400°C after 5 h of calcination and is restored in AY219 solution (Figure 2.11). Furthermore, the stable adsorption capacity of 1024 mg/g is maintained after 3 cycling tests. The values of remnant magnetization (*Mr*) for Fe_3O_4 and Fe_3O_4@Mg_3Al–CO_3 LDH in their experiments were 7.51 and 0.67 emu/g respectively (Figure 2.12a).

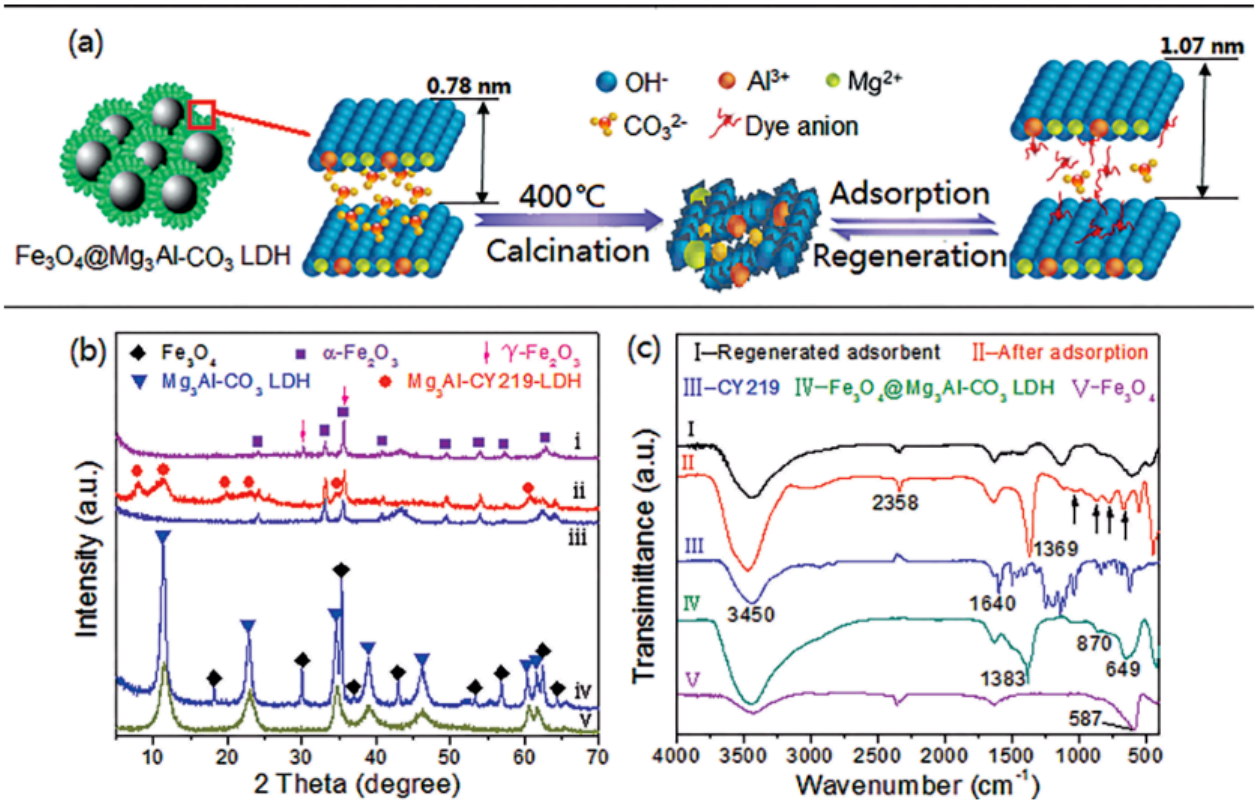

Figure 2.11 ***(a)*** *Scheme of the phase evolution of the $Mg_3Al–CO_3$ LDH shell during calcinations, dye adsorption and regeneration;* ***(b)*** *XRD patterns of (i) regenerated adsorbent, (ii) adsorbent after dye adsorption, (iii) fresh adsorbent, (iv) Fe_3O_4@$Mg_3Al–CO_3$ LDH, and (v) $Mg_3Al–CO_3$ LDH;* ***(c)*** *FTIR spectra of (I) regenerated adsorbent, (II) adsorbent after dye adsorption, (III) dye AY219, (IV) Fe_3O_4@$Mg_3Al–CO_3$ LDH, and (V) Fe_3O_4.*

L. Lu et al. (2016) prepared hierarchically porous $MgFe_2O_4$/γ-Fe_2O_3 magnetic microspheres for removing the dyes Congo red (CR) and Minocycline (MC) from wastewater. They consisted of nanocrystallites with a grain size of 8 nm that exhibited excellent adsorption capacities of 259.1 mg/g and 200.8 mg/g for CR and MC respectively. Their magnetic hysteresis loops (Figure 2.12b) displayed typical S-shaped curves, indicating the super-paramagnetism of the products. The coercivity field (*Hc)*, remnant magnetization (*Mr*) and saturation magnetization (*Ms*) of γ-Fe_2O_3 were 10.1 Oe, 0.35 emu g^{-1} and 32 emu g^{-1}, while those of $MgFe_2O_4$/γ-Fe_2O_3 were 6.8 Oe, 0.32 emu g^{-1} and 34.9 emu g^{-1}, respectively.

The engagement of different ratios of ferrimagnetic $MgFe_2O_4$ and/or weak-ferromagnetic α-Fe_2O_3, could increase the complexity of the RM-LDHs, and the aluminium content could affect the paramagnetic and superparamagnetic phases (Heredia *et al.*, 2013). The magnetic

behaviour therefore depends on the synthesis process and conditions (Sundararajan *et al.*, 1984).

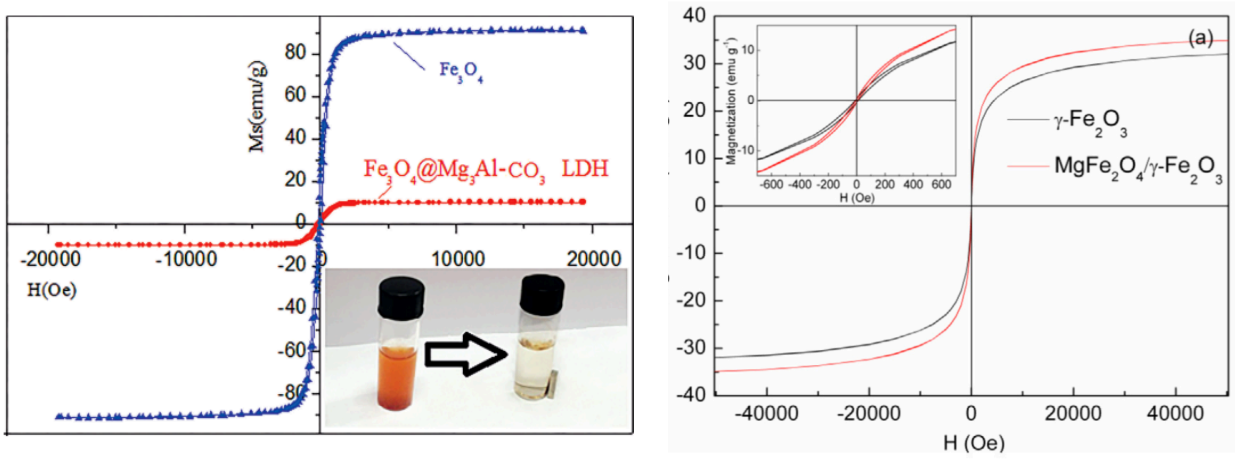

Figure 2.12 ***(a)*** *Magnetization curves of Fe_3O_4 and Fe_3O_4@$Mg_3Al–CO_3$ LDH measured at room temperature. The inset demonstrates the separation of adsorbent from solution using a magnet, by Yan et al. (2015);* ***(b)*** *Magnetization curves of γ-Fe_2O_3 (600 °C) and $MgFe_2O_4$/γ-Fe_2O_3, applied magnetic field at room temperature, with the field sweeping from -50 to 50 kOe (L. Lu et al. 2016).*

2.3.3.3 Impact of Ti contents

Corresponding to Section 2.2.1 and Section 2.3.2, other than the intercalation of anion species into the LDH product, the raw material RM itself is also capable of immobilising trace metals. One main reason is that the finely grained oxide particles (e.g. Fe_2O_3, Al_2O_3, TiO_2) with a texture like aluminium silicates have a high surface area and positive charge density (Gupta and Sharma, 2002). Sahu, R. Patel, et al. (2010) assessed the activated CO_2-neutralised RM for arsenate removal and suggested that the hydroxyl surfaces of mixtures of Fe, Al and Ti oxides offer strong affinity for As by forming inner-sphere complexes. Das et al. (2009) synthesised the Ti^{4+} containing Mg-Al LDH using the acid digestion solution of titanium-rich bauxite as the raw material. $MgTiO_3$ could be identified from the XRD pattern in calcined Ti-LDH (700°C). The incorporation of Ti^{4+} in LDHs enhanced anion exchange capacity but exhibited smaller surface areas (Das et al. 2009). A novel colloidal TiO_2/LDH was prepared, with a high surface area which accelerated the photodegradation of Acid Orange 7 (AO7) (Bauer, Jacques and Kalt, 1999).

2.3.4 Governing Pre-Treatments and Process Variables

Based on the aforementioned methods, modified co-precipitation and salt-oxide methods are proposed to synthesise RM-LDHs in this research. The pre-treatments and mechanical dispersion aim to obtain highly dispersed and high surface energy particles to initiate the reaction. The key parameters considered in this section are (Othman *et al.*, 2009; Yanmin Yang *et al.*, 2012; Paikaray and Hendry, 2014):

1. Pre-treatments (heat treatment and grinding);
2. Dispersion;
3. The M^{II}/M^{III} ratio;
4. Aging temperature & time.

According to the examples listed in Table 2.8, the salt-oxide method usually leaves the pH as it develops. It is also evident in the literature that a highly alkaline environment is recommended for Mg-Al-Fe LDHs synthesis. Paikaray & Hendry (2014) found that the formation of Mg-Fe-SO_4^{2-}-CO_3^{2-} LDH was favoured at pH $\geq$ 9. Therefore, the pH is not deliberately adjusted in the following study, but the initial and final pH are measured.

2.3.4.1 Pre-treatment I: Calcination/ heat treatment

As summarized in Table 2.5, extensive experiments have indicated that inactivated RM hardly reacts with metal salts. Heat treatment is a crucial procedure to activate RM. Liu et al. (2016) examined the thermal behaviour of RM under various heating conditions. Figure 2.13a and Figure 2.14 indicate the thermal decomposition profile for raw RM. Key findings alongside the elevated temperature (350-800°C) are as follow:

1) Around 350°C, dehydroxylated silicates form
2) Below 430°C, mass loss is associated with the loss of water or dehydroxylation from hydroxides, e.g. goethite transforms to hematite and gibbsite transforms to boehmite;
3) Around 520°C, boehmite in RM transforms to transition alumina;
4) At 600-700°C, carbonates (calcites) decompose and oxygen releases;
5) Below 800°C, alumina quartz and hematite are not influenced by heating.

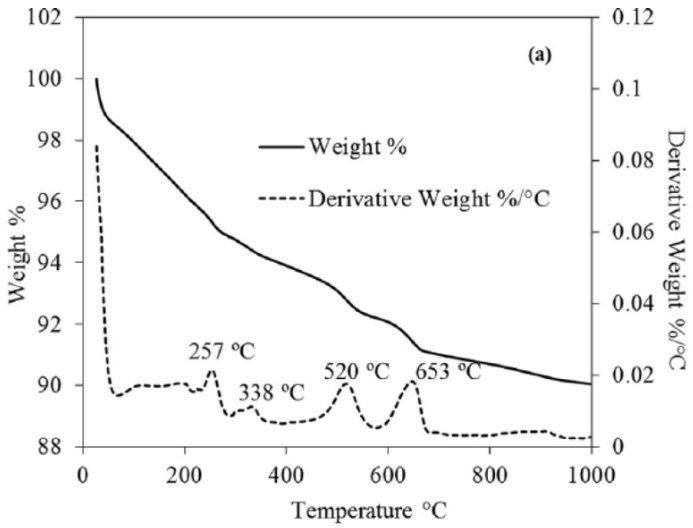

$Al(OH)_{3(s)} \rightarrow AlO(OH)_{(s)} + H_2O_{(g)}$ (573K)

$Al_2O_3.3H_2O_{(s)} \rightarrow Al_2O_3.H_2O_{(s)} + 2H_2O_{(g)}$ (573K)

$2AlO(OH)_{(s)} \rightarrow Al_2O_{3(s)} + H_2O_{(g)}$ (above 573K)

$2FeO(OH)_{(s)} \rightarrow Fe_2O_{3(s)} + H_2O_{(g)}$ (544 K)

(a) ***(b)***

Figure 2.13 ***(a)*** *The thermal behavior of red mud [thermogravimetric analysis (TGA) by Liu et al. (2016);* ***(b)*** *Reactions of different oxides at high temperatures during calcination of RM by Uzun & Gülfen (2007).*

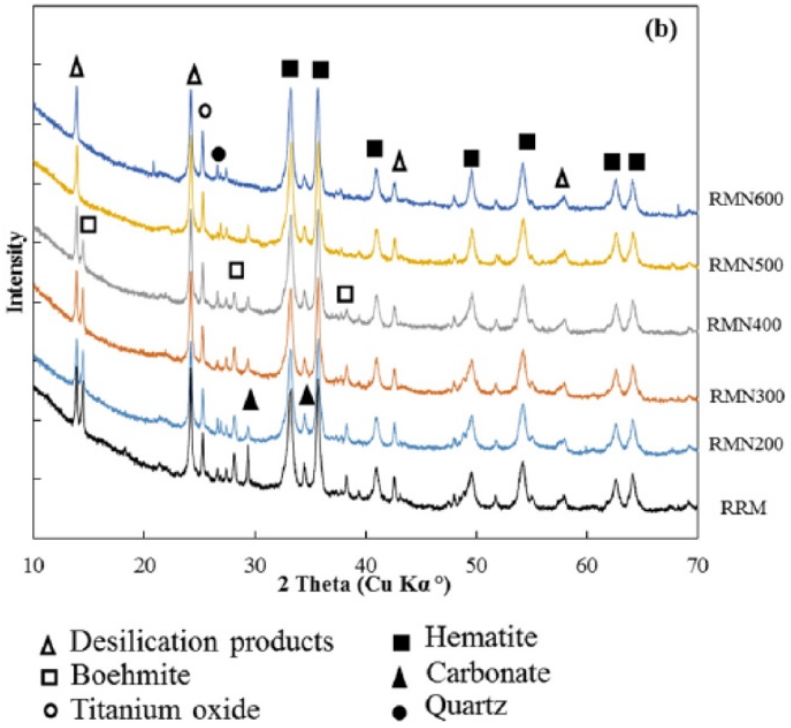

Figure 2.14 Thermal behaviour of red mud X-ray diffraction (XRD) profile (Liu et al. 2016).

Uzun & Gülfen (2007) investigated the impact of calcination on the extractable components of RM in sulphuric acid. The weight loss of RM at different temperatures was in good agreement with the above findings. Based on Figure 2.15, the dissolution rate above 873 K (600°C) decreased, since less soluble oxides started to form. 600°C was considered as the optimum temperature to maximise the activity of RM solids.

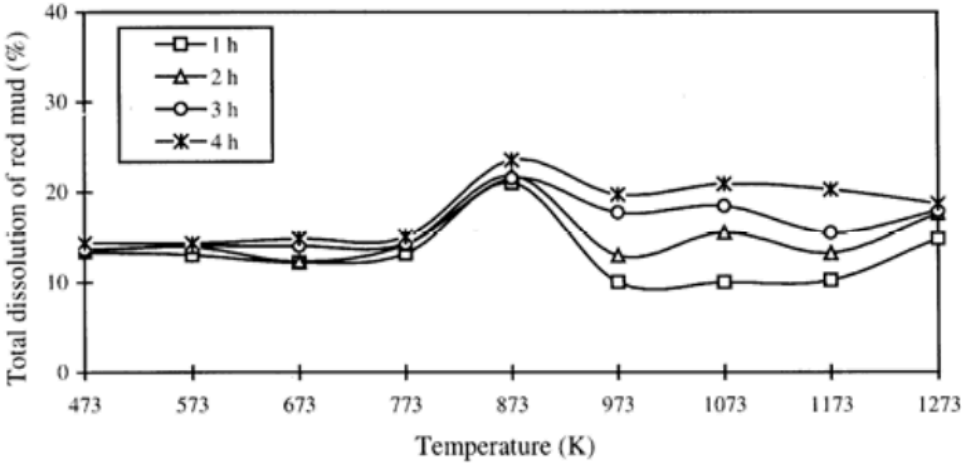

Figure 2.15 Effect of calcination temperature and time (1 g calcined RM in 100 mL 1 M H_2SO_4, temperature 298 K; leaching time 120 min; agitation rate 400 rpm) (Uzun & Gülfen 2007).

2.3.4.2 Pre-treatment II: Grinding

Since the synthesis deals with solid raw materials, and considers the surface chemistry of RM, the reaction has to include a dissolution-precipitation process (Stanimirova and Kirov, 2003). However, this conversion normally proceeds slowly. Mechanochemical approaches therefore may have the potential to overcome the barriers as a supplement to the basic salt-oxide method. Grinding has been widely considered to equip the raw materials with decreased particle size and induce stress in the particles, which as a result enhances their reactivity and solubility (Ay, Zümreoglu-Karan and Mafra, 2009; Budhysutanto *et al.*, 2010; Qu *et al.*, 2016). Without grinding, for instance, through the direct hydrothermal treatment of MgO, Al_2O_3 in $NaNO_3$ solution, a considerable amount of brucite $Mg(OH)_2$ is formed in the LDH product (Xu and Lu, 2005). Grinding also improves the crystallinity of LDH at a relatively lower temperature or shorter aging time compared with the direct hydrothermal process. Normally, grinding can be divided into dry grinding of metal hydroxides or metal salts with sodium hydroxide (Khusnutdinov and Isupov, 2007) and wet grinding of the metallic salt solution (Iwasaki, Yoshii, *et al.*, 2012; Qu *et al.*, 2016).

Dry grinding

The operation of grinding helps to activate the hydroxide or metallic salts to a weakened crystal structure (Qu *et al.*, 2016). Tongamp et al. (2007) conducted a two-step milling route and advised that solid-state grinding facilitated the transformation of $Mg(OH)_2$ and $Al(OH)_3$ into amorphous and/or near amorphous phases and created new active sites for further

reactions. Ay et al. (2009) manually ground a powder mixture of $Mg(NO_3)_2 \cdot 6H_2O$ and $Al(NO_3)_3 \cdot 9H_2O$ with NaOH pellets in a mortar. The paste produced was then washed and dried under vacuum. The product showed all diffraction characteristics of LDH structure but with lower crystallinity compared to co-precipitation.

As also reviewed in Table 2.8, Zhang et al. (2013) milled MgO and Al_2O_3 for 1 h in ambient air by a planetary ball mill prior to hydrothermal treatment. The authors observed that the pH of the pre-milled MgO and Al_2O_3 mixture was notably higher than that of the un-milled mixture, suggesting that dry grinding improved the chemical activity of the starting materials. During the subsequent hydrothermal process, hydrolysis and dissociation of the activated MgO and Al_2O_3 occurred quicker to form iconic species (Figure 2.16). Highly-crystallised and well-dispersed $Mg_2Al–NO_3$ LDH products were obtained.

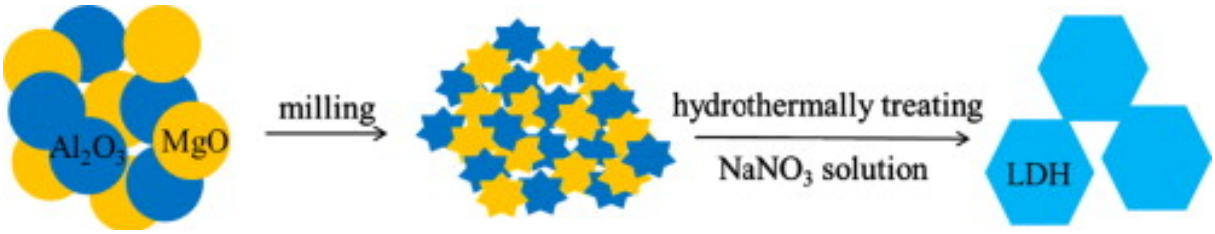

Figure 2.16 Mechano-hydrothermal route to synthesize LDH by Zhang et al. (2013).

Wet grinding

In a study by Budhysutanto et al. (2010), aluminium trihydroxide (ATH, i.e. gibbsite $Al(OH)_3$) and MgO were taken as the raw materials for the synthesis of $Mg_4Al_2(OH)_{14}•4H_2O$. Among various pre-treatment techniques, mixed wet grinding of MgO and ATH in water achieve the strongest effect, including the largest reduction in particle size, complete MgO transformation, the highest ATH conversion, etc. A reaction mechanism is proposed in Figure 2.17. The formation of amorphous $Mg(OH)_2$ is accompanied by an increase in pH of the solution to >11. At this basic condition, ATH dissolves in the solution as $Al(OH)^{4-}$. Zhang et al. (2013) also explored a similar mechano-hydrothermal method for LDH synthesis from MgO and Al_2O_3, revealing that pre-milling induces the complete transformation of the starting materials.

Grinding of MgO in ethanol is another option, which yields small MgO particles while preventing the formation of crystalline brucite in the pre-treatment procedure upon prolonged contact with water. Another advantage is to effectively avoid the interference of CO_2 from

the ambient air so that more amorphous $Mg(OH)_2$ with a higher solubility can form after the temperature is increased and the reaction takes place. In addition, wet-grinding in organic solvents is employed to produce iron-based LDH (Iwasaki, Shimizu, *et al.*, 2012).

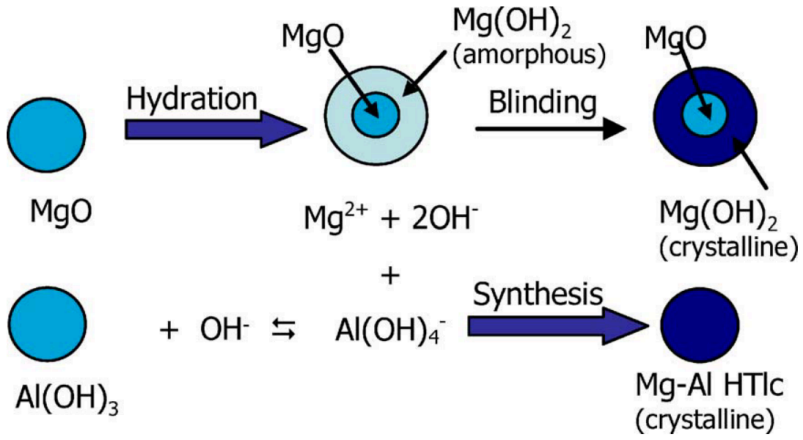

[Wet grinding]

Figure 2.17 Mechano-hydrothermal route to synthesize LDH (Budhysutanto *et al.*, 2010).

2.3.4.3 Variable I: Dispersion

As mentioned in Section 2.3.2, regarding the salt-oxide method, to minimize the MgO particles being trapped by the $Mg(OH)_2$ and enhance the LDH phase formation, the dispersion method is considered. Valente et al. (2009) studied the influence of mechanical dispersion time upon particle size distribution. The study included the dispersion of pristine MgO and the boehmite-aluminium nitrate solution (BANS). When the particle size of the precursors and the reaction mixture is reduced, more particles and reactive surfaces become available.

According to Valente et al. (2009), MgO completed the conversion to $Mg(OH)_2$ after 10 min – 300 rpm agitation and the average particle size of MgO in water did not see considerable reduction after 30 min (Figure 2.18a). The dispersion study of BANS by Valente et al. (2009), indicated that a substantial decrease in the average particle size was achieved when dispersing for longer time (Figure 2.18b). The author proposed 30 min was the optimum time for both MgO and BANS dispersion. The reaction mixture of MgO and BANS was dispersed at 8000 rpm considering a larger viscosity. As observed from Figure 2.18c, a homogeneous distribution was gained. A dispersion time of 60 min was selected for the optimal results.

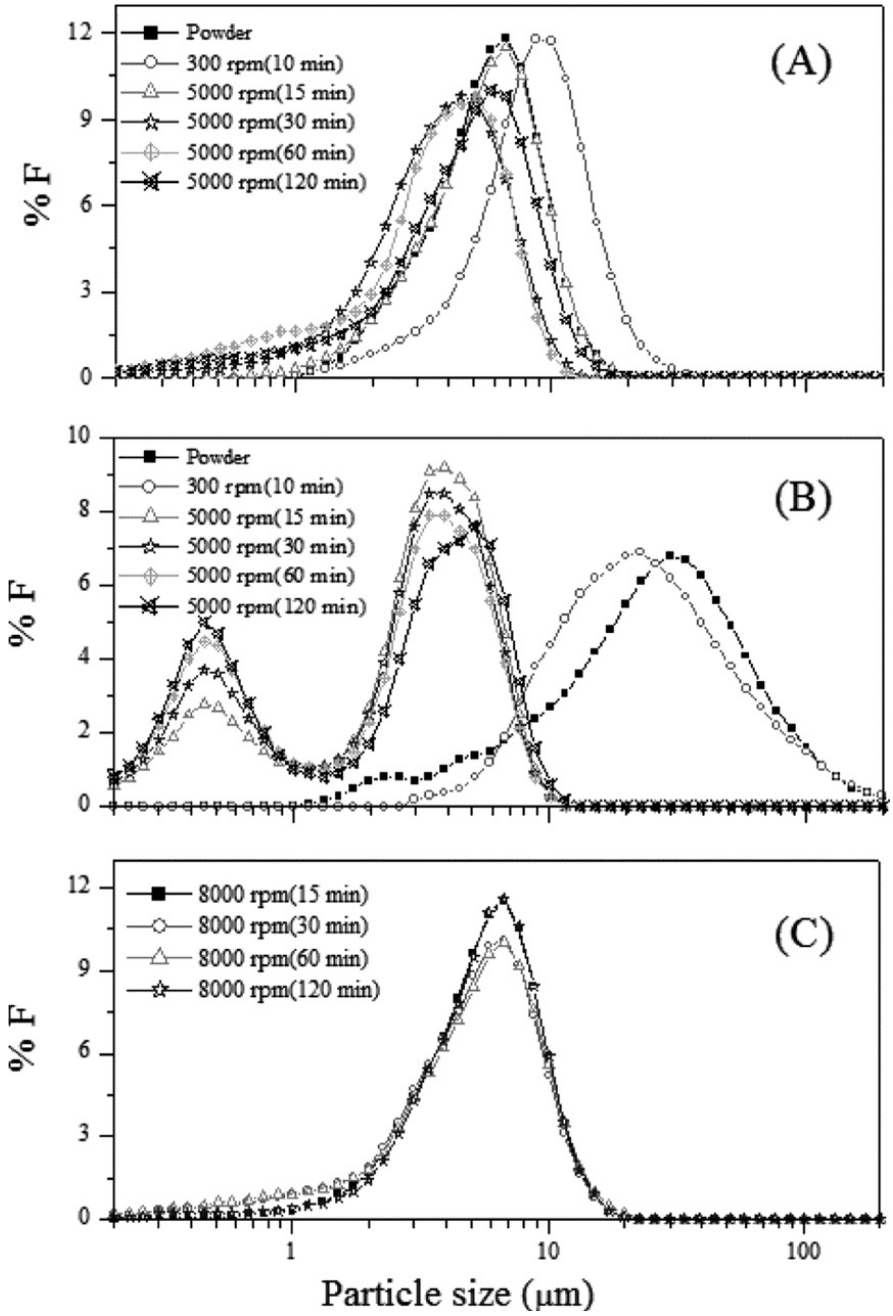

Figure 2.18 Particle size distribution resulting from the dispersion in water of ***(a)*** *MgO,* ***(b)*** *boehmite-aluminum nitrate solution, and* ***(c)*** *reaction mixture of (a) and (b).*

2.3.4.4 Variable II: M^{II}/M^{III} ratio

The formation of LDHs and the acid-base properties of mixed metal oxides (CLDH) are governed by the M^{II}/M^{III} molar ratio (Othman *et al.*, 2009). The initial M^{II}/M^{III} ratio is usually retained in final LDH products if suitable precipitation conditions are given, according to previous elemental chemical analysis (Ferna *et al.*, 1998; Rozov *et al.*, 2010). Most of the mixed double hydroxides can be obtained through adjusting the M^{II}/M^{III} ratio (see Table 2.8). Table 2.11 summarises some of the common LDHs and their M^{II}/M^{III} range. Brindley & Kikkawa (1979) noted that a low M^{II}/M^{III} ratio may result in the formation of $Al(OH)_3$ while a high M^{II}/M^{III} ratio leads to the precipitation of $Mg(OH)_2$, owing to either excessive Al or Mg containing octahedra in the sheets. Taking Mg-Fe-CO_3 LDH as an example, the molar ratio of Mg^{2+}/Fe^{3+} is usually in the range of 2-3.

Table 2.11 Chemical composition range of various LDH (Rives, 2001).

M^{II}-M^{III}-X	$pH_{formation}$	M^{II}/M^{III} (R) range
[Zn-Al-Cl]	7.0	$1.0 \leq R \leq 5.0$
[Zn-Al-Cl]	10.0	$1.0 \leq R \leq 3.0$
[Ni-Cr-Cl]	11.5	$1.0 \leq R \leq 3.0$
[Ni-Cr-CO_3]	13.0	$1.0 \leq R \leq 2.0$
[Cu-Cr-Cl]	5.5	$1.6 \leq R \leq 2.3$
[Zn-Al-CO_3]	9.0	$1.7 \leq R \leq 2.3$
[Mg-Al-CO_3]	8.0	$1.0 \leq R \leq 3.0$
[Zn-Cr-Cl]	4.5	$R \approx 2.0$
[Zn-Cr-Cl]	10.0	$2.0 \leq R \leq 3.0$
[Mg-Fe-CO_3]	-	$2.7 \leq R \leq 5.6$
[Ni-Al-ClO_4]	10.0	$1.0 \leq R \leq 3.0$
[Co-Fe-Cl]	9.0	$1.8 \leq R \leq 4.0$
[Co-Fe-CO_3]	9.0	$1.0 \leq R \leq 3.0$

In addition, varying the M^{II}/M^{III} ratio also causes changes in the crystallinity and crystallite size of the LDHs (Shekoohi *et al.*, 2017), the layer spacing, the particles sizes and the surface area (Miyata, 1980). Benselka-Hadj Abdelkader et al. (2011) produced Mg-Fe-CO_3 LDH with various Mg/Fe molar ratios of 2-5 via the co-precipitation method. They also proposed the influence of Mg/Fe was apparent and at the molar ratio = 3, the good crystallinity and higher LDH content in sample were obtained, as partially described in Figure 2.19. This finding is in good agreement with the above Table 2.11 and with those previously reported (Ferreira *et al.*, 2004; Yiqiong Yang *et al.*, 2012). In addition, different M^{II}/M^{III} ratios also

affect thermal stability. Shekoohi et al. (2017) conducted thermogravimetric analysis and found that the Mg-Al nano-hydrotalcite with a molar ratio of 1:1 exhibited the highest thermal stability in respect to samples with 3:1 and 5:1 ratio.

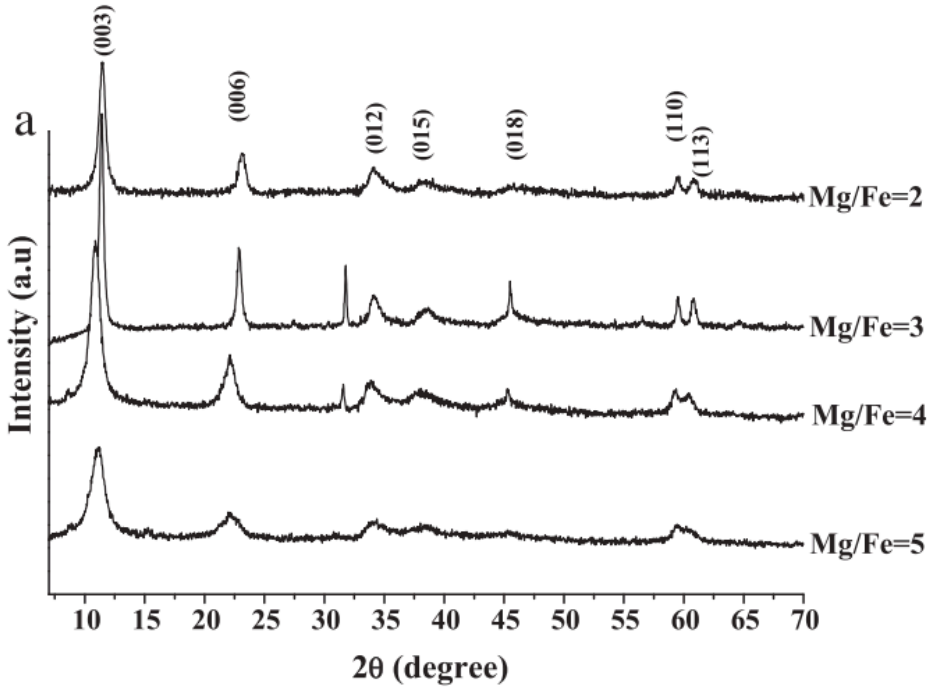

Figure 2.19 XRD patterns of MgFe-LDH with various Mg/Fe ratios (Benselka-Hadj Abdelkader *et al.*, 2011).

2.3.4.5 Variable III: Aging time & temperature

It has been found that prolonged aging time increases the crystallinity of LDH products (Hickey, Kloprogge and Frost, 2000; Adachi-Pagano, Forano and Besse, 2003; He *et al.*, 2006). As temperature increases during co-precipitation, the availability of relatively more octahedrally-coordinated Fe^{3+} increases, which enhances LDH formation. The influence of aging can be observed from diffraction peaks of resultant products (Figure 2.20). The featured LDH peaks become sharper with extended thermal treatment. In addition, the crystals become bigger particles as aging temperature and duration increase (Hickey, Kloprogge and Frost, 2000; Yanmin Yang *et al.*, 2012).

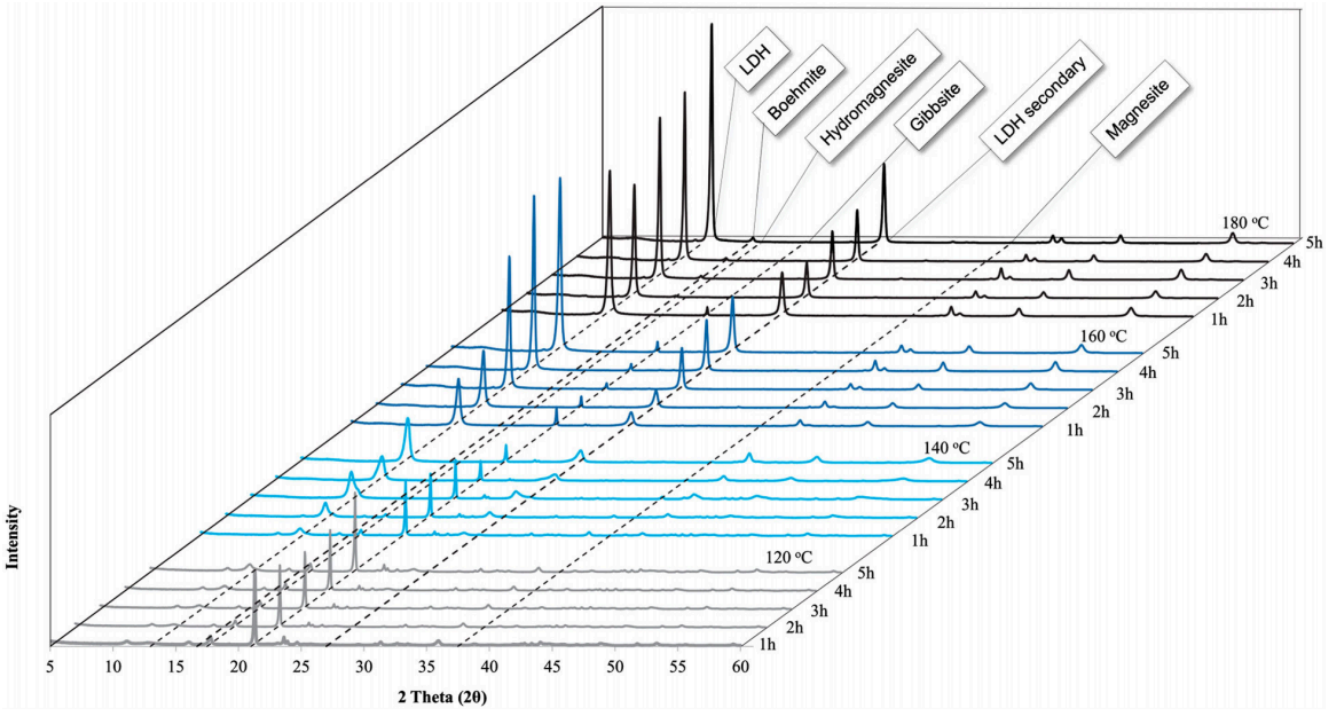

Figure 2.20 XRD results for experiments conducted for the hydrothermal synthesis of hydrotalcite at temperatures varying between 120°C and 180°C and reaction times varying between 1 h and 5 h (Labuschagné *et al.*, 2018).

On the other hand, Paikaray & Hendry (2014) investigated the formation of a ferric LDH and suggested that the phenomena 'crystallinity increased as the aging temperature and time increased' was limited. They found that prolonged thermal exposure (after 5 days at 65°C or 1 day at 95°C) of LDH precipitation may also lead to a loss of crystallinity. Combined with the synthesis results of Adachi-Pagano et al. (2003), the aging time of 18 h should be guaranteed and 48 h still favours the better crystallinity of MgAl-CO_3 LDH (reaction conditions: Mg^{2+}/Al^{3+} = 3, urea/ (Mg^{2+}/Al^{3+}) = 3.3, T = 90°C, deionised water).

2.4 Characterisation and Evaluation of As-synthesised Products

To determine whether LDH phases have been synthesised, the product materials should first meet the 'golden rules' and also exhibit the distinctive characteristics of a typical LDH in 'role plays'. Often, standard characterisation tools can only provide limited information on the material, precise qualification and quantitation of the LDH structure are not often achievable. Assessing certain peculiarities of LDH such as adsorptive performance and 'memory effect' have been suggested to answer this question.

See Figure 2.21, the 'Golden rules' refers to a set of standard structure characterisation methods including: (1) Crystallinity study by Powder XRD; (2) Morphology observation by SEM; (3) Lattice vibration profile by FTIR; (4) Thermal properties by TG-DTA. Here, the 'role plays' of LDH refer to its anion removal performance, thermal stability and memory effect, which provide direct information on estimating RM-LDH's properties and potential applications.

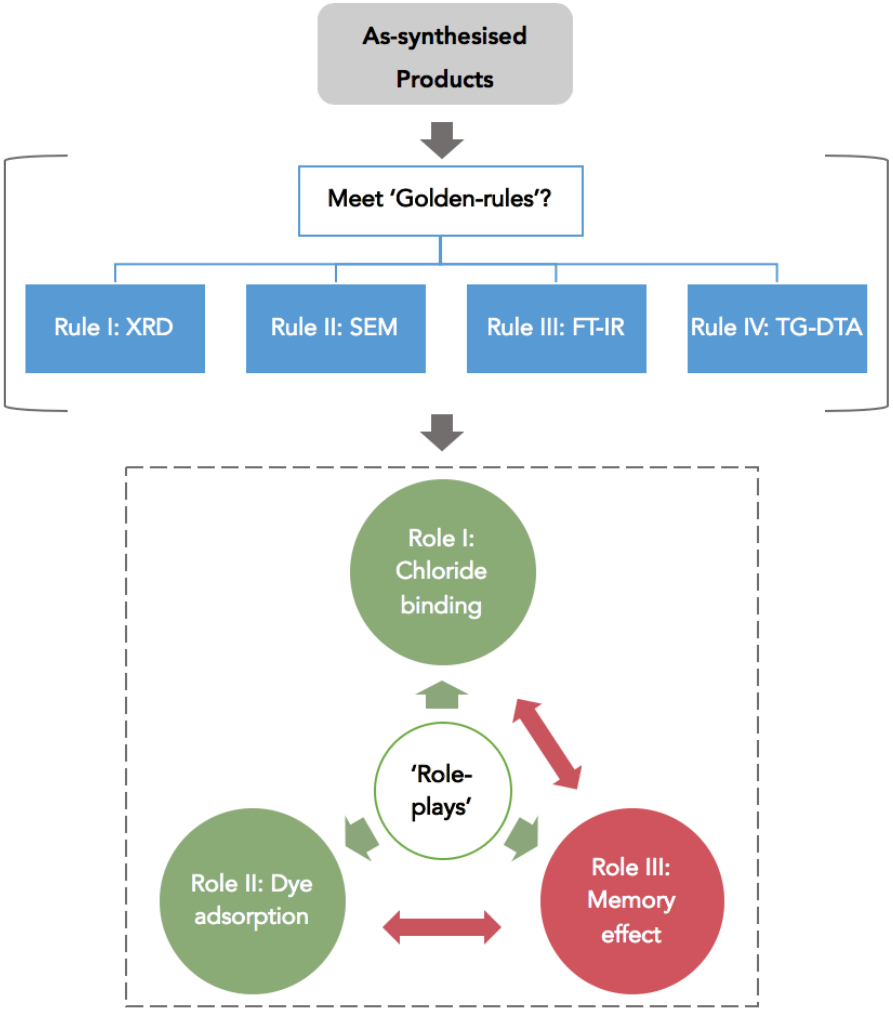

Figure 2.21 Framework of characterisation and evaluation of as-synthesised products

2.4.1 'Golden Rules' of LDH Structure

2.4.1.1 Rule I: Crystallinity XRD

X-ray diffraction (XRD) patterns are the most common tool for identifying the layer structure and comparing the degree of crystallinity. The representative XRD patterns of the LDH phase (3R stacking) are shown in Figure 2.22. The presence of three narrow, symmetric, strong reflection peaks (003), (006), (009) at low 2θ values, weaker, less symmetric peaks (110) and (113) at high 2θ values between 60°-63° reveals a well-crystalline-layered structure (Millange, Walton and O'Hare, 2000). The main peaks at around 11° and 24° 2θ (d_{003} plane) are assigned to hydrotalcite (00-035-0965). Based on the position of the crystallographic indices (00*l*), the corresponding basal *d*-spacing values *d*(00*l*) can be determined by the Bragg equation, as shown in Table 2.12. It is known that the *d*-spacing value can reflect the size of the interlayer guest anion species (Misra, 1992; Olanrewaju *et al.*, 2000; Huang *et al.*, 2015). For the common CO_3^{2-} form of LDHs, the d_{003} and d_{006} are *ca*. 7.8 Å and 3.9 Å respectively; whereas for NO_3^--LDHs, the *d*-spacing are *ca*. 8.8 Å and 4.4 Å respectively (Brindley and Kikkawa, 1978). The more intense the peaks, the higher the degree of the crystallinity of LDH is (Adachi-Pagano, Forano and Besse, 2003; He *et al.*, 2006).

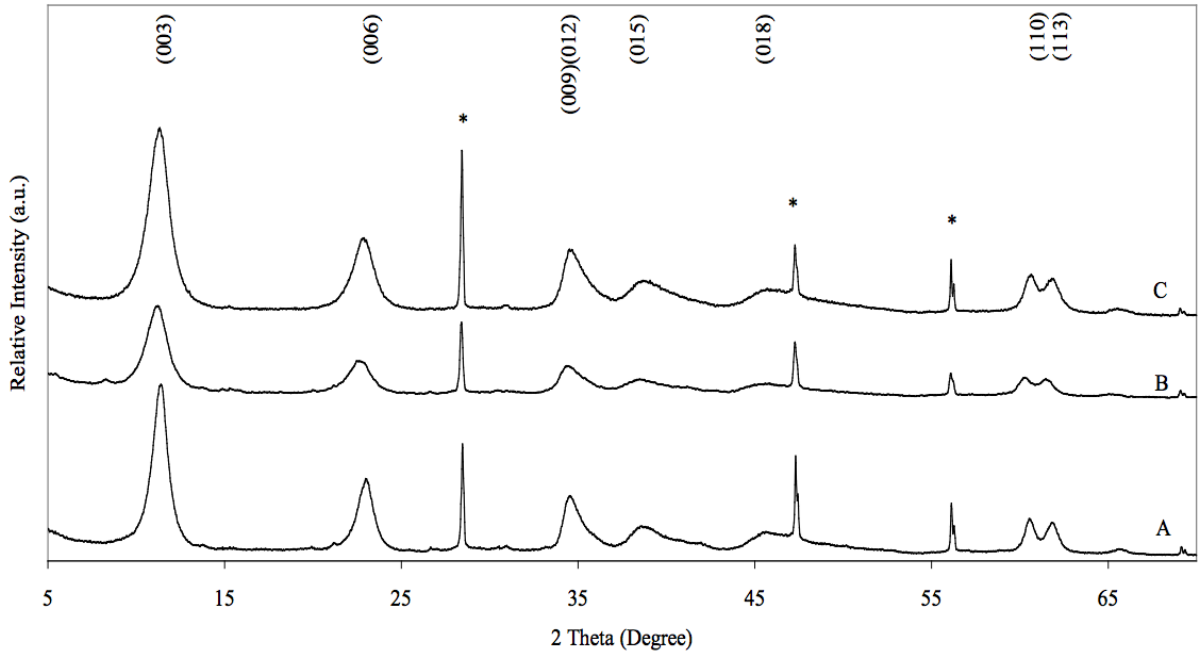

Figure 2.22 XRD patterns of original layered double hydroxides synthesized by coprecipitation method with various cations composition. A – Mg/Al; B- Mg/Co/Al; C- Mg/Ni/Al. Reflections from Si crystal used as a reference are marked with asterisk (Klemkaite *et al.*, 2011).

Table 2.12 Crystallographic data and crystallite size of synthesized layered double hydroxides (Klemkaite *et al.*, 2011)

Sample name	d_{003} (Å)	d_{006} (Å)	d_{110} (Å)	Cell parameters (Å) c	a	Crystallite size (Å) 003	110
Mg/Al	7.77	3.86	1.53	23.25	3.06	91	111
Mg/Co/Al	7.93	3.92	1.53	23.59	3.07	61	83
Mg/Ni/Al	7.87	3.89	1.53	23.40	3.05	64	85

2.4.1.2 Rule II: Morphology SEM

Scanning electron microscopy (SEM) is another tool to confirm the microstructural features of LDH materials. In general, the size scale of lamellar texture and hexagonal crystals of LDH are several decades' nanometre. Figure 2.23 shows the featured SEM image for LDHs (Adachi-Pagano, Forano and Besse, 2003; Shan *et al.*, 2015). Wang et al. (2017) prepared the Mg/Al/Fe-LDH and Mg/Al-LDH via a co-precipitation method. As revealed in Figure 2.24, both samples presented mainly platelet structures and morphological homogeneity, while the particle size of Mg/Al/Fe-LDH was smaller and the surface of the Fe-containing LDH was more bouffant.

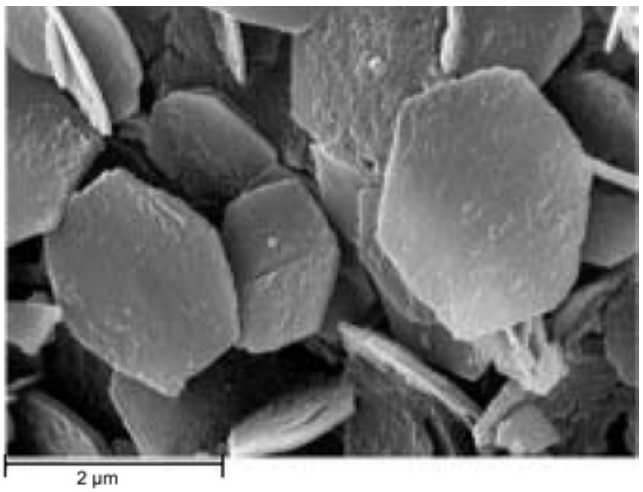

Figure 2.23 SEM image of MgAl-CO_3 LDH synthesized by the urea method in water (Adachi-Pagano, Forano and Besse, 2003)

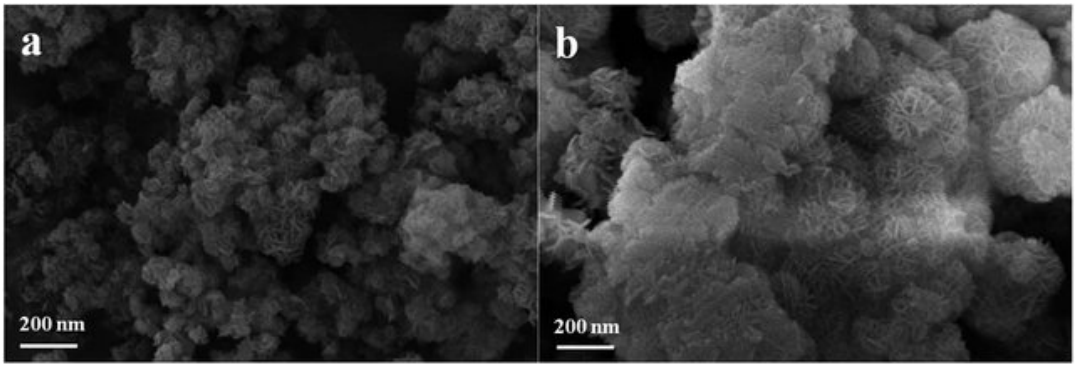

Figure 2.24 SEM images of ***(a)*** *Mg/Al/Fe-LDH and* ***(b)*** *Mg/Al-LDH* (Wang *et al.*, 2017).

In particular, Qian et al. (2015) provided insight into the morphologies of RM and Mg/Al/Fe-LDHs-D, as displayed in Figure 2.25. It can be seen that RM has larger agglomerates of particles, while the synthesised Mg/Al/Fe-LDHs-D has comparatively smaller agglomerates of particles, which implies better dispersity.

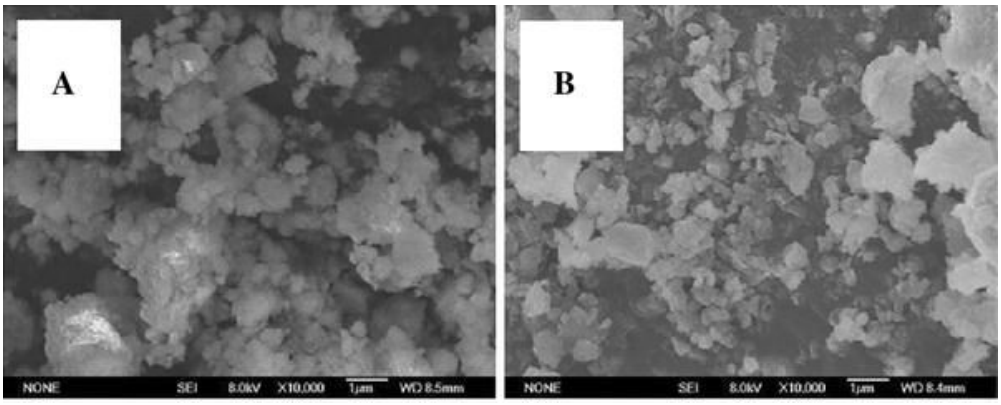

Figure 2.25 SEM photographs: ***(a)*** *RM;* ***(b)*** *Mg/Al/Fe-LDHs-D (Qian et al. 2015).*

2.4.1.3 Rule III: FT-IR spectroscopic study

The FT-IR spectrums of Mg-Al-CO_3 LDH and calcined LDH in the region between 400 and 4000 cm^{-1} are displayed in Figure 2.26. The strong and broad absorption band at 3600-3200 cm^{-1} centred around 3450 cm^{-1} is assigned to the stretching of hydroxyl groups (O-H) associated with interlayer water molecules and hydrogen bonding. Another weak band around 1620 cm^{-1}(δ_{HOH}) corresponds to water deformation (Li *et al.*, 2004). The intermediate frequency bands between 1000-1800 cm^{-1} are related to intercalated and adsorbed anions. The strong band at 1360-1400 cm^{-1} and/ or 1320-1340 cm^{-1} (ν_3, asymmetric stretching) are usually attributed to the vibration of monodentate and bidentate species (e.g. interlayer CO_3^{2-}) (Palmer and Frost, 2009). The two bands around 880 cm^{-1} (ν_2) and 670 cm^{-1} (ν_4) are characteristic of the bending of CO_3^{2-} (Millange, Walton and O'Hare, 2000; El Gaini *et al.*,

2009). The other bands in the low frequency range between 400 cm^{-1} and 1000 cm^{-1} are ascribed to M-O, O-M-O and M-O-M (metal-oxygen-metal) lattice vibrations (Huang *et al.*, 2015). However, it should be highlighted that the results of FTIR studies of the synthesised products are inconclusive (Millange, Walton and O'Hare, 2000).

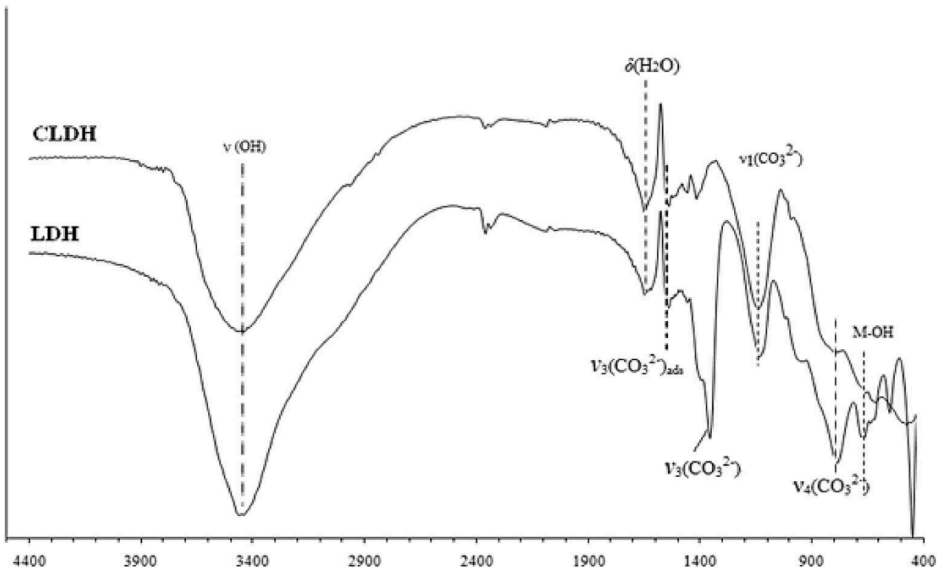

Figure 2.26 Infrared absorption spectrum for the Mg–Al–CO_3 LDH and CLDH samples recorded at room temperature (Elhalil *et al.*, 2016).

2.4.1.4 Rule IV: TG-DTA

Thermogravimetric analysis (TGA) and differential thermogravimetry (DTG) are performed in this research to examine the type of RM-LDHs and their thermal stabilities. Figure 2.27 and Figure 2.28 depict the representative TGA curves of Mg/Al LDH and Mg/Al/Fe LDH. It is well demonstrated that LDHs are thermally stable up to 240-300°C (Constantino and Pinnavaia, 1995). The mass changes below that are attributed to the removal of external surface water and interlayer water (Constantino and Pinnavaia, 1995; Millange, Walton and O'Hare, 2000). As observed from Figure 2.27, the endothermic process of water removal continues up to 216°C. The loss of interlayer hydroxyl and carbonate anions from the brucite-like layers occurs in the range of 250-500°C. The single mass loss in this range confirms the coupling of dehydroxylation and decarbonation process (Palmer, Frost and Nguyen, 2009). The LDH compounds then transform to mixed metal oxides. The final weight loss is due to the elimination of volatile anions from the sample.

Rozov et al. (2010) pointed out that the increase in the mole fraction of Fe in LDH products can result in a lower dehydroxylation temperature from 230°C to 180°C, which is in good

agreement with (Vulic, Reitzmann and Lázár, 2012). Likewise, the temperature of decarbonation is brought forward from 440°C to 407°C (Figure 2.28). Klemkaite et al. (2011) noted that the transition metals in the LDH samples negligibly effect thermal stability. Other possible characteristics of RM and RM-LDHs in terms of calcination/ heat treatment can be found in Section 2.3.4 and Section 2.4.2.

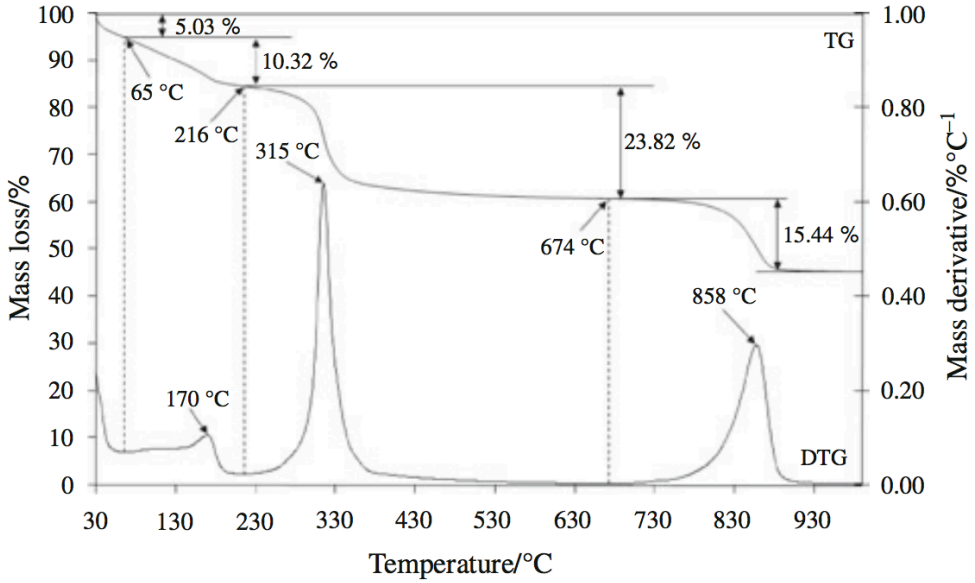

Figure 2.27 TG and DTG curve of the 3:1 Mg^{2+} /Al^{3+} hydrotalcite (Frost, Palmer and Grand, 2009).

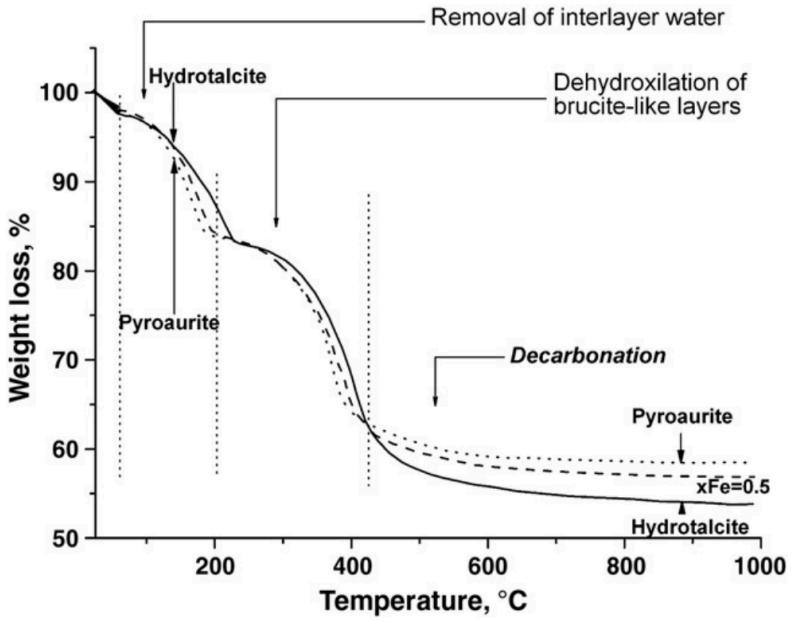

Figure 2.28 TGA curves of hydrotalcite–pyroaurite ($Mg_3(Al, Fe)(OH)_8(CO_3)_{0.5}$ nH_2O) samples. The applied heating rate was 5°C/min. Samples were dried for 15 min at 60°C before analysis (Rozov *et al.*, 2010).

2.4.2 'Role-Play' as LDH Products

In order to acquire a well-rounded understanding of LDH products, as well as to assess the effectiveness of waste modification, if at all, the as-prepared RM-LDHs have been employed in several applications in this research. These applications and distinctive characteristics of a typical LDH are defined as 'role plays' in the present study (see Figure 2.21). As mentioned in Section 2.3.3 and Section 2.4.1, LDHs and their hybrids are promising materials to adsorb inorganics as well as organic anions in aqueous environments. The adsorption behaviour depends heavily on the nature of the adsorbent, especially its porosity and specific surface area (Guo, Yin and Yang, 2018). The LDH-based materials synthesised from industrial waste RM might be promising and low-cost adsorbent candidates. On the other hand, owing to the existence of OH- groups on the layer surface and the high exchangeable anion capacity, LDHs materials have become increasingly popular in wastewater treatment studies.

Practical applications provide more concrete observations of as-synthesised RM-LDHs in microstructure studies and allow the products to be compared against commercial Mg/Al-LDH as well as existing LDH studies. Therefore, the aforementioned characteristics of LDHs can be better assessed. Two potential applications of RM-LDHs are studied: one is as chloride inhibitor in concrete; the other is for removing Remazol Brilliant blue R (RBB) from wastewater. Various factors controlling the morphology of LDH have been discussed in Section 2.3. In this section, the design of chloride binding LDH is introduced. A literature review of organic dye adsorption by LDHs is presented in Section 2.5.

2.4.2.1 Role-play I: Design of chloride binding LDH

Chloride ingress is one of the major reasons for the corrosion of steel reinforcement. To improve the durability of cementitious materials, various protecting inhibitors against Cl^- attack have been researched. LDH and CLDH minerals have extraordinary potential as 'sinks' for Cl^- ions in cementitious materials (Yoon, Moon, Bae, Duan, Emmanuel P Giannelis, *et al.*, 2014; Ke, Bernal and Provis, 2017). The formation of hydrotalcite-like phases have often been identified in long-term cured alkali-activated slag cement (AAS) as well as in concretes containing ground granulated blast furnace slag (GGBFS), which is responsible for binding chlorides (Haha *et al.*, 2011, 2012; Khan, Kayali and Troitzsch, 2016).

Mechanism of chloride binding

Lv et al. (2006b) reported that calcined MgAl-CO_3 LDH exhibited an adsorption capacity of 149.5 mg/g for chloride from an aqueous solution in N_2 atmosphere. The author compared the removal result with different sorbents studied in recent years, as seen in Table 2.13. After chloride adsorption, the reconstructed CLDH showed a basal spacing of 0.773 nm, which was slightly larger than that of the MgAl-CO_3 LDH precursor (0.748 nm). Based on the XRD analysis (Figure 2.29), Lv et al. (2006b) claimed that the chloride ion was incorporated into the reformed structure. Similarly, Xu et al. (2017) noted that basal spacing associated with the diffraction peak (*003*) of Mg/Al-NO_3 LDH decreased from 0.87 to 0.76 nm after Cl^- substitution.

Table 2.13 Comparative study on the uptake capacity of CLDH with other reported sorbents for chloride ion, adapted from Lv et al. (2006b)

Sorbent	Uptake capacity	Reference
Double hydrous oxide ($Fe_2O_3 \cdot Al_2O_3 \cdot xH_2O$)	70 mg/g	Chubar et al. (2005)
Weakly acidic and weakly basic ion exchange resins	85.2 mg/g (2.40 meq/g)	Koul and Gupta (2004)
Mg–Al oxide (Mg/Al molar ratio of 2.0)	109.3 mg/g (3.08 meq/g)	Kameda et al. (2002)
Mg–Al oxide (Mg/Al molar ratio of 3.0)	102.6 mg/g (2.89 meq/g)	Kameda et al. (2002)
CLDH ($Mg_{0.80}Al_{0.20}O_{1.1}$)	149.5 mg/g	This work

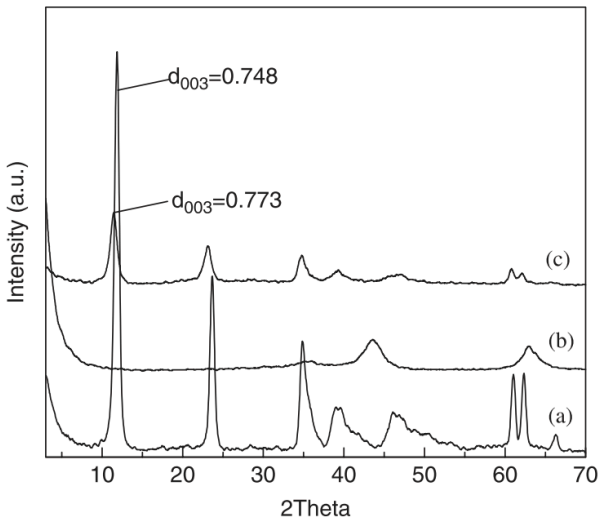

Figure 2.29 Powder XRD patterns for (a) MgAl–CO_3 LDH, (b) CLDH, and (c) CLDH after uptake of chloride ion Lv et al. (2006b).

Yoon et al. (2014) simulated the adsorption process of chloride onto CLDH in a cement matrix and proved that the Mg/Al-CLDH also rebuilt the layered structure. The measured and theoretical binding capacities of the CLDHs were 153 mg g^{-1} and 257 mg g^{-1}, respectively, which was in good agreement with Lv et al. (2006b). The kinetic data fitted the pseudo second-order kinetic model better. To further quantify the mechanism for chloride adsorption on CLDH, Ke et al. (2017) investigated calcined Mg/Al-LDH (CLDH) as a chloride inhibitor in simulated pore solutions. Following the reconstruction of its LDH structure, the aqueous anions maybe intercalate into the interlayers. A possible reaction between CLDH and chloride-rich solutions through the exchange of interlayer species could be expressed as:

$$Mg_{1-x}Al_xO_{1+x/2} + x \cdot Cl^- + (m+1+x/2)H_2O \rightarrow Mg_{1-x}Al_x(OH)_2Cl_x \cdot mH_2O + x \cdot OH^-$$

It should be noted that the concentrations and competition of different ions in the aqueous solution have an important impact on the solid phase at equilibrium. Therefore, the chloride-rich simulated pore solutions should be prepared with a varying $[Cl^-]/[OH^-]$ ratio but with a constant total Na^+ concentration and total ionic strength (Ke, Bernal and Provis, 2017). Ideally, a higher initial $[Cl^-]/[OH^-]$ ratio and the absence of carbon favour the uptake of Cl^- ions over OH^- ions (e.g. CH-4 solution in Table 2.14 results in the largest Cl binding capacity of *ca.* 250 mg/g). It has been demonstrated that hydrotalcite-group minerals are effective chloride binders even in high alkalinity conditions.

Table 2.14 Stoichiometric compositions of the simulated chloride-rich pore solution in experiments (Ke, Bernal and Provis, 2017).

	Concentration (mol/L)				$[Cl^-]/[OH^-]$	Total ionic strength, I (mol/L)
	NaCl	NaOH	Na_2CO_3	Total Na^+		
Carbonate-free solutions						
CH-1	0.10	0.90	0	1.00	0.1	1.00
CH-2	0.25	0.75	0	1.00	0.3	1.00
CH-3	0.50	0.50	0	1.00	1.0	1.00
CH-4	0.75	0.25	0	1.00	3.0	1.00
Carbonated solutions						
CH3-1	0.50	0.30	0.10	1.00	1.7	1.10
CH3-2	0.50	0.10	0.10	0.80	5.0	0.90

(0.4 g solids were added to 40 g prepared solutions in centrifuge tubes for adsorption study)*

Figure 2.30 displays the XRD analysis of the CLDH after being immersed in chloride. The *(003)* basal peak position of the reconstructed LDH is centred at 11.6°. The widths and intensities of these peaks vary with different Cl concentrations. This is most likely the result of changes in the amount of bound Cl impacting on the regularity of the layered structure. With the aid of other characterisation techniques (chemical analysis, TG-MS analysis), Ke et al. (2017) concluded that for Mg-Al CLDH, surface adsorption in the diffuse layer is the main binding mechanism, responsible for around 90% of the total chloride uptake, with the remaining 10% originating from direct ion-exchange.

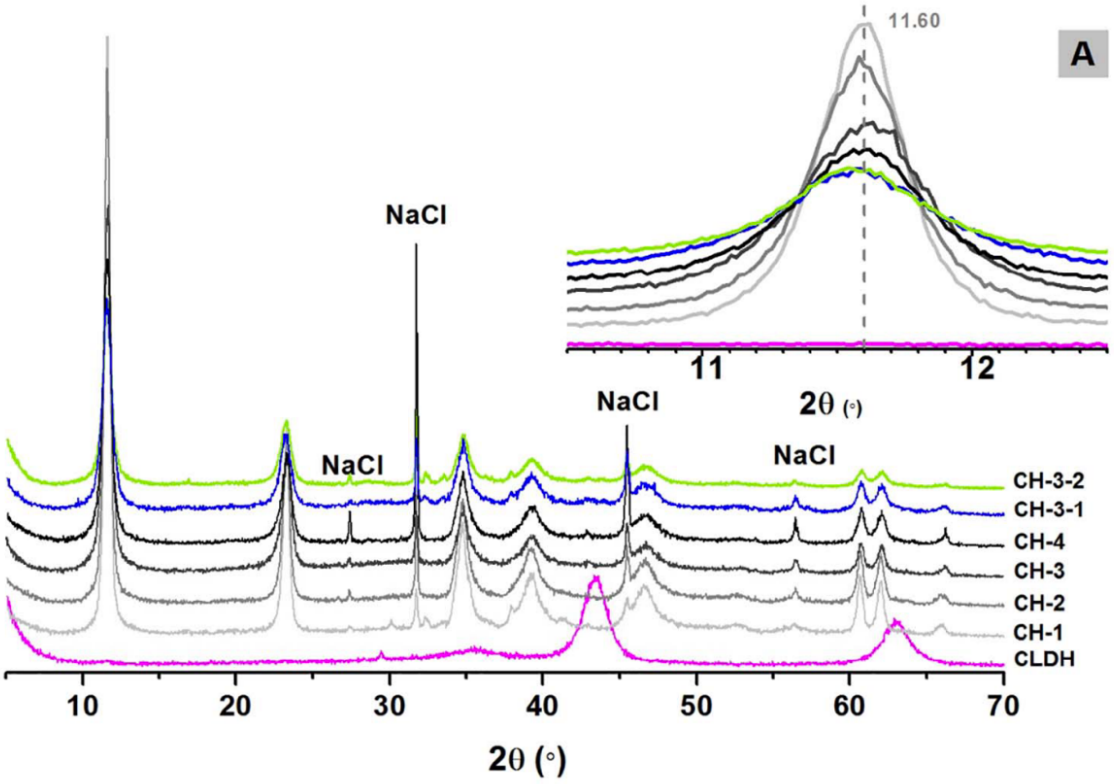

Figure 2.30 XRD patterns of recrystallised LDH in chloride-rich simulated pore solutions – 7 days after the first filtration, with the pattern of the original CLDH (Ke, Bernal and Provis, 2017)

2.4.2.2 Role-play II: Adsorption of organic dyes

In the past years, several investigations have been carried out to explore the applicability of red mud in dye removal. Based on the review by Bhatnagar et al. (2011), the affinity of different dyes on the RM surface has been examined, including Rhodamine B, Methylene Blue, Congo Red, and Procion orange dye. Ion exchange is proposed to be the main mechanism of adsorption. Table 2.15 presents a brief overview of various dye adsorption

studies involving RM. It is evident from the literature that RM is not particularly effective for dye removal. The review of dye adsorption onto LDHs refers to Section 2.5.

Table 2.15 Adsorption capacity of red mud for the removal of different dyes from water (Wang, Ang and Tadé, 2008; Bhatnagar *et al.*, 2011)

Adsorbent	Adsorbate	Amount adsorbed	Reference
Red mud	Congo Red	4.05 mg/g	(Namasivayam and Arasi, 1997)
Red mud	Procion Orange	6.0 mg/g	(Namasivayam, Yamuna and Arasi, 2002)
Red mud	Acid Violet	1.37 mg/g	(Namasivayam, Yamuna and Arasi, 2001)
Red mud	Rhodamine B	(1.01–1.16) × 10^{-5} mol/g	(Gupta *et al.*, 2004)
Red mud	Fast Green	(7.25–9.35) × 10^{-6} mol/g	(Gupta *et al.*, 2004)
Red mud-Heat	Methylene Blue	0.48 mg/g	(Wang *et al.*, 2005)
Red mud	Methylene Blue	2.49 mg/g	(Wang *et al.*, 2005)
Red mud - Acid activated	Congo Red	7.08 mg/g	(Tor and Cengeloglu, 2006)
Red mud – Acid treated	Remazol Brilliant blue R	27.8 mg/g	(Ratnamala, Shetty and Srinikethan, 2012)

In this study, Remazol Brilliant blue R (RBB) was selected as the dye medium to investigate the impact of synthesis on sorption properties, since in the literature, both RM-based materials and LDHs have been frequently studied for RBB removal (Benselka-Hadj Abdelkader *et al.*, 2011; Ratnamala, Shetty and Srinikethan, 2012; Guo *et al.*, 2013). Thus, the performance of RM and synthetic RM-LDHs can be compared accordingly. He *et al.* *(*2012) reported that the sorption capacity for brilliant blue from wastewater was 166.67 mg/g on LDH powder, and was approximately 26.0 mg/g on red mud (Ratnamala, Shetty and

Srinikethan, 2012). RBB belongs to the acidic dye class and its structure is shown in Figure 2.31.

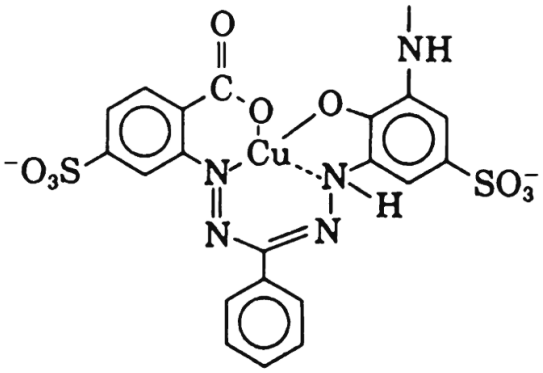

Figure 2.31 Structure of Remazol Brilliant Blue dye by Ratnamala et al. (2012).

2.4.2.3 Role-play III: Thermal stability & Memory effect

A valuable adsorbent should meet these key features: high adsorption capacity, rapid adsorption kinetics and excellent recycle properties. According to Section 2.3.2 and Figure 2.7, the 'memory effect' of LDH is a critical feature and an important advantage for wastewater treatment. The reconstruction process normally depends on the calcination temperature and chemical composition of the LDH structure. The calcination temperature is very important and sensitive, because it is the deciding factor as to whether or not the reconstruction of the layered structure is successful. The chosen temperature should ensure LDH layers collapse but not exceed that the formation of spinel phases starts. In general, the calcination temperature for Mg-Al LDH is set between 400-600°C (Valcheva-Traykova, Davidova and Weiss, 1993). Constantino & Pinnavaia (1995) noted that the thermally dehydrated LDH samples should be transferred quickly to XRD measurements or stored in a vacuum drying chamber to minimise the rehydration effect.

Mineral phases

Constantino & Pinnavaia (1995) outlined the calcination process of LDH in Figure 2.32. It can be seen that the calcined LDH at 250°C has a high level of structural disorder. The formation of an MgO phase is identifiable from 450°C. The $MgAl_2O_4$ and MgO crystalline phases become evident when calcined at 900°C.

However, if the calcination leads to the formation of the $M^{II}M^{III}_2O_4$ spinel, LDH cannot be fully regenerated, which is also noted in Section 2.3.2. Taking the nature of the cations into account, $MgAl_2O_4$, $MgFeAlO_4$, or $MgFe_2O_4$ would form. Ferna et al. (1998) previously found

that the decomposition of the Mg-Al-Fe LDH is nearly complete at 450°C for 2 h and only residual hydroxyl groups continue to be removed in the range of 450-750°C, while the MgAl spinel only appears from *ca.* 900°C upwards (Sato *et al.*, 1988). A prolonged calcination time from 2 h to 24 h does not radically change the crystallinity of the species formed (Ferna et al. 1998).

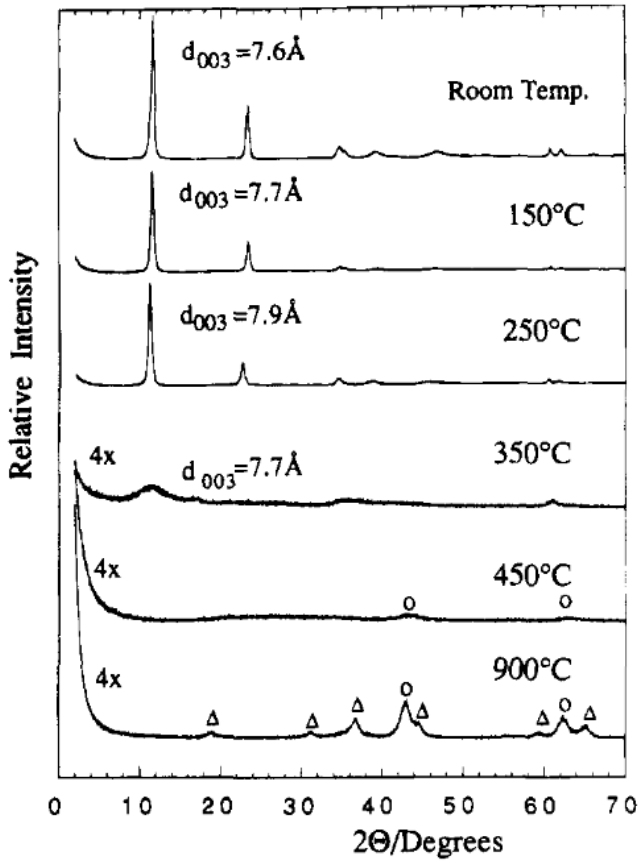

Figure 2.32 XRD patterns of $Mg_{2.49}A1$-LDH samples after heating for 2 h under nitrogen at the temperatures indicated and recording the diffraction patterns in air at room temperature. Diffraction peaks corresponding to MgO and MgA1204 spinel are labelled o *and* Δ *, respectively* (Constantino and Pinnavaia, 1995).

In the study by Heredia et al. (2013), Mg-Fe LDH samples were calcined in the atmosphere of air for 9 h at three different temperatures (550, 700, 850°C). The XRD patterns (Figure 2.33) showed that Fe^{3+} species existed as $MgFe_2O_4$ and α-Fe_2O_3. The rise in the calcination temperature encouraged the generation of spinel $MgFe_2O_4$ and periclase Mg(Fe, Al)O, which increased the magnetization of saturation. However, it is notable that with the increase in Fe^{3+} content in the LDH layer structure, the surface area diminished since the Al_2O_3 amorphous phase reduced.

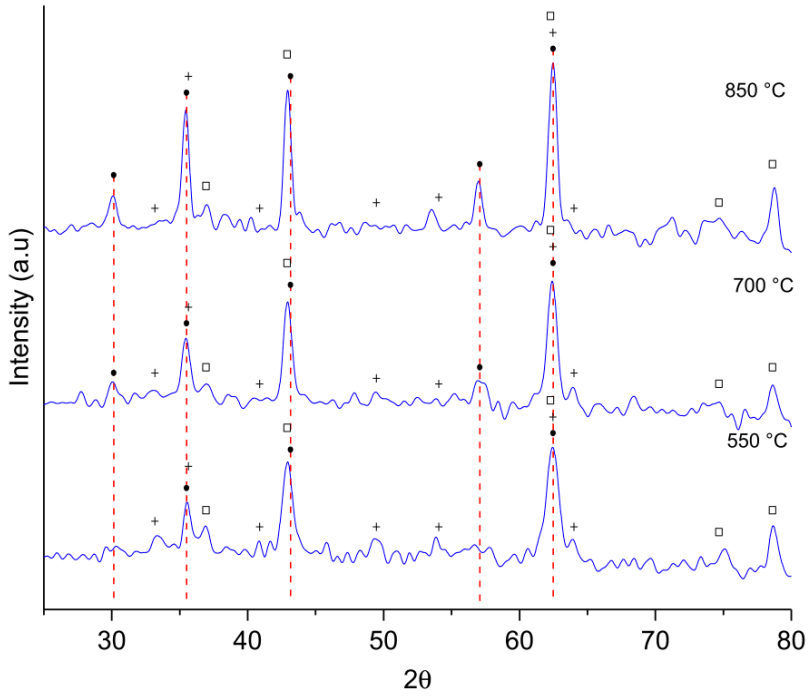

Figure 2.33 X-ray diffraction patterns of Mg-Fe LDH at different temperatures. (□) periclase MgO, (●) spinel $MgFe_2O_4$,(+) α-Fe_2O_3, by Heredia et al. (2013).

Surface area & pore size

Most of the as-synthesised LDHs originally have a low surface area. Thermal treatment significantly increases their surface area, assigned to the expulsion of CO_2 and H_2O from the LDH (Heredia et al. 2013). As Lv et al. (2006) report, thermally treated Mg-Al- CO_3^{2-} LDHs (2:1 Mg/Al, 400 ºC) and (3:1, Mg/Al, 500 ºC) has a surface area of 122.2 and 223.3 m^2/g respectively. The specific surface area of the Mg–Fe LDH increases from 35.4 to 131 m^2/g and the pore volume from 0.545 to 0.767 ml/g through heating at 500 °C (Guo *et al.*, 2013). A comparison of surface area and pore size before and after has been studied by various researchers (Extremera *et al.*, 2012; Yang *et al.*, 2016), as shown in Table 2.16.

Table 2.16 Textural Analysis of the LDHs at 100ºC and 500ºC (Valente *et al.*, 2009)

	specific surface area ($m^2\ g^{-1}$)		total pore volume ($cm^3\ g^{-1}$)		average pore diameter (Å)			
					100 °C		500 °C	
sample	100 °C	500 °C	100 °C	500 °C	I	II	I	II
MgAl	93	227	0.445	0.987	36	422	49	345
MgCuAl	50	230	0.281	0.882	39	424	56	343
MgNiAl	63	223	0.377	0.852	40	324	61	330
MgZnAl	32	140	0.137	0.428	92	411	34	345
MgFeAl	47	145	0.234	0.495	64	243	65	336

2.5 Adsorption of Organic Dyes to LDH

Every year, about 7×10^5 tons of dyes are discharged from different industries (Zubair *et al.*, 2017), like textile, printing, paper and leather industries. Disposal of these dyes without any treatment may pose significant risks to the environment, as they decrease light penetration and photosynthesis. In addition, they are either toxic, mutagenic or carcinogenic to human beings (Carmen and Daniel, 2012; Hu *et al.*, 2016; Chubar *et al.*, 2017; Pourfaraj *et al.*, 2017; Zubair *et al.*, 2017). Organic dyes are generally highly stable and recalcitrant to degradation. Therefore, it is difficult to destroy them or decompose them to secondary harmless chemicals. A more realistic way is to remove organic dyes from wastewater by adsorption using effective sorbents.

Adsorption refers to 'an accumulation of matter at the interface between an aqueous solution phase and a solid adsorbent without the development of a three–dimensional molecular arrangement' (Series, Chemical and Washington, 1987). It distinguishes from absorption which refers to 'the diffusion of an aqueous chemical species into a solid phase' (Series, Chemical and Washington, 1987). The adsorption of organic dyes to LDH lays the foundation of the application of LDH in dye treatment in soil and water. This section primarily reviews the mechanisms and characteristics of organic dyes adsorption onto LDH in aqueous solution.

2.5.1 Mechanisms of Organic Dyes Adsorption to LDHs

As discussed in Section 2.3.2, layered double hydroxides (LDHs), also known as anionic clays, are a group of minerals with anionic exchange property (Rives, 2001; Paikaray *et al.*, 2014). They possess versatile applications in environmental remediation and industrial processes as adsorbents, catalyst, drug delivery carriers, anion exchangers or flame retardant etc. (Valente, Cantu and Figueras, 2008; Yanmin Yang *et al.*, 2012). As sorbent materials, LDHs have been used for a wide range of pollutants from aqueous environments, ranging from oxyanions, phosphate, metals, radioactive materials, and through to organic pollutants as dyes, pesticides, herbicides and PPCPs (Goh, Lim and Dong, 2008; Hashim *et al.*, 2016; Yang *et al.*, 2016; Gu *et al.*, 2018; Li *et al.*, 2018; Johnston *et al.*, 2021). As introduced in Section 2.4.2.2, Remazol brilliant blue R (RBB) dye was employed as case study to better understand the synthesised products.

The anions and hydroxyl groups in the interlayer are bonded to the principal layers by either coulomb forces or hydrogen bonding, thus equip LDHs with high anion exchange capacity (Palmer, Frost and Nguyen, 2009; Yang, Fischer and Polder, 2013). In addition to anion exchange, intercalation, electrostatic interaction, hydrogen bonding and physical adsorption also contribute to the removal of dyes by LDH in aqueous solution. Table 2.17 summaries the mechanisms identified in the adsorption of dyes to LDHs from the literature. It can be found that, in most cases, more than one mechanism contributed to the adsorption of dyes to LDHs, depending on the type of both dyes and LDHs. Different mechanisms have different environmental implications. Therefore, each of these mechanisms are reviewed below.

Table 2.17 Summary of the maximum adsorption capacity and adsorption mechanisms of dyes on LDHs (Q_{max} - maximum adsorption capacity, N.A. - not available)

Adsorbent	**Sorbate**	**Q_{max} (mg/g)**	**Adsorption mechanisms**	**References**
Mg/Al-CO_3-LDH	Remazol brilliant blue R	54.59	Ion exchange, surface adsorption	(Benselka-Hadj Abdelkader *et al.*, 2011)
Calcined Mg/Al-CO_3-LDH		613.6	Intercalation,	
Mg-Al-LDH hierarchical framework	Remazol brilliant blue R	212.8	N.A.	(He *et al.*, 2012)
Mg-Fe-NO_3-LDHs	Metanil yellow azoic dye	40.22-53.76	Physical adsorption	(Nejati *et al.*, 2011)
Mg/Fe-LDH	Acid orange 10 dye	76.4	Anion exchange	(Benselka-Hadj Abdelkader *et al.*, 2011)
Calcined Mg/Fe-LDH		378.8	Surface adsorption and anion exchange	
Mg-Fe-CO_3-LDH	Congo red dye	104.6	N.A.	(Ahmed and Gasser, 2012)

CaAl-LDH-NO_3	Sunset yellow dye	398.41	H bonding, electrostatic interaction, intercalation and anion exchange	(De Sá, Cunha and Nunes, 2013)
Mg-Al LDH	Methylene blue dye	48.64	Physical adsorption, intercalation and ion exchange	(Aguiar *et al.*, 2013)
	Acid blue 25 dye	260.70		
	Reactive blue 4 dye	281.50		
Mg/Fe LDH	Acid brow 14 dye	41.7	Anion exchange, electrostatic attraction and H bonding	(Guo *et al.*, 2013)
Calcined Mg/Fe LDH		370.0	intercalation	
Mg-Al-LDH	Reactive red dye	59.49	Anion exchange and electrostatic interaction	(Shan *et al.*, 2015)
	Congo red dye	37.16		
	Acid red 1 dye	108.0		
Calcined Mg+Zn/Al+Fe LDH	Isolan dark blue dye	12.1-31.8	Anion exchange and intercalation	(Abou-El-Sherbini *et al.*, 2015)
Mg-Al-LDH	Congo red dye	111.11	Electrostatic interaction	(Lafi *et al.*, 2016)
CoFe-LDH	Methyl orange dye	>1206	External surface adsorption and anion exchange	(Ling *et al.*, 2016)
NiFe-LDH	Methyl orange dye	205.76	Anion exchange, physical adsorption and intercalation	(Y. Lu *et al.*, 2016)

Mg/Fe LDH	Indigo carmine dye	55.5	N.A.	(Ahmed, brick and Mohamed, 2017)
Calcined Mg/Al LDH	Acid yellow 42 dye	1265.9	N.A.	(R. M. M. dos Santos *et al.*, 2017)
Organo MgAl LDH	Acid red GR, Disperse orange 11, and Basic yellow 2 dyes	424.54-789.62	Partitioning, H bonding, electrostatic intercalation and physical adsorption	(Zhang *et al.*, 2017)
CuMgAl LDH	Methyl orange dye	123.5	Physical adsorption, electrostatic intercalation and H bonding	(Bharali and Deka, 2017)
	Bromothymol blue dye	146.2		
	Erichrome black-T dye	90.5		
	Congo red dye	44.5		
MgAl-NO_3 LDH	Reactive red-120 dye	800	N.A.	(Boubakri *et al.*, 2018)
	Reactive blue bezaktiv-150 dye	910		

I. Anion exchange

As mentioned in Section 2.3.1, hydrated anions (e.g., CO_3^{2-}, HCO_3^-) are typically located in the interlamellar area of LDH lattice to maintain electroneutrality. These abundant anions give LDH relatively high anion exchange capacity (AEC). As reported by Abou-El-Sherbini et al. (2015), the AEC values of LDHs varies from 202 to 663 mEq per 100 g. Even if sometimes, the original interlayer anions are difficult to be exchanged from, the anion exchange may still occur on the surface of layers. Figure 2.34 illustrates the CO_3^{2-} on the outer planner surface were readily replaced by anionic dye anions. Therefore, when negatively charged dyes exist in the environment, they can easily be exchanged with the anions from LDH. To the best of the author's knowledge, anion exchange is the most important mechanism determining the adsorption of organic dyes to LDH. Chubar et al.

(2017) believes that 'LDH is the most promising candidate for the next-generation inorganic anion exchanger'.

Anion exchange is a diffusion process (Hu *et al.*, 2016), therefore, its kinetics is controlled by either film or intra-particle diffusion, which will be discussed later in Section 2.5.2. It can be imagined that surface area and pore structure can affect the kinetics of dye adsorption to LDH through anion exchange as it is diffusion controlled. In the view of bonding energy, anion exchange is generally regarded as a weak bond. Therefore, in practical water treatment, the adsorbed dyes on LDH can be easily desorbed and the LDHs can be reused for many cycles. This made LDH a cost-effective material for dye removal in wastewater.

II. Intercalation

Intercalation refers to the entrance of dyes to the interlayer space of LDH structure. It is actually distinguished from adsorption. However, in aqueous adsorption tests, it is very difficult to separate adsorption and intercalation. Therefore, they are discussed together.

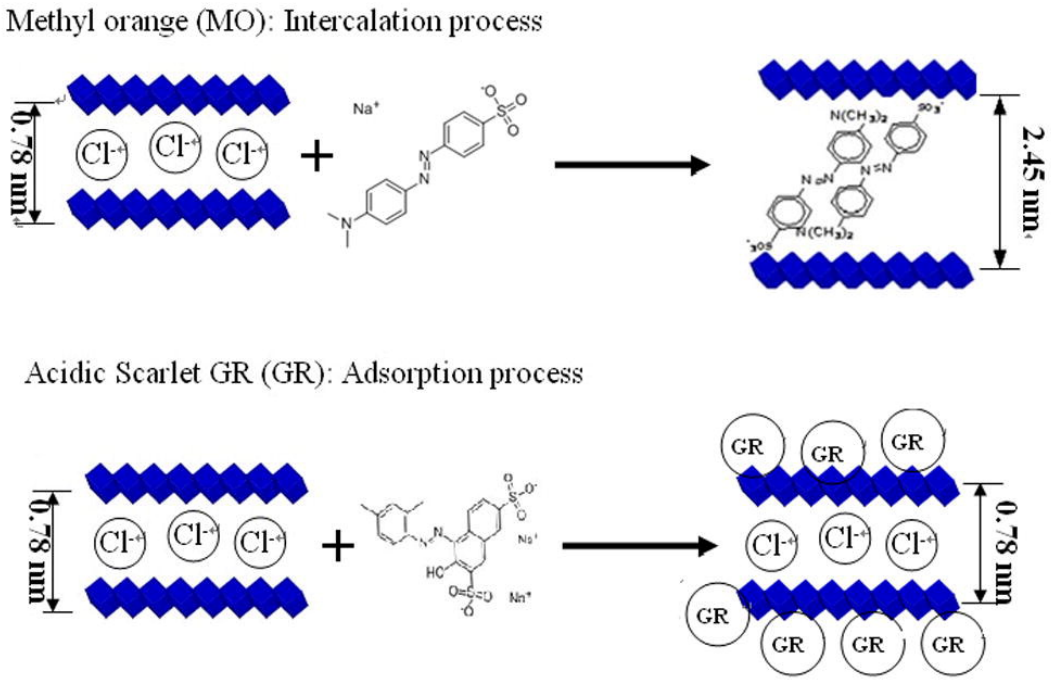

Figure 2.34 Schematic diagram of MO and GR interacted with Ca-Al LDH, by Zhang et al. (2012).

Intercalation has been extensively reported as a mechanism for dye removal by LDH in aqueous solutions (Teixeira *et al.*, 2014; Alexandrica *et al.*, 2015; Zubair *et al.*, 2017). Abou-El-Sherbini et al. (2015) observed that the mechanisms of dye removal in aqueous solutions

turn from anion exchange to intercalation after the calcination of LDH, due to the loss of strongly-held CO_3^{2-}. Alexandrica et al. (2015) noted that both adsorption and intercalation contribute to the removal of anionic dye by LDH in aqueous solutions. For example, Zhang et al. (2012) investigated removal of Methyl Orange (MO) and Acidic Scarlet GR (GR) by Ca-Al LDH. The characterisation tests revealed that MO was intercalated into the interlayers, whereas GR was only adsorbed onto the surface (Figure 2.34).

The calcination (heated at 400 °C and above) of LDH turns it to mixed metal oxides (CLDH). When the CLDH is placed into anionic solutions, it can reconstruct its layered structure. The interlayer of the newly formed double-layer structure can therefore hold more dyes through intercalation. Guo et al. (2013) noted the Brilliant Blue sorption capacity of CLDHs was more than 10 times bigger compared to its parent LDHs. The authors argued that reconstruction is the predominant adsorption mechanism for majority of dyes removal by CLDH. The calcination-rehydration process was described as follows, in which dye AB 14 was intercalated by chemisorption:

$$[Mg_{1-x}Fe_x(OH)_2](CO_3)_{x/2} \rightarrow Mg_{1-x}Fe_xO_{1+x/2} + (x/2)CO_2 + H_2O \quad (1)$$

$$Mg_{1-x}Fe_xO_{1+x/2} + (x)AB14 + (1 + x/2)H_2O \rightarrow [Mg_{1-x}Fe_x(OH)_2](AB\ 14)_x + xOH^- \quad (2)$$

In another adsorption study, Guo et al. (2018) provided a schematic drawing of the reconstruction process of Zn-Al CLDH in MO aqueous solution (Figure 2.35). For practical application, the dye-loaded LDH can be heated at 400°C or above to discharge the dyes. Then they can be reused relying on the memory effect. This provides LDH higher sustainability and lower cost as a sorbent.

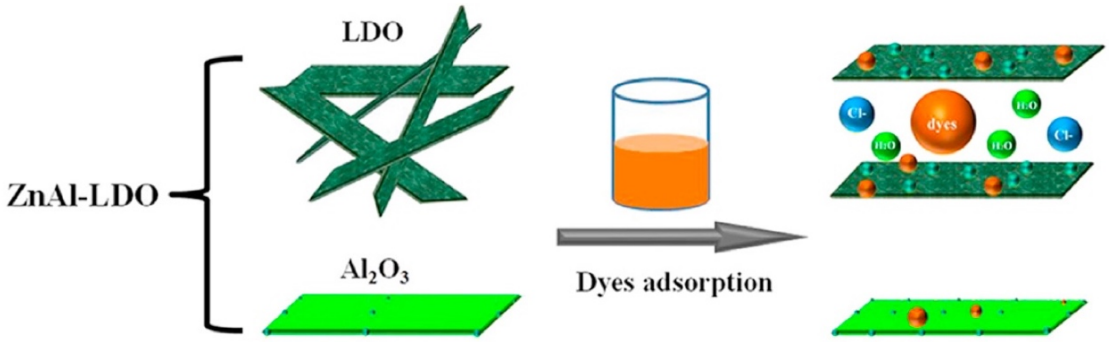

Figure 2.35 Adsorption mechanism of Congo Red (CR) and Methyl Orange (MO) onto layered double metal oxides LDO (i.e. after Zn-Al LDH calcined at 500°C for 2 h), by Guo et al. (2018).

III. Electrostatic interaction

When the surface of LDH is positively charged, it can electrostatically attract negatively charged anions. Likewise, if the surface of LDH is negatively charged, it can attract positively charged cations. Therefore, electrostatic interaction is dependent on both the charge of LDH and organic dyes. The surface charge of LDH is related to its pH at point of zero charge (pH_{pzc}). If the ambient pH is lower than the pH_{pzc} of LDH, its surface will be positively charged, and therefore it can adsorb anionic dyes through electrostatic interaction. If the ambient pH is higher than the pH_{pzc} of LDH, the negatively charged LDH can adsorb cationic dyes through electrostatic interaction. The stability of adsorbed dyes on LDH is highly dependent on the ambient pH. Changes in environmental pH may lead to desorption of electrostatically bonded dyes on LDH. Therefore, in practical wastewater treatment, this can be used to discharge the adsorbed dyes on LDH and subsequently aid the reuse of it. A range of studies claim that electrostatic interaction as one of the mechanisms of dye adsorption to LDH (Benselka-Hadj Abdelkader *et al.*, 2011; Hu *et al.*, 2016).

IV. Hydrogen bonding

The hydrogen from LDH can adsorb negatively charged dyes through hydrogen bonding. Hydrogen bonding has been extensively observed in adsorption studies of dyes to LDHs (Tichit and Coq, 2003; Guo *et al.*, 2013; Chakraborty and Nagarajan, 2015; Yang *et al.*, 2015; El Hassani *et al.*, 2017; Zhang *et al.*, 2017; Zhao *et al.*, 2017). Hydrogen bonding has a weak binding energy. The dyes adsorbed on LDH through hydrogen bonding can be easily desorbed, making it easier for the reuse of LDH in wastewater treatment.

V. Physical adsorption

Physical adsorption refers to the interaction between dyes and LDH through van der Waals force. It occurs in nearly all adsorption processes. However, physical adsorption has a very week binding energy and is reversible (Shen *et al.*, 2017). It is highly related to the surface area and pore structure of LDH, as more abundant adsorption sites can aid physical adsorption. Although physical adsorption itself may not play a significant role in dye adsorption onto LDH, it is very important for other adsorption mechanisms (e.g., anion exchange and electrostatic interaction). Because dyes need to be seated on LDH through physical adsorption, before it can have chemical interaction with LDH.

Effect of calcination on dye adsorption

Table 2.18 indicates that calcined LDHs are able to take up a larger amount of acidic dyes than non-calcined LDHs (Table 2.17). Apart from intercalation (via structural reconstruction), the increased sorption capacity of CLDHs can be attributed to their higher surface area, stronger anion exchange activity and the presence of more basic sites (Alexandrica *et al.*, 2015). Another advantage calcination bringing about is the rapidness, as reconstruction is considered to be far more efficient than film diffusion and pore diffusion (Yang *et al.*, 2016).

Table 2.18 Adsorption capacities and experiment conditions of CLDHs for the removal from aqueous solution, adapted from Yang et al. (2016)

LDHs	Synthesis	Dyes	Optimum pH	Adsorption capacity (mg g^{-1})	Kinetic model	Isotherm
C–Mg–Fe LDH	Coprecipitation	Methyl orange	—	194.9	2nd	L
C–Mg–Fe LDH	Coprecipitation	Acid brown 14	4–11	370.0	2nd	L
C–Mg–Fe LDH	Coprecipitation	Orange G	3–13	378.8	2nd	L
C–Mg–AL LDH	Coprecipitation	C.I. acid blue 9	—	194.48	—	L
C–Mg–Al LDH	Opal inverse	Orange II	—	1550.5	—	L
C–Mg–AL LDH	—	Acid blue 113	—	2544	Avrami's	L
C–Mg–Al LDH	Coprecipitation	Acid blue 29	—	36	—	L
C–Mg–AL LDH	Coprecipitation	Indigo carmine	5–9	1343	—	F
C–Mg–AL LDH	Coprecipitation	Remazol red 3BS	6	134.4	2nd	L
C–Mg–Al LDH	Coprecipitation	Acid green 68:1	3–10	154.8	2nd	L
C–Mg–Al LDH	Coprecipitation	Brilliant blue R	3.5–13	615	2nd	F
C–Mg–AL LDH	Coprecipitation	Benzopurpurin 4B	—	417.36	—	—
C–Mg–Al LDH	Coprecipitation	Acid red G	10	93.1	—	—
C–Mg–Al LDH	Coprecipitation	Acid orange 10	4	665	2nd	L
C–Mg–Ni–Al LDH	Coprecipitation	Methyl orange	6–9	375.4	2nd	L
C–Ni–Al LDH	Coprecipitation	Remazol brilliant violet	6	150	—	—
C–Zn–Al LDH	Hydrothermal	Methyl orange		—	2nd	L
C–Zn–AL LDH	Coprecipitation	Methyl orange	6	181.9	2nd	F
C–MnO_x–Zn–Al LDH	Intercalation reduction	Methyl orange	—	617.28	2nd	R–P
C–Au–Zn–Al LDH	Coprecipitation	Methyl orange	—	627.51	—	L
C–GO–Ni–Al LDH	Hydrothermal	Methyl orange	—	210.8	2nd	R–P

2.5.2 Characteristics of Organic Dyes Adsorption to LDH

The characteristics of organic dyes adsorption to LDH are crucial for its practical application and engineering design. Batch adsorption tests in aqueous solutions are most typically used to determine the characteristics of organic dyes adsorption to LDH. The characteristics include isotherms, kinetics, pH-dependence etc.

2.5.2.1 Adsorption Isotherms

Adsorption isotherms are typically obtained through equilibrium study. It indicates how the molecules distribute between the liquid and solid phase when reaching the equilibrium state. A certain amount of adsorbent is mixed with solutions containing different sorbate concentrations. The mixtures are typically shaken at a designated time to reach equilibrium. The adsorbed amount of sorbate by adsorbent at equilibrium is plotted against the equilibrium concentration of sorbate. Empirical models are typically used to fit the results to obtain the isotherm curves and other parameters. Table 2.19 lists the empirical models that are typically used for isotherm fitting. It can be observed that both the non-linear and linear forms of the models can be used. Among all the models listed in Table 2.19, Langmuir and Freundlich models are most frequently used in existing adsorption studies.

The non-linear form of Langmuir model is:

$$q_e = \frac{Q_{max} b C_e}{1 + b C_e} \tag{2.1}$$

Where Q_{max} (mg/g) is the maximum monolayer adsorption capacity, b is the Langmuir isotherm constant (L/mg), q_e is the adsorbed amount of sorbate on adsorbent at equilibrium and C_e (mg/L) is the equilibrium concentration of sorbate in solution. Q_{max} is typically used to compare the adsorption capacities among different adsorbents. The equilibrium parameter R_L, as shown in Eqn. (2.2), can be used to express the essential characteristics of a Langmuir isotherm.

$$R_L = \frac{1}{1 + b C_{max}} \tag{2.2}$$

Where b is defined as per equation 1, C_{max} (mM) is the highest initial sorbate concentration. The value of R_L indicates the type of the isotherm to be either unfavourable ($R_L > 1$), linear ($R_L = 1$), favourable ($0 < R_L < 1$) or irreversible ($R_L = 0$).

The non-linear Freundlich model is:

$$q_e = K_f C_e^{1/n} \quad (2.3)$$

Where K_f (mg/g) is the Freundlich isotherm constant, n represents the adsorption intensity, q_e and C_e are the same as per equation 1. "1/n" ranges between 0 and 1 and is a measure of adsorption intensity or surface heterogeneity. A lower 1/n value indicates a greater degree of heterogeneity on the surface of adsorbent.

Table 2.19 Adsorption isotherm models (Foo and Hameed, 2010)

Isotherm	Nonlinear form	Linear form	Plot	Reference
Langmuir	$q_e = \frac{Q_o b C_e}{1+bC_e}$	$\frac{C_e}{q_e} = \frac{1}{bQ_o} + \frac{C_e}{Q_o}$ $\frac{1}{q_e} = \frac{1}{Q_o} + \frac{1}{bQ_o C_e}$ $q_e = Q_o - \frac{q_e}{bC_e}$ $\frac{q_e}{C_e} = bQ_o - bq_e$	$\frac{C_e}{q_e}$ vs C_e $\frac{1}{q_e}$ vs $\frac{1}{C_e}$ q_e vs $\frac{q_e}{bC_e}$ $\frac{q_e}{C_e}$ vs q_e	[38]
Freundlich	$q_e = K_F C_e^{1/n}$	$\log q_e = \log K_F + \frac{1}{n}\log C_e$	$\log q_e$ vs $\log C_e$	[48]
Dubinin–Radushkevich	$q_e = (q_s)\exp(-k_{ad}\varepsilon^2)$	$\ln(q_e) = \ln(q_s) - k_{ad}\varepsilon^2$	$\ln(q_e)$ vs ε^2	[52]
Tempkin	$q_e = \frac{RT}{b_T}\ln A_T C_e$	$q_e = \frac{RT}{b_T}\ln A_T + \left(\frac{RT}{b_T}\right)\ln C_e$	q_e vs $\ln C_e$	[57]
Flory–Huggins	$\frac{\theta}{C_o} = K_{FH}(1-\theta)^{n_{FH}}$	$\log\left(\frac{\theta}{C_o}\right) = \log(K_{FH}) + n_{FH}\log(1-\theta)$	$\log\left(\frac{\theta}{C_o}\right)$ vs $\log(1-\theta)$	[60]
Hill	$q_e = \frac{q_{sH} C_e^{n_H}}{K_D + C_e^{n_H}}$	$\log\left(\frac{q_e}{q_{sH}-q_e}\right) = n_H \log(C_e) - \log(K_D)$	$\log\left(\frac{q_e}{q_{sH}-q_e}\right)$ vs $\log(C_e)$	[61]
Redlich–Peterson	$q_e = \frac{K_R C_e}{1+a_R C_e^g}$	$\ln\left(K_R\frac{C_e}{q_e} - 1\right) = g\ln(C_e) + \ln(a_R)$	$\ln\left(K_R\frac{C_e}{q_e} - 1\right)$ vs $\ln(C_e)$	[64]
Sips	$q_e = \frac{K_S C_e^{\beta_S}}{1+a_S C_e^{\beta_S}}$	$\beta_S \ln(C_e) = -\ln\left(\frac{K_S}{q_e}\right) + \ln(a_S)$	$\ln\left(\frac{K_S}{q_e}\right)$ vs $\ln(C_e)$	[68]
Toth	$q_e = \frac{K_T C_e}{(a_T + C_e)^{1/t}}$	$\ln\left(\frac{q_e}{K_T}\right) = \ln(C_e) - \frac{1}{t}\ln(a_T + C_e)$	$\ln\left(\frac{q_e}{K_T}\right)$ vs $\ln(C_e)$	[69]
Koble–Corrigan	$q_e = \frac{AC_e^n}{1+BC_e^n}$	$\frac{1}{q_e} = \frac{1}{AC_e^n} + \frac{B}{A}$	–	[70]
Khan	$q_e = \frac{q_s b_K C_e}{(1+b_K C_e)^{a_K}}$	–	–	[71]
Radke–Prausnitz	$q_e = \frac{a_{RP} r_R C_e^{\beta_R}}{a_{RP} + r_R C_e^{\beta_R - 1}}$	–	–	[43]
BET	$q_e = \frac{q_s C_{BET} C_e}{(C_s - C_e)[1+(C_{BET}-1)(C_e/C_s)]}$	$\frac{C_e}{q_e(C_s-C_e)} = \frac{1}{q_s C_{BET}} + \frac{(C_{BET}-1)}{q_s C_{BET}}\frac{C_e}{C_s}$	$\frac{C_e}{q_e(C_s-C_e)}$ vs $\frac{C_e}{C_s}$	[73]
FHH	$\ln\left(\frac{C_e}{C_s}\right) = -\frac{\alpha}{RT}\left(\frac{q_s}{q_e d}\right)^r$	–	–	[74]
MET	$q_e = q_s\left(\frac{k}{\ln(C_s/C_e)}\right)^{1/3}$	–	–	[75]

Figure 2.35 and Table 2.20 show the adsorption isotherm of acid brown 14 dye on LDH and calcined LDH. The plots are the results of equilibrium study. The solid line is the Langmuir isotherm fitting curve of the results. The solid-dash line is the Freundlich isotherm curve of the results. It can be observed from the fitting results (Table 2.20) that Langmuir model, with higher R^2 values, was better fitted for the results than Freundlich model. This suggests the adsorption of the acid brown 14 day to the LDH and CLDH was monolayer adsorption. The Q_{max} values of the LDH and CLDH from Langmuir fitting were 41.7 and 370.0 mg/g, respectively.

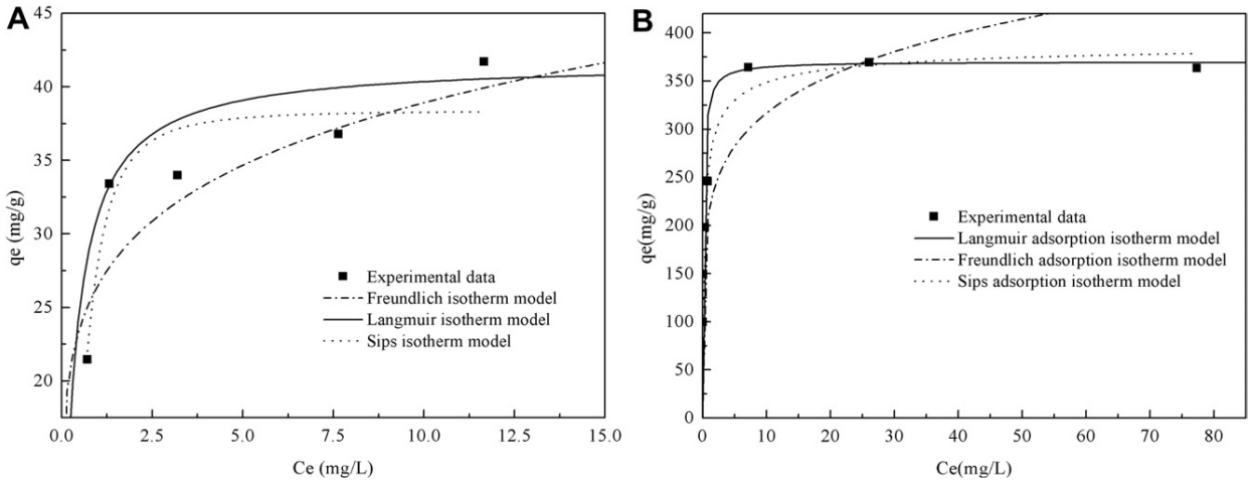

Figure 2.35 Adsorption isotherm of acid brown 14 dye on LDH and calcined LDH (Guo *et al.*, 2013).

Table 2.20 Parameters of adsorption isotherm of acid brown 14 dye on LDH and calcined LDH (Guo *et al.*, 2013).

Material	Langmuir isotherm model			Freundlich isotherm model		
	q_m (mg/g)	K_L (L/mg)	R^2	K_F ($mg^{1-1/n}L^{1/n}/g$)	$1/n$	R^2
LDH	41.7	3.00	0.991	26.5	0.188	0.771
CLDHs	370.0	6.76	0.999	215.7	0.167	0.877

According to Yang et al. (2016), for the system between uncalcined LDHs and dye pollutant, Langmuir more frequently represents the equilibrium than Freundlich. That extrapolates that LDHs is likely to form a monolayer on surface with a finite number of identical sites and there is limited interaction between adsorbed molecules. Similar phenomena are observed for majority of CLDHs-dye adsorption system. Sometimes, other isotherm model like Redlich-Peterson better describes the system (Y. X. Zhang *et al.*, 2014), suggesting the adsorption is not an ideal monolayer adsorption. However, the isotherms are inadequate to fully define the sorption mechanism, other characterisation methods should be carried out.

In Section 2.5.1, Table 2.17 summarises the calculated Langmuir Q_{max} values of the adsorption of different dyes to different LDHs. It can be observed that the adsorption capacities vary significantly depending on the type of both dyes and LDHs. The values of Q_{max} are from 12.1 mg/g to higher than 1206 mg/g. Calcined LDHs generally shows higher Q_{max} values than non-calcined LDHs.

2.5.2.2 Kinetics

Kinetics reveal the time dependence of an adsorption process. For kinetics study, a certain amount of adsorbent is mixed with a solution containing fixed concentration of sorbate. The adsorbed sorbate amount on the adsorbent is measured and plotted at different designated time. Similar to isotherm, the kinetics results are typically fitted by empirical models to indicate the kinetics in more depth. Pseudo first order, pseudo second order and intraparticle diffusion models are three of the most commonly used kinetics models.

The pseudo first order model can be expressed as:

$$q_t = q_e(1 - e^{-k_1 t}) \tag{2.4}$$

Where k_1 (h^{-1}) is the rate constant of pseudo first order adsorption. q_e (mg/g) is the equilibrium adsorption capacity, and q_t (mg/g) is the adsorbed amount of sorbate at time t.

The pseudo second order model can be expressed as:

$$q_t = \frac{k_2 {q_e}^2 t}{1 + k_2 q_e t} \tag{2.5}$$

Where k_2 (g/mg h) is the pseudo second order rate constant. q_e and q_t are as per Equation (4). In practical application, both non-linear and linear forms of pseudo first and second order models are used. Figure 2.36 and Table 2.21 show a typical kinetics data of dye adsorption on LDH and the fitting using the two pseudo models. It can be observed that the regression coefficient and other parameters can be observed through data fitting. These parameters can be used to compare the kinetics of dye adsorption among different LDHs.

Table 2.21 kinetics parameters for the adsorption of methylene blue on PDOPA-LDH, Q_e is the equilibrium adsorption capacity (Zhao *et al.*, 2017)

Models	Parameters	Initial concentration (mg/L) 50
Pseudo-first-order equation	$Q_{e\ (cal)}$ (mg/g)	98
	k_1 (min^{-1})	0.2446
	R^2	0.9918
Pseudo-second-order equation	$Q_{e\ (cal)}$ (mg/g)	105
	k_2 (g mg^{-1} min^{-1})	0.004546
	R^2	0.9952
Intraparticle diffusion	k_p (mg g^{-1} $min^{-0.5}$)	3.814
	C	73.63
	R^2	0.6821

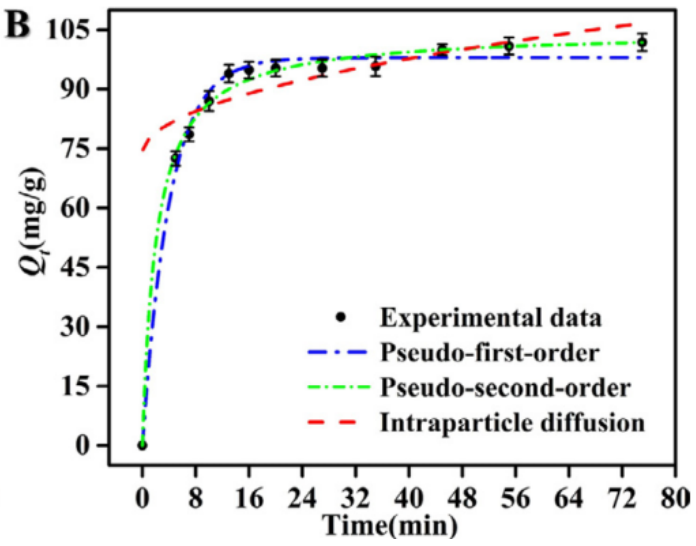

Figure 2.36 kinetics of methylene blue adsorption on PDOPA-LDH, Q_t is the adsorbed amount of sorbate at time t (Zhao *et al.*, 2017).

In addition, the pseudo first and second order models, intraparticle diffusion model is typically used to fit the kinetics data and reveal the diffusion dynamics. It can be expressed as

$$q_t = k_i t^{0.5} + C \tag{2.6}$$

Where k_i (mg/g $h^{-0.5}$) is the coefficient of intraparticle diffusion. q_e and q_t are as Eqn. (2.4).

From a kinetic view, there are four stages in an adsorption process (Choy *et al.*, 2004):

1) Transport of sorbate from the bulk solution to the exterior film surrounding of the adsorbent (remain in liquid phase);
2) Movement of sorbate across the external liquid film boundary layer to external surface sites of adsorbent (defined as film diffusion);
3) Migration of sorbate within the pores of the adsorbent by intraparticle diffusion (defined as intraparticle diffusion);
4) Adsorption of sorbate at internal surface sites.

All the four processes control the kinetics of the adsorption. However, in a shaking-based laboratory adsorption study, the transport of sorbate from the bulk solution to the exterior film (Step 1) is very fast, and the time costed can be neglected. The adsorption of sorbate at the surface sites (Step 4) is also rapid. Therefore, in most adsorption processes, film diffusion (Step 2) and intraparticle diffusion (Step 3) are the rate-controlling steps. The intraparticle diffusion model (Eqn. (2.6)) can be used to identify the film and diffusion steps of an adsorption.

Figure 2.37 shows the kinetics data of acid yellow 42 adsorption to a calcined LDH fitted by intraparticle diffusion model. The first stage (k_{D1}) is regarded as the film diffusion step. The second stage (k_{D2}) is attributed to intraparticle diffusion step, while the third stage (k_{D2}) was regarded as a slow-down of intraparticle diffusion to equilibrium. It can be observed from Figure 2.37 that, although both film and intraparticle diffusion control the kinetics of acid yellow 42 adsorption to the calcined LDH, intraparticle diffusion is the main rate-limiting step.

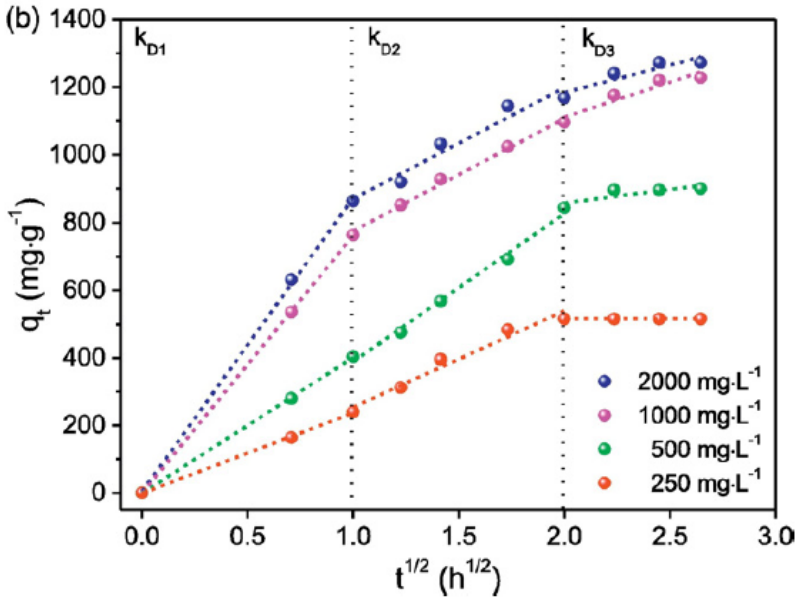

Figure 2.37 Intraparticle diffusion modelling of acid yellow 42 adsorption to calcined LDH (R. M. M. dos Santos *et al.*, 2017).

2.5.2.3 pH dependence

The adsorption of organic dyes to LDH is a pH-dependent process. The influence of solution pH on the adsorption is typically investigated for a better understanding of the adsorption characteristics and mechanisms. As mentioned in Section 2.5.1, the ambient pH determined whether LDH is positively or negatively charged, and subsequently its electrostatic interaction with dyes. In addition, the anion exchange between anionic dyes and the anions in LDH can also be affected by solution pH. De Sá et al (2013) investigated the influence of initial solution pH on the adsorption of sunset yellow FCF dye to a Ca-Al-NO_3 LDH and identified a significant influence of initial solution pH on the dye adsorption to the LDH (Figure 2.38). They proposed the mechanisms for both pH below and above the pH_{pzc} (7.29) of the LDH: for the solution pH values below pH_{pzc}, both anion exchange and electrostatic interaction contributes to the adsorption of the dye to the LDH; for the solution pH values

above pH_{pzc}, deprotonation of surface hydroxyls groups occurred and the positive change of LDH deceases, and the increased OH^- in the solution competed with the negatively charged dye for anion exchange with the LDH.

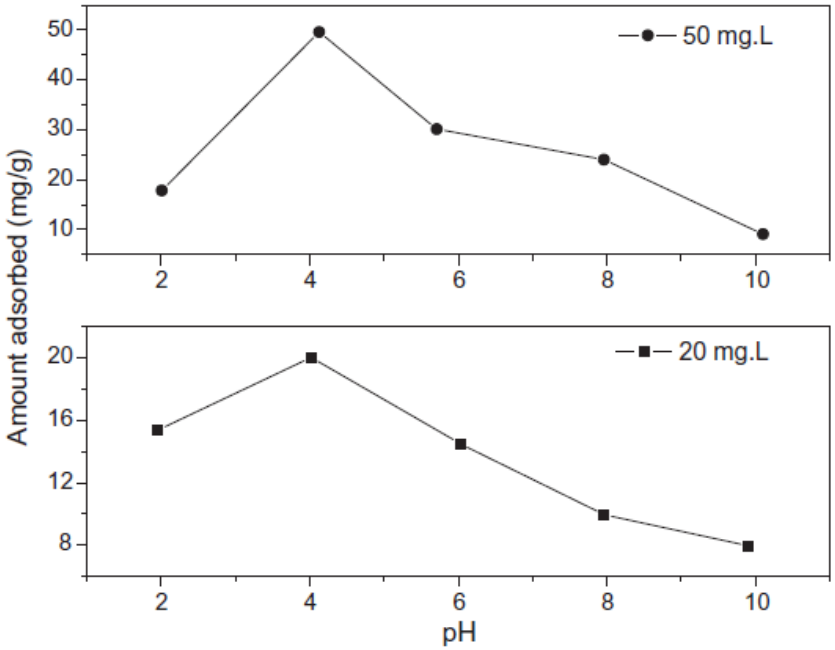

Figure 2.38 Effect of initial solution pH on the adsorption of sunset yellow FCF dye to CaAl-LDH-NO_3 (De Sá, Cunha and Nunes, 2013).

2.5.3 Laboratory Testing of the Adsorption Mechanisms and Characteristics

Laboratory tests are typically used to indicate the mechanisms and characteristics of dye adsorption to LDH. Micro-structural tests, including X-ray diffraction (XRD), Fourier transformed infrared (FT-IR) spectra etc., are used to directly indicate the adsorption mechanisms. Batch adsorption tests, as introduced in Section 2.5.2, are used to indicate the characteristics of the adsorption onto adsorbents. Batch adsorption test results, such as the isotherm and kinetics, can also be used to reflect the adsorption mechanisms indirectly. In practical study, micro-structural and adsorption tests are typically carried out together for a better understanding of the adsorption mechanisms and characteristics of dye onto LDH.

XRD

After dye adsorption, the changes in XRD patterns of LDH can reflect the potential adsorption mechanisms. The interlayer spacing is determined by the size and orientation of the charge-balancing anion (Guo, Yin and Yang, 2018). Adsorption onto LDH and reconstruction of CLDH both may bring changes to the basal spacing, which can be calculated from the XRD results. Guo et al. (2013) conducted the adsorption study of Acid Brown 14, as shown in Figure 2.39. For LDH, the XRD patterns after adsorption of acid brown 14 showed typical peaks of crystallinity of LDH, suggesting a preservation of the layered structure. The structural change occurred in the interlayer distance, which proved a topotactic anion exchange mechanism. For the calcined LDH, after the adsorption of acid brown 14, the layered structure of the LDH material was reconstructed, suggesting a 'memory effect' of the calcined LDH.

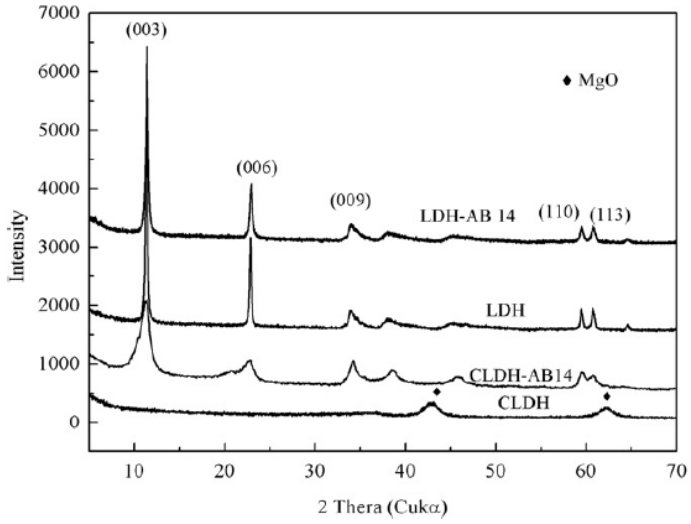

Figure 2.39 XRD patterns of LDH and Calcined LDH (CLDH) before and after acid brown 14 adsorption (Guo *et al.*, 2013).

Similar observations were obtained by Zhu et al. (2005), of which the XRD patterns are included in Figure 2.40. After the *Brilliant Blue R (*BBR) adsorption, the XRD patterns of the recovered LDHs (d_{003} = 7.55 Å) remained almost unchanged compared with the original LDHs (d_{003} = 7.43 Å). The XRD pattern of CLDHs confirmed that layered structure was completely destroyed after calcination at 500°C for 8 h. The peak positions of the CLDHs-BBR and the original LDHs were similar, implying that the layered structure of LDH were reconstructed from CLDHs in the presence of dye solutions. However, the (003) and (006) peaks were broadened (d_{003} = 7.76 Å) and the peak intensity reduced due to the reductions in crystallinity.

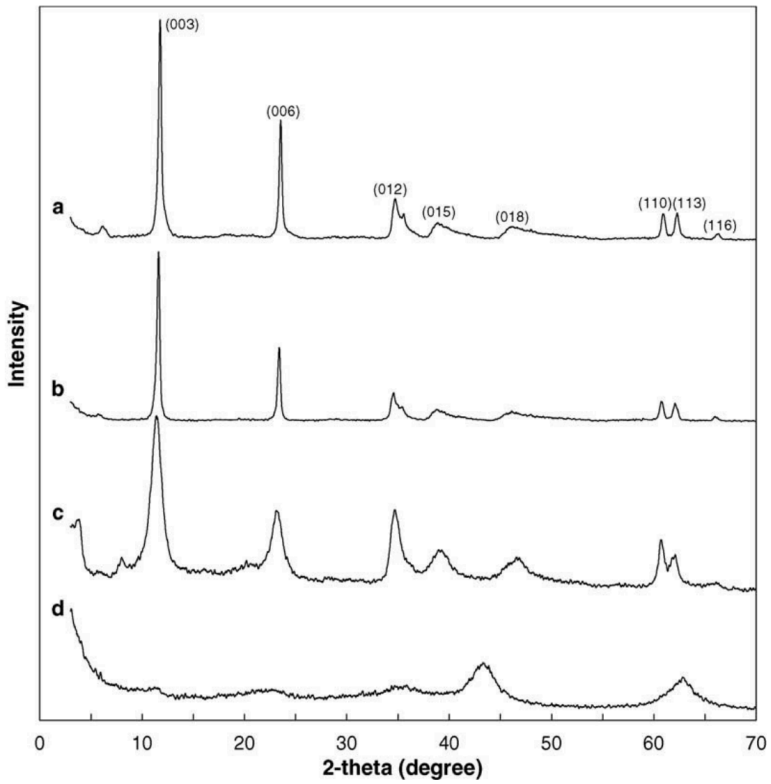

Figure 2.40 XRD patterns of layered double hydroxides (LDHs) and calcined LDHs (CLDHs) before and after BBR sorption. ***(a)*** *LDHs,* ***(b)*** *LDHs after BBR sorption;* ***(c)*** *CLDHs after BBR sorption; (d) CLDHs; adapted from Zhu et al. (2005).*

FT-IR

FT-IR was used to study the fundamental vibrations and associated rotational-vibrational structure of LDH. After dye adsorption, if the original peaks represented the functional groups of LDH change, then it meant that the interactions between the dye and these functional groups were adsorption mechanisms. The FT-IR spectra of NiAl LDHs before and after methyl orange adsorption are shown in Figure 2.41. Several new bands can be observed

on the NiAl LDHs after dye adsorption, suggesting that dye molecules were anchored on the adsorbent surfaces. The O-H peak of the f-NiAl LDH after dye adsorption did not change, suggesting that hydrogen bonding did not participate in dye adsorption. In contrast, the O-H peak of c-NiAl LDH after dye adsorption shifted from 3472 to 3459 cm^{-1}, suggesting that hydrogen bonding participated in dye adsorption. The peaks of M–O–M and O–M–O stretching shifted after dye adsorption, suggesting that the metal ions were complexed with $-SO_3^-$ groups of dye on the surface of f-NiAl LDH.

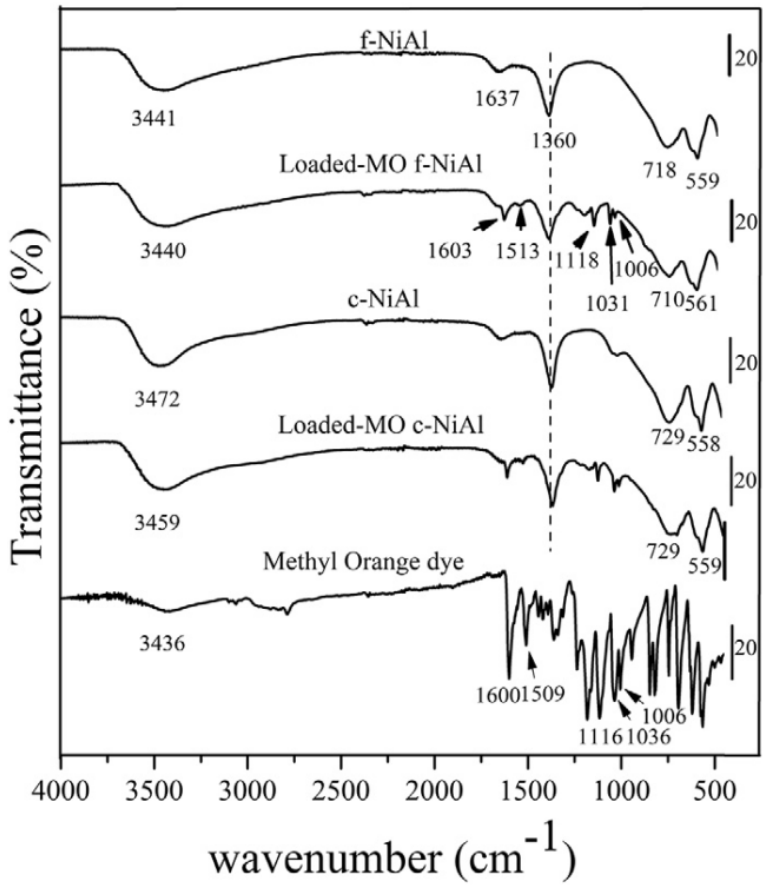

Figure 2.41 FT-IR spectra of NiAl LDHs before and after methyl orange dye adsorption (El Hassani *et al.*, 2017).

Other techniques

In addition to XRD and FT-IR, scanning electron microscopy (SEM) and energy dispersive X-ray (EDX) were used to examine the surface morphology and elemental composition of LDH before and after dye adsorption and reflected the potential adsorption mechanisms (Yang *et al.*, 2015). BET techniques and thermogravimetric analysis (TGA) were also used to understand the adsorption mechanisms (Abou-El-Sherbini *et al.*, 2015; R. M. M. Santos *et al.*, 2017; Guo, Yin and Yang, 2018).

2.6 Research Gaps and Scheme of Thesis

The literature review provided the background information, theory guidelines and work by other researchers that shaped the ideas proposed in the present thesis. It has addressed a number of knowledge gaps and trends that have attracted insufficient attention. This section aims to connect the most significant findings from previous sections, state the rationale behind using RM for LDH synthesis and then summarise the key implications for setting up the experiments.

2.6.1 Summary of Red Mud Management Challenges

Despite the fact that much research has been conducted to investigate feasible options for RM reuse, so far the actual portion of RM utilisation is still negligible, and estimated at less than 2.5% of annual RM production (Balomenos, 2018). The extensive, high-added-value use of RM has not come to fruition. The main barriers to reusing bauxite residue not only lie in the techno-economic viability of solutions, but also in the legislative environment for implementing the solutions.

One large volume reuse option is as an embankment landfill for road construction; the other may be realised by refilling open bauxite mining pits and by rehabilitating bauxite residue disposal area (BRDA) through vegetation development (Sutar *et al.*, 2014). For nearly all the other aforementioned applications in building materials, pollution control and metal recovery, a fairly high temperature is required. The bulk utilisation of red mud remains a distant target.

2.6.2 Summary of RM-LDHs Synthesis Challenges

As introduced above, the synthesis and applications of LDH materials are of great interest. LDHs have enormous potential to open up new possibilities for a number of chemical applications. Though extensive investigations of LDH have been conducted, limited research has so far considered industrial waste RM as a raw material. In this research, instead of acting as a monotonous Al or Fe oxide source, RM aims to act as a combined source of Al and Fe oxides along with other mineral impurities. The main difficulties lie in the material preparation and activation, in the unfamiliarity of transforming RM to RM-LDH products and also in the evaluation of as-synthesised RM-LDHs. Further understanding of the operation factors that affect the formation, particle morphology and crystallization of LDH is also valuable. It would contribute greatly to developing a sustainable process for scaling up LDH production in general (Yanmin Yang *et al.*, 2012).

2.6.3 Summary of RM-LDHs Evaluation Challenges

To determine whether LDH phases have been synthesised, the product materials are required to meet a number of criteria as shown in Figure 2.21. Often, standard characterisation tools can only provide limited information about the various LDH structures. Therefore, the assessment of certain peculiarities of LDH such as their adsorptive performance and their response to calcination have been suggested. As reviewed in section 2.5, although considerable progresses have been achieved in the field of adsorption and degradation of dyes by LDH and LDH-based materials (mixed metal oxide materials), the adsorption capacities of LDHs are highly tailorable depending on the effect of calcination, nanomaterials, metal oxides impurities, etc. The adsorption mechanisms are investigated based on adsorption studies, using a range of micro-structural and chemical analysis methods, to aid in understanding and designing RM-LDHs for future research.

2.6.4 Summary of Research Gaps:

1) There is a lack of incentive for industries to utilise RM as iron and alumina sources. To develop more economically feasible remediation and re-use technologies, further understanding of the solid alkalinity and surface chemistry of RM are critical (Power, Gräfe and Klauber, 2011).

2) The challenges and potential of replacing soluble salts by reactive oxides as cation sources to syntheses LDH are of significant technological interest (see Section 2.3.2). Nevertheless, limited studies have considered industrial waste RM to act as the metal sources. Linking the utilisation of RM to the synthesis of LDH is an innovative approach but could be a promising production approach for engineering applications.

3) Due to the complexity of RM as a whole, designing an effective salt-oxide synthetic method poses significant challenges. In addition, factors like pre-treatment techniques (calcination, grinding) and operation variables (Mg/Al ratio, aging time, calcination temperature etc.) add extra uncertainty in predicting the synthesis process.

4) The determination of the LDH phase in mixed products and the evaluation of the synthesised products quantitatively and qualitatively are currently still unknown and have not been investigated systematically before.

5) Conventional LDHs can be deployed for multi-purposes, and therefore assessing RM-LDHs in practical applications is essential; attempts have been made to apply them in

sorption studies for chloride and anionic dye removal. The kinetics and mechanisms in both adsorption processes should be further explained by a variety of analytical tools.

6) The formation of such hybrid materials is uncommon; it is important to understand their potential and drawbacks. Determining the optimum RM-LDH and designing it for enhanced adsorptive performances may be of interest for industrial utilisation; however, such trials have not yet been made.

The present thesis focusses on the novel synthesis routes of RM-LDHs, and investigates the crystallinity, morphology characteristics and thermal stability of the prepared RM-LDHs and their applications in chloride binding and dye removal. The research framework of the following chapters is outlined in Figure 2.42.

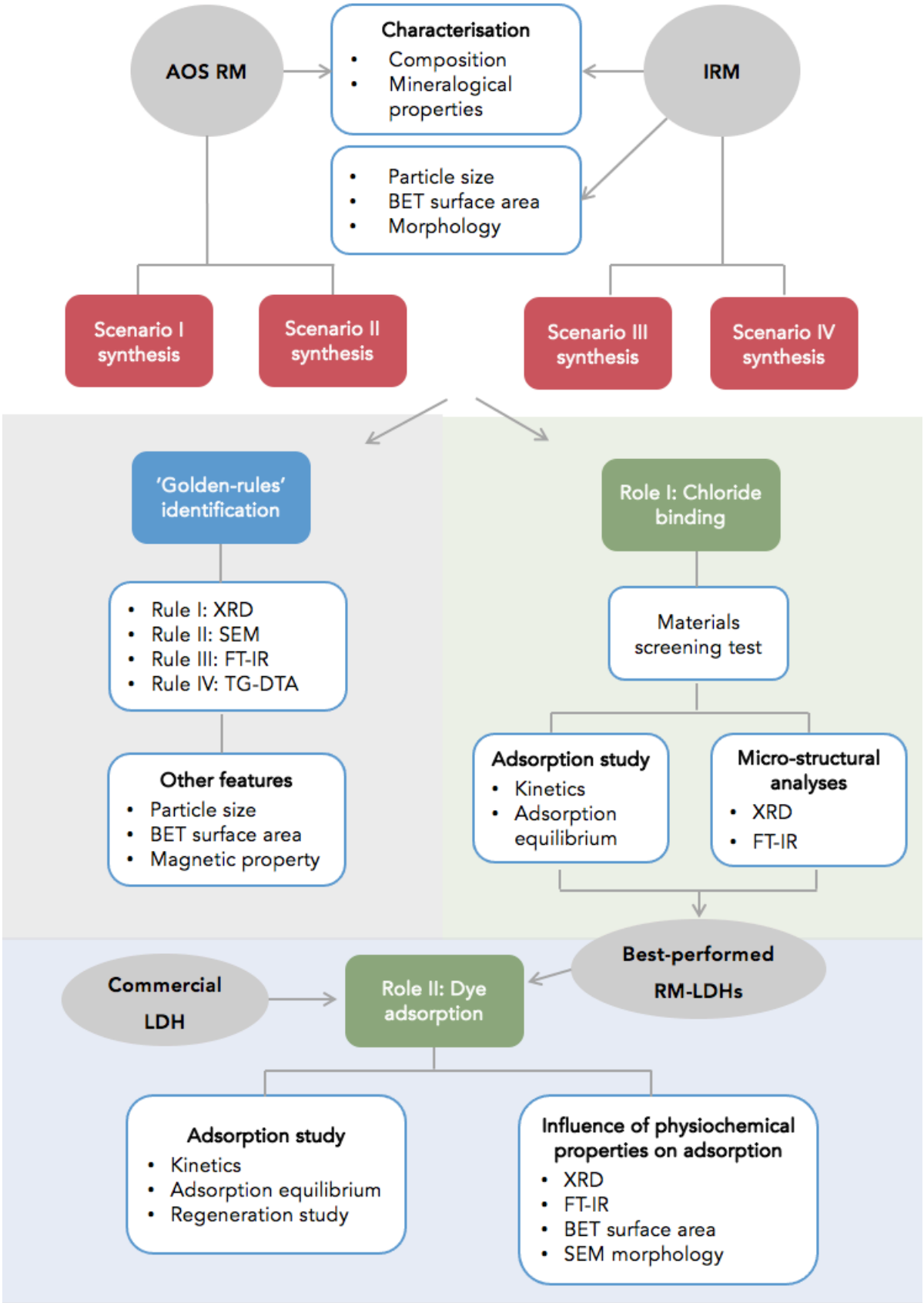

Figure 2.42 Research scheme proposed for this thesis

Chapter 3 Materials and Experimental Methods

This chapter presents details of the raw materials used in this thesis and their physical and chemical properties as well as the procedures of sample preparation, the characterisation methods and all experimental procedures employed including the adsorption studies.

3.1 Materials

The main material used was red mud as well as a large number of different chemicals, which are all detailed below.

3.1.1 Red Mud

Fresh red mud was obtained from two EU alumina plants for use in this study: one was directly provided by Aluminium-Oxide Stade GmbH (AOS) in Germany and the other was originated from the Aughinish Limerick plant, Ireland, and kindly offer by Professor Soutsos' research group in Queen's University Belfast. Basic information on these two alumina plants is given in Table 3.1. As mentioned in Section 2.1.4, refineries process red mud in different ways (see Table 2.3). Aluminium Oxid Stade GmbH currently adapts the lagooning disposal method. This means that after intensive washing, the bauxite residue is pumped through pipelines to the disposal area. In comparison to other refineries worldwide, AOS (Germany) operated a very efficient cleaning procedure of bauxite residue, resulting in minimum caustic liquor losses (Dentoni, Grosso and Massacci, 2014). Aughinish (Ireland) has employed dry stacking since their start-up, in which the bauxite residue disposal area is bounded by peripheral impermeable embankments and lined (Dentoni, Grosso and Massacci, 2014).

Table 3.1 The Alumina Plants of Fresh Bauxite Residue (from supplier information)

Business Name	Property Owner	Start Up	Location	Disposal Method	Geographic Coordinates
Stade	Aluminium-Oxid Stade GmbH	1973	Germany	Lagooning	53°38'49.59"N, 9°30'6.09"E
Aughinish	Rusal	1983	Ireland	Dry stacking	52°37'35.00"N, 9°3'53.00"W

AOS red mud (AOS RM) was used in the layered double hydroxide (LDH) synthesis study, whose appearance is shown in Figure 3.1 (a-b). Ireland red mud (IRM) was also taken as a raw material in the following synthesis and 'Role-play' studies, whose images are shown in Figure 3.1 (c-d). Their key physiochemical properties and elemental composition are displayed in Table 3.2. The minerals composition is deducted using X-ray diffraction (XRD), considering the metal centres (Fe, Na, Al, Ca and Ti) and the bridging groups such as O, SiO_4 and CO_3 that constitute the mineral array, which are discussed in detail in Section 4.1.

(a)

(b)

(c)

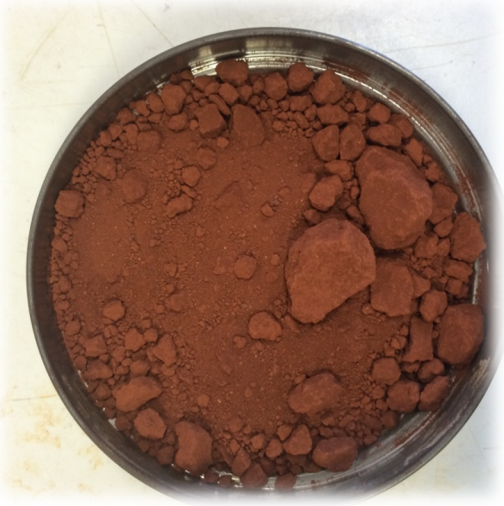

(d)

Figure 3.1 (a) The raw AOS RM, (b) Ground AOS RM & calcined AOS RM; (c) IRM in transport container, (d) The dried IRM in a pan.

Table 3.2 Physiochemical compositions of fresh AOS red mud and Ireland red mud

Raw materials	Parameters			Mass fraction *w*/%						
	Moisture (%)	pH (in water)	Cation Exchange Capacity (CEC)	Fe_2O_3	Al_2O_3	SiO_2	TiO_2	Na_2O	CaO	SO_3
AOS RM	14.07	10.70	5.8	58.5	11.6	4.8	9.4	3.2	2.7	/
IRM	21.83	10.19	5.3	39.5	16.4	10.0	9.0	7.1	5.6	0.4

Note: Chemical compositions were determined using X-ray fluorescence (XRF) analysis. The XRF result of AOS RM was provided by the supplier, while that of IRM was conducted by Dr. Liwu Mo in Nanjing Industry University, China.

3.1.2 Chemicals

A number of materials and chemicals were required for the work reported in this thesis. These included reactive magnesium oxide MgO (M_{50}), calcined from magnesite, which was obtained from Sanyuan, China. The chemical composition of M_{50} is shown in Table 3.3 and it was mainly used for synthesis study in Chapter 4.

Table 3.3 Chemical compositions of reactive MgO (M_{50}), reported by Mo *et al.* (2015)

Raw material	Reactivity (seconds)	Chemical composition (%)								
		SiO_2	Fe_2O_3	Al_2O_3	CaO	MgO	K_2O	Na_2O	SO_3	Loss
MgO	50	2.76	0.26	0.42	3.18	88.52	0.03	0.06	0.61	3.62

Remazol Brilliant blue R (RBB), used for the sorption study in Chapter 6, was purchased from Sigma-Aldrich, UK. Its molecule structure is displayed in Figure 3.2.

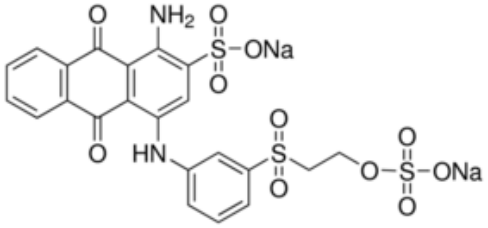

Figure 3.2 Molecule structure of Remazol Brilliant blue R (RBB)

Other chemicals used in preparation of various samples or assisted in analytical work are commercially available in laboratory reagent grade, whose chemical and physical properties were acquired from the suppliers and specified in Table 3.4. All chemicals were used without further purification. All solutions were prepared with deionised water. All glassware was cleaned thoroughly, rinsed with distilled water and dried at 60ºC in oven.

Table 3.4 Details of the chemicals used in experimental work

Chemical	Manufacture	Purity	Molecular Formulae	Where used
Magnesium chloride hexahydrate	Fisher scientific	99.5%.	$MgCl_2.6H_2O$	Synthesis
Aluminum chloride hexahydrate	Fisher scientific	≥ 99%.	$AlCl_3.6H_2O$	Synthesis
Hydrotalcite, synthetic (also called as 'LDH')	Sigma-Aldrich	99.6%.	$Mg_6Al_2(CO_3)(OH)_{16}\cdot 4H_2O$	Adsorption
Sodium hydroxide - pearl	Fisher scientific	99.3%	NaOH	Various
Sodium chloride	Fisher scientific	99%	NaCl	Various
Sodium carbonate anhydrous	Fisher scientific	≥ 99.5%.	Na_2CO_3	Various
Nitric acid	Fisher scientific	70%	HNO_3	pH adjustment
Hydrochloric acid	Fisher scientific	~36%	HCl	Alkalinity
Sulfuric acid	Fisher scientific	>95%	H_2SO_4	pH adjustment
Titanium standard solution 1000 ppm	Fisher scientific	for A.A.S.	Ti single element	Chemical composition
Sodium standard solution 1000 ppm	Fisher scientific	for A.A.S.	Na single element	Chemical composition
Iron standard solution 1000 ppm	Fisher scientific	for A.A.S.	Fe single element	Chemical composition
Aluminium standard solution 1000 ppm	Fisher scientific	for A.A.S.	Al single element	Chemical composition
Calcium standard solution 1000 ppm	SPEX CertiPrep	for ICP/MS	Ca single element	Chemical composition
Magnesium standard solution 1000 ppm	Fisher scientific	for A.A.S.	Mg single element	Chemical composition

3.2 Experimental Procedure

Since the accuracy of any solution concentration will have a profound impact on the precision of the final results, volumetric flasks were always employed rather than other graduated measuring containers for standard solution preparation. Standard procedures of liquid transfer, dilution and level to calibration mark were strictly followed.

3.2.1 Pre-treatment of Red Mud

The red mud was thoroughly homogenised by manual shaking, and the sub-sample was oven dried at 65ºC for 5 days (refer to Section 3.3.1.1). The image of oven is shown in Figure 3.2a. In laboratory analysis, the soil-like sample is typically sieved to less than 2 mm particle size prior to characterisation analysis. Solid weightings were completed by an electronic balance that corrects to 4 decimal places. As reviewed in Section 2.3.4, there have mainly been two pre-treatment methods for red mud, which are calcination and grinding. The detailed procedures are specified in Section 4.2. Figure 3.2b displays the automatic mortar grinder used for dry grinding and wet grinding.

(a) *(b)*

Figure 3.2 (a) Temperature-controlled Oven; (b) Mortar Grinder RM 200 - Retsch®

3.2.2 Synthesis of RM-LDHs

RM was homogenised and dried at 105°C, and ground to pass through a 53-micron sieve (Qian, Li and Chen, 2015). The subsequent procedures varied, depending on different RM sources and synthesis scenarios, as explained in Section 4.2. The material weights were calculated from the associated molar ratio and the operation values were chosen based on the conclusions of Table 2.8 and Section 2.3.4 – 'Governing Variables'. For example, in a typical Scenario III – 'Dry grinding synthesis' (see Section 4.2.3.1), 5 g RM and 6.39 g MgO were dry ground in the mortar grinder for 45 mins, and roasted together at 650°C for 4 h in a muffle furnace with a heating rate of 10°C /min. The roasted powder was transferred into a 250 mL conical beaker, then 100 mL Na_2CO_3 solution (0.96 $mol \cdot L^{-1}$) and 100 mL water were added to achieve a liquid to solid ratio (L/S) ≈ 20. The addition was carried out in an emulsifying machine -- IKA Ultra-Turrax T25 model with a rotor speed of 5000 $rpm \cdot min^{-1}$. The resulting slurry had molar ratios Mg/(Al+ Fe) ≈ 3.0 and $[CO_3^{2-}]/(Al^{3+}+Fe^{3+}) \approx 2.0$.

The slurry was magnetically stirred and aged at 70°C in a water bath for 3 days, whose typical setting-up is shown in Figure 3.3. After aging, the suspension was centrifuged, thoroughly washed and dried at 100°C for 24 h, denoted as RM-LDHs. Calcined sample, which were labelled as RM-CLDHs, were obtained after 4 h calcination at 500°C in air by a muffle furnace. The calcination parameters were chosen based on the thermal decomposition study of Mg-Al-Fe LDHs (Hibino and Tsunashima, 2000; Heredia *et al.*, 2013).

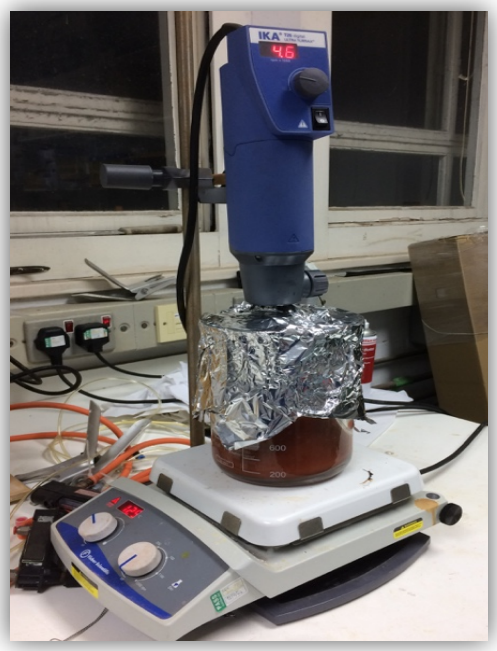

Figure 3.3 Example of the experiment setting-up for slurry aging

3.2.3 Adsorption Study

In order to better understand the as-synthesised RM-LDHs and compare their performances against that of existing materials in practical applications, batch adsorption experiments were carried out in polyethylene tubes in laboratory, including kinetics, the influence of initial solution pH and adsorption equilibrium studies. Most of these suspension samples were prepared in either duplicate or triplicate to achieve statistically valid average data.

Sodium chloride was selected as the Cl^- source for investigating the 'Role-play I: design of chloride binding LDH' (see Section 2.4.2). Meanwhile, RBB was selected as the target anionic dye for the adsorption study 'Role-play II: adsorption of organic dyes', where the performances of RM-LDHs, RM-CLDHs and commercial hydrotalcite have been studied.

The concentration of the sorbate adsorbed to the adsorbent, C_s was calculated using Eqn. (3.1), where C_i is the initial sorbate concentration in solution, C_{aq} is the final sorbate concentration in solution, V is the volume of solution, and m is the mass of the adsorbent.

$$c_s = \frac{(C_i - C_{aq}) \cdot V}{m} \tag{3.1}$$

3.2.3.1 Adsorption Study for Chloride

The batch adsorption experiments were carried out in 50 mL polyethylene tubes in a temperature-controlled lab (20±1°C). 0.4 g of solids were added to 40 mL prepared solutions and shaken. The specific solid to liquid ratio was chosen to ensure that, even at the lowest Cl^- concentration, the total Cl^- content in the liquid would be sufficient to occupy all the available ion-exchangeable interlayer sites. Preliminary tests were first conducted to select the feasible types of LDHs for further studies. A series of as-synthesised RM products were tested and compared in two groups of chloride solutions: 500 ppm & 0.75 M (as equivalent to 26625 ppm Cl^-), as shown in Table 3.5. After reaching equilibrium (7 days), the suspensions were separated using the centrifuge at 3900 min^{-1} for 4 min. The chloride concentration was then measured using Ion Chromatography (IC), refer to Section 3.3.2.3.

Afterwards, the selected RM products and the commercial LDH were investigated for adsorption isotherm study, which was conducted using NaCl solutions ranged from 0 to 1000 ppm and left for 7 days. The kinetic study employed 500 ppm NaCl solution. Suspensions were shaken at 200 rpm and the chloride contents were measured at selected time intervals: 5 min, 10 min, 20 min, 30 min, 1 h, 2 h, 3 h, 6 h, 12 h, 24 h, 36 h, 48 h, 72 h, 5 days or 7 days.

Table 3.5 Compositions of the concentrated and diluted Chloride solution

	Concentration		[Cl-]/[OH-]
	NaCl	NaOH	
CH-1	0.75 mol/L	0.25 mol/L	3.0
CH-2	500 ppm as Cl-	0	N/A

3.2.3.2 Adsorption Study for RBB

The batch adsorption experiments were carried out in 50 mL polyethylene tubes in a temperature-controlled lab (20 ±1°C). Aqueous RBB dye solution was prepared by dissolving an accurate amount of RBB in deionised water as the 1000 mgL^{-1} stock solution and then diluting it to required concentrations (20-800 ppm). A typical image is shown in Figure 3.4. The adsorbent-adsorbate mixture was centrifuged, filtrated with a 0.45 μm glass fibre filters (GF/A) after the designated shaking time, as illustrated in Figure 3.5. Residual RBB concentration was measured by UV-Vis (refer to Section 3.3.2.2), while the solids were washed twice and dried overnight at 80°C under air condition.

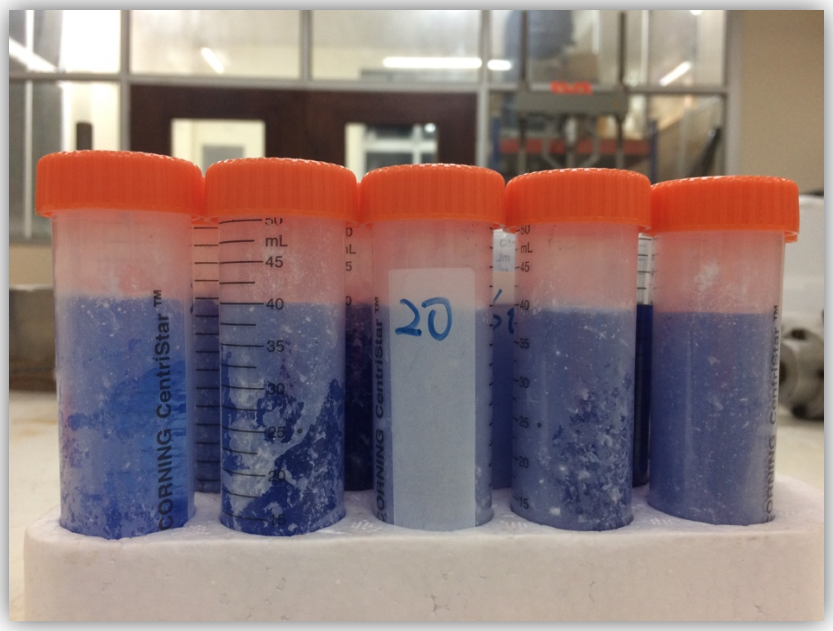

Figure 3.4 Examples of RBB-adsorbent samples before reaching equilibrium

(a) *(b)*

Figure 3.5 (a) Centrifuge, (b) Examples of adsorbent-adsorbate mixtures after centrifugation

In order to assess the adsorption kinetics of RBB on RM-LDHs, 0.1 g of adsorbent was added to 40 mL solutions of 400 ppm RBB solutions (pH=5). The mixture was shaken at 200 rpm for 5 min, 10 min, 20 min, 30 min, 1 h, 2 h, 3 h, 6 h, 12 h or 24 h. These tests confirmed that the adsorption equilibrium was reached within 24 h. The kinetic data were fitted using pseudo first order model, second order model and intraparticle diffusion model (Paranavithana *et al.*, 2016). These models applied were presented in Section 2.5.2.2 - Eqn. (2.4-2.6).

In order to construct the adsorption isotherm for RM-LDHs at room temperature, 0.1g RM-LDHs was added to 40 mL solutions (pH=5) containing different concentrations (20, 40, 60, 100, 200, 400, 600 or 800 ppm) of RBB. The mixture was shaken at 200 rpm for 24 h. For the equilibrium study, the experimental data was fitted by Langmuir and Freundlich isotherm models respectively, which are typically used to describe the adsorption isotherm and predict the sorption mechanisms (Foo and Hameed, 2010). The non-linear form of Langmuir model and Freundlich model were presented in Section 2.5.2.1 - Eqn. (2.1-2.3).

3.3 Tests and Testing Procedure

3.3.1 Physicochemical Properties

All laboratory analyses in this study were conducted in a temperature-controlled lab, which is at 20°C±1°C and 50%±2% relative humidity. Except from properties obtained from the supplier or existing literature, relevant physicochemical properties of the materials were tested as set out in the following sections, including the moisture content, pH, alkalinity, total cation exchange capacity (CEC), acid neutralisation capacity (ANC) and chemical compositions. Replicate analyses were always carried out for quality control, and the precisions have been checked and controlled within relative standard deviation (RSD) of ± 10 %. The related apparatus and instruments are introduced in the following sub-sections.

3.3.1.1 Moisture content

The water content by mass is the ratio of the mass of water contained in the pore spaces of soil material, to the solid mass of particles in that material, expressed as a percentage (D2216., 1998). It is a principal index parameter that is required in other characterisation measurements. The ASTM standard test method D2216 is based on removing soil moisture by oven-drying a soil sample until the weight remains constant. A sub-sample of 50 g raw bauxite residues was placed into a specimen container and placed in an oven, whose temperature was maintained between 110°C±5°C. A constant dry mass can be ascertained, when further heating causes less than 1% additional mass loss. To calculate the water content, w, as a percentage of the dry soil weight:

$$w = \left[\frac{M_{cms} - M_{cds}}{M_{cds} - M_c}\right] \times 100 = (M_w \div M_s) \times 100 \quad (3.2)$$

Where

M_{cms} = mass of container and moist specimen, g
M_{cds} = mass of container and oven dry specimen, g
M_c = mass of container, g
M_w = mass of water ($M_w = M_{cms} - M_{cds}$), g
M_s = mass of oven dry specimen ($M_s = M_{cds} - M_c$), g

3.3.1.2 pH

Test of the pH was based on ASTM standard test method D4972, which determines the degree of acidity or alkalinity in waste materials suspended in water or a 0.01M calcium chloride solution (D4972., 2001). 20 mL of reagent water was added to 20 g of air-dried waste sample, and the suspension was continuously stirred for 5 min. The bauxite residue suspensions were left to stand for 1 h to allow the standard solid-liquid contact, then the pH was measured using a pH sensitive electrode system.

3.3.1.3 Alkalinity

Alkalinity is the quantitative capacity of a water sample to neutralise an acid to a set pH, which is a measurement of the corrosive compounds primarily due to hydroxide, carbonate and bicarbonate ions. Hydroxide ions and carbonate ions exist at pH levels greater than 8.3 (Lutpi and Zhu, 2010), as presented in Eqn. (3.3)-(3.4). In the pH range of 8.3-4.5, bicarbonate ions in samples gradually convert to carbonic acid H_2CO_3, as shown in Eq. (3.5). The alkalinity can be determined in accordance to standard method APHA (1992) (Arnold E. Greenberg, 1992). Titration of 0.1 *N* H_2SO_4 against 20 mL bauxite residue liquor (obtained from 30 g RM solid: 30 mL distilled water) was carried out, until endpoint pH 8.3 and pH 4.5 respectively. Total alkalinity and alkalinity specification of three forms can be determined according to Eqn. (3.6) and Table 3.6, respectively.

$$OH^- + HCl \rightarrow H_2O + Cl^- \tag{3.3}$$

$$CO_3{}^{2-} + HCl \rightarrow HCO_3{}^- + Cl^- \tag{3.4}$$

$$HCO_3{}^- + HCl \rightarrow H_2CO_3 + Cl^- \tag{3.5}$$

$$\text{Total alkalinity, mg } CaCO_3 \text{ /L} = \frac{A \times N \times 50000}{mL\ sample} \tag{3.6}$$

Where A = mL standard acid used

N = normality of standard acid

Table 3.6 Alkalinity Relationships

Result of Titration	Alkalinity due to		
	OH^-	CO_3^{2-}	HCO_3^-
P = 0	0	0	T
P < ½ T	0	2P	T – 2P
P = ½ T	0	2P	0
P > ½ T	2P - T	2(T – P)	0
P = T	T	0	0

Note: P – phenolphthalein alkalinity (to endpoint pH 8.3), T – total alkalinity

3.3.1.4 Total Cation Exchange Capacity (CEC)

Cation and anion exchange capacities of a soil demonstrate the capacity of that soil to retain exchangeable cations in the field (Gillman, 1979). It is a key feature affecting soil structure stability, nutrient availability and soil pH. Because there exist no exchangeable acidic cations in alkaline conditions, the sum of exchangeable K, Na, Ca, Al, Fe, Mn and Mg ions is regarded as the total cation exchange capacity (CEC), as the expression in Eqn. (3.7). The test procedure was based on the methods of Gillman and Sumpter (1986) and Schwertfeger and Hendershot (2009), where exchangeable cations were removed from dry and sieved soil with 0.1 mol/L $BaCl_2$ solution. Then the suspension was shaken for 2 h, centrifuged for 10 min at 2500 rpm and filtrated to separate out the supernatant. The concentrations of cation ions in the extracts were subsequently determined by ICP-OES, as illustrated in Section 3.3.2.1.

$$CEC = [Na^+] + [K^+] + [Ca^{2+}] + [Mg^{2+}] + [Al^{3+}] + [Fe^{3+}] \quad (3.7)$$

Where [ ] represents cmol/kg, i.e. cent mole positive charge per kg of soil

3.3.1.5 Acid Neutralisation Capacity (ANC)

Acid neutralisation capacity (ANC) indicates the ability of the residue to neutralise acid to a specific pH endpoint (Johnson, Brandenberger and Baccini, 1995; Gräfe, Power and Klauber, 2011). For RM slurry, both porewater species and mineral solids contribute to the measured ANC and govern the acid-based chemistry behavior (Khaitan, Dzombak and Lowry, 2009).

Standard Test CEN/TS 15364 was conducted to examine the overall buffering capacity of the bauxite residue (CEN/TC 292, 2006). Briefly, a minimum of 8 dried subsamples were mixed with deionised water containing pre-determined amounts of nitric acid (0.1 or 1.0 M HNO_3) or base (1.0 M NaOH) at a L/S = 10 (150 mL reagents: 15 g dry mass), to obtain pH values in the range of 4-12. The suspensions were kept stirring for 48 h and their pH were measured after each stage (three stages in total). When the pH equilibrium was reached, the acid/base neutralisation curve could be plotted accordingly. The $ANC_{pH4.5}$ is calculated from Eqn.(3.8), meaning the fixed endpoint pH 4.5 is reached (Sahu, R. K. Patel and Ray, 2010; Payán *et al.*, 2012).

$$ANC_{pHx} = A_{pHx} \times \frac{N_{pHx}}{M} / 1000 \tag{3.8}$$

Where

- A_{pHx} = the amount of acid needed in mL to reach pH=x for sample weight M;
- ANC_{pHx} = the acid neutralisation capacity expressed in mol/kg from acid/base neutralisation curve at pH = x;
- N_{pHx} = the acid normality selected based on the buffer capacity amount around pH = x expressed in mol/L;
- M = the sample weight expressed in kg.

3.3.1.6 Chemical Composition

Aqua regia digestion test was carried out based on the standard method ISO 11466. 1.0g sub-samples of original RM were digested in 12mL of hot aqua regia (water bath at 100 °C) for 60 min to determine the pseudo-total metal loads present. After diluting it for 100 times, its metal concentrations (Al, Cu, Fe, Mg, Na, Ti) were determined using ICP-OES. Since the quantities of metals digested by the aqua regia were only representative-totals, to obtain more absolute-total would require XRF analysis.

3.3.2 Concentration Measurements

Three instruments have been mainly employed for the concentration measurements, depending on the nature of species. Metal concentrations were usually determined by Inductively Coupled Plasma-Optical Emission Spectrometry (ICP-OES), RBB amounts were determined using Ultraviolet–visible spectroscopy (UV-Vis), while the concentrations of chloride were detected by Ion Chromatography (IC) in this thesis.

3.3.2.1 Inductively Coupled Plasma-Optical Emission Spectrometry (ICP-OES)

For measuring the cations constituent in solution, ICP analysis was always conducted. A Perkin Elmer Inductively Coupled Plasma–Optical Emission Spectrometry (ICP-OES), as shown in Figure 3.6, was used for detecting the concentrations of trace metals in sample solutions. Liquid sample injected into ICP chamber is being vaporised, the metal atoms are being exited by the Argon plasma and their electrons reach a higher energy level. When the excited atoms drop back to low energy position, energy is emitted in the form of photons (light). The emission rays are then captured by a monochromator-like device to display wavelength signal. Each element in the periodic table corresponds to a distinct set of emission wavelengths that are measured with a spectrometer. The intensity of emission represents the concentration of the element in the solution.

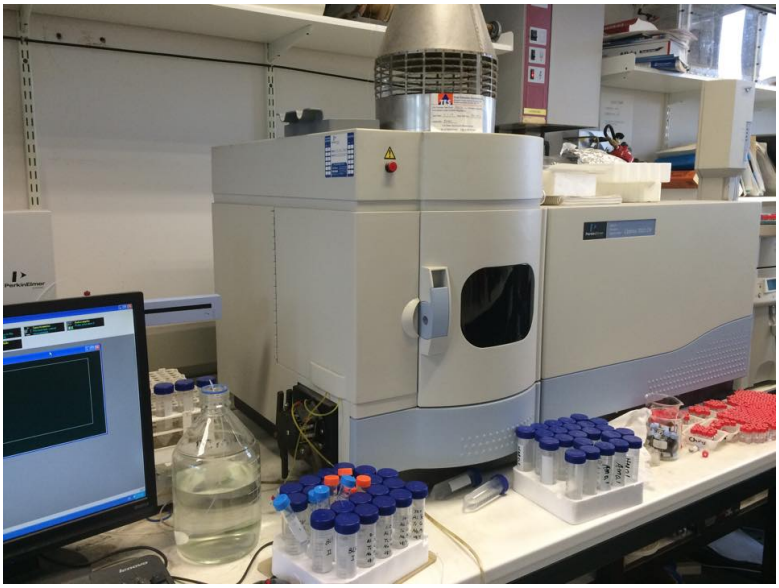

Figure 3.6 Setting-up of Perkin Elmer Optima ICP-OES

At least one blank sample is needed to build up the background baseline. A series of calibration standards containing the elements of interest were prepared to establish a

calibration curve. As shown in Figure 3.7, the reference standards were diluted to 0.1 ppm, 1.0 ppm, 10 ppm, and 50 ppm in this experiment. A brief of setting-up and testing procedure is demonstrated below:

1) Initiate the Argon gas pumping system and switch on the plasma;
2) Filter the original sample through a syringe filter (pore size of 0.45 μm) to avoid blockages of the equipment. Then dilute with deionized water to ensure within the calibration range and acidify by adding concentrated HNO_3 in a polyethylene bottle;
3) Program the testing method, that is, input the calibration standards values, choose calibration equation, number sample positions and set up washing frequency (samples are normally tested for 3 replicates and extra washing time is called up once the concentration exceeds 10 ppm) (Palmer and Frost, 2011);
4) Check the accuracy of the calibration before proceeding to sample measurements.

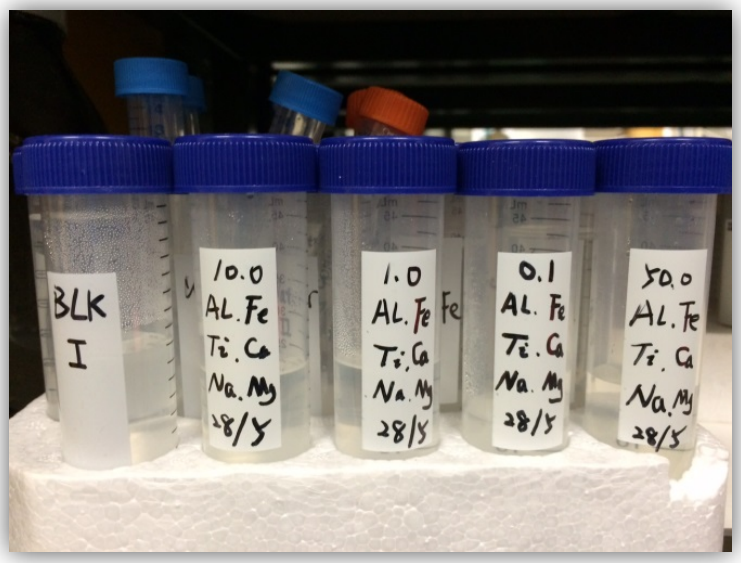

Figure 3.7 Examples of calibration standards (AL, Fe, Mg, Ca, Ti and Na)

For the accuracy of data analysis, limit of detection (LOD) should be noted, which is the concentration when the measured signal differs significantly form the background. It can be calculated based on the following Eqn. (3.9). The LODs are indicated in Table 3.7.

$$LOD = \frac{C_1 - C_0}{I_1 - I_0}(3\sigma) \tag{3.9}$$

Where C_1 = concentration of the high sample

C_0 = concentration of the blank

I_1 = raw intensity of the high sample (cps)

I_0 = raw intensity of the blank (cps)

3σ (sigma) = a confidence factor × standard deviation from a number of measurements of the blank (cps)

Table 3.7 Limit of Detection (LOD) of ICP-OES

Element	Concentration (mg/L)
Al	0.00261
Ca	0.05282
Fe	0.00001
Mg	0.00280
Na	0.00201
Ti	0.00026
K	0.00281

3.3.2.2 Ultraviolet–visible spectroscopy (UV-Vis)

Ultraviolet-visible spectroscopy is frequently used to quantify different analytes, such as transition metal ions, highly conjugated organic compounds, and biological macromolecules. The concentrations of RBB were measured using Perkin Elemer UV-Vis Lambda 35, as shown in Figure 3.8. It is a simple double beam spectrometer that has a single light source providing the visible and near ultraviolet radiation, a monochromator and a splitter to get the beam to a reference cell and a sample cell, as shown in Figure 3.9. The detector converts the incoming light into a current and plots the absorbance (A) against wavelength. The relationship between absorbance and the intensities passing through both cells is given by Eqn. (3.10). Meanwhile, the Beer-Lambert law states that the absorbance of a solution is directly proportional to the concentration of analyte:

$$\mathrm{A} = log_{10}\frac{I_o}{I} = \varepsilon \mathrm{bc} \qquad (3.10)$$

Where I_0 = intensity of the reference cell

I = intensity of the sample cell

ε = the molar absorptivity of the absorbing species, $M^{-1}cm^{-1}$

b = the path length of the cuvette or sample holder, normally 1 cm

c = the concentration of the solution, M

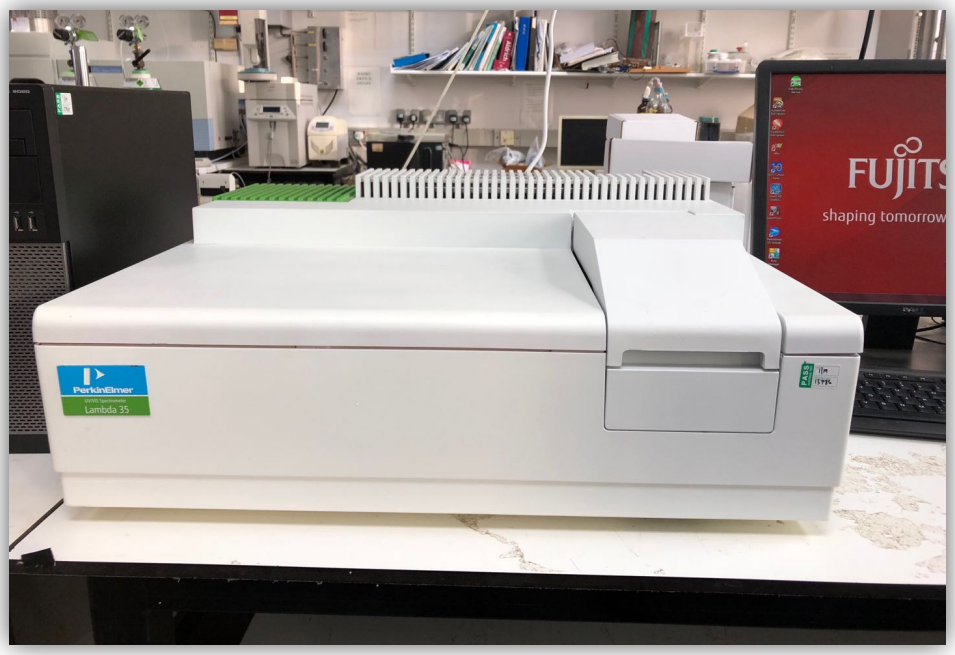

Figure 3.8 Perkin Elemer UV-Vis Lambda 35

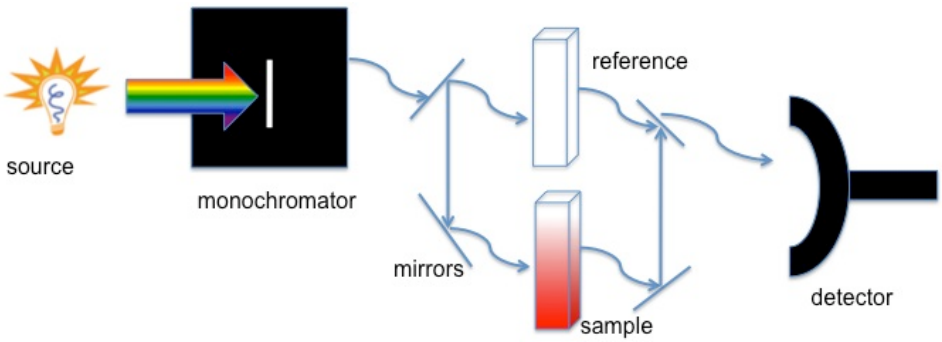

Figure 3.9 Illustration of a double beam UV-Vis instrument (Barron, 2020)

The preliminary scan of RBB standard showed that the maximum adsorption happens at a wavelength of 592 nm, which is represented in Figure 3.10. As Beer's law is constrained to dilute solutions (<0.01 M), a diluted calibration line of RBB solutions from 5 ppm to 200 ppm was built up (see Figure 3.11). The calibration line displayed a good linear fit (R^2 = 0.9989) and was checked time to time to ensure the accuracy. The lower limit of detection (LOD) was determined to be 1.1 ppm, therefore readings below this value were noted as

'N/A' in the calculation (Akul Mehta, 2012). Dilution was required if the sample's concentration is expected to be higher than 200 ppm.

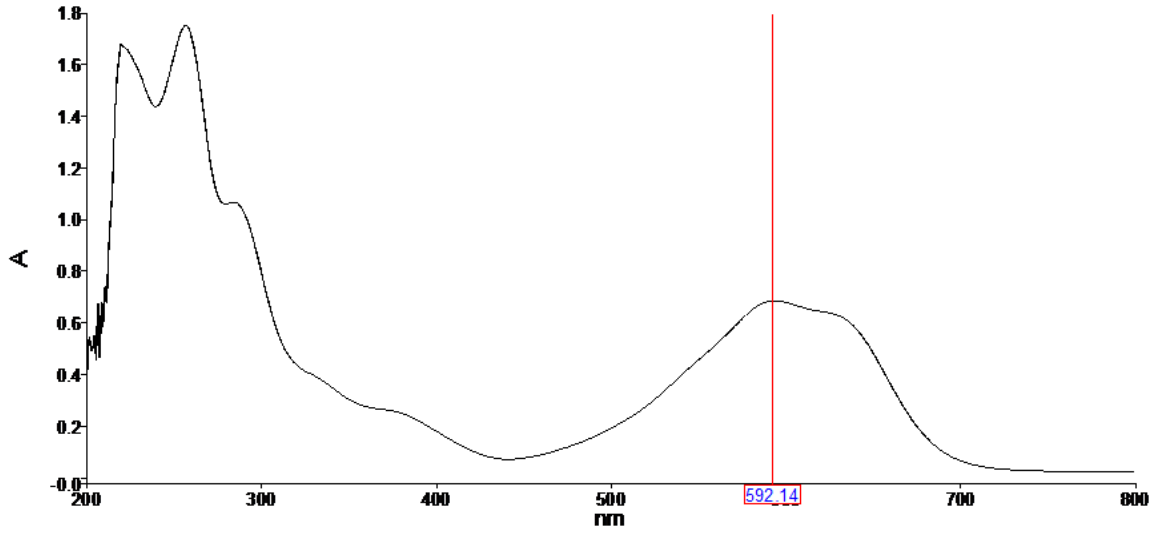

Figure 3.10 The UV-Vis absorbance spectrum of RBB at 200 mg/L in solution

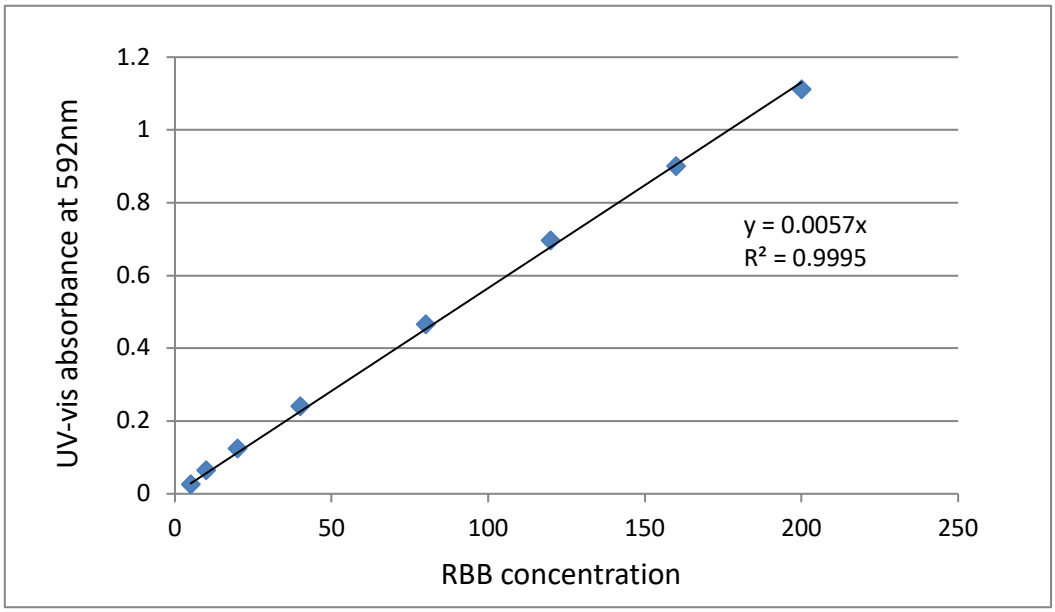

Figure 3.11 Calibration curve for diluted RBB solution at 592 nm.

For minimising the effects of particles, before the analysis with UV-Vis, the RBB samples were filtrated through Thermo Scientific Chromanol 0.20 µm glass fibre filters. However, calibration test observed that the glass fibre filter is still capable to remove 10-15% of RBB from the diluted solutions. There exists an equilibrium between the filtered solution and the residue in the filter. After 3-4 passes of suspension through the filter, the adsorption of the RBB on the filter does not occur anymore. Ferrero (2007) also highlighted the same issue.

3.3.2.3 Ion Chromatography (IC)

Ion Chromatography is a method for measuring concentrations of ionic species by separating ions based on their interactions with resin (stationary phase) and the eluent (mobile phase). Analyte is injected into a carrier fluid (the eluent) and the combination passes through a pressurized chromatographic column containing stationary adsorbent. Ion species in the analyte have different affinity for the adsorbent, which are then partitioned between the stationary adsorbent and the eluent flow. Different species therefore will move down the column at various speeds and go to an electrical conductivity detector. The chromatogram depicted peaks versus different retention times.

In the present study, the concentration of chloride ion was measured by the Metrohm 790 Compact IC with 813 Compact Autosampler (Figure 3.12). The eluent (1.8 mM Na_2CO_3/1.7 mM $NaHCO_3$) was prepared according to the methodology by Brinton, Antweiler and Taylor (1996). Eluent flow rate was kept at 0.50 mL/min, avoiding the system pressure to be too high. For continuous operation of the suppressor module, the regeneration solution (20 mmol/L H_2SO_4) and the rinsing solution (distilled H_2O) were prepared and filled. Prior to analysis, the samples were filtered through Thermo Scientific Chromanol 0.20 μm glass fibre filters.

The chromatogram of Cl standard was scanned, indicating the retention time of chloride was at approximately 13 min. Multiple-point calibration was then carried out using a series of external chloride standards (blank, 10 ppm, 50 ppm, 100 ppm, 200 ppm). The areas of chloride peaks were taken as the base of calibration. The calibration curve obtained is presented in Figure 3.13, which denotes a good linear fit y=0.0886x-2.4128 (R^2 = 0.9996). It is necessary to dilute the analytes to be within the range of calibration line.

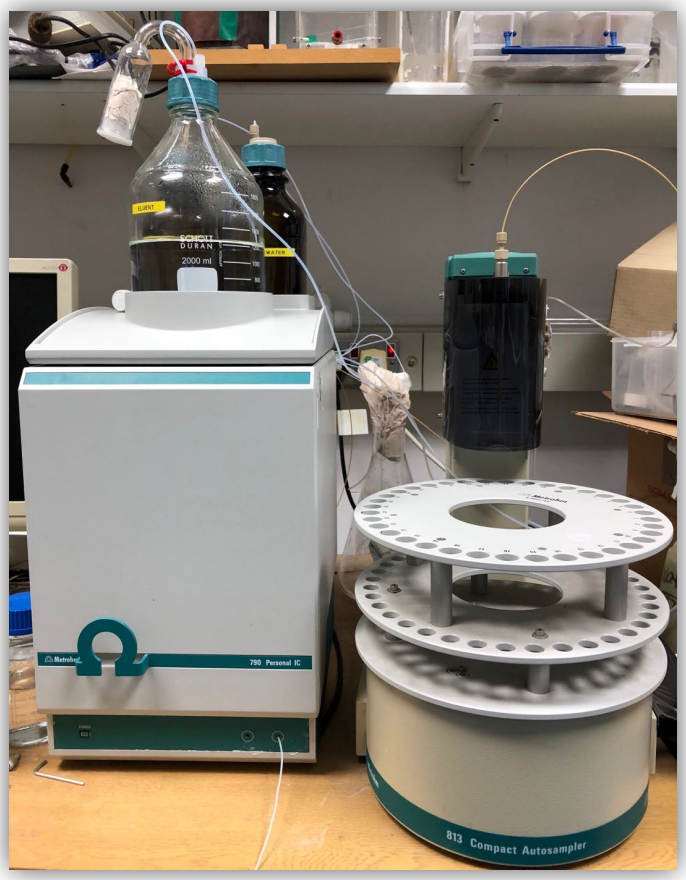

Figure 3.12 Metrohm 790 Compact IC

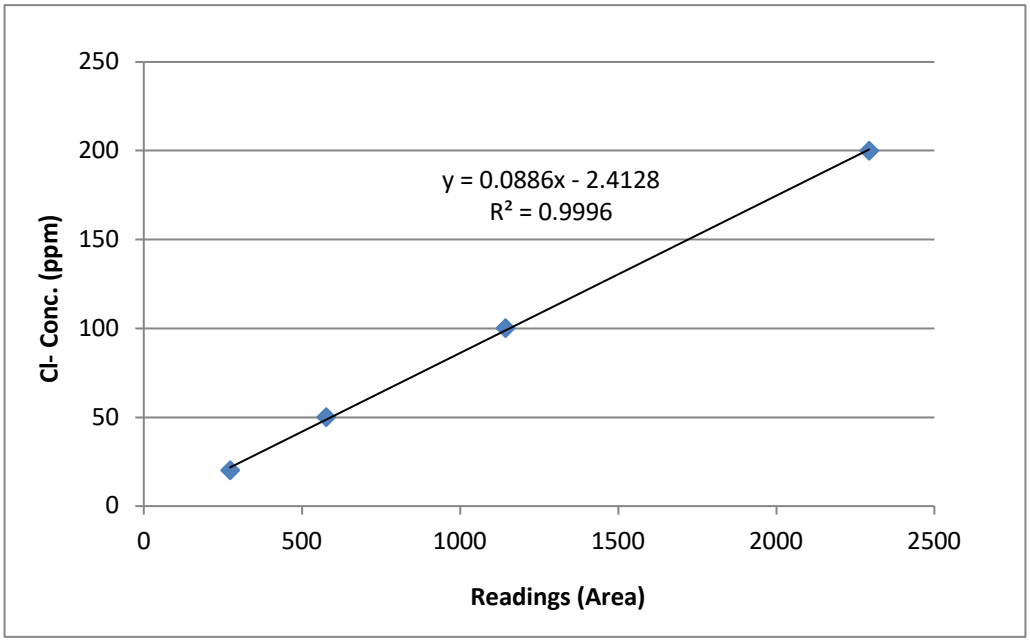

Figure 3.13 Calibration curve for diluted sodium chloride solution

3.3.3 Micro-structural Analysis

In order to further investigate the adsorption mechanisms of chloride and RBB on the as-synthesised products, the samples before the adsorption were washed three times, oven dried at 60°C for 48 h and analysed using the methods in this section. After the adsorption, these procedures were repeated to form a comparison. Prior to micro-structural analyses, the samples were always stored in vacuum drying chambers, as shown in Figure 3.14.

Figure 3.14 Vacuum drying chambers with a pump used to store samples

3.3.3.1 Powder X-ray diffraction (XRD)

The XRD instrument and sample preparation are demonstrated in Figure 3.15 (a-b), respectively. Dry samples were ground and mounted on a flat holder. XRD patterns were collected on a Siemens D500 X-ray diffractometer with a Cu-Ka radiation (wavelength λ=0.1541 nm) at 40 kV and 35 mA. Scanning was operated in the 2θ range from 5° to 80°, at a counting time of 1 s/step and a resolution of 0.04°/step.

The obtained peaks from the XRD patterns were searched and matched in the PDF-2004 database using PANalytical X'Pert High Score software. The crystallographic information and crystallite site have been estimated according to Pérez-Ramírez *et al.* (2001).The lattice parameter *a* corresponds to the average cation-cation distance within the LDH layers and is calculated according to Eqn. (3.11):

$$a = 2 \times d(110) \tag{3.11}$$

The parameter c, is related to the thickness of the brucite-like layer and the interlayer distance, assuming a 3R polytypism for the LDH, which is expressed in Eqn. (3.12):

$$c/3 = 1/2 \times (d(003) + (2 \times d(006) \quad (3.12)$$

The crystallite size is determined by the Scherrer equation (3.13), considering the (003) basal reflection.

$$L = \frac{0.9\lambda}{\beta cos\theta} \quad (3.13)$$

Where L is defined as the volume-averaged thickness of the crystallites, λ is the wavelength of the radiation used, β is the full width at half-maximum in radians, and θ is the Bragg diffraction angle (Pérez-Ramírez *et al.*, 2001).

(a) *(b)*

Figure 3.15 (a) Siemens D500 X-ray diffraction diffractometer; (b) Samples preparation for XRD analysis

3.3.3.2 Thermogravimetric analysis (TGA)

Thermogravimetric analysis (TGA) measures the weight loss with precision while heating up the samples. TGA tests were conducted using Mettler Toledo TGA/DSC instrument, as shown in Figure 3.16. The sample was placed into a ceramic crucible and heated as the designed temperature programme. Each sample was hold at 50°C for 30 min and heated at a rate of 10°C/min from 50°C to 800°C, under N_2 flow (30 mL min^{-1}). The derivative thermogravimetric analysis (DTG) curves of the sample were obtained by calculating the first order derivative of the TGA curves. Minerals were identified based on TG and DTG (curves that show precise records of weight losses and thermal decomposition characteristics.

Figure 3.16 Mettler Toledo TGA/DSC connected to N_2 supply

3.3.3.3 Fourier-transformed infrared spectroscopy (FT-IR)

Fourier-transformed infrared spectroscopy (FT-IR) was used to study the fundamental vibrations and associated rotational-vibrational structures, which are reported in all the results chapters. The infrared spectrums of samples were tested by a VERTEX 70v Fourier-transform infrared spectroscopy spectrometer (BRUKER) between wavenumbers 4000 to 600 cm^{-1} at resolution of 1 cm^{-1}. The spectrums were plotted against each other to characterise the synthetic products and the variation before and after adsorption process.

3.3.3.4 Scanning electron microscopy and energy dispersive X-ray analysis (SEM)

The selected RM-LDH products were further analysed using Scanning Electron Microscopy (SEM) as presented in Chapter 4 & 6. The samples were coated with gold and their surface morphologies and elemental compositions were investigated by a FEI Nova NanoSEM FEG instrument with energy dispersive x-ray (EDX) at 5 kV or at 10 kV (Figure 3.17). The SEM images taken were at 500, 1000 and 2500x magnifications.

Figure 3.17 FEI Nova NanoSEM FEG instrument and computer desk

3.3.3.5 Brunauer–Emmett–Teller (BET) analysis

The Brunauer–Emmett–Teller (BET) surface area of the samples were measured by a Tristar II 3020 (Micromeritics) instrument. The t-Plot micropore area and external surface area could be determined. BJH adsorption/ desorption pore distribution reports were obtained, so that the pore size distribution curve could be plotted.

Chapter 4 Synthesis Routes of RM-LDHs Using Red Mud

This chapter investigates the layered double hydroxide (LDH) synthetic methods starting with the two red muds obtained, mainly AOS RM and IRM. The chapter starts with introducing the mineralogical compositions of the raw materials. Afterwards, four different scenarios are put forward and the influences of pre-treatment and process variables are investigated. This chapter also identifies the basic physiochemical characteristics of as-synthesised products and as a result the optimum scenario and corresponding parameters are selected. Various characterisation tools are then employed to evaluate if the selected RM-LDHs meet the 'golden rules' of typical LDHs. Finally, other physical features such as particle size, BET surface area and magnetic behaviour are studied and compared with commercial Mg-Al LDH.

4.1 Characterisation of the Original Red Mud

4.1.1 AOS Red Mud

4.1.1.1 X-ray diffraction analysis

In combination with the XRF data (Table 3.2), the following minerals and compounds were identified in the original AOS RM by XRD analysis (Figure 4.1a): the iron minerals hematite [Fe_2O_3] and goethite [FeO(OH)], the aluminum minerals gibbsite [$Al(OH)_3$], and the sodium compounds cancrinite and/ or sodalite [$Na_4(Si_3Al_3)O_{12}Cl$]. These mineralogical results show good agreement with XRD patterns in the literature, e.g. that presented by Sahu, Patel and Ray (2010), as shown in Figure 4.1c. An amorphous content was detected from the high background noise, which could be also due to the iron fluorescence. Rivas Mercury *et al.* (2011) suggested that 10-25% of red mud consists of amorphous oxides. The amorphous phase may be attributed to amorphous iron oxide, aluminum oxide, silicon oxide and sometimes desilication product (DSP).

Figure 4.1b confirms that after being treated at 650°C for 4 h, goethite and gibbsite phase disappeared from the AOS CRM. Furthermore, the intensity of hematite [Fe_2O_3] peaks was increased, which suggests that phase transformation has taken place. Based on the study of Rivas Mercury *et al.*(2011), gibbsite is no longer observed when the temperature reached 350°C. Quartz [SiO_2] and rutile [TiO_2] were unaffected under this heating condition.

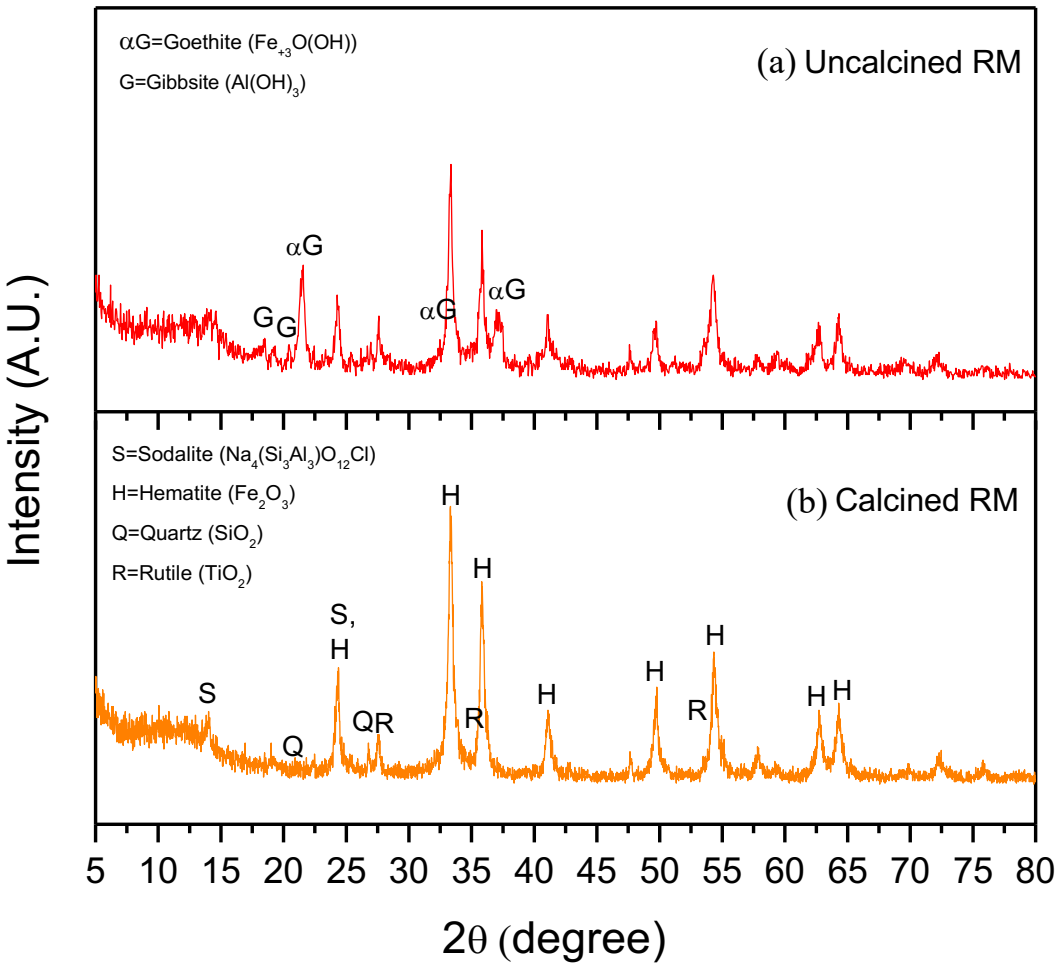

(c) RM in the literature

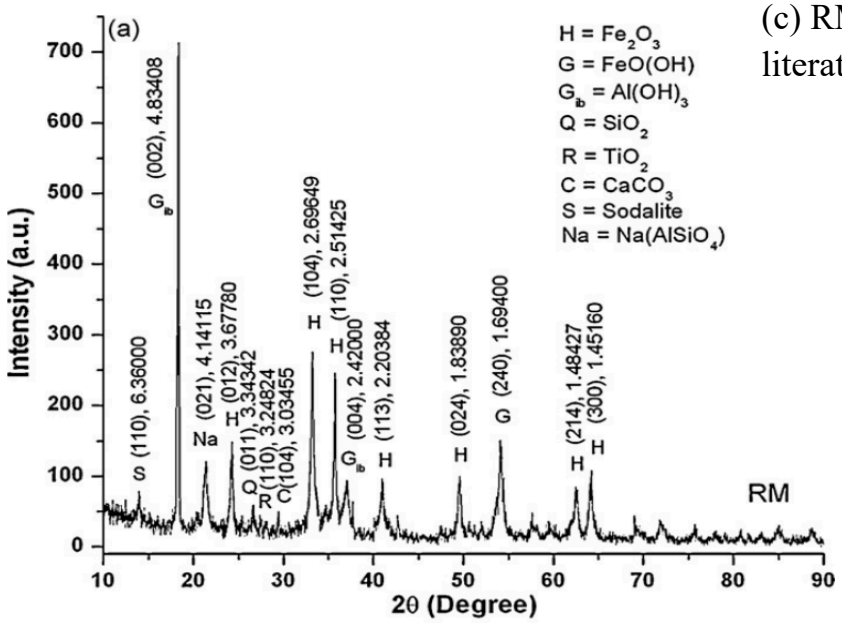

Figure 4.1 Powder XRD patterns of the (a) AOS RM, (b) AOS CRM (c) RM from R&D Laboratory of NALCO, Damanjodi Orissa, India; characterised by Sahu, Patel and Ray (2010)

4.1.1.2 Thermogravimetric analysis

The thermal gravimetric analysis for AOS RM samples before and after calcination are given in Figure 4.2. AOS RM exhibits three main stages of weight loss (TGA curve) and three endotherm peaks (DTG curve):

(i) The 1st stage in the range of 20-150°C was attributed to the evaporation of physically adsorbed water.

(ii) The 2nd weight loss (150-400°C) represented 6.0% and is due to the loss of structural/chemically adsorbed water from desilication products (sodalite, cancrinite, etc.) (Pascual *et al.*, 2009). Its corresponding endotherm peak at 289°C is associated with the dehydration of gibbsite [γ-$Al(OH)_3$] and goethite [FeO(OH)] to form boehmite [γ-AlOOH] and hematite [Fe_2O_3] respectively (Agatzini-Leonardou *et al.*, 2008; Rivas Mercury *et al.*, 2011).

(iii) The 3rd stage between 400-600°C is associated with the transformation of boehmite (γ-AlOOH) or polymorphic phase, diaspore (α-AlOOH) to transition alumina (Pascual *et al.*, 2009). As shown on the DTG curve, the 2nd endothermic peak at 464°C corresponds to the dehydroxylation of boehmite (Atasoy, 2005; Pascual *et al.*, 2009). The next endothermic peak at 578°C is likely associated with the α-β transformation of quartz (Raman and Nedungadi, 1940; Atasoy, 2005), when quartz is a major oxide observed in red mud sample.

(iv) Finally, the minor weight loss occurred above 650°C, corresponding to the decomposition of calcium carbonate (Borra *et al.*, 2015). In addition, a few endothermic reactions may also initiate between 600-1000°C (Pascual *et al.*, 2009), depending on the composition and silicate content, for examples:

$$Na_2CO_3 + CaCO_3 \longrightarrow Na_2Ca(CO_3)_2 \quad (4.1)$$

$$[Na_2O \cdot 3CaO \cdot 6SiO_2] + [Na_2O \cdot 2SiO_2] \longrightarrow [Na_2O \cdot 2CaO \cdot 3SiO_2] + liquidus \quad (4.2)$$

On the other hand, no distinct endotherm peak could be identified from the thermal decomposition profile for the AOS CRM (Figure 4.2). The weight loss started with free water evaporation of about 2.1%. The free water content of the AOS CRM is similar to the original AOS RM. It can be observed that the main weight loss ended at 300°C, although a very steady weight loss continued till 1000°C. These fluctuations at very high temperature can be assigned to the amorphous decomposition and to the formation of new silicates (Pascual *et al.*,

2009; Rivas Mercury *et al.*, 2011). No featured endotherm peaks for gibbsite and goethite are observed in the DTG curve. This is confirmed by the disappearance of gibbsite and goethite peaks for AOS CRM in the XRD study (Figure 4.1).

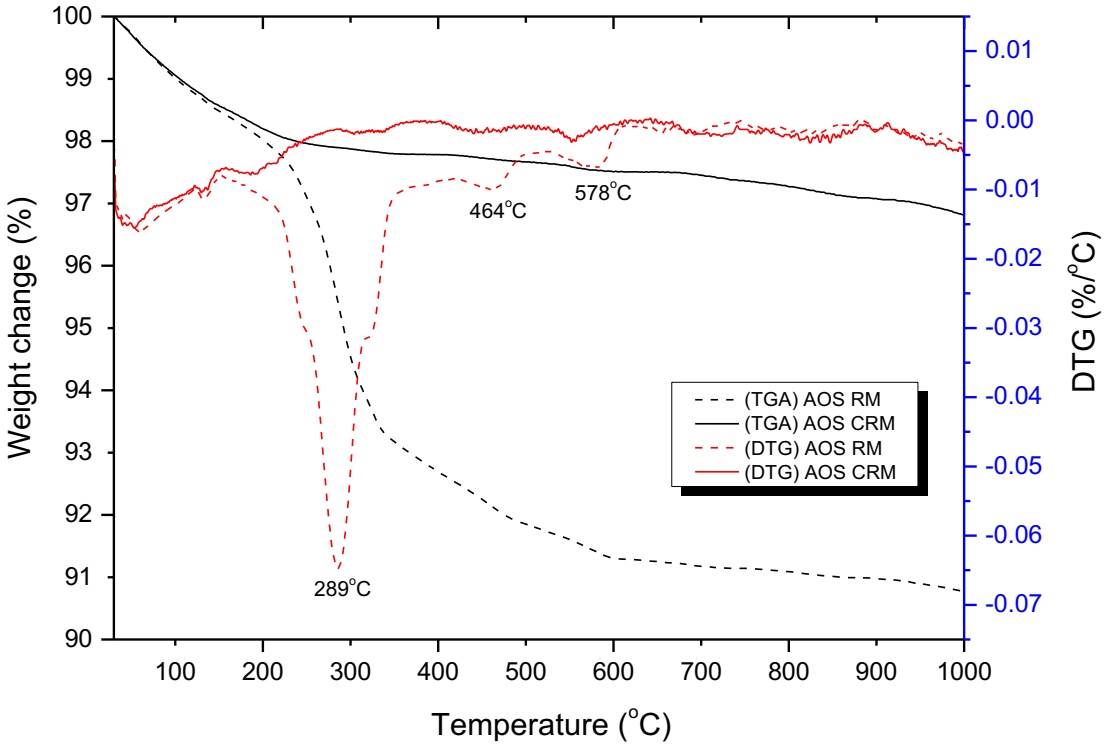

Figure 4.2 TGA-DTG curves of the raw AOS RM and AOS CRM

The weight loss recorded before and after the calcination process was 1.14 g of 15.01 g, which was 7.6% of the total weight. The XRF results (Table 3.2) reveals that the mineralogical composition of the AOS RM is 58.5% of Fe_2O_3 and 11.6% of Al_2O_3. If one takes all the iron oxide and aluminium oxide as goethite and gibbsite and assumes that all the goethite and gibbsite had transformed to hematite and transition alumina after calcination, then the mass fractions of Fe and Al in the AOS CRM would be 44.5% and 6.7%, respectively.

4.1.2 Ireland Red Mud (IRM)

4.1.2.1 X-ray diffraction analysis

XRD analysis of the original IRM (Figure 4.3a) was able to identify the following mineral phases: hematite [Fe_2O_3], goethite [FeO(OH), gibbsite [$Al(OH)_3$] and boehmite [AlO(OH)], cancrinite and/or sodalite [$Na_4(Si_3Al_3)O_{12}Cl$], quartz [SiO_2], calcite [$CaCO_3$] and rutile [TiO_2]. Similar to the AOS RM, an amorphous content is detected based on the high background noise. However, the gibbsite and boehmite content are considerably higher than that of the AOS RM. Those identified components are in line with the phases reported for red mud originated in various locations (Agatzini-Leonardou *et al.*, 2008; Rivas Mercury *et al.*, 2011; Borra *et al.*, 2015).

According to Figure 4.3b, the calcined IRM (Cal-IRM) mainly contains diiron oxide [Fe_2O_3], perovskite [$CaTiO_3$], while cancrinite and/or sodalite, quartz (SiO_2) and rutile (TiO_2) remained. Upon calcination at 650°C, gibbsite, boehmite, goethite and calcite are no longer observed. However, XRD cannot identify the nearly amorphous Al_2O_3 and AlO(OH) (Xu and Lu, 2005).

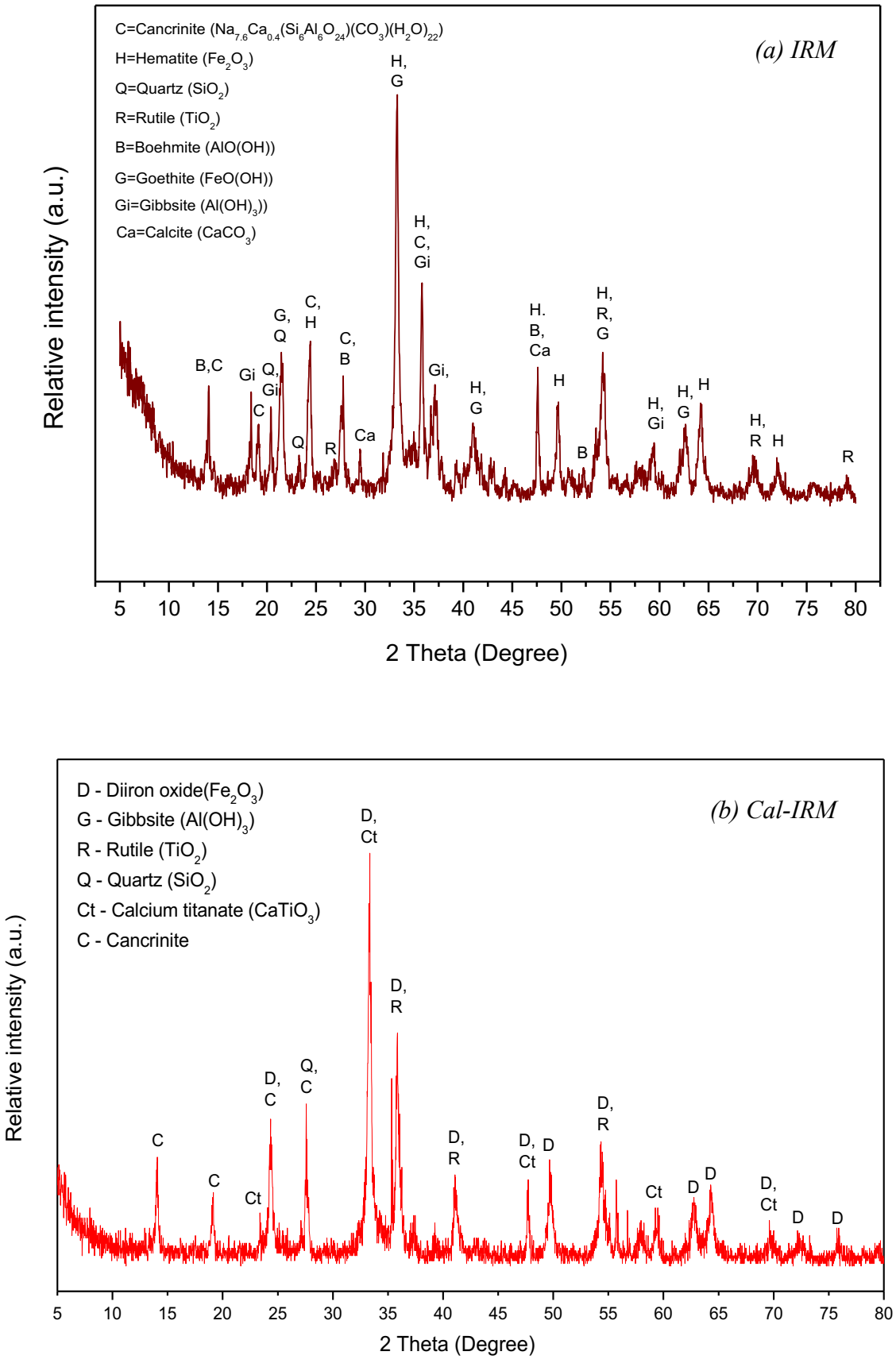

Figure 4.3 Powder XRD patterns of (a) raw IRM and (b) Cal-IRM

4.1.2.2 Thermogravimetric analysis

The thermal gravimetric analysis for IRM samples before and after calcination are shown in Figure 4.4. IRM presents three main steps of weight loss (TGA curve) and four endotherm peaks (DSG curve):

(i) The 1st step in the range of 20-150°C is attributed to the evaporation of physically adsorbed water, representing about 1.0 wt%.

(ii) The 2nd weight loss (150-400°C) accounts for 6.0 wt% and is due to the evaporation of chemically adsorbed water from desilication products (sodalite, cancrinite, etc.) (Pascual *et al.*, 2009). The endotherm peak at 269°C corresponds to the transformation of gibbsite [$Al(OH)_3$] to alumina; the consecutive peaks at 309°C and 351°C are associated to the dehydration of goethite [FeO(OH)] and perhaps Al-goethite [α-(Fe,Al)OOH] (overlap effects), when goethite contains aluminium as an isomorphous substitution (Laskou, Margomenou-Leonidopoulou and Balek, 2006; Rivas Mercury *et al.*, 2011).

(iii) During the 3rd step (400-700°C), there is no endotherm peak observed between 450-550°C (boehmite decomposition). Therefore, it implies that gibbsite went through the reaction pathway to form cryptocrystalline kappa alumina (Whittington and Ilievski, 2004; Gan, Madsen and Hockridge, 2009), as follows:

$$2Al(OH)_3 \longrightarrow Al_2O_3\text{-}\chi + 3H_2O \longrightarrow Al_2O_3\text{-}\kappa \quad (4.3)$$

Different from AOS RM, an endotherm peak appeared at 644°C on the DTG curve of IRM. It could be related to calcite decomposition, since calcite is detected in XRD. As Laskou, Margomenou-Leonidopoulou and Balek (2006) suggested, it may also be ascribed to the dehydroxylation of Mg-rich chamosite.

(v) The weight loss above 700°C, is attributed to the continuous dehydroxylation and transformation of Bayer desilication products, e.g. kaolinitic clay (Rivas Mercury *et al.*, 2011). Furthermore, the decomposed calcite is able to react with titanium oxide between 560°C and 720°C (Pascual *et al.*, 2009), as follows:

$$CaO + TiO_2 \longrightarrow CaTiO_3 \quad (4.4)$$

Calcium titanite is observed from the XRD curve of Cal-IRM (Figure 4.3). On the other hand, it is not present in the original IRM. Therefore, it can be confirmed that reaction (4.4) occurred during IRM calcination.

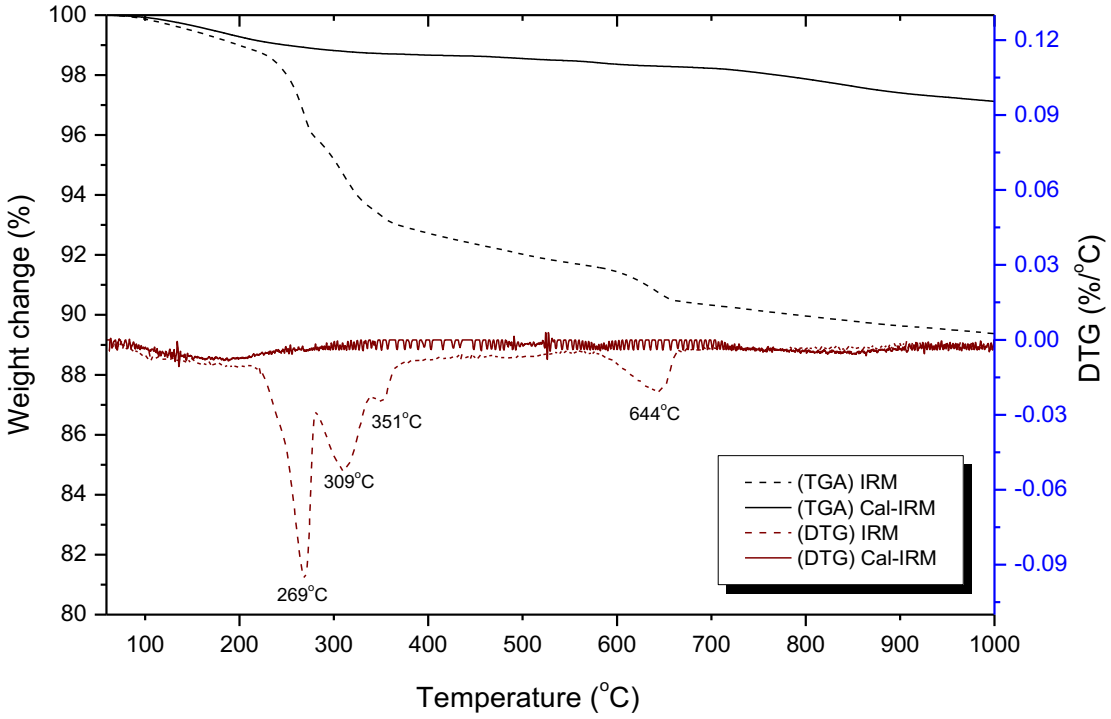

Figure 4.4 TGA-DTG curves of raw IRM and Cal-IRM

For Cal-IRM, less than 3.0 % total weight loss is detected on the TG plot. There appears no significant endotherm peak in the temperature range of 150-650°C, indicating that Al-OH and Fe-OH groups no longer exist, i.e. gibbsite and goethite are not presented in the Cal-IRM sample. It is in agreement with the previous observation from the XRD analysis of Cal-IRM (Figure 4.3), in which the gibbsite and goethite peaks disappeared after calcination at 650°C.

Taking into account the data set of IRM's XRF analysis (Table 3.2), the mass fraction of Fe_2O_3 and Al_2O_3 are 39.47% and 16.36% respectively. The weight loss recorded before and after the calcination process was 2.02 g of 25.01 g, which was 8.0% of the total weight. Again, assuming all the Fe and Al components have transformed to hematite and transition alumina after calcination, the Fe and Al account for 30.0% and 9.4%, respectively.

4.1.2.3 FT-IR spectroscopy

The FT-IR spectra of IRM and Cal-IRM are displayed in Figure 4.5. The positions of the absorption bands for both samples are nearly the same. A broad band at ~3240-3040 cm^{-1} and a weak band at ~1640 cm^{-1} are observed, which are assigned to O-H stretching vibrations and H-O-H bending vibrations inside the aluminosilicate structure, respectively (Castaldi *et al.*, 2008). The adsorption band at ~1502 cm^{-1} is linked with stretching vibrations of C=O,

confirmed the presence of chemisorbed CO_3^{2-} groups in fresh IRM and Cal-IRM (Sahu, R. K. Patel and Ray, 2010). Zhao *et al.* (2004) pointed out the peak around 1400 cm^{-1} could be attributed to nitrate, which might be present in both cancrinite and sodalite. The strong deformations bands at ~993 and ~1112 cm^{-1} are attributed to Si-O and Si(Al)-O vibration (Castaldi *et al.*, 2010), while bands at ~808 cm^{-1} correspond to O-Si-O (Sahu, R. K. Patel and Ray, 2010). The peaks at ~680 and ~610 cm^{-1} are characteristic bending of Si-O-Al (Barnes, Addai-Mensah and Gerson, 1999). Intensities of these peaks related to Si are not decreased in Cal-IRM, suggesting calcination does not alter mineral phases like cancrinite, sodalite and quartz. Overall, the spectra support the findings in the XRD analyses. However, FT-IR measurement cannot differentiate the mineral transformations of Fe, Al oxides (Bhatnagar *et al.*, 2011).

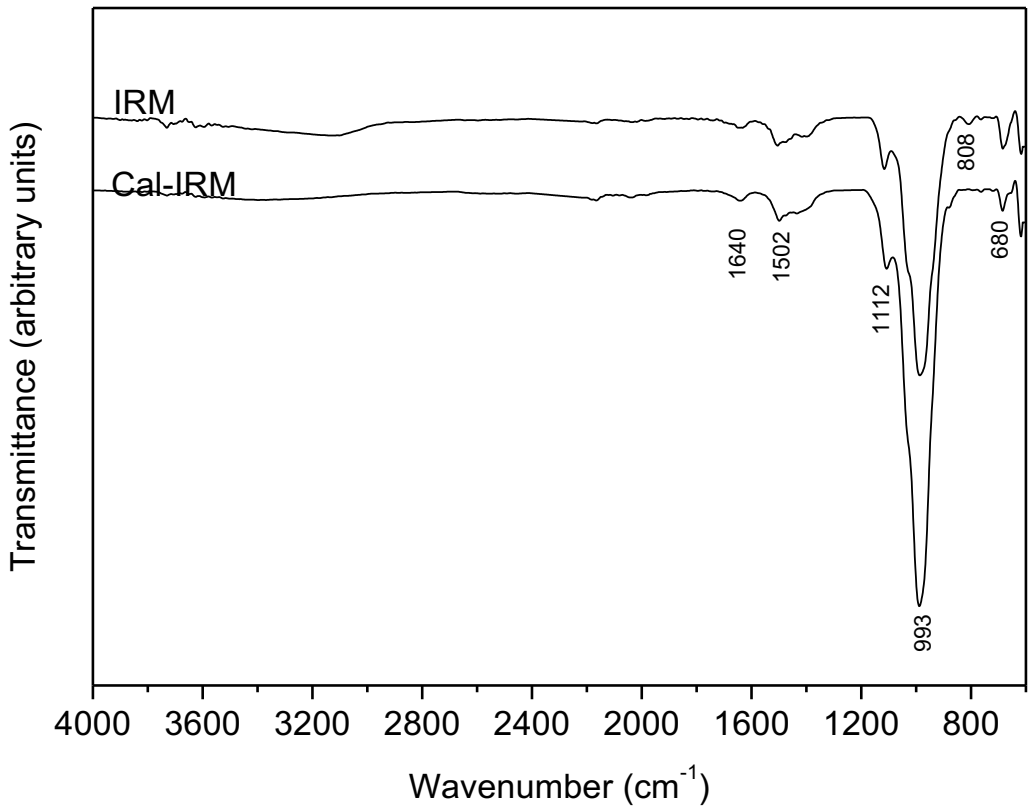

Figure 4.5 FT-IR of raw IRM and Cal-IRM

4.1.2.4 Particle Size

The IRM samples before and after calcination were measured for particle size distribution. Figure 4.6 shows that most IRM particles have a diameter between 0.2 and 0.05 μm, and

more than 90% of them are smaller than 0.05 mm, which well agrees with Khairul, Zanganeh and Moghtaderi (2019). The average particle size of IRM and its resulting calcined IRM (Cal-IRM) are 0.12 μm and 0.10 μm respectively; both are clay-dominated particles (Six *et al.*, 2000). The particle size distribution of Cal-IRM became slightly wider and smaller particles (less than 0.05 μm) increased at 650°C, if compared with original IRM. That indicates that calcination is likely to reduce the particle size of red mud, due to the phase transition of goethite to hematite and gibbsite to alumina.

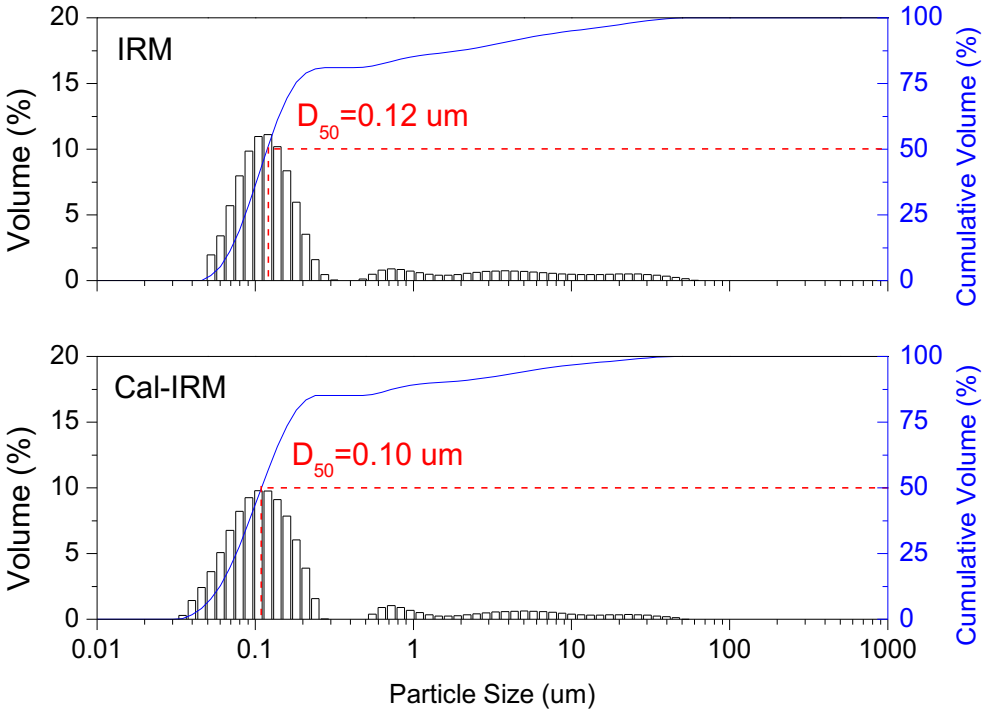

Figure 4.6 Particle size distributions of IRM and Cal-IRM, calcination 650°C for 4 h

4.1.2.5 BET Surface Area

The BET analyses of IRM and Cal-IRM obtained by N_2 adsorption are shown in Table 4.1 and the pore size distributions are drawn comparatively in Figure 4.7. Nitrogen sorption porosimetry method is able to provide information for pores with the range of 2-200 nm. The BET analyses show that IRM (15.8 m^2/g) presents lower surface area than Cal-IRM (24.1 m^2/g). The measured values are comparable with previous reports (Grafe, Power and Klauber, 2009; Ujaczki *et al.*, 2018). This difference in surface area can be interpreted by the removal of the intercalated water and carbon dioxide from IRM leading to the formation of channels and pores or can be partially explained by the variation in particle size (Figure 4.6).

Table 4.1 Surface area and pore size of IRM and Cal-IRM (at 650°C for 4 h*)*

	BET surface area S_{BET} (m^2/g)	t-plot micropore area (m^2/g)	t-plot external surface area (m^2/g)	Average pore width (nm)	Total pore volume (cm^3/g)
IRM	15.8	3.69	12.1	11.31	0.045
Cal-IRM	24.1	3.14	21.0	8.98	0.054

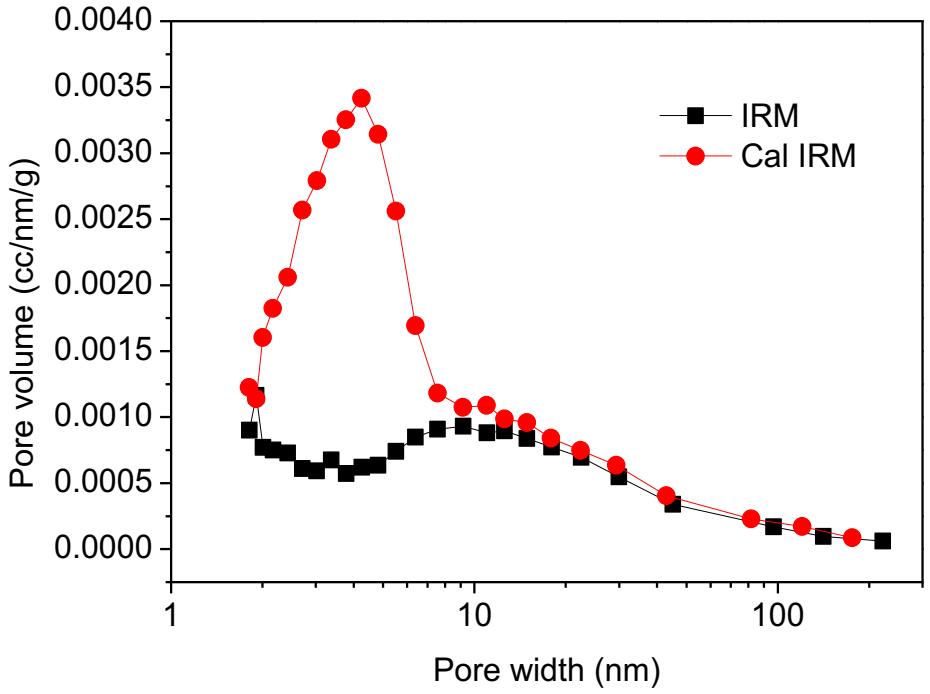

Figure 4.7 Pore size distribution of IRM and Cal-IRM

After calcination at 650°C, the total pore volume increased slightly from 0.045 to 0.054 cm^3/g, however, the average pore width decreased from 11.31 to 8.98 nm (see Table 4.1). The order of increase of the average pore size is reversed with S_{BET}. This suggests that the increase in the S_{BET} of IRM upon calcination was not resulted from the increase of pore size but attributed to the increase of pore volume or pore population. The mesoporous structures in IRM (2-50 nm) present very flat pore volumes between 0.0003 to 0.0008 cc/nm/g (Lawrence *et al.*, 2017). On the other hand, a narrower pore size distribution was observed for Cal-IRM. The mesopores with diameters 2-10 nm exhibit significantly larger pore volumes, which are in a range of 0.0010-0.0035 cc/nm/g. The change in the pore size distribution partially explains for the increase on the surface area after calcination.

4.1.2.6 Morphology Characterisation

Scanning electron microscopy (SEM) images of IRM and Cal-IRM were taken in order to understand their surface structures. From the SEM micrography showed in Figure 4.8, IRM particles are poorly crystallised and are constituted by agglomerates mostly <2.0 μm. The aggregates are formed by fine particles of different sizes and irregular shapes. The small, homogeneously distributed granules may correspond to iron and titanium (Agatzini-Leonardou *et al.*, 2008).

As seen in Figure 4.9 (a-b), the overall porous structure of Cal-IRM is largely determined by the nature of the initial IRM feedstock. After calcination at 650°C, the percentage of small aggregates that have a diameter less than 2.0 μm decreased, while aggregates >5.0 μm increased according to Figure 4.9a. This change is associated with the dehydration of goethite to hematite (Antunes *et al.*, 2012). Furthermore, a few darker pores could be observed after calcination, suggesting that deeper channels or craters may form during the thermal decomposition of CO_3^{2-} from IRM.

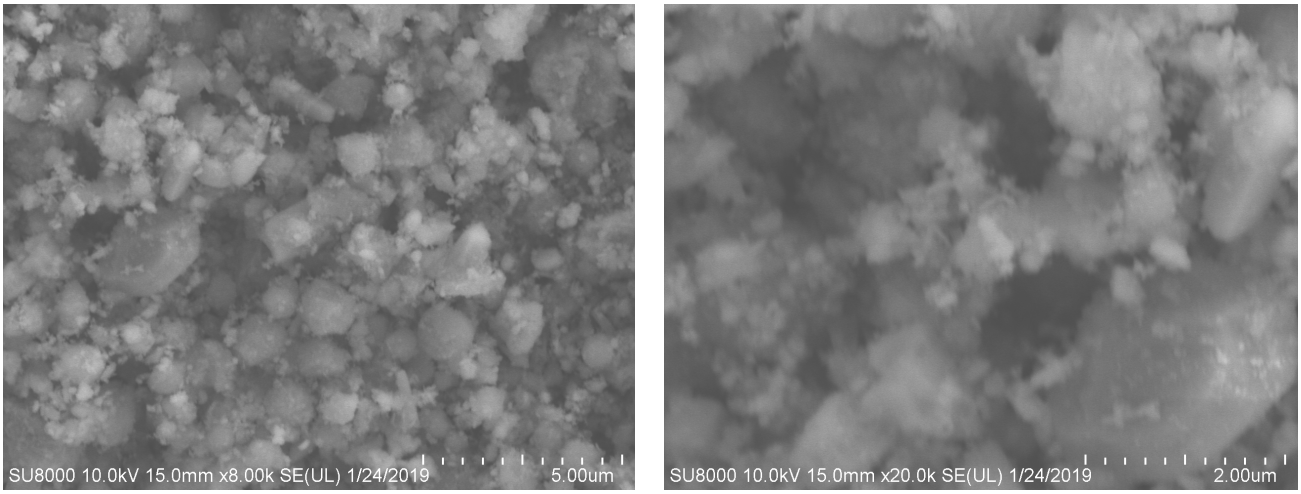

(a) *(b)*

Figure 4.8 Scanning electron microscopy images of (a-b) raw IRM

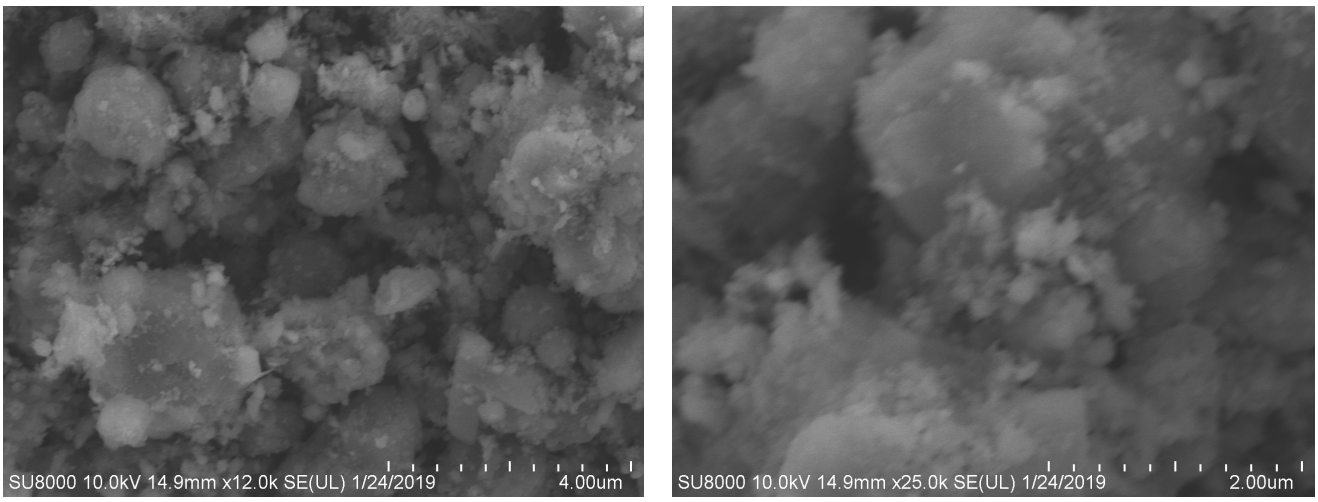

(a) *(b)*

Figure 4.9 Scanning electron microscopy images of (a-b) Cal-IRM

4.2 Synthesis process selection

Following the discussion in Section 2.3, the present section aims to investigate and develop a modified co-precipitation or salt-oxide method for RM-LDH synthesis. RM materials were directly employed as a source of metal oxides. As outlined in Figure 2.42 as well as in Section 3.2.2, AOS RM involves in Scenario I & II process, while IRM participates in Scenario III & IV process. The proposed procedures are described in schemes in this section. According to Section 2.3.4, thermal or mechanochemical pre-treatments have been considered; and a number of variables including grinding, dispersion, M^{II}/M^{III} ratio, intercalated anions, aging time have been assessed.

4.2.1 Scenario I - AOS RM with $MgCl_2$

4.2.1.1 Synthesis process

Scenario I process is illustrated in Figure 4.10 and Table 4.2, which imitates the mechanism of seawater neutralisation of RM waste, as aforementioned in Section 2.1.5. The traditional RM seawater neutralisation involves a complex precipitates system, where more than 15 mineral components were identified by Hanahan *et al.* (2004). McConchie, Clark and Davies-McConchie (2002) adopted brines with high concentrated Ca and Mg to neutralise RM slurry, where the Ca:Mg ratio was adjusted to favour particular mineral precipitates, termed Bauxsol^{TM}. Brucite [$Mg(OH)_2$] and hydrotalcite [$Mg_6Al_2CO_3(OH)_{16}$] were the main solids obtained in the reaction, while gibbsite [$Al(OH)_3$], hydrocalumite [$Ca_2Al(OH)_7{\cdot}3H_2O$] and p-aluminohydrocalcite [$CaAl_2(CO_3)_2(OH)_4{\cdot}3H_2O$] were also found in the Bauxsol^{TM} mixure

(McConchie, Clark and Davies-McConchie, 2006; Clark, Johnston and Reichelt-Brushett, 2015). The associated chemical reactions can be expressed below as Eqn. (4.5)-(4.8).

<Hydrotalcite>

$$6MgCl_{2\,(aq)} + 2[Al(OH)_4]^-{}_{(aq)} + 8OH^-{}_{(aq)} + {CO_3}^{2-}{}_{(aq)} + 12Na^+{}_{(aq)} \rightarrow Mg_6Al_2(CO_3)(OH)_{16} \cdot 4H_2O + 12NaCl_{(aq)} \quad (4.5)$$

$$8MgCl_{2\,(aq)} + 2[Al(OH)_4]^-{}_{(aq)} + 12OH^-{}_{(aq)} + 1/2{CO_3}^{2-}{}_{(aq)} + 15Na^+{}_{(aq)} \rightarrow Mg_8Al_2Cl(CO_3)_{0.5}(OH)_{20} \cdot 4H_2O + 15NaCl_{(aq)} \quad (4.6)$$

<Para-aluminohydrocalcite>

$$CaCl_{2\,(aq)} + 2[Al(OH)_4]^-{}_{(aq)} + 2{CO_3}^{2-}{}_{(aq)} + 2Na^+{}_{(aq)} \rightarrow CaAl_2(CO_3)_2(OH)_4 \cdot 3H_2O + 4OH^-{}_{(aq)} + 2NaCl_{(aq)} \quad (4.7)$$

<Carbonate in solution>

$$CO_2 + 2Na^+ + 2OH^- \rightarrow 2Na^+ + {CO_3}^{2-} + H_2O \quad (4.8)$$

Table 4.2 Proposed Scenario I experimental parameters

Parameters	Value
$MgCl_2$: RM	3:1 or 4:1 (molar ratio)
L/S ratio	20
Aging	70°C, 72 h
Magnetic stirring speed	200 (rpm)
Wash of precipitates	3 times
Drying	80°C, overnight

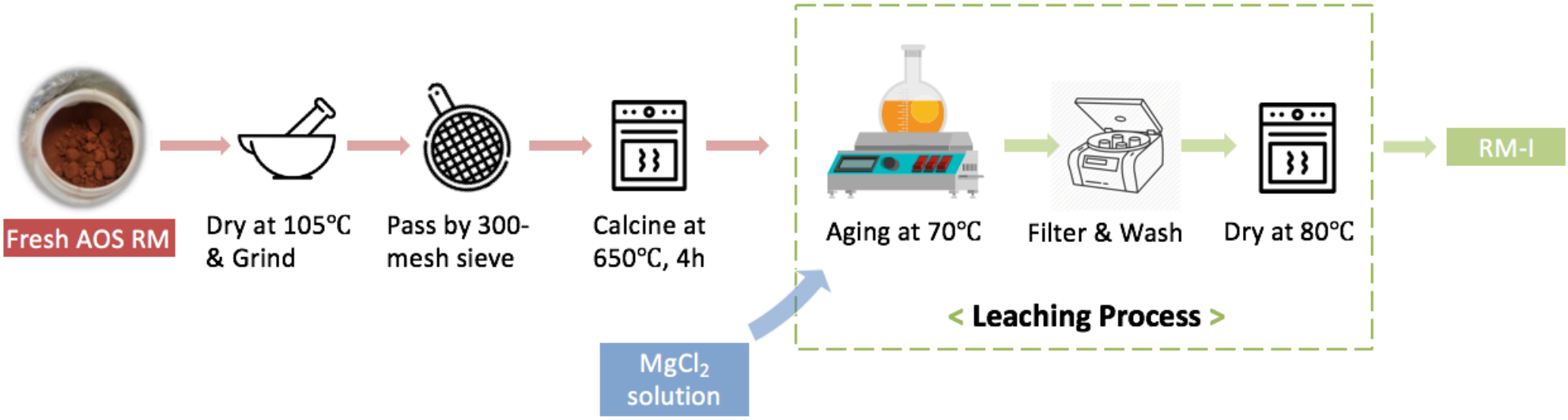

Figure 4.10 Proposed Scenario I synthesis process

It is known that certain amount of carbonate (CO_3^{2-}), aluminate ($Al(OH)_4^-$) and free hydroxide (OH^-) exist in the liquid phase of 'fresh' red mud (Grafe, Power and Klauber, 2009). Through the addition of brines to the RM liquor, the Mg/Al molar ratio is controlled between 2 and 5 (Paikaray and Hendry, 2014). A constant pH (9-11) is normally maintained by occasionally adding NaOH during the synthesis. Depending on the pH and the Mg/Al ratio, two types of LDHs are reported to form, which are $Mg_8Al_2(OH)_{12}(CO_3^{2-},SO_4^{2-})\cdot$ and $Mg_6Al_2(OH)_{12}(CO_3^{2-},SO_4^{2-})\cdot$ (Palmer, Frost and Nguyen, 2009; Palmer and Frost, 2011; Couperthwaite *et al.*, 2014). CO_3^{2-} and SO_4^{2-} are the dominant anions intercalated into the interlayer. Optimising the synthesis conditions and increasing the aging time could encourage the product to be more crystalline and homogeneous (Labajos, Rives and Ulibarri, 1992). The brines neutralisation process resembles to the co-precipitation method used for the synthesis of hydrotalcite-like compounds.

The alkalinity of RM liquid phase has been eliminated relatively quickly via the precipitation alkalinity OH^-, CO_3^{2-} and $Al(OH)_4^-$, which leads to a pH of approximately 8.5 to 9.0 (Hanahan *et al.*, 2004; Kirwan *et al.*, 2013; Rai *et al.*, 2013). The pH variations are recorded in Figure 4.11.

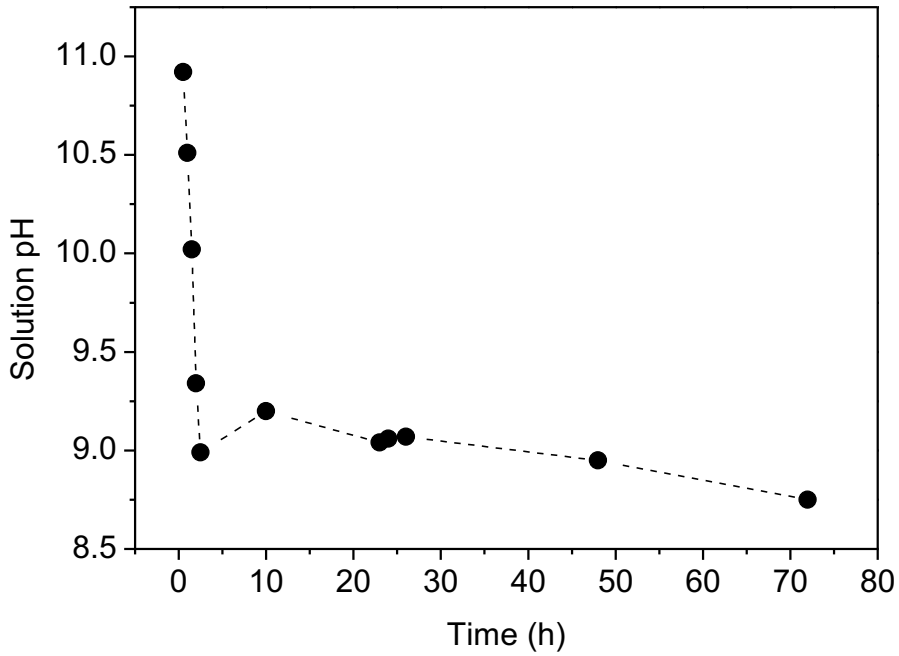

Figure 4.11 The pH of Scenario I reaction measured after the addition of $MgCL_2$

4.2.1.2 Products Obtained

Figure 4.12 displays the XRD pattern of the as-prepared scenario I RM products (RM-I). Corresponding to the basal spacing reported in the literature by Lv *et al.* (2006), Islam and Patel (2009) and Yue *et al.* (2017), the (003) plane of Cl^- intercalated LDH often exhibits a peak in the region of 2θ = 11.0-11.8° (see also Figure 2.29-30). Accordingly, the typical LDH peaks with Cl^- species cannot be identified, suggesting layered structure has not formed or exists in minor content. This is probably due to the lack of alkalinity in the suspension. Since the pH (see Figure 4.11) stabilised at ~9.0 after 72 h leaching, Al may not all exhibit as $[Al(OH)_4]^-$. As a result, the reaction (4.5) or (4.6) was difficult to move forward. The diffractogram was analysed with X'Pert High Score software to search for different phases. The peaks near 9.5°, 14.0° and 30.0° are likely attributed to hydromagnesite $[Mg_4(OH)_2(CO_3)_3{\cdot}3H_2O]$, whose pattern is denoted as 'y' in Figure 4.12. Hematite and the silicate compound howieite are the main mineral phases responsible for the other peaks. Different ratios of $MgCl_2$ to RM does not put considerable effects on the mineral composition of final products. Compared with original AOS CRM (Figure 4.1), the crystallinity of RM-I is not enhanced, whereas the amorphous content is still high.

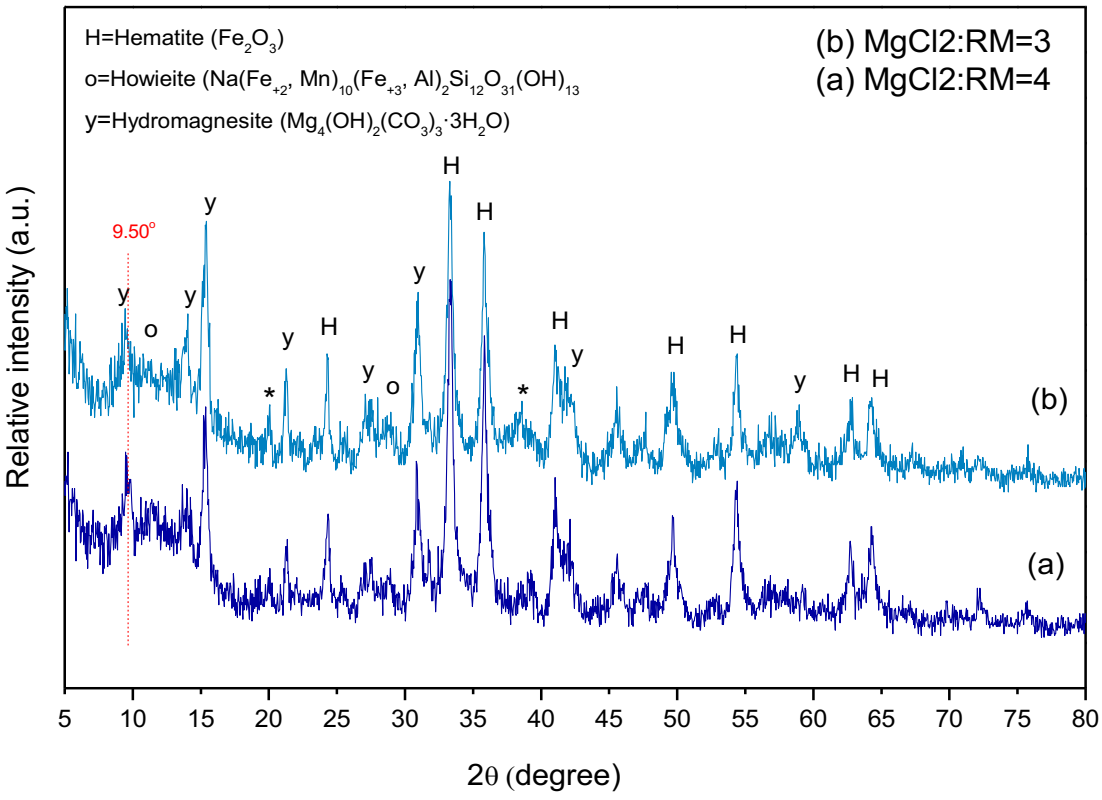

Figure 4.12 Powder XRD patterns of the RM-I products at L/S=20 where (a) $MgCl_2$:RM=3:1, (b) $MgCl_2$:RM=4:1; (*) Brucite $Mg(OH)_2$

4.2.2 Scenario II – AOS RM with reactive MgO

4.2.2.1 Synthesis process

A modified calcination-rehydration method was proposed to produce Mg/Al/Fe-LDHs from red mud (RM) and reactive MgO. The reaction principle is similar to the dispersion-precipitation method or to the salt-oxide method, involving dissociation, hydrolysis and peptization of the insoluble oxides, as explained in Table 2.7 (Turner and Brydon, 1962; Mascolo and Marino, 1980; F. Zhang *et al.*, 2014). The synthetic process is illustrated in Figure 4.14, the reaction parameters and pH are recorded in Table 4.3 and Figure 4.13, respectively. The AOS RM was calcined either individually or together with MgO at 650°C for 4 h. Then the resultant mixture was added by Na_2CO_3 solution. Generally, the suspension was left for aging at 70°C for 72 h. The obtained precipitate was then filtered, washed with distilled water, and dried at 80°C overnight. The ratio between MgO and RM was adjusted, and the corresponding products were compared.

Table 4.3 Proposed Scenario II experimental parameters

Parameters	Value
MgO: RM	2:1 to 4:1 (molar ratio)
L/S ratio	20 or 40
Na_2CO_2 solution	$[CO_3^{2-}]$: [Al+Fe] = 2.0
Aging	70°C, 72 h
Magnetic stirring speed	200 (rpm)
Wash of precipitates	3 times
Drying	80°C, overnight

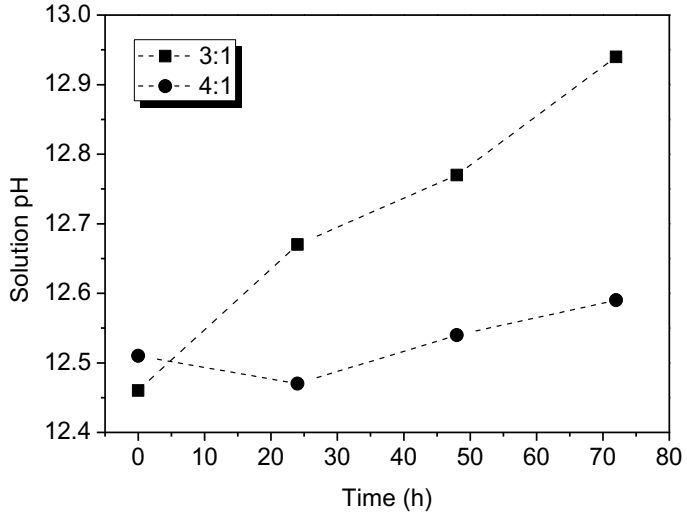

Figure 4.13 The pH of Scenario II reaction via Route (a) while L/S=20, MgO:RM=3:1 or 4:1

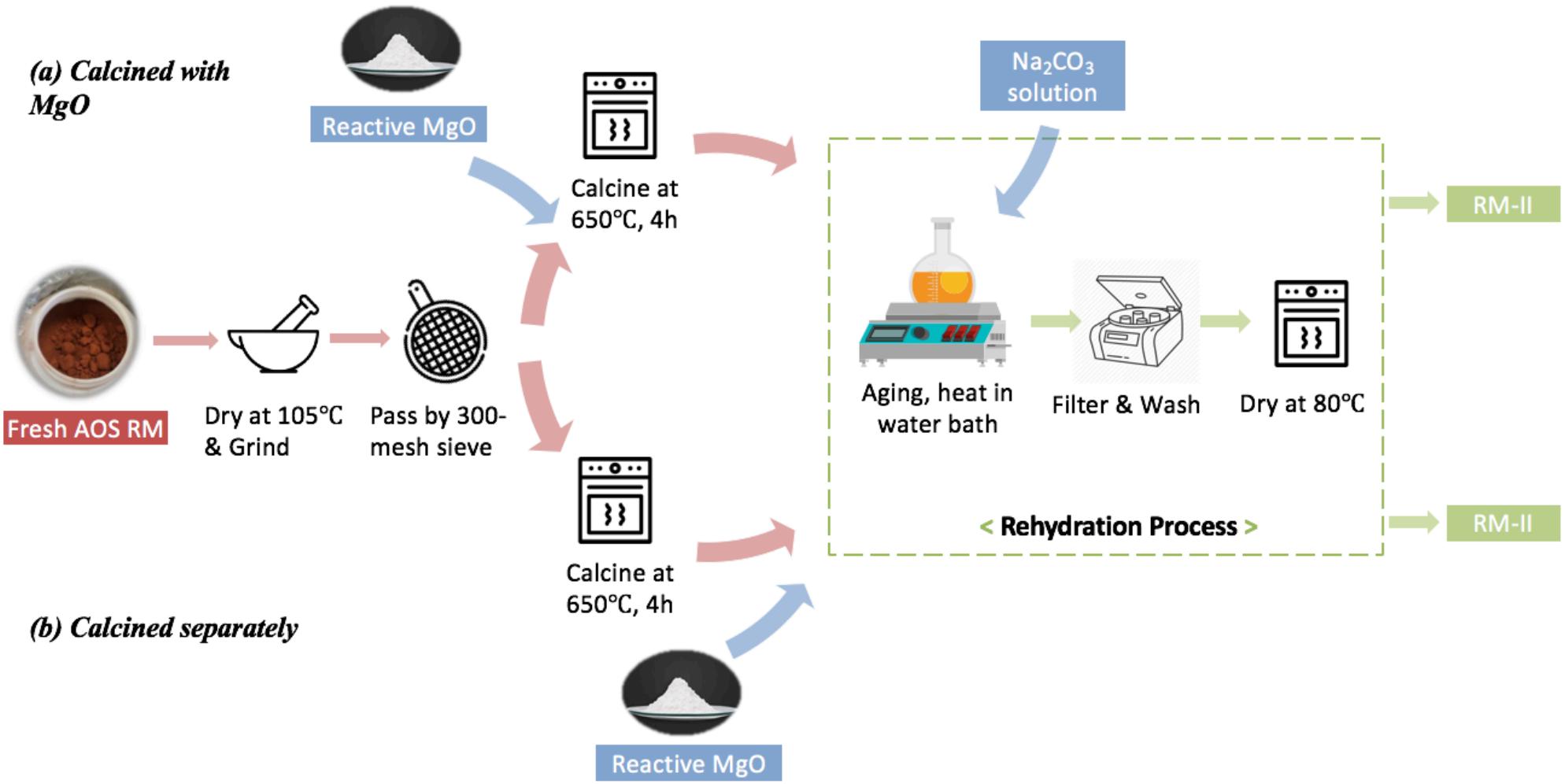

Figure 4.14 Proposed Scenario II synthesis process while RM (a) calcined with MgO, (b) calcined separately

4.2.2.2 Products obtained

Figure 4.15 presents the XRD diagrams of the calcined (MgO + RM) mixtures with different ratios of MgO to RM. It clearly demonstrates that no LDH phase could be observed before the leaching process happened. This is taken as a blank comparison to that of RM-II products.

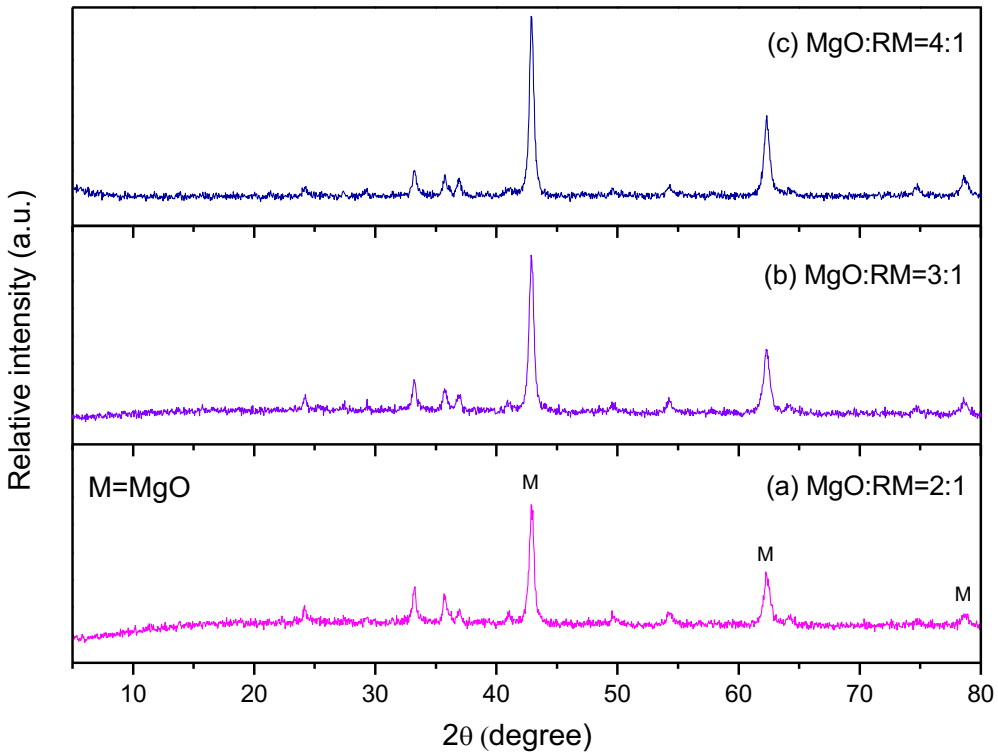

Figure 4.15 Powder XRD patterns of the calcined (RM + MgO) mixture before leaching

The XRD powder patterns of the scenario II RM products (RM-II) from Route (a) with different liquid-to-solid and Mg/(Al+Fe) ratios are presented in Figure 4.16, and the lattice parameters are provided in Table 4.4. The (003), (006), (110) reflections are in good agreement with characteristic layered structures (Constantino and Pinnavaia, 1995), indicating that crystalline-layered LDHs have formed. The $d_{(003)}$ basal space are within the reference values (7.53-7.96 Å) of CO_3^{2-}-bearing interlayer phases, which confirms the intercalated ions are primarily CO_3^{2-}. Given the complexity of RM, a large amount of impurities can still be observed in the as-synthesised RM-II. As shown in Figure 4.16, brucite [$Mg(OH)_2$] and the aluminosilicate contents of RM remained in the product.

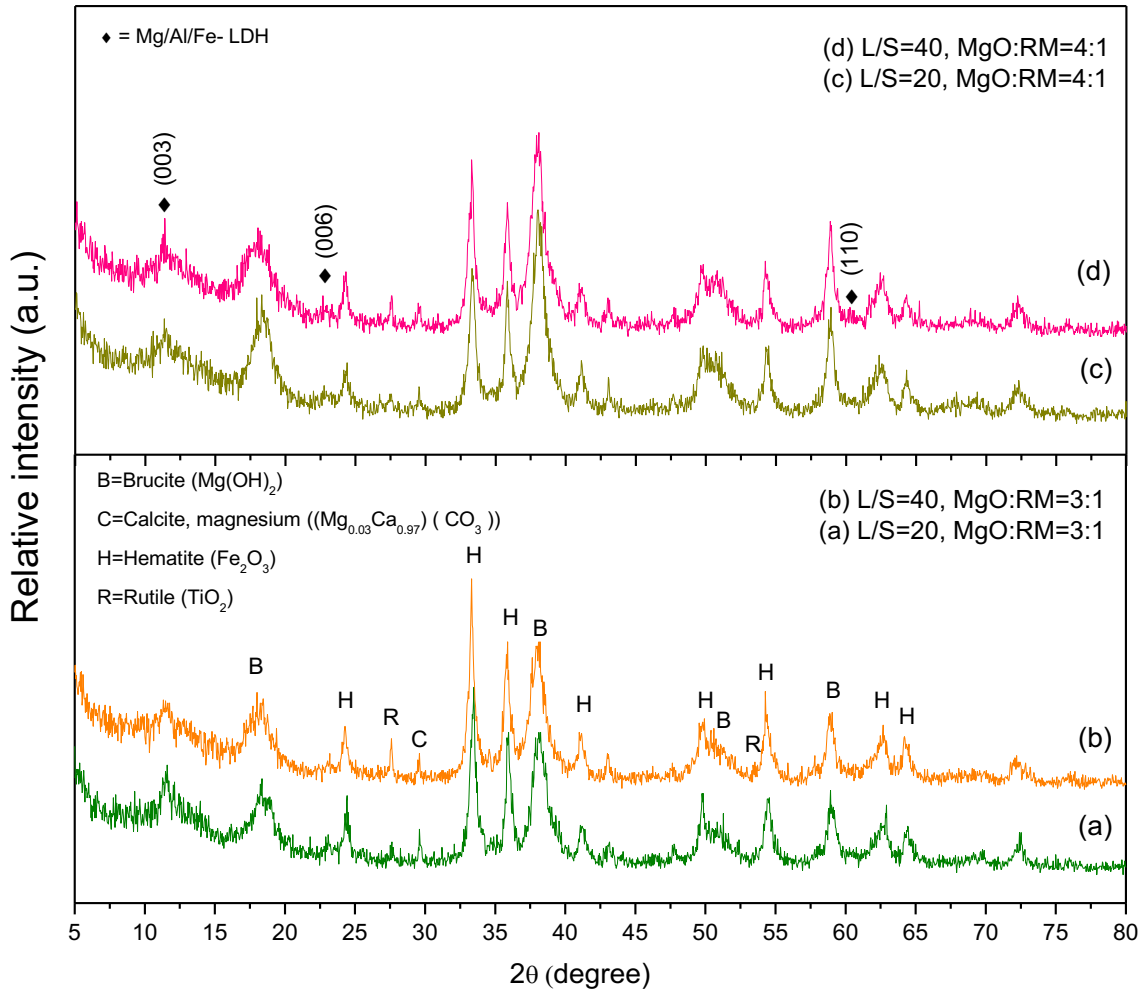

Figure 4.16 Powder XRD patterns of the RM-II products via Route (a), while MgO:RM=3:1 (a) L/S=20, (b) L/S=40; and while MgO:RM=4: (c) L/S=20 and (d) L/S=40

Table 4.4 Lattice of RM-II products with different parameters

RM-II Samples	d_{003} ($\dot{A}$)	d_{006} ($\dot{A}$)	d_{100} ($\dot{A}$)	a ($\dot{A}$)	c ($\dot{A}$)
(a) L/S=20, MgO:RM=3:1	7.613	3.847	1.533	3.066	22.839
(b) L/S=40, MgO:RM=3:1	7.659	3.840	1.525	3.050	22.977
(c) L/S=20, MgO:RM=4:1	7.714	3.873	1.553	3.106	23.142
(d) L/S=40, MgO:RM=4:1	7.809	3.907	1.550	3.100	23.427

4.2.2.3 Effect of L/S and M^{II}/M^{III} Ratio

According to Figure 4.16 and Table 4.4, under different L/S conditions, the RM-II products exhibit no many differences. That suggests neither the hydration of MgO nor the leaching percentages of iron and/or aluminium was notably influenced by the L/S ratio. As discussed in Table 2.8, L/S that equals to 10-20 is often taken as the optimum value. Therefore, to avoid producing excessive liquid waste, L/S=20 is applied in the following studies.

The influence of M^{II}/M^{III} ratio on the final products were studied at different calcination conditions, which are displayed in Figure 4.16 and Figure 4.17, respectively. The cell parameter , i.e. the cation-cation distance in the brucite-like layers, is associated with the isomorphic substitution of Mg^{2+} by Al^{3+} and Fe^{3+}, which have different ionic radius in the order of $Al^{3+} < Fe^{3+} < Mg^{2+}$, 67.5, 78.5 and 86 pm, respectively (Ferna *et al.*, 1998). As can be seen in Table 4.4, with the increase of Mg/(Al+Fe) ratio, ***a*** increases, diffraction peaks shift to lower angle, and ***c*** also increases, indicating more Mg^{2+} cations occupy the layer plates. However, an increase of M^{II}/M^{III} ratio from 3:1 to 4:1, seems not release more $Fe(OH)_4^-$ and $Al(OH)_4^-$ from the RM structure. On the other hand, it leads to higher amount of precipitate brucite in the final product, whose peaks become more intense in Figure 4.16 (c-d). In addition, Sharma *et al.* (2007) addressed that given a fixed hydrothermal treatment condition, the crystallinity of LDH decreases with an increase in the Mg/Al molar ratio. Similarly, it is concluded by Salomão *et al.* (2011), the hydration-dissolution-co-precipitation process of MgO and $Al(OH)_3$ is an equilibrium system, where 60 wt% of MgO is an optimum ratio. Based on the content of LDH percentage solely, the molar ratio of MgO: RM = 3:1 is selected throughout the present study.

4.2.2.4 Effect of Calcination

When the synthesis process went through Route (b) in Figure 4.14, the calcination of RM was carried out separately. Except from the calcination process, all the other procedures followed exactly same as Route (a). The corresponding products are displayed in Figure 4.17. Compared with Figure 4.16, RM-II products originated from Route (b) reveal less significant LDH patterns (marked in black dots). It implies MgO may act as an alkali-activator during the thermal treatment. As a result, RM could release larger amounts of soluble Na, Al and Si species from aluminosilicates structure for the formation of LDH. This observation is supported by other research studies. Ye *et al.* (2017) pointed out that the dissolution efficiency of Al_2O_3 is considerably improved when more than 10 wt% Na_2O was added to

RM and calcined together. Gu *et al.* (2014) also discovered that MgO is effective to activate ground granulated blast furnace slag and induce more amount of hydrotalcite-like phase.

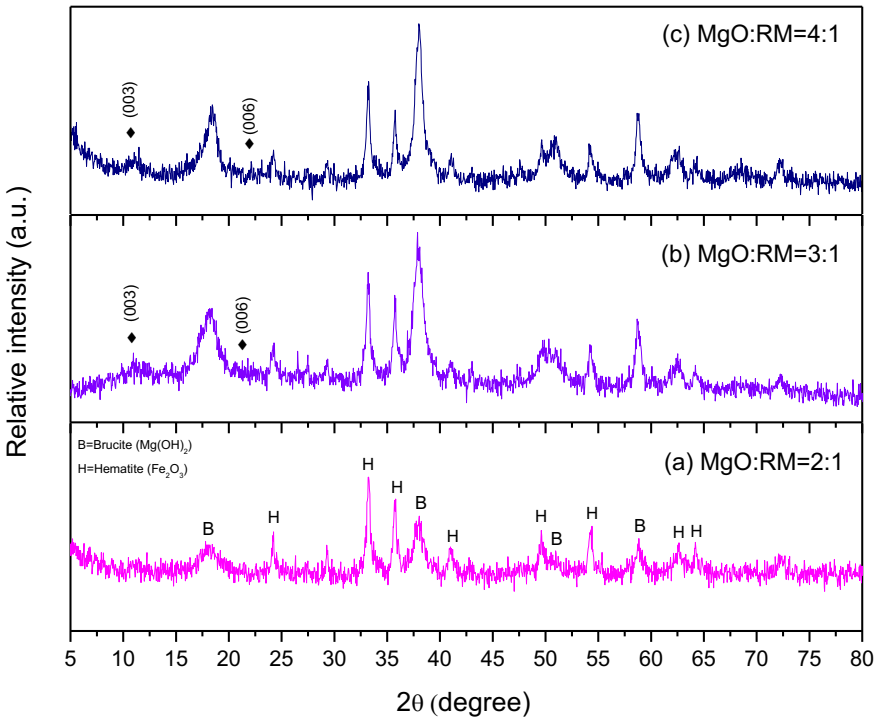

Figure 4.17 Powder XRD patterns of the RM-II products via Route (b) - RM calcined separately, while L/S=20 (a) MgO:RM=2:1 (b) MgO:RM=3:1 (c) MgO:RM=4:1

4.2.3 Scenario III – IRM with MgO

4.2.3.1 Synthesis process

Low content of LDHs was observed in RM-I and RM-II products, which is not satisfactory. It is highly likely due to the limited amount of accessible Al in AOS RM. Since IRM contains more Al components based on its XRF analysis (Table 3.2), Scenario III utilises IRM as the raw material. Scenario III also attempts to enhance the activity of red mud, through grinding RM for a prolonged period and dispersing the mixed slurry before the aging process. The synthesis procedures are illustrated in Figure 4.18. As discussed in Section 2.3.4.2, mechanochemical pre-treatment II includes dry grinding and wet grinding. Route (a), the dry grinding method consists of grinding the (IRM+MgO) mixture in the mortar for 1 h, calcining together at 650°C for 4 h and putting the mixture into contact with Na_2CO_3 solution. The alternative wet-grinding Route (b) involves adding ethanol to the solid mixture of (Cal-IRM + MgO) and grinding the mixture for 1 h. The slurry is then dried in the oven, mixed with Na_2CO_3 solution and allowed to age at 70°C for 72 h. The resulting precipitates are then filtered, washed with distilled water and dried at 80°C for overnight. The detailed experimental conditions of pre-treatment and synthesis are listed in Table 4.5. The reaction pH of different pathways is plotted in Figure 4.23.

Table 4.5 Proposed Scenario III experimental parameters

Material preparation	Value	Process	Conditions
Mg: RM	3:1 or 4:1 (molar ratio)	Dry grinding	1 h, strength 5
Ethanol: solid	10: 1	Wet grinding	1 h, strength 6
Na_2CO_2 solution	$[CO_3^{2-}]$: [Al+Fe] = 2.0	Dispersion	1 h, 8000 rpm
L/S ratio	20	Aging	70°C, 72 h
		Magnetic stirring	200 (rpm)
		Wash of precipitates	3 times
		Drying	80°C, overnight

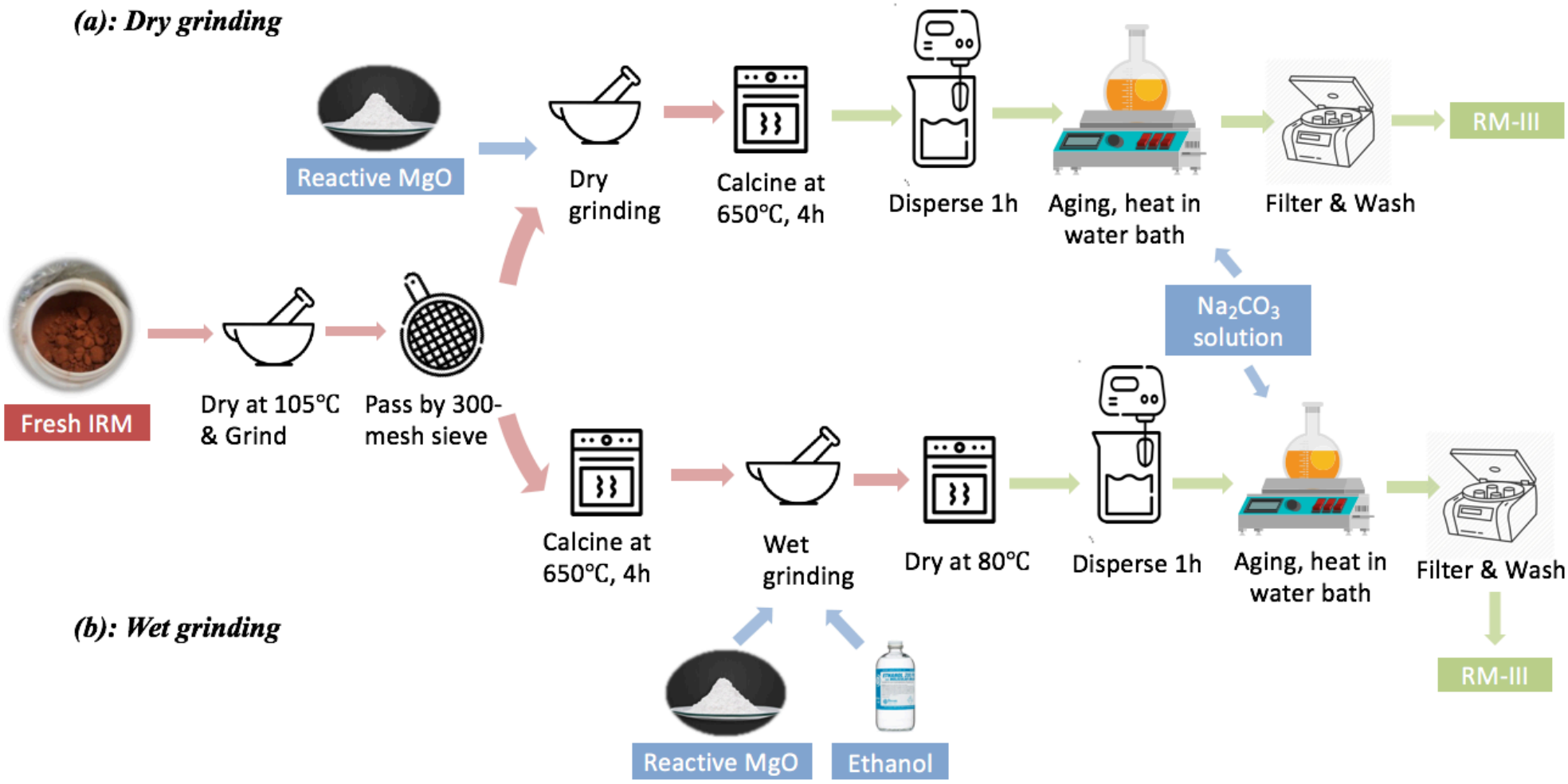

Figure 4.18 Proposed Scenario III synthesis process (a) Dry grinding, (b) Wet grinding

4.2.3.2 Products obtained

The XRD patterns of the RM-III products (RM-d-LDH & RM-w-LDH) are shown in Figure 4.19 and Figure 4.20, respectively. The typical pattern of layered double hydroxides structure can be observed, with sharp and symmetric reflections corresponding to characteristic (003) and (006) planes at lower 2θ values, and broader and asymmetric reflections from (102)/(012) plane. Furthermore, two typical reflections of (110) and (113)/(112) planes can be distinguished at ~60° 2θ. The results reveal the existence of a well-crystalline LDH structure. The corresponding basal spacing and lattice parameters, as listed in Table 4.6, were calculated for a hexagonal unit cell on the basis of rhombohedral R-3m symmetry (Cavani, Trifirò and Vaccari, 1991). The parameters agree well with those reported for LDH-like compounds (Wang *et al.*, 2017). Therefore, the samples are named as RM-d-LDH (for dry-grinding) and RM-w-LDH (for wet-grinding) respectively, depending on the grinding method. Table 4.7 presents the major mineral phases of RM-LDHs, which are deduced via the 'search & match' function in X'Pert Highscore software.

The interlamellar distances (d_{003}) of RM-d-LDH and RM-w-LDH are both 7.78 Å, indicating CO_3^{2-} anions incorporated between the layers. Cell parameters a=3.14 Å and c=23.31 Å are in accordance with the literature values (a=3.11 Å and c=23.41 Å) for pyroaurite [$Mg_3(Al,Fe)(OH)_8(CO_3)_{0.5}\cdot nH_2O$] (Cavani, Trifirò and Vaccari, 1991; Rozov *et al.*, 2010), which imply that Fe^{3+} is the dominant trivalent ion in the LDH synthesised. In addition, bayerite phase [$Al(OH)_3$] is not observed, but brucite phase [$Mg(OH)_2$] is clearly marked in Figure 4.19a & 20a. The overlap with brucite phase at ~60° results in the poor resolution of (113) or (112) reflection for the synthesised RM-LDHs.

Table 4.6 Crystallographic data and crystallite size of RM-LDHs from scenario III

RM-II samples	d_{003} (Å)	d_{006} (Å)	d_{110} (Å)	Cell parameters (Å)		Crystallite size (Å)
				a	c	(003)
RM-d-LDH	7.78	3.88	1.57	3.14	23.31	14
RM-w-LDH	7.78	3.89	1.59	3.12	23.37	14

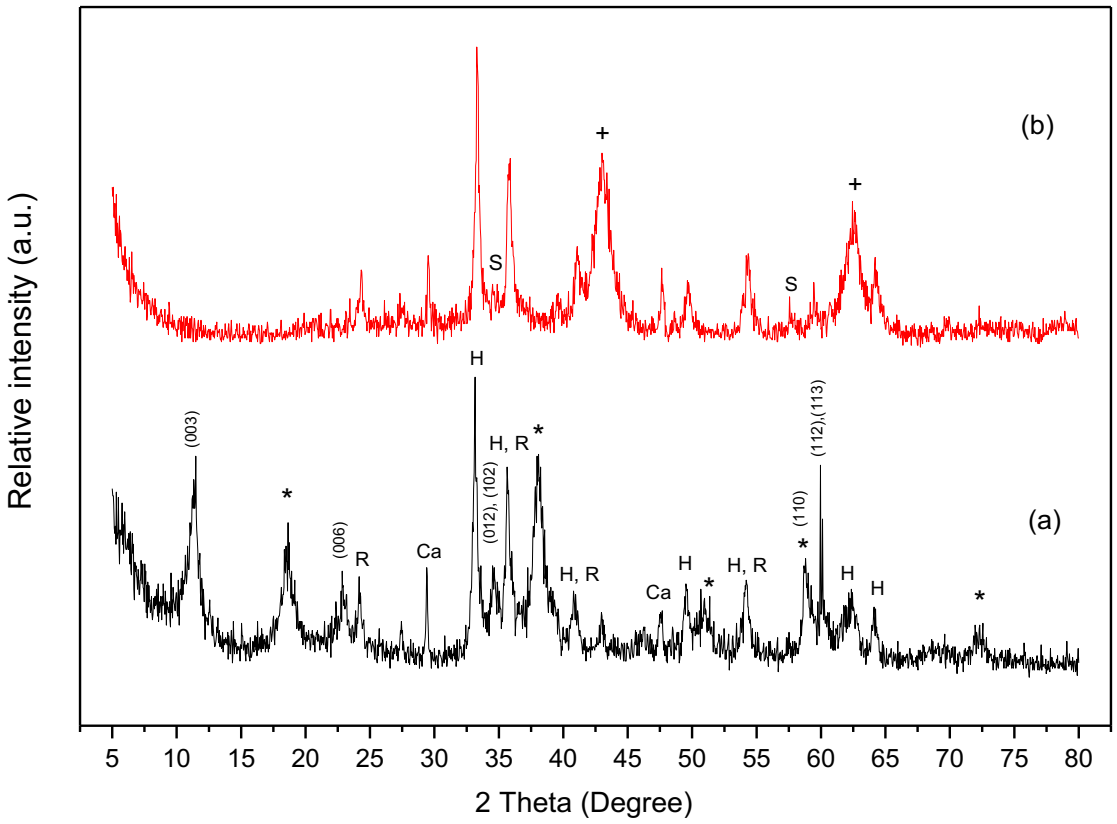

Figure 4.19 XRD patterns of RM-d-LDH synthesised before (a) and after calcination (b) at 500°C. (*) Brucite $Mg(OH)_2$, (+) Periclase MgO, (H) Hematite Fe_2O_3, (R) Rutile TiO_2, (Ca) Calcite($CaCO_3$), (S) Spinel $MgFe_2O_4$

Table 4.7 List of major minerals phases recognised in RM-LDHs from X'Pert software

Reference Code	Chemical Formula	Compound Name
01-089-8103	Fe_2O_3	Hematite
01-073-2224	TiO_2	Rutile
00-044-1482	$Mg(OH)_2$	Brucite, syn
01-071-1447	$(Mg_6Fe_2(OH)_{16}CO_3(H_2O)_{4.5})_{0.25}$	Sjoegrenite
01-089-0460	$(Mg_{0.667}Al_{0.333})(OH)_2(CO_3)_{0.167}(H_2O)0.5$	Hydrotalcite, syn
01-083-0577	$Ca(CO_3)$	Calcite
01-077-2364	MgO	Periclase, syn

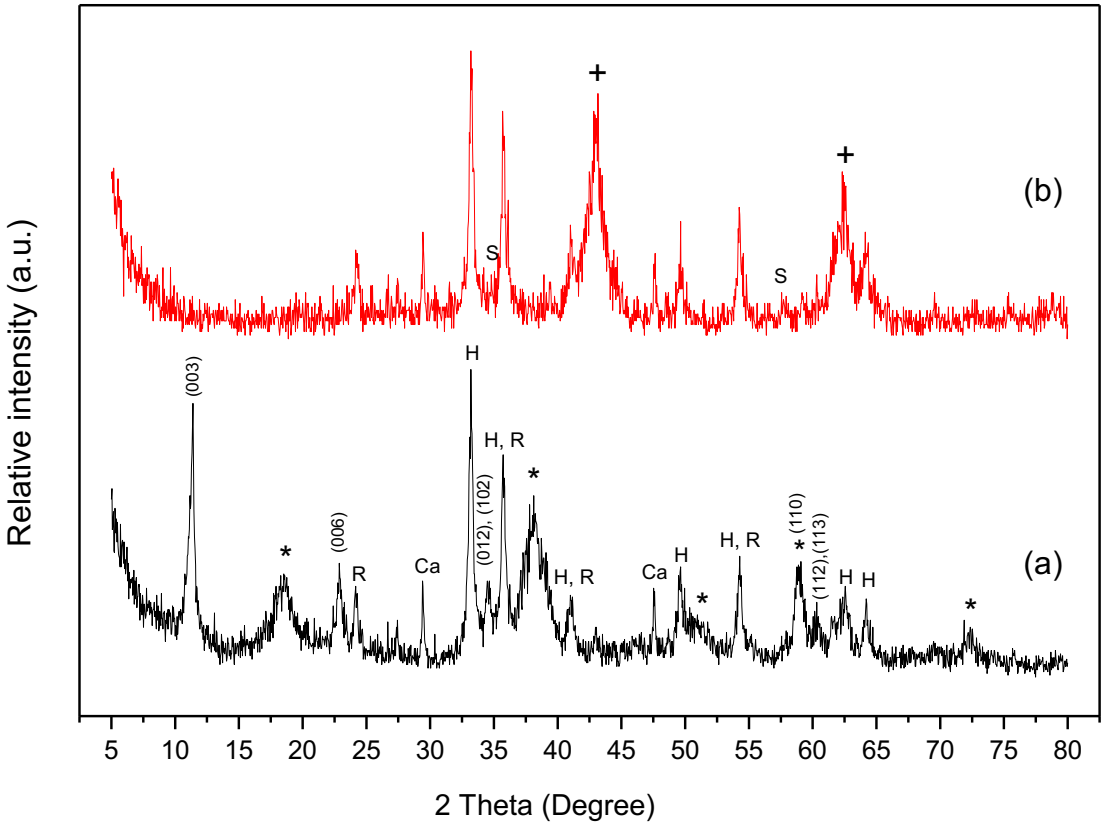

Figure 4.20 XRD patterns of RM-w-LDH synthesised before (a) and after calcination (b) at 500°C. (*) Brucite $Mg(OH)_2$, (+) Periclase MgO, (H) Hematite Fe_2O_3, (R) Rutile TiO_2, (Ca) Calcite($CaCO_3$), (S) Spinel $MgFe_2O_4$

According to the XRF analysis (see Table 3.2), the original IRM contains Ti at around 9 wt% as TiO_2. Meanwhile, the XRD analysis of IRM (see Figure 4.3) identified the presence of rutile (TiO_2). However, the PANalytical X'Pert High Score search system is unable to distinguish the change of Ti content in RM-LDHs. Bhagwat *et al.*, (2019) prepared magnesium titanate ($MgTiO_3$) nanoparticles by using TiO_2 and magnesium nitrate $(MgNO_3)_2{\cdot}6H_2O$ as precursors. The authors presented the crystalline structure of $MgTiO_3$ nanoparticles, as shown in Figure 4.21. It shows the characteristic peaks of $MgTiO_3$ mostly overlap with that of hematite. Pratapa *et al.* (2015) also explored the synthesis of $MgTiO_3$ using Mg and Ti metal powders and confirmed the co-existence of $MgTiO_3$, MgO and TiO_2 in all products. As a result, the presence of $MgTiO_3$ in RM-LDHs is highly likely but inadequate to be affirmed from the XRD analyses.

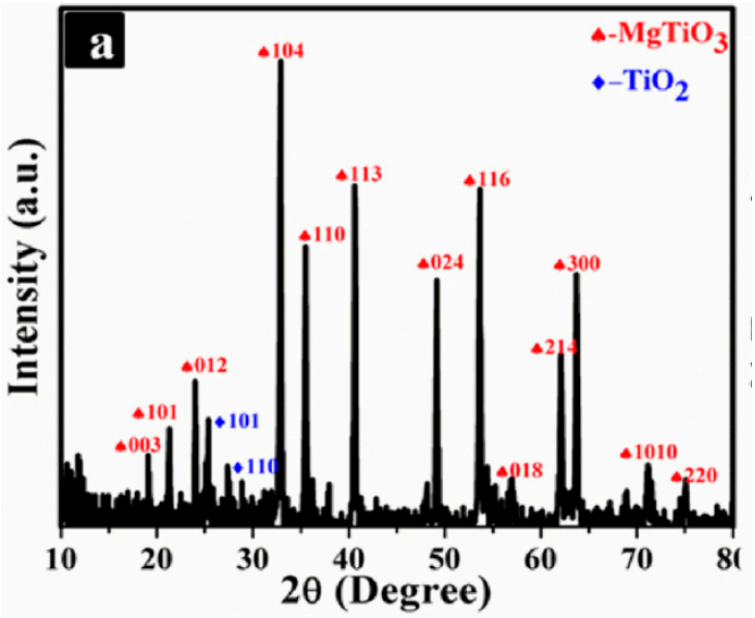

Figure 4.21 XRD patterns of MgTiO3 nanoparticles (Bhagwat *et al.*, 2019).

The lack of reference material and the structural disorder of RM-LDHs prevent us from performing Rietveld structural refinements and precise quantitative analysis of diffraction data (Rozov *et al.*, 2010; Speakman, 2011). To estimate the proportion of LDHs in the final RM-LDHs product, semi-quantification via X'pert Highscore software has been conducted. Firstly, the composition of amorphous phase has been considered based on the XRD patterns of RM and synthesised RM-LDHs. The absence of discernible broad halos in the IRM pattern (Figure 4.3) implies that the amorphous phase is not at large quantity. And alumina (Al_2O_3) contained in IRM is mainly identified as crystalline boehmite (AlO(OH)) and/or small amount as amorphous Al_2O_3. On the other hand, Figure 4.19a presents a slightly broad halo at 2θ =15-35°, but not in Figure 4.19b. It suggests that the crystalline diffraction peaks may be broadened due to microcrystalline or nanocrystalline, rather than due to amorphous materials (He *et al.*, 2013). Therefore, amorphous phases have not been taken as a major component in the semi-quantification. Although the accuracy of this estimation is limited, nearly all different selections of LDH phase in the X'pert Highscore modelling system suggest the LDHs content in the range of 20-30 wt%. And if dual LDH phases (e.g. Mg-Al LDH and Mg-Fe LDH) are considered, the maximum hydrotalcite-like compounds could reach to 33 wt% approximately. Brucite and hematite are the main impurities presented in RM-LDHs, which accounts for around 30 wt% and 20 wt% respectively.

4.2.3.3 Effect of Pre-treatment Process

As introduced in Section 2.3.4.2, grinding may induce stress in the solid particles, which decreases the particle size, increases the chemical potential of the materials and therefore their solubility. The pH of the pre-ground MgO and RM mixture reached to >12.95 when dissolved in solution, which is higher than that of the un-ground MgO and RM suspension (pH ~ 12.5). It suggests that grinding facilitates the hydrolysis and dissociation of the activated MgO and Al_2O_3. Wet-grinding is effective to reduce the particle size of the active MgO without the formation of large crystal $Mg(OH)_2$ prior to the reaction, so more amorphous $Mg(OH)_2$ can be formed and less blinding occurs.

The (*) addresses the peaks associated with brucite [$Mg(OH)_2$] and (+) indicates periclase [MgO] peaks. From Figure 4.20a, less amount of $Mg(OH)_2$ is observed in RM-w-LDH than that of RM-d-LDH. There mainly have two reasons for the phenomenon: (1) wet grinding produces smaller MgO particles, which prevents the formation of crystalline brucite in the suspension; (2) limited interference of CO_2 would favour the formation of amorphous brucite with higher solubility; both resulting in less blinding of MgO particles (see Figure 2.17), so that more $Mg(OH)_2$ could participate in the formation of LDH as described in Figure 2.9 – Route B. After the calcination, RM-w-CLDH presents higher intensities of MgO peaks, whereas RM-d-CLDH shows more noticeable peaks of spinel [$MgFe_2O_4$]. This fact implies that the initial thermal treatment of MgO and RM mixture at 650°C inevitably leads to the formation of spinel, who does not involve in the synthetic process of LDH.

The XRD reflections of the RM-w-LDH are slightly shaper, indicating the LDH phases in RM-w-LDH are more crystalline than that in RM-d-LDH. However, the difference may be small since their crystallite sizes are almost identical (see Table 4.6). In order to better distinguish the difference of dry-grinding and wet-grinding, the other physical and chemical properties of different RM-LDH are further investigated in Section 4.3 & 4.4.

4.2.3.4 Effect of Dispersion

The effect of continuous dispersion during the aging stage by means of a batch disperser (refer to Figure 3.3) is investigated. As studied in Section 2.3.4.3– Variable I, dispersion in the beginning of reaction is effective in reducing the particle size and encouraging the conversion of MgO to $Mg(OH)_2$. Based on the XRD analysis (Figure 4.22), prolonged dispersing process during the aging does not affect the mineralogical structure of RM-w-LDH. It supports the finding by Valente et al. (2009) that dispersion longer than 1 hour does not further reduce the particle size of reactants. Therefore, from economic consideration, the mixture of MgO and Cal-IRM is dispersed for 1 hour. This comparison also implies the good repeatability of this synthesis method.

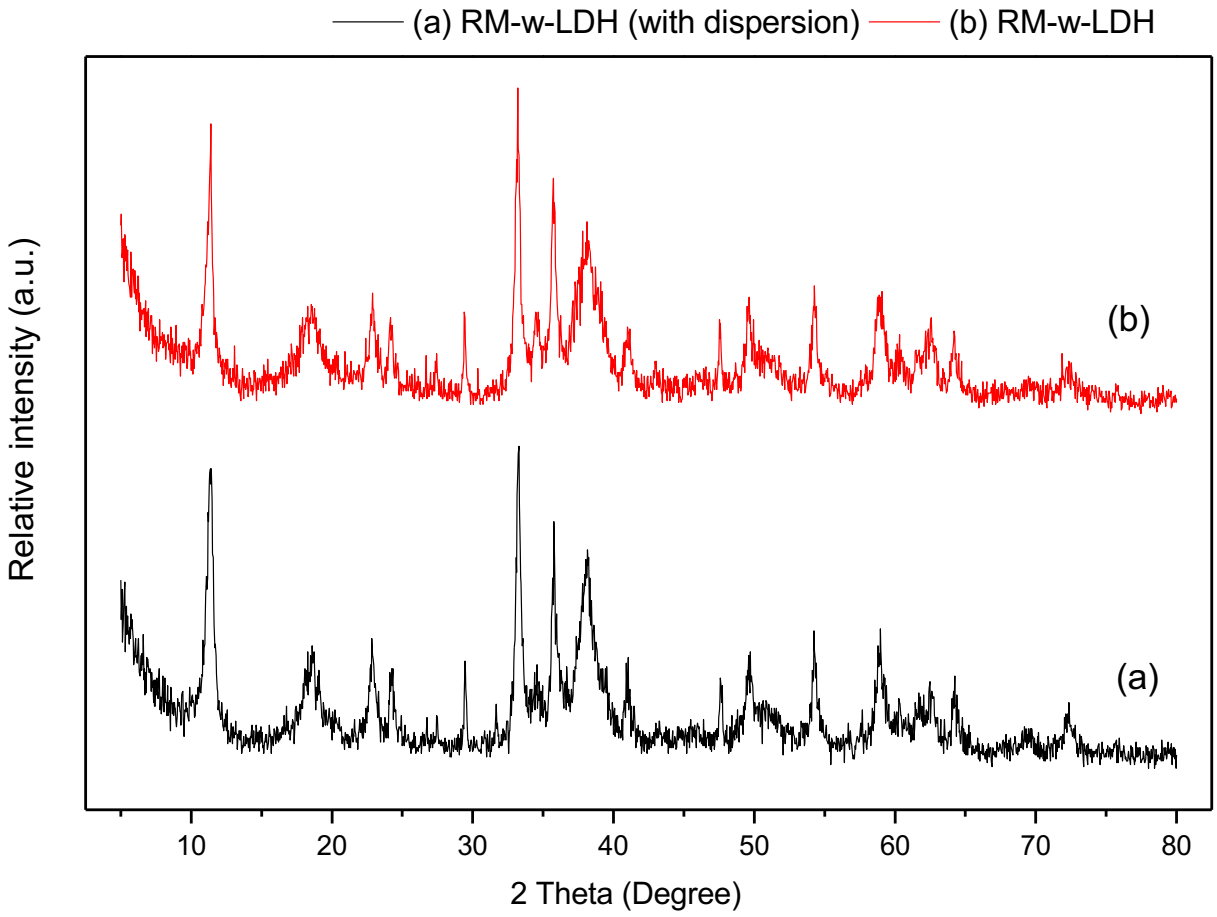

Figure 4.22 *XRD patterns of RM-w-LDH synthesised (a) with dispersion (b) without dispersion during the aging process*

4.2.3.5 Effect of Anions

Figure 4.23 shows the XRD pattern of a series of as-prepared RM-III samples without the addition of Na_2CO_3 solution. The symmetric peaks (003) and (006) at lower 2θ of LDH structure are hardly observed. The weak peak appeared around 2θ = 11.6°, indicating Cl^- and/or OH^- containing LDHs present but in very limited amount. It demonstrates that the present concentrations of monovalent Cl^- and OH^- are insufficient in building up the layer structure in the salt-oxide dominated circumstance. Numerous studies have reported that anions with multiple charges are more easily intercalated into LDHs (Vaccari, 1998; Costa *et al.*, 2012). Curtius *et al.* (2013) estimated the Gibbs free energy of formation (G^o_{298}) for $Mg_3Al(OH)_8Cl$-LDH and $Mg_3Al(OH)_8(CO_3)_{0.5}$-LDH, which are -3619.14 kJ/mol and -3746.90 kJ/mol, respectively. It confirms that carbonate-bearing LDH is thermodynamically favoured and CO_3^{2-} may be more versatile for preparing the layered structures with highest degree of crystallinity in the present reaction. For the intercalation of Cl^-, an increased concentration of free Cl^- and a lower pH are required (Ke, Bernal and Provis, 2017). The peak at 2θ = 18° is attributed to the characteristic peak of $Mg(OH)_2$.

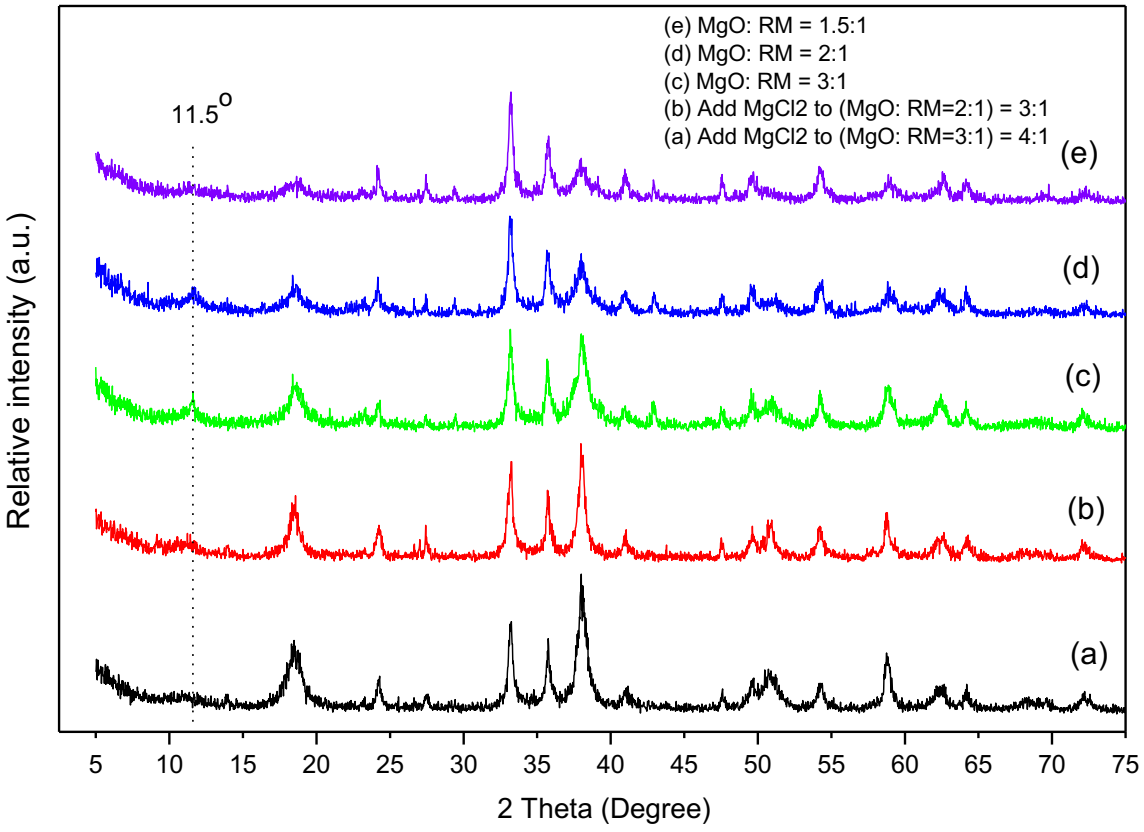

Figure 4.23 Powder XRD patterns of the RM-III products via Route (a) without the addition of Na_2CO_3, *(a) Add $MgCl_2$ to (MgO:RM=2:1)=3:1, (b) Add $MgCl_2$ to (MgO:RM=3:1)=4:1, (c) MgO:RM=3:1, (d) MgO:RM=2:1, (e) MgO:RM=1.5:1*

Figure 4.24 summaries the pH of the relevant reactions in Scenario III. When the (Cal-IRM + MgO) mixture was dispersed in the slurry, amorphous $Mg(OH)_2$ began to form, accompanied by an increase in pH to 12.95. During the synthetic process, the pH of RM-w-LDH and RM-d-LDH system maintained above 12.91. At this basic condition, aluminium trihydroxide (ATH) dissolves in the solution as $Al(OH)_4^-$. Grinding of the ATH causes size reduction and possibly internal stress that contribute to its dissolution rate.

Without the addition of Na_2CO_3 solution, the pH of (MgO + RM) system was in the range of 11.9-12.5. This lower pH could reduce the formation of $Al(OH)_4^-$ species in the system. Apart from the absence of CO_3^{2-} anions, lower concentration of $Al(OH)_4^-$ species hindered the accumulation of LDH phases (Xu and Lu, 2005). When $MgCl_2$ salt was employed to make up the M^{II} component, the pH dropped substantially to just above 8.0. Based on Table 2.7, this pH condition favours neither the movement of MgO to Mg^{2+}, nor the dissociation of $Al(OH)_3$. Therefore, very limited LDH formation was detected.

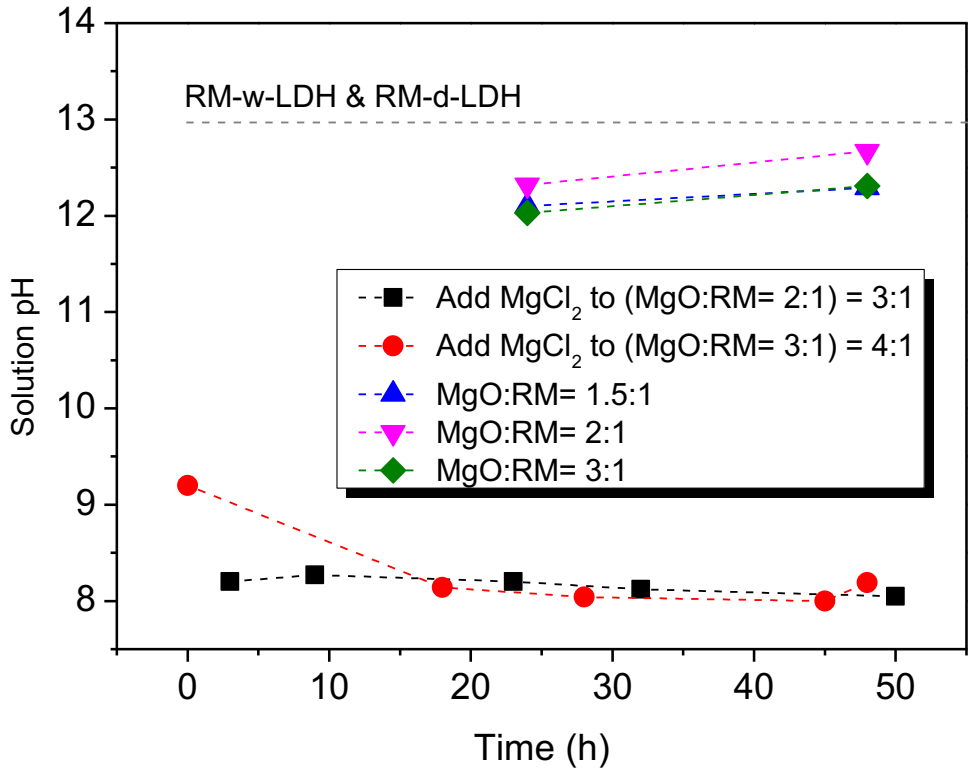

Figure 4.24 The pH of Scenario III reaction measured during the leaching process

4.2.4 Scenario IV – IRM with MgO & $Mg(NO_3)_2$

4.2.4.1 Synthesis process

Scenario IV intends to synthesise RM-LDH through an novel salt-oxide method, which is mainly based on a previous study by Valente *et al.* (2009). The flow chart below (Figure 4.25) describes the typical experimental procedure. The molar ratio of Mg to (Al+Fe) in the system was kept close to 3:1. Considering the property of Cal-IRM, Al_2O_3, $Al(OH)_3$ and $Fe(OH)_3$ are the main trivalent metal sources. In the first step, the reactive MgO was dispersed, marked as suspension (A). In parallel, the Cal-IRM was added to $Mg(NO_3)_2$ solution and dispersed, marked as suspension (B). Magnesium salt ($Mg(NO_3)_2$) was deployed, aiming to (1) provide cations to make up an intended M^{II}/M^{III} molar ratio and (2) adjust the pH to incorporate the insoluble trivalent metal sources in RM. Afterwards, (A) was mixed up with (B), marked as suspension (C). Subsequently, suspension (C) was dispersed at a higher speed of 8000 rpm, facilitating the contact between the metallic sources. Thereafter, the slurry was aged in water bath for 72 h at 70°C. During the aging process, cling firm and tinfoil were covered on top of the flask to maintain the temperature and prevent the influence of carbonate ions. The resultant slurry was centrifuged, and the precipitate was collected, washed with deionised water and dried overnight. The parameters and conditions applied are stated in Table 4.8.

Table 4.8 Proposed Scenario IV experimental parameters

Material preparation	Value	Process	Conditions
L/S ratio of (A)	10	Dispersion of (A)	6000 rpm, 30 mins
L/S ratio of (B)	10	Dispersion of (B)	6000 rpm, 30 mins
L/S ratio of (C)	20	Dispersion of (C)	8000 rpm, 60 mins
MgO: Cal-IRM: $Mg(NO_3)_2$	2.5:1:0.5 (in molar)	Aging	70°C, 72 h
$Mg(NO_3)_2$solution	0.5 mol/L in (B)	Magnetic stirring	300 (rpm)
		Wash of precipitates	3 times
		Drying	80°C, overnight

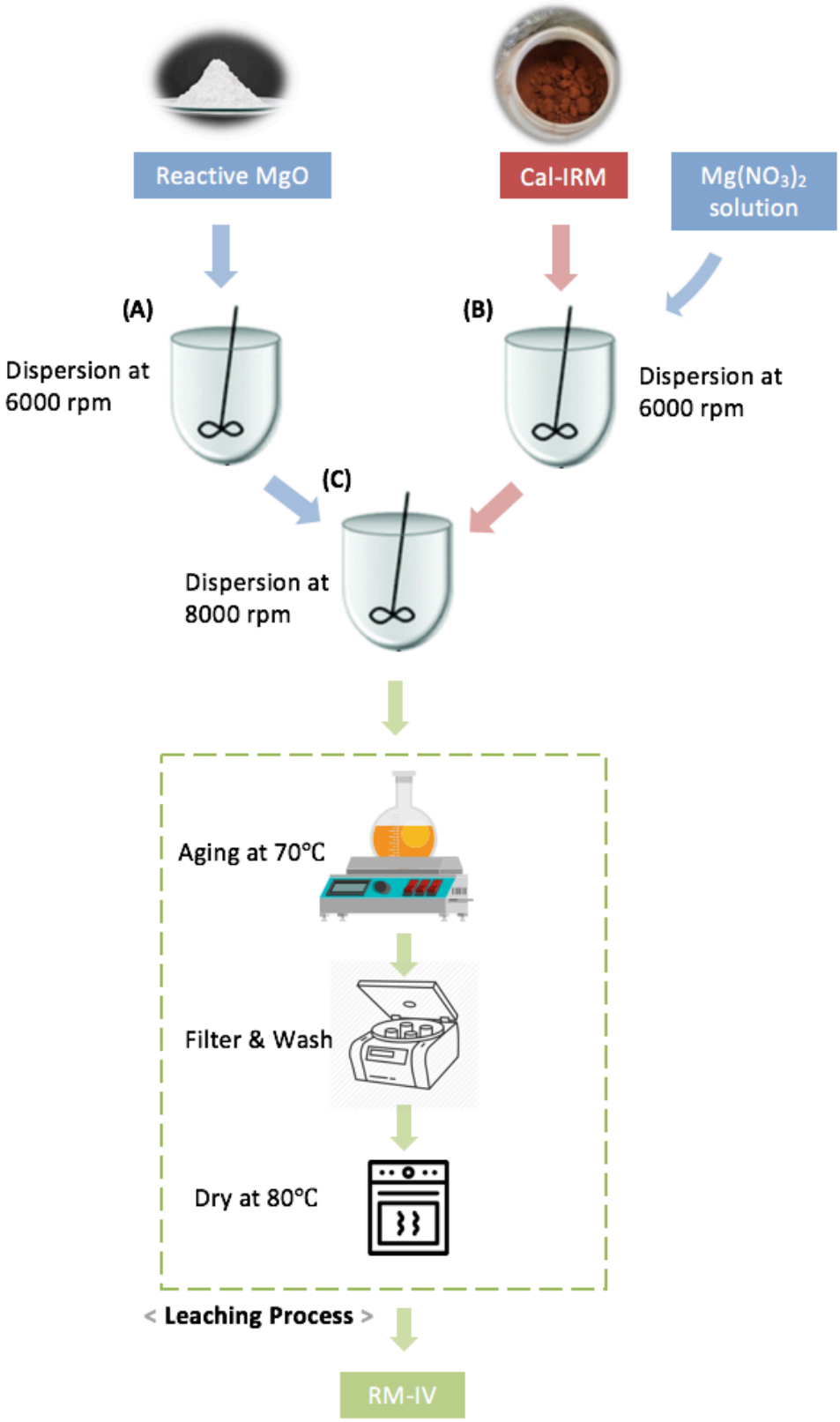

Figure 4.25 Proposed Scenario IV synthesis process

Figure 4.26 reveals the pH variation with different $Mg(NO_3)_2$ molarity from 0 to 1.0 mol/L. Accordingly, when 0.5 moll/L magnesium nitrate solution was prepared in suspension (B), the initial pH was approximately 5.5. It is lower than the system proposed by Valente *et al. (*2009), where the pH of suspension (B) was in the range of 2-3. Depending on the nature of aluminium oxides and hydroxides in Cal-IRM, limited amount of Al^{3+} species will occur in this acidic-neutral medium.

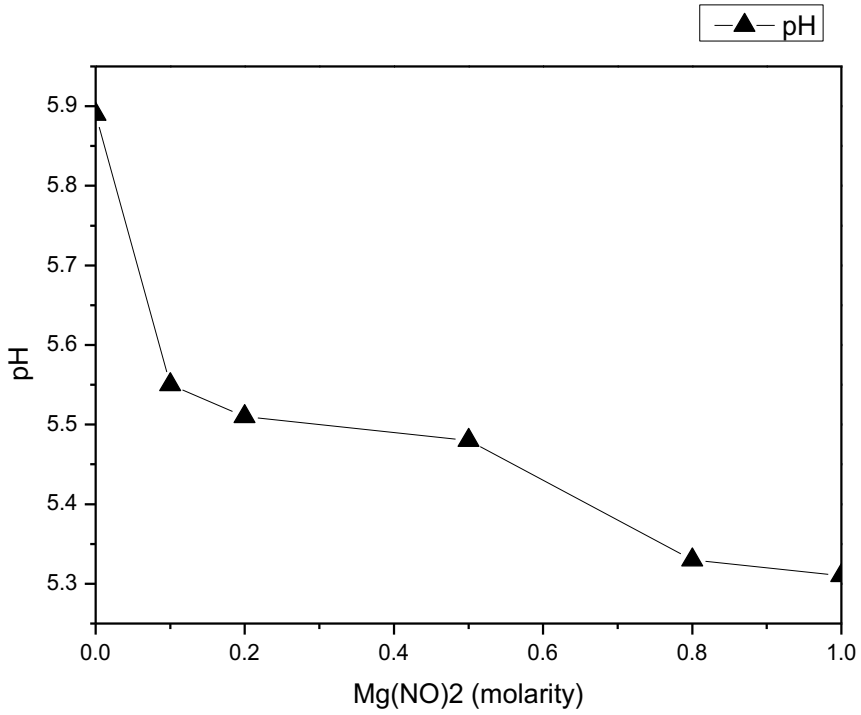

Figure 4.26 The pH of $Mg(NO_3)_2$ solution under different molarity

The reaction's evolution was monitored during the aging process. The initial pH value of the system (C) was about 7.9, then it stables at ~7.8 after 48 h and as the reaction proceeded, the final pH was 7.7. It is lower than the case designed by Valente *et al. (*2009). The pH attained after the dispersion by the authors was about 9.

4.2.4.2 Products obtained

The XRD pattern of the RM-IV product having aged for 72 h is represented in Figure 4.27d. The weak reflections of the (003) and (006) planes at low 2θ values (10-24°), which are in agreement with the characteristic reflections of LDH structure, suggest the appearance of hydrotalcite phase. The basal spacing $d_{003} = 8.12$ Å is close to those previously reported for nitrate-containing LDHs (Mandal *et al.*, 2009; Darmograi *et al.*, 2015), implying the presence of NO_3^- anions between the layers. Other crystalline phases such as $Mg(OH)_2$ and Fe_2O_3 are identified in the XRD pattern. Although compared with the RM-III products, RM-IV sample exhibits lower crystallinity of LDH phase, they show an easy and economical way for LDH preparation in large quantities.

Table 4.9 Crystallographic data of RM-LDHs from scenario IV

Samples	d_{003} (Å)	d_{006} (Å)
RM-IV products	8.15	4.04

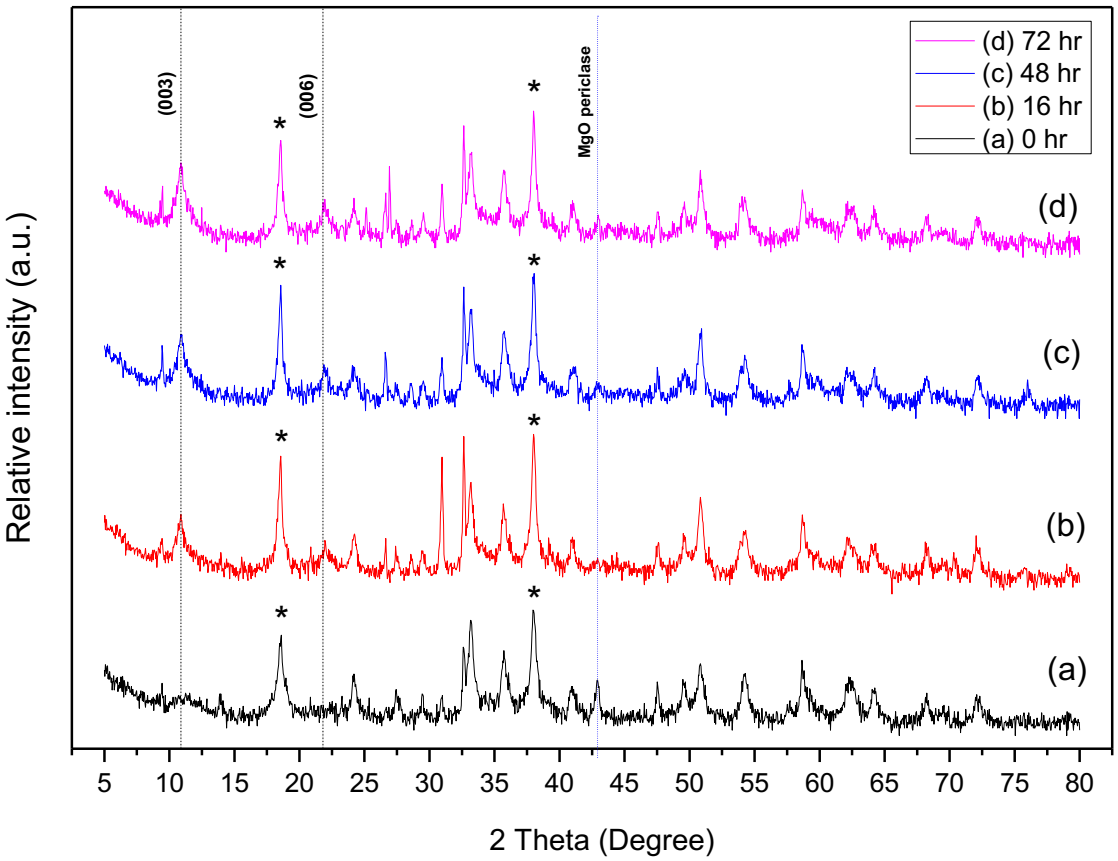

Figure 4.27 Powder XRD patterns of the RM-IV products obtained at t_{aging} of (a) 0 h, (b) 16 h, (c) 48 h, (d) 72 h (*) Brucite $Mg(OH)_2$

A dissolution – precipitation - recrystallisation mechanism is proposed for this scenario, which has been previously examined in Section 2.3.2 – 'III Salt-oxide method'. Table 2.7 explains the possible reactions involved to form LDHs. The hydration products of MgO are Mg^{2+} and $Mg(OH)_2$ in suspension (A). A pH between 6 and 11 is achieved. In suspension (B), the pH environment created by $Mg(NO_3)_2$ is in the range of 5.3-5.9 (Figure 4.26), which is difficult for Al_2O_3 to be ionised to Al^{3+} or $Al(OH)_4^-$ during the hydration process. Therefore, Al_2O_3 and $Al(OH)_3$ are the predominant products of suspension (B). Because the pH of suspension (C) is around 7.8, which is not that basic as that of Scenario III, a small portion of Al_2O_3 and $Al(OH)_3$ actually dissociates to $Al(OH)_4^-$ (Xu and Lu, 2005). In this slightly basic condition, two pathways to form LDH phase may both occur during the aging process, i.e. $Al(OH)_4^-$ deposit onto $Mg(OH)_2$ and Mg^{2+} deposit onto $Al_2O_3/Al(OH)_3$ (see Figure 2.9). Consequently, a limited amount of LDH is detected. Salomão *et al.* (2011) previously investigated the hydration degree (W_{HExp}) of MgO, $Mg(OH)_2$, calcined alumina and $Al(OH)_3$ in detail. The authors pointed out that by mixing up MgO and $Al(OH)_3$, hydrotalcite peaks appear, on the contrary, the characteristic peaks of MgO, $Mg(OH)_2$ and $Al(OH)_3$ are reduced considerably (see Figure 4.28).

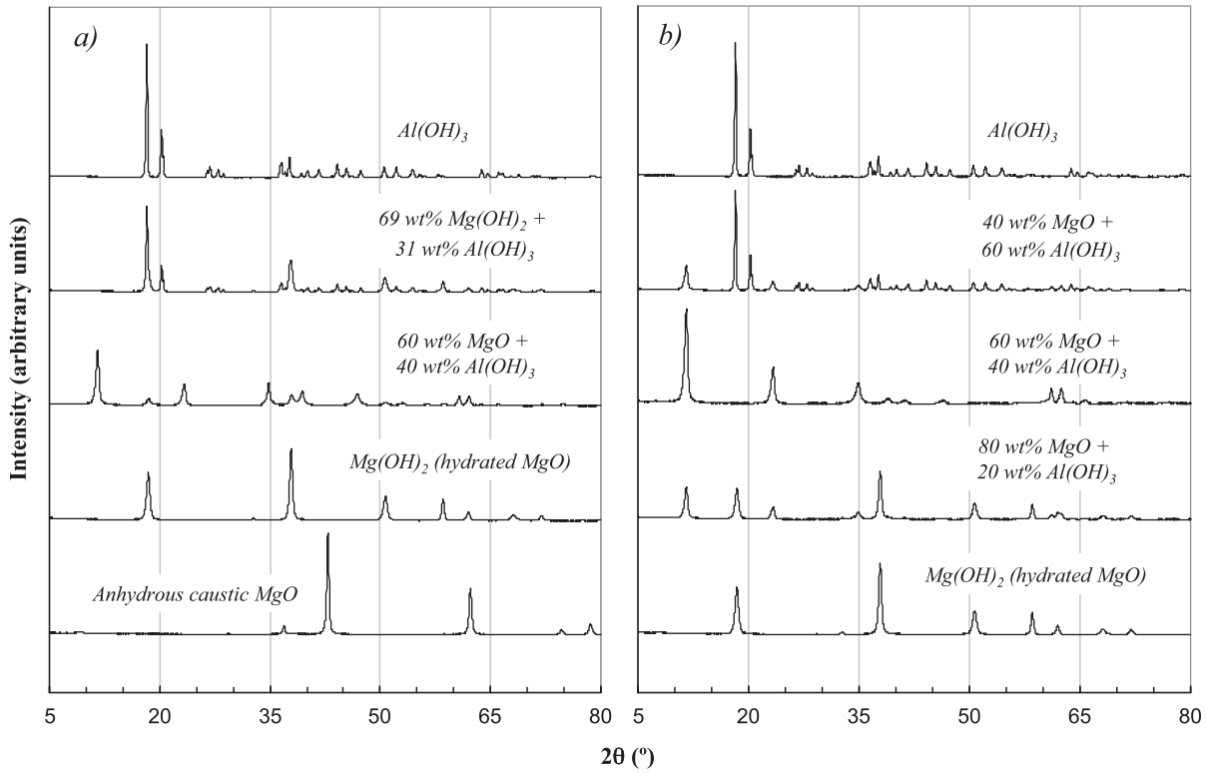

Figure 4.28 X-ray diffraction (XRD) profiles for the raw materials tested, after 7 days at (a) 50°C and (b) 80°C.

4.2.4.3 Effect of Aging

The evolution of aging is investigated by collecting the products at different reaction times (Figure 4.27). The characteristic diffraction peaks of LDH are highlighted in dashed line. The growth progress of LDH phase could be clearly tracked. Along with prolonged aging, the fraction of LDH in the mixture and the degree of crystallinity both increased. This is due to the progressive development of LDH crystals (Sharma *et al.*, 2007). It could be inferred that the particle sizes also increase with aging time. No significant changes in lattice parameters are observed.

Meanwhile, the peaks corresponding to brucite [$Mg(OH)_2$] and MgO also remained in the final products, indicating the starting material did not react completely. Nevertheless, their reflections became weaker in the order of 0 > 16 > 48 > 72 h. That demonstrates more starting materials transform to LDH phase with longer aging time. Similar trend of LDH formation with regards to aging time was reported by Zhang *et al.* (2014). The authors prepared Mg-Al-Fe-NO_3 LDH from $Mg(OH)_2$, $Al(OH)_3$ solids and $Fe(NO_3)_3$ solution through conventional mechanochemical method. They discovered the starting materials $Mg(OH)_2$ and $Al(OH)_3$ almost reacted completely after milling for 12 h.

As discussed in Section 2.3.4.5 and specifically in Figure 2.20, generally, longer aging within a rational duration is proved to favour the formation of LDH and increase its crystallinity (Sharma *et al.*, 2007). However, Paikaray and Hendry (2014) pointed out the possible negative effects on crystallinity resulted from overlong thermal exposure. Therefore, aging for 72 h is employed throughout the present study.

4.2.5 Discussion of Synthesis Scenarios

In the present work, Scenario III (refer to Figure 4.18) was selected as the most effective method to synthesis LDH using RM. Figure 4.29 shows the mixture of RM-MgO after the pre-treatment and one RM-LDH product obtained from Scenario III. Various factors have been screened above, including the source of RM, L/S ratio, M^{II}/M^{III} ratio, effect of calcination and pre-treatment, influence of dispersion and aging, and choice of anions. The preferred experimental conditions are listed in Table 4.10. They are mostly based on qualitative observations, therefore are inconclusive.

(a) *(b)*

Figure 4.29 (a) The (RM + MgO) mixture after the dry grinding and calcination (b) Example of RM-LDH product of Scenario III

The possible mechanism for LDH formation from MgO and RM has been discussed in previous sections. To sum up, it roughly follows the 'dissociation-deposition-diffusion' mechanism, as shown in Figure 2.9. Grinding yields well-mixed starting materials with fine particles, thus accelerates the later reaction (Zhang *et al.*, 2013). Initially, the hydration of reactive MgO, triggers a significant increase in the pH of the aqueous suspension. When it happens in the presence of iron and aluminium oxides/ hydroxides, its dissociation and further hydrolysis are favoured, since $M^{III}(OH)_3$ solids are taking up OH^- to form $M^{III}(OH)_4^-$ anions. In this salt-oxide system, as Salomão *et al.* (2011) pointed out that, the sources of Mg and Al species are shifting the equilibrium themselves. The simultaneous occurrence of $Mg(OH)_2$, $M^{III}(OH)_4^-$ and CO_3^{2-} in a strong alkaline environment is suitable for LDH precipitation (Valente, Cantu and Figueras, 2008; Qu *et al.*, 2016). The theoretical and stoichiometric reaction can be expressed as below:

$$6Mg(OH)_2 + 2Al(OH)_3 + 3H_2O + CO_2 \rightarrow Mg_6Al_2(OH)_{16}(CO_3)\cdot 4H_2O \quad (4.9)$$

Table 4.10 Parameters selection for the preferred synthesis conditions

No.	Parameters	Conditions	Comments
(1)	Red mud source	Ireland RM	IRM possess remarkably more reactive Al or Fe components for LDH formation.
(2)	Pre-treatment	Dry grinding, wet grinding	Both worked well. No significant difference was observed from the XRD analysis.
(3)	Calcination	Depends on (2)	If RM is calcined separately or together with MgO, depends on the pre-treatment method.
(4)	L/S ratio	20	Based on observation from Scenario II, L/S = 20 offers a satisfied result.
(5)	M^{II}/M^{III} ratio	3.0	By comparing M^{II}/M^{III} = 2:1, 3:1 & 4:1, 3:1 is the most efficient.
(6)	Dispersion	No dispersion during aging	Dispersion seems not affect the quantity of LDH phase, although the crystallinity size was not compared.
(7)	Aging	70°C, 72 h	Based on the track of reaction of Scenario IV, aging does enhance the formation of LDH.
(8)	Anion environment	CO_3^{2-}	Carbonates are favourable for producing crystalline, stable LDH structure.

Overall, three main drawbacks should be pointed out in this salt-oxide based methodology:

1) The synthetic process may be highly sensitive to the origin of red mud. For instance, IRM is more capable of offering active iron and aluminium oxides/ hydroxides than AOS RM.
2) The final products inherited the impurities in RM; and the starting material MgO also induced the formation of brucite.
3) The synthetic methodology still involved time-energy consuming process, especially compared to the traditional co-precipitation method starting from metal salts.

However, this proposed synthetic strategy does not need a large amount of commercial metal salts required in conventional methods. Instead, the waste material red mud and reactive magnesia are simply mixed and aged in an aqueous suspension, showing the versatility of the method. The potential of using RM for LDH synthesis has been clearly demonstrated. Therefore, alternative methods would be of technological interest. A few possible modifications are suggested as below:

1) An optimum ratio of M^{II}/M^{III} has not been ascertained for Scenario III. The purity of RM-LDH could be further enhanced if a M^{II}/M^{III} molar ratio close to the LDH stoichiometry is found (Xu and Lu, 2005).
2) The pH of suspension is a crucial factor that determines the efficiency of dissociation/ hydration of the raw materials and hence the LDH precipitation. For Scenario IV, decrease the pH in step (B) would enhance the dissociation of Fe or Al hydroxides; as the reaction proceeds, control of the pH between 8-10 in suspension (C) may facilitate the formation of $M^{III}(OH)_4^-$ (Valente *et al.*, 2009). NH_4OH is suggested to enhance the pH, avoid introducing CO_3^{2-} anions or resulting in secondary crystalline phases.
3) Calcined alumina, is reported to be chemically stable (Salomão *et al.,* 2011). Instead, in Scenario III, un-calcined IRM may be able to directly provide $Al(OH)_3$, which is ready to be dissolved as $Al(OH)_4^-$ in the strong basic media.
4) Further hydrothermal or microwave treatment can be considered to enhance the crystallinity as well as shorten the aging time (Benito *et al.*, 2008).

Section 4.3 & 4.4 will mainly focus on the RM-LDHs synthesised from Scenario III. In order to confirm the synthesis of LDH phase, the structure characteristics of RM-LDHs will be assessed against the ‘golden rules’ of LDHs, as reviewed in Section 2.4.1,

4.3 Golden Rules

4.3.1 Rule I: Crystallinity XRD

The similarities and differences with the representative XRD pattern of LDH structure phase (Figure 2.22) have been discussed in Section 4.2. The LDH phases are evident in the as-synthesised products from Scenario II, III & IV. Their *d*-spacing values accurately reflect the anion intercalates between the interlayer space, depending on various feedstocks. The thermal stability and memory effect can also be assessed by XRD analysis. It should be noted that both the calcination temperature and the chemical composition of LDH sheets have significant influence on the resulted CLDH. As illustrated in Section 2.4.2.3, in order to prevent the formation of Mg-Al-Fe spinel and protect the 'memory effect' of LDH, calcination temperature is controlled below 500°C in the experiment.

After calcination at 500°C, the layered structure of RM-d-LDH was destroyed and the characteristic reflections of $Mg(OH)_2$ disappeared (Figure 4.19b). Instead, broad and non-symmetric reflections (+) at 43° and 63° are observed that indicates the formation of the defect periclase MgO structure, which is made up of Mg, Fe, Al mixed multi-metal oxides. Apart from Fe_2O_3, the characteristic diffractions of the spinel ferrite $MgFe_2O_4$ with the peaks at 30° and 57° have been observed (Heredia *et al.*, 2013), who starts to form at 450°C during the calcination (Valente *et al.*, 2010; Benselka-Hadj Abdelkader *et al.*, 2011; Vulic, Reitzmann and Lázár, 2012). It suggests that Mg^{2+} is replaced by Fe^{3+} and Al^{3+}. Similar trend is also observed on the calcination product of RM-w-LDH (Figure 4.20b), hereby a decomposition of its LDH structure and elimination of most interlayer anions and water can be confirmed. These findings agree well with previous reports in the literature (Ferna *et al.*, 1998; Heredia *et al.*, 2013). Accordingly, RM-LDHs meet the Rule I and Role-play III for the featured LDH structure.

4.3.2 Rule II: Morphology SEM

To further analyse the microstructural features of the as-synthesised products, SEM images were studied. Figure 4.30 shows the SEM/EDX images of RM-d-LDH. EDX analyses were performed and confirmed the major elements are Mg, Fe, Si, Al and Br. A corresponding EDX result gave an element composition of Mg: Fe: Al = 3: 0.71: 0.21. The micrographs reveal well-dispersed platelet structures, small and exfoliated sheets, which are consistent with the Mg/Al/Fe LDH samples in other research (see also Figure 2.25) (Iwasaki, Shimizu, *et al.*, 2012; Heredia *et al.*, 2013; F. Zhang *et al.*, 2014). Xu and Lu (2005) described this feature as LDH sheets grown on the surface of MgO or Al_2O_3. These platelets present an average thickness of < 30 nm and a lateral dimension about 200-500 nm. Besides, sand rose morphology could also be observed (the remarked square in Figure 4.30a), which is a common characteristic for LDH formed by inter-grown small crystallites (Wang *et al.*, 2013).

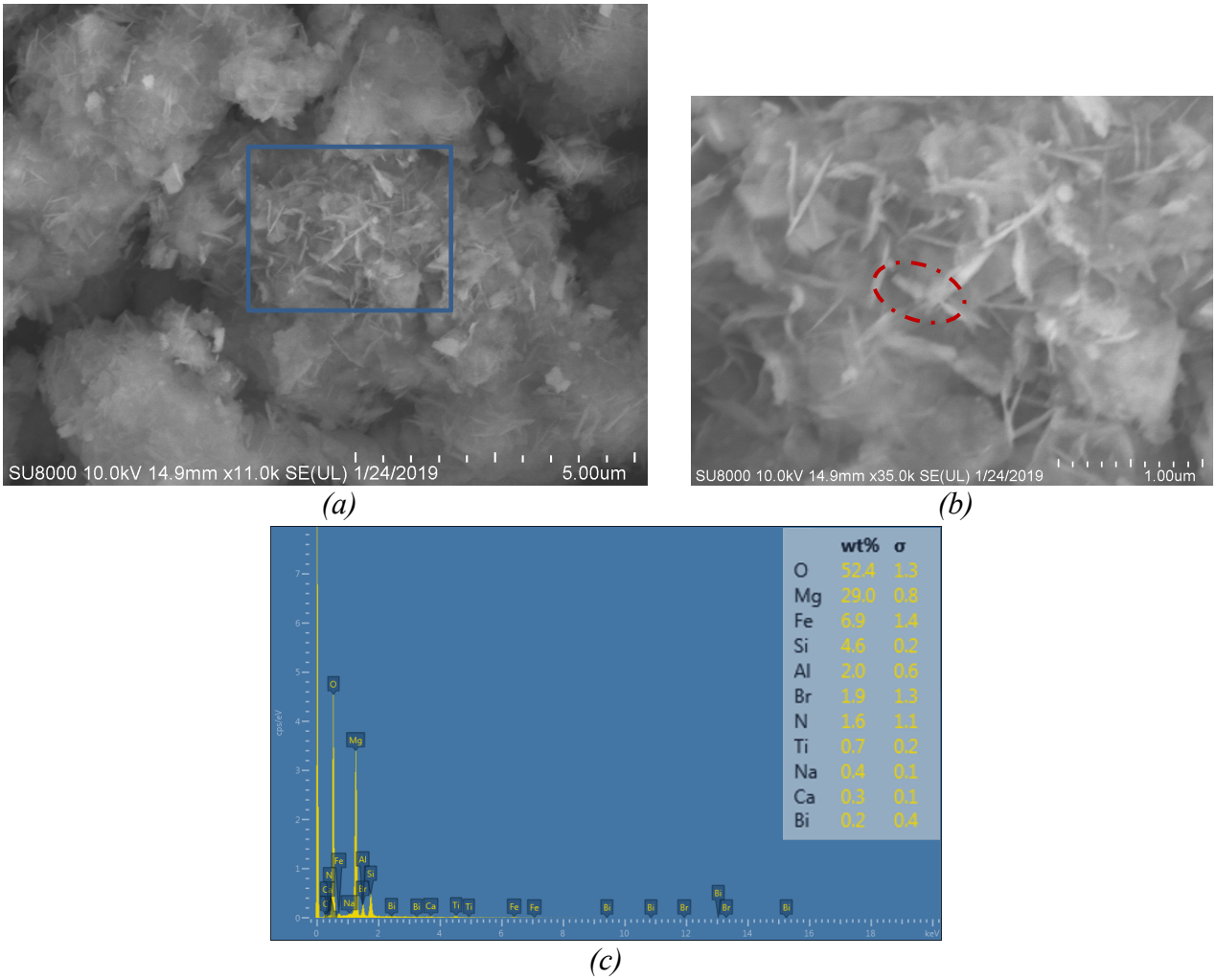

Figure 4.30 Scanning electron microscopy images of (a-b) RM-d-LDH, (c) Chemical analysis by energy dispersive X-rays (EDX) of point marked in *(b)*.

Lamellar texture can also be observed from RM-w-LDH sample (Figure 4.31). However, for both RM-LDH solids, the presence of hexagonal platelet could not be clearly seen. In comparison, RM-d-LDH exhibits relatively higher morphological homogeneity and better dispersed platelets; whereas RM-w-LDH presents more irregular aggregation of small crystallites. According to Figure 4.31, the aggregates have an average diameter of 1-5 μm and the nanoplatelets are about 100-500 nm in length, similar to those of the RM-based LDH mechanochemically synthesised by Qian et al. (2015) and the Mg-Al-Fe hydrotalcite produced by Ma *et al.* (2011).

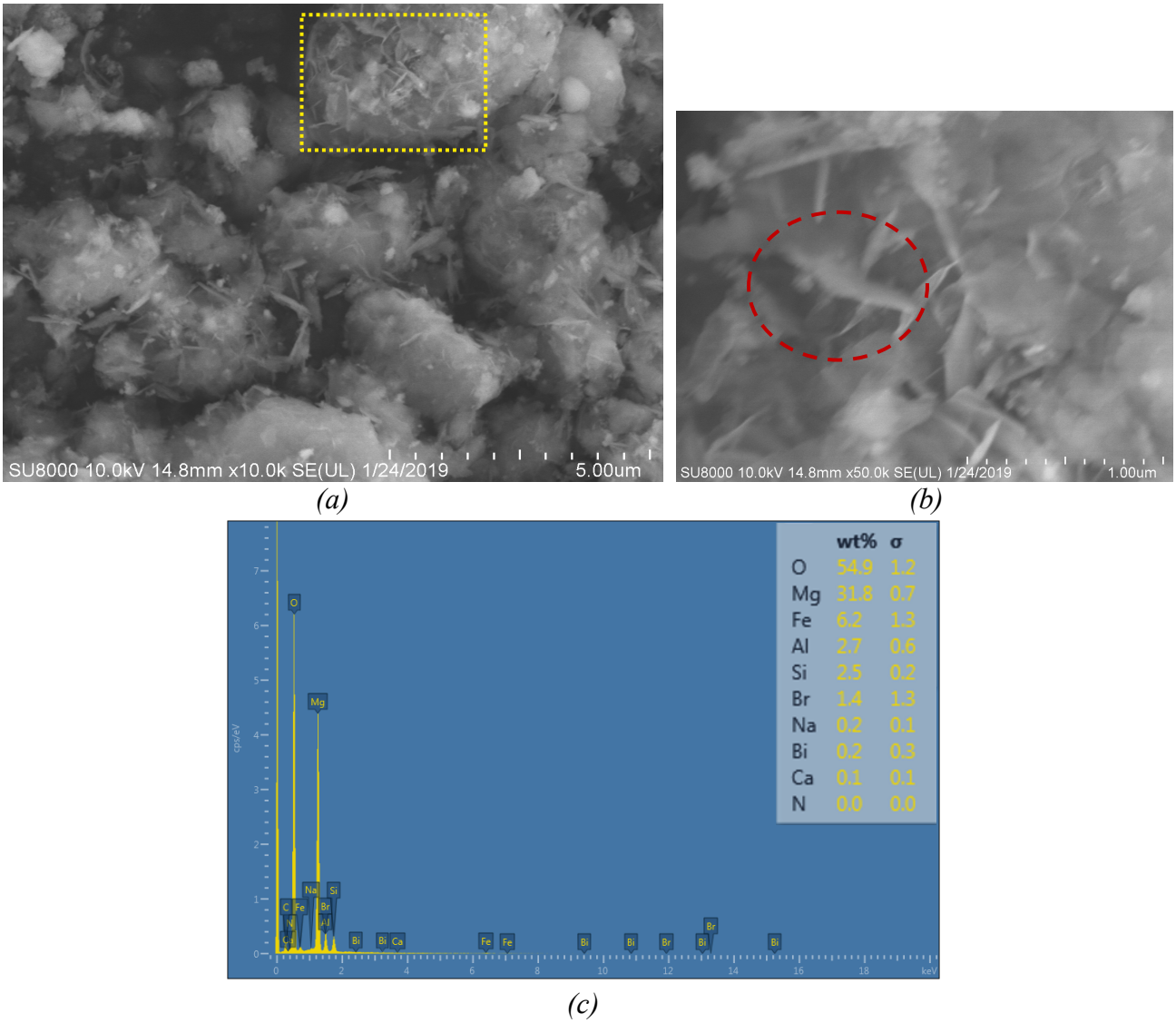

(a) *(b)*

(c)

Figure 4.31 Scanning electron microscopy images of (a-b) RM-w-LDH; (c) Chemical analysis by energy dispersive X-rays (EDX) of point marked in *(b).*

The morphology of LDH can be affected by the nature and the extent of M(III) ion substitution. According to Figure 4.31c, a typical element composition of Mg, Fe, Al near and at the surface of the composite are 3: 0.58: 0.25. This indicates that Fe(III)-incorporated LDH likely dominate the RM-w-LDH but meanwhile Mg-Al hydrotalcites are also present, which is similar to RM-d-LDH. Vulić, Hadnadjev and Marinković-Nedučin (2008) compare the SEM images with various content of M(III) in Figure 4.32, where M(III) is Al or/and Fe. The dash rectangle highlights the M(II): M(III) ~2.3, nearest to the ratio proposed in this PhD study. The blue brace row exhibits the highest similarity with Figure 4.30b & 31b. That further implies that LDHs have been synthesised and Mg-Fe LDH may dominate the RM-LDHs.

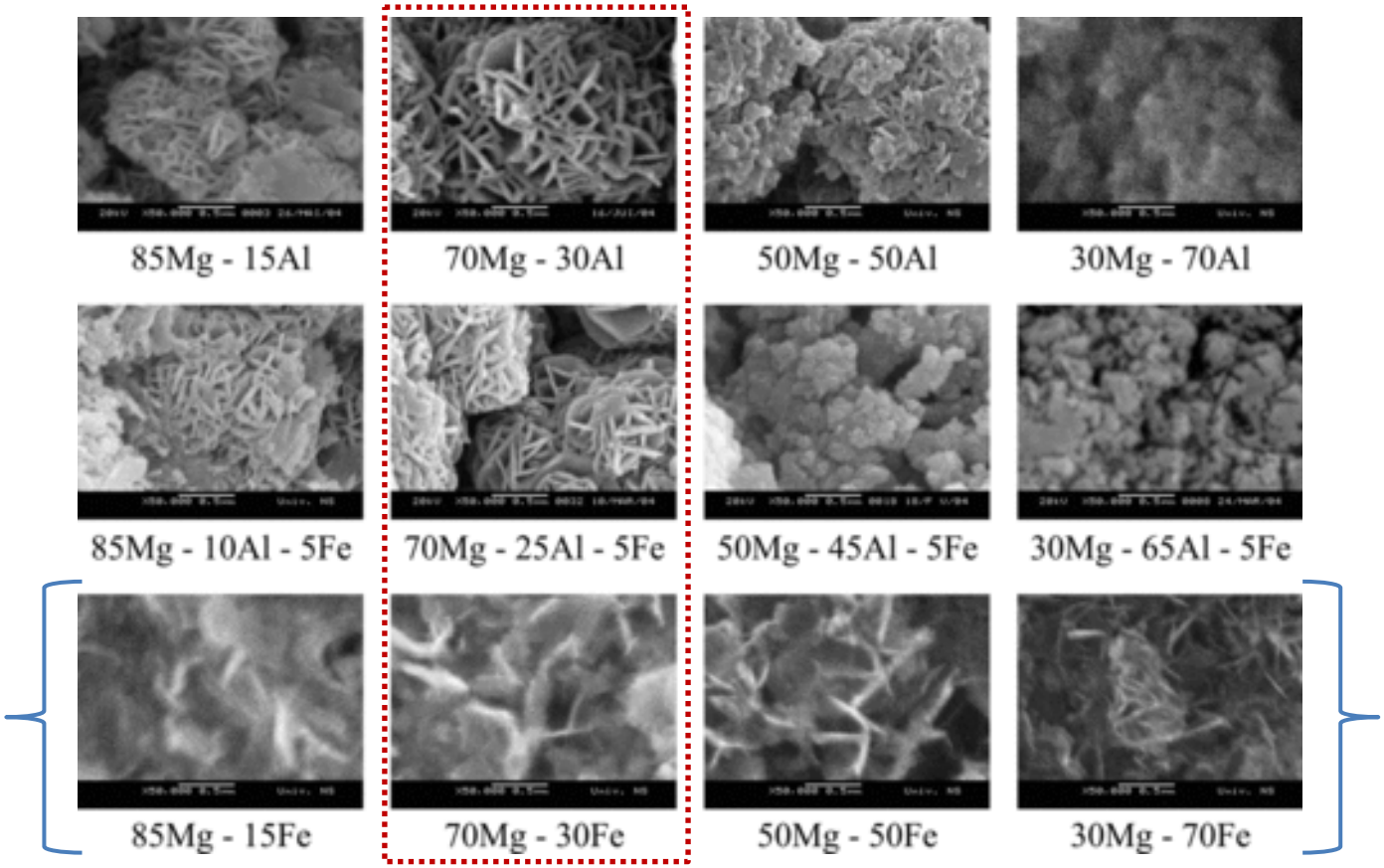

Figure 4.32 SEM micrograph of Mg–Al, Mg–Al–Fe and Mg–Fe-mixed oxides (magnification size: 50000×), by Vulić, Hadnadjev and Marinković-Nedučin (2008).

However, the nanostructures of $Mg(OH)_2$ also present very similar nanoflakes as the remarked square with estimated size of < 250 nm (Yunessnia lehi and Akbari 2017). Therefore, combining the implication from XRD analysis, it can be deducted that additional single M(III) hydroxide or $Mg(OH)_2$ may also exist.

The SEM micrographs of RM-w-CLDH are shown in Figure 4.33. Much less platelets are observed, with collapsed structure and more dense packing. R. M. M. Santos *et al.* (2017) presented very similar observation after the calcination of LDH. It is worth mentioning that RM-w-CLDH (Figure 4.33b) shows a relatively smooth surface roughness. Heredia *et al.* (2013) explained that this phenomenon is due to sintering of the oxides (Al_2O_3, MgO and iron oxides).

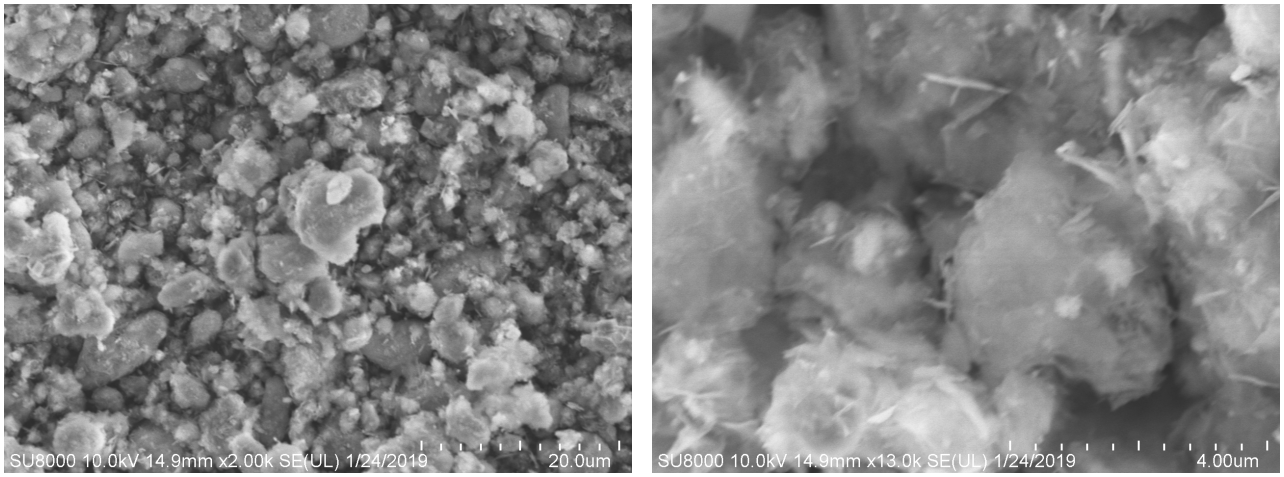

(a) *(b)*

Figure 4.33 Scanning electron microscopy images of (a-b) RM-w-CLDH

4.3.3 Rule III: FT-IR spectroscopic study

The FT-IR spectra of RM-LDHs and RM-CLDHs (Figure 4.34) agree well with the typical results obtained by hydrotalcite-like compounds (Ferna *et al.*, 1998; Ahmed and Gasser, 2012; Lin, Fang and Chen, 2014). The broad band observed in the range of 3100-3523 cm^{-1} is attributed to O-H stretching vibration of the layer surface and/or interlayer water molecules, with a wide range of strength (Abou-El-Sherbini *et al.*, 2015), which became weaker and shifted to lower degree after calcination. The weak bands at ~2166 cm^{-1} and ~1650 cm^{-1} are due to the H-O-H bending vibration of interlayer water molecules (Wang *et al.*, 2017). The strong band appeared at ~1385 cm^{-1} is due to the asymmetric vibration of the interlayer CO_3^{2-} ions (F. Zhang *et al.*, 2014). The bands observed in the low-frequency region of the spectrum are associated with the lattice vibration modes in the double layered sheets. The strong deformations bands at ~1003 and ~1010 cm^{-1} are attributed to Si-O and Si(Al)-O vibration (Castaldi *et al.*, 2010). The band around ~660 cm^{-} is assigned to the M-O bond (M = Al, Mg, Fe) (Cavani, Trifirò and Vaccari, 1991). It is noteworthy that the free OH groups in $Mg(OH)_2$ are responsible for the peak at ~3695 cm^{-1} (F. Zhang *et al.*, 2014), implying the starting material remained in the final product, especially for RM-w-LDH.

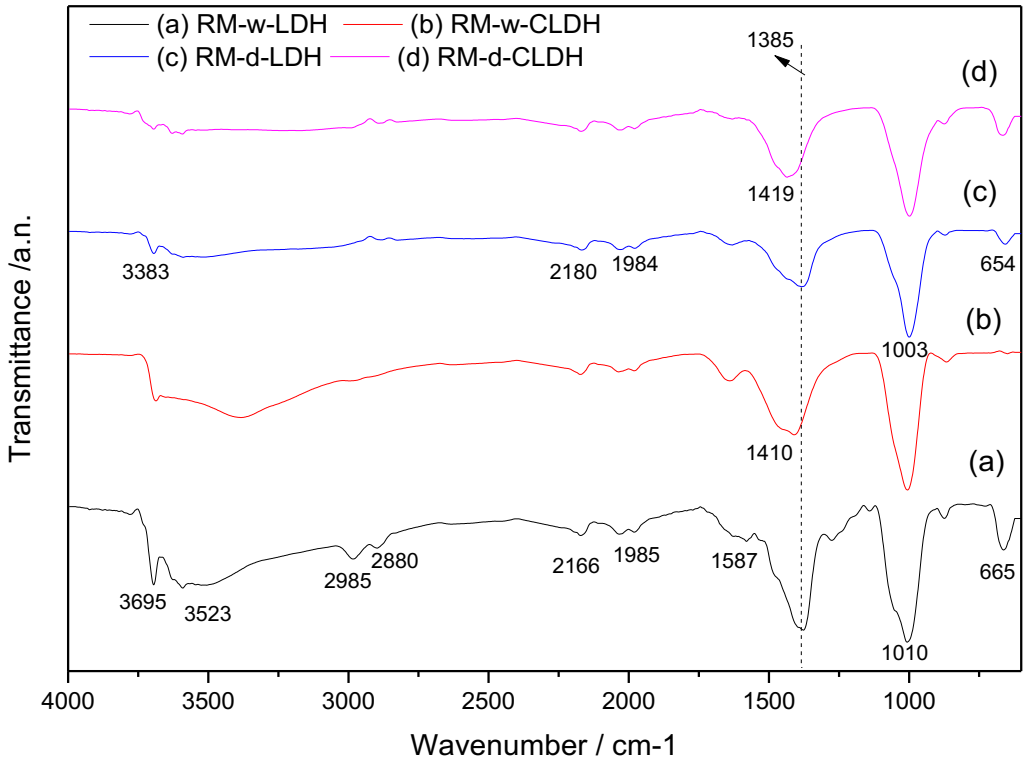

Figure 4.34 FTIR spectra of (a) RM-w-LDH (b) RM-w-CLDH (c) RM-d-LDH, (d) RM-d-CLDH

Comparing Figure 4.34a & 34c, the FT-IR spectrum of RM-w-LDH demonstrates stronger characteristics of LDH-like structures than RM-d-LDH. The bands attributed to metal-OH vibrations disappeared from RM-w-CLDH after calcination. The bands corresponding to OH^- and CO_3^{2-} vibrations were weakened but still present, suggesting absorption of water and CO_2 from air occurred during the collection and storage time, which is in agreement with the observation of Abou-El-Sherbini et al. (2015). On the other hand, Zhang *et al.* (2014) noted that $Mg(OH)_2$ presents a characteristic bond at ~1400 cm^{-1} (refer to Figure 4.35a), which may explain for the bands observed at ~1410 cm^{-1} and ~1419 cm^{-1} after calcination of RM-LDHs in Figure 4.34b & 4.34d, respectively.

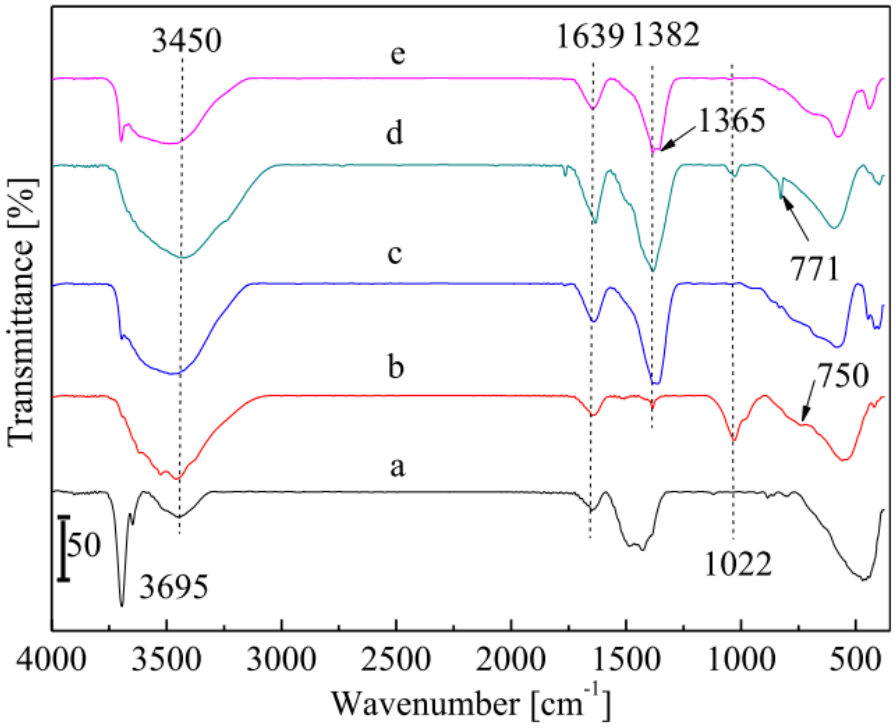

Figure 4.35 FT-IR spectra of (a) $Mg(OH)_2$, (b) $Al(OH)_3$, (c) MC-LDH by mechanochemical method, (d) MHT-LDH (T_{ht} =80°C, t_{ht} =12 h) by mechano-hydrothermal method, and (e) HT-LDH by hydrothermal method. $Ratio_{Mg/Al/Fe}$ of LDHs = 9:1.5:1.5, by Zhang et al. (2014).

4.3.4 Rule IV: TG-DTA

The thermal behaviour of RM-d-LDH is investigated, as illustrated in Figure 4.36. The DTG curve shows three temperature maxima, 1st at 172.3°C (weight loss =3.51%) is associated with the evaporation of intercalated water, and 2nd at 372.6°C (weight loss= 18.25%) refers to the decomposition of interlayer carbonate and hydroxyl groups of the lamellae, and 3rd small peak at 608.3°C (weight loss = 3.93%) is due to continuous dehydroxylation and decarbonation to form oxide metals. The presence of $Mg(OH)_2$ impurity may broaden the 2nd endothermic peak of RM-d-LDH, as $Mg(OH)_2$ owns a strong derivative weight peak at 393°C upon decomposition (Pang *et al.*, 2011). However, single mass loss is observed in this range (250-500°C), indicating the coupling of dehydroxylation and decarbonation process (Pérez-Ramírez *et al.*, 2001), which confirms the existence of a united brucite-like structure (i.e. one composed of di- and trivalent cations, refer to Figure 2.6).

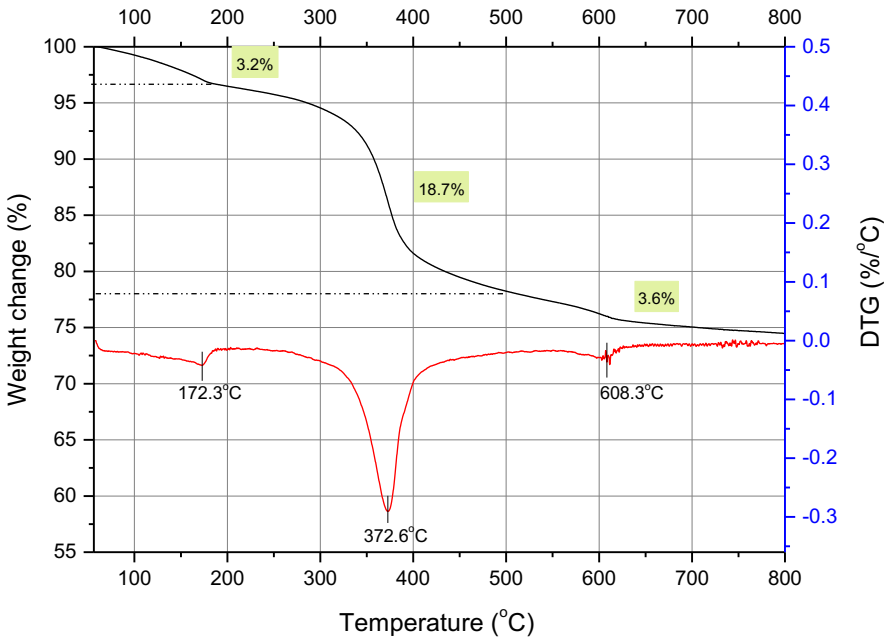

Figure 4.36 TGA and its derivative scan for RM-d-LDH

Similar to RM-d-LDH decomposition, RM-w-LDH (Figure 4.37) also demonstrates three distinct stages of weight loss. That is in agreement with the TG-DTG curves of typical hydrotalcites, as discussed in Section 2.4.1.4 - Rule IV. The weight losses occurred at temperature maxima of 182°C, 384.3°C and 633.5°C respectively, with 3.6% for loss of the interlayer water, 19.5% for decomposition of the layered structures and 2.6% for removal of strongly held hydroxyl and carbonate groups. The corresponding peaks shift to slightly higher temperatures compared with RM-d-LDH, suggesting a stronger brucite-like structure.

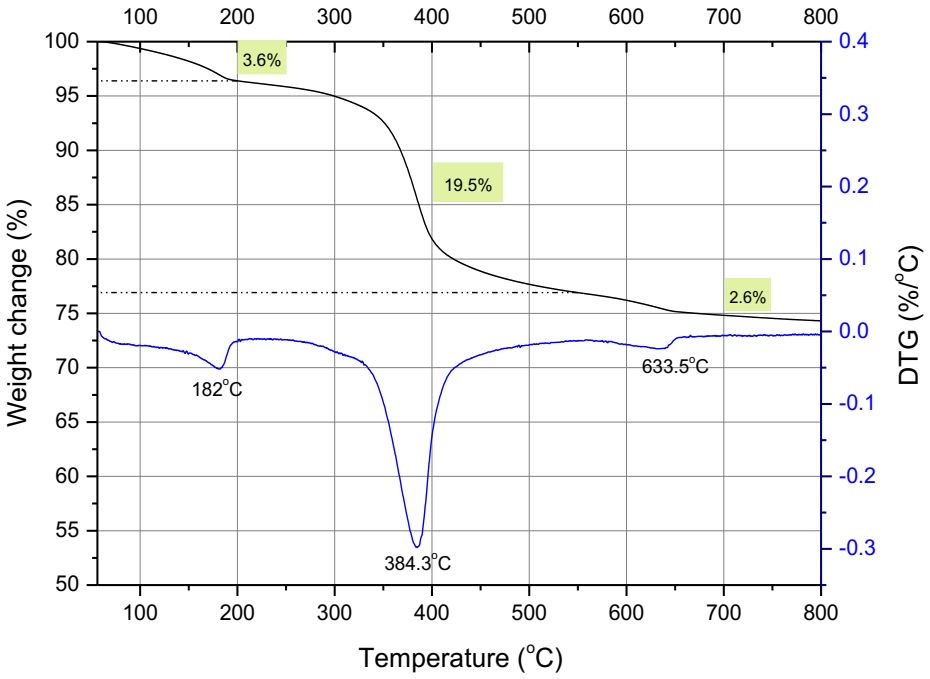

Figure 4.37 TGA and its derivative scan for RM-w-LDH

The thermal results obtained in this study are compared with the TGA analysis by Heredia *et al.* (2013), including the weight loss and the DTG maximum temperature (Figure 4.38). Heredia *et al.* (2013) investigated the thermal characteristics of LDHs with different Fe^{3+} percentage in detail. It can be observed from Figure 4.38a, the maximum endothermic peaks in the DSC profile centred between 345°C and 396°C and they shifted to lower temperature when the content of Fe was increased. The positions of corresponding endothermic peaks of the RM-LDH products (Figure 4.36-37) are closer to those of the HT_{75} and HT_{50} samples. Figure 4.38b demonstrates a decrease in the total weight loss with an increase in the Fe content. The amount and proportion of weight loss in each stage for RM-d-LDH and RM-w-LDH are most similar to those of the HT_{75} sample. Therefore, a high composition of Fe ($Fe^{3+}/Fe^{3+} + Al^{3+}$= 50-75%) likely exists in RM-LDHs, which agrees well with the EDX results. The rich Fe content could subsequently enlarge the brucite interlayer distance and weaken the brucite-like structure (Paikaray and Hendry, 2012; Heredia *et al.*, 2013). As a result, in comparison with pure Mg/Al LDH materials (Figure 2.27), a lower dehydroxylation temperature of the brucite-like sheets (372.6°C and 384.3 °C maxima) and a relatively lower mass loss (25.5% and 25.5%) are observed in RM-LDH product. Same effects caused by Fe^{3+}content on thermal behavior have previously been reported by Yun Zhao *et al.* (2002), Vulić, Hadnadjev and Marinković-Nedučin (2008) and Rozov *et al.* (2010).

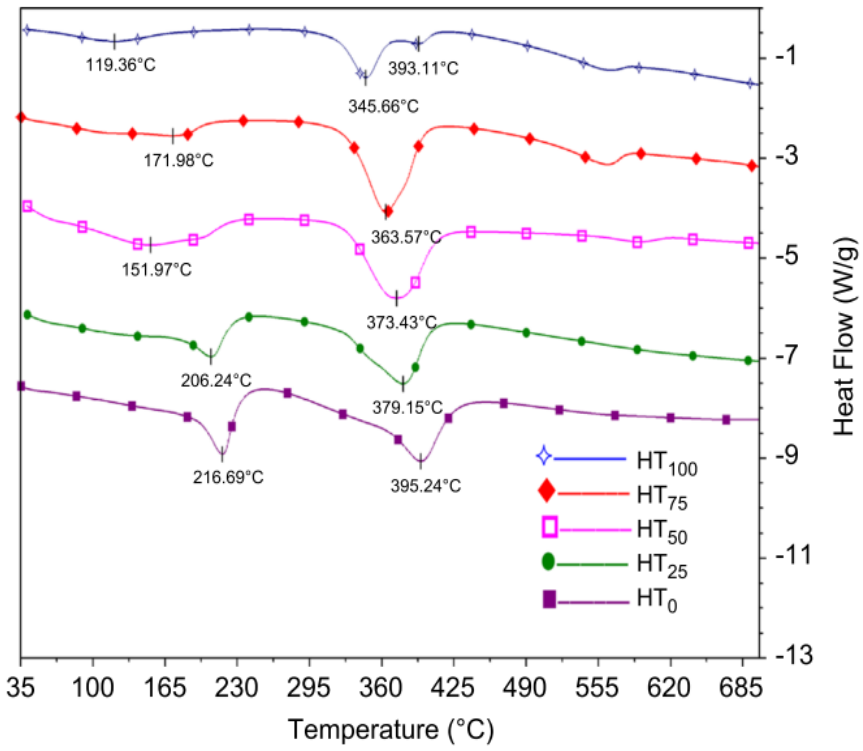

(a) DSC curves for LDH with different iron percentages.

(e.g. HT_{75} represents = 75%, theoretical M^{2+}/M^{3+} ratio = 3)

Table 3
Results of the TGA–DSC for different samples.

Sample temperature range (°C)	Observed weight loss (%)	DSC maximum (°C) ± 0.01 °C
HT_0		
Until 100	1.92	45.22
100–300	15.6	261.9
300–550	25.19	395.03
Total weight loss	42.71	
HT_{25}		
Until 100	1.57	64.41
100–300	13.84	206.62
300–550	25.14	378.73
Total weight loss	40.55	
HT_{50}		
Until 100	1.19	64.33
100–300	8.99	151.97
300–550	26.62	373.43
Total weight loss	36.8	
HT_{75}		
Until 100	1.87	102.59
100–300	5.56	179.34
300–550	22.94	363.37
Total weight loss	30.37	
HT_{100}		
Until 100	1.53	119.36
100–300	4.08	120
300–550	15.86	345
Total weight loss	21.47	

(b) Results of the TGA–DSC for different samples.

Figure 4.38 Literature thermal analysis for Mg-Al-Fe LDH, by Heredia et al. (2013)

4.4 Other Characteristics of As-synthesised Products

To better understand the physical properties of the synthesised RM-LDHs, this section focuses on their particle size, BET surface area and pore size distribution. In addition, as discussed in Section 2.3.3.2, the impact of Fe content in the original material is considered. The magnetic behavior of the RM-LDHs is therefore investigated.

4.4.1 Particle size

As shown in Figure 4.39, RM-d-LDH has an average particle diameter of 6.61 μm, ranging from 2 to 30 μm; while RM-w-LDH has a narrower distribution from approximately 1.5 μm to 15 μm, centred at 4.37 μm, which are consistent with the SEM observations. That suggests that RM-w-LDH owns more uniform and finer particles. Therefore, the wet-grinding method results in samples with better dispersity. In addition, compared with Figure 4.6, the particle sizes of RM-d-LDH and RM-w-LDH were significantly increased from that of the starting materials IRM and Cal-IRM (D_{50} = 0.12 μm, 0.10 μm respectively). The proportion of small silt-sized particles (2-50 μm) has reached to more than 90% in RM-LDH samples. Conventional coprecipitation method usually yields LDH aggregates with size of 1-10 μm (Yun Zhao *et al.*, 2002). Wang et al. (2017) pointed out that the particle size of Fe-containing LDH was much smaller than Mg-Al LDH.

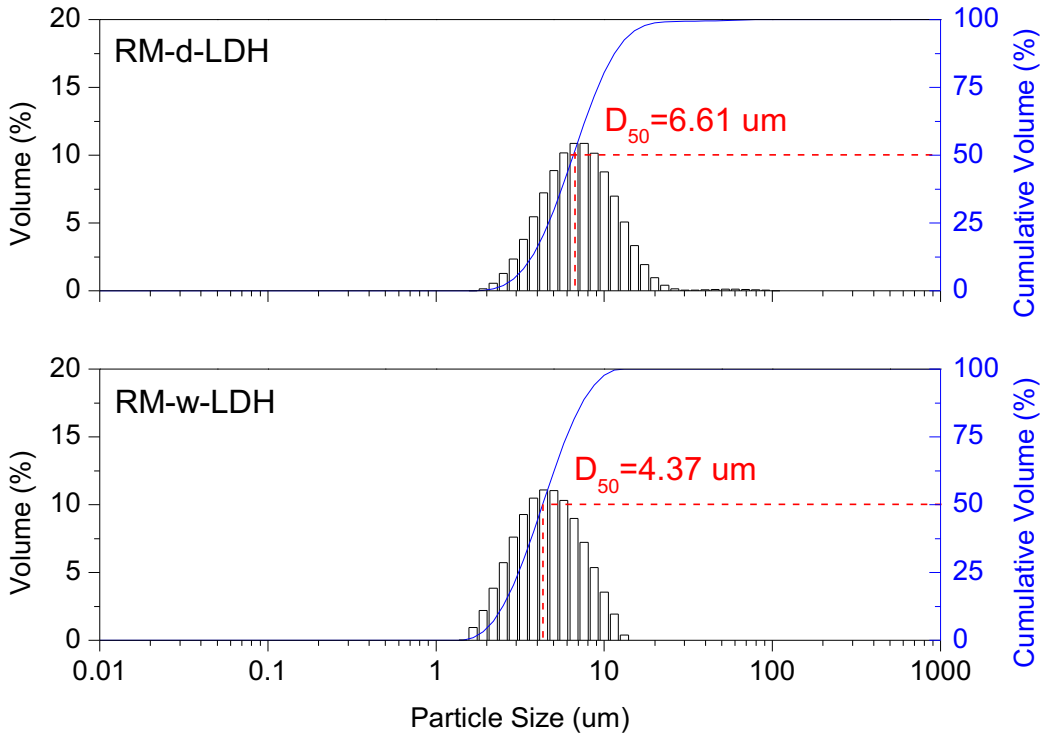

Figure 4.39 Particle size distributions of RM-d-LDH and RM-w-LDH

As shown in Figure 4.40, RM-w-CLDH sample presents bimodal particle size distribution with maxima around 5.0 and 60 μm, and a mean size of about 6.61 μm. It is in agreement with the SEM observation in Figure 4.31. A higher degree of agglomeration over a wider distribution range than RM-w-LDH is observed for RM-w-CLDH. RM-w-CLDH mostly contains silt particles with diameters between 2-50 μm. However, calcination led to the formation of sand-sized particles (> 50m) appeared after the calcination, accounting for approximately 20 vol%.

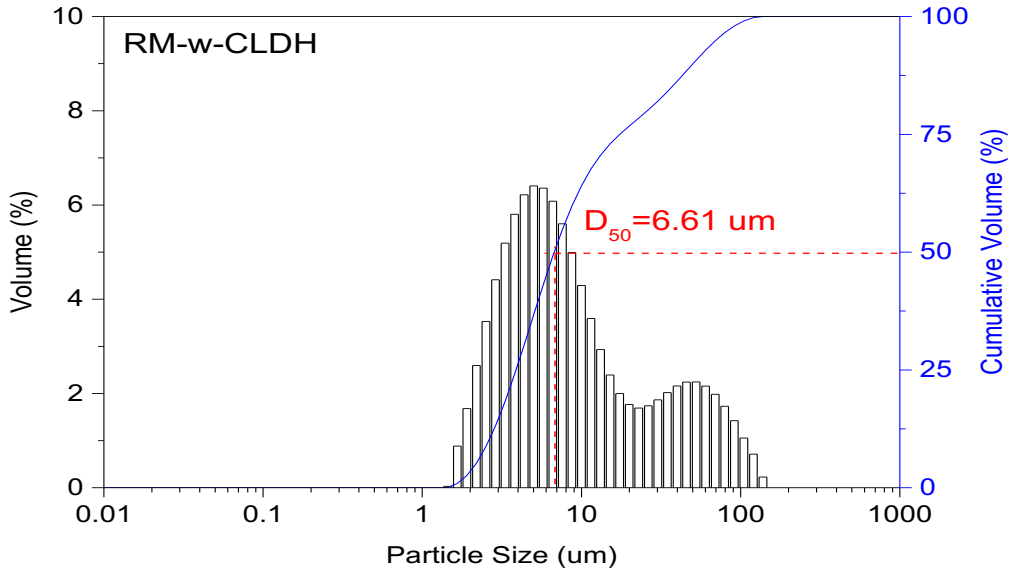

Figure 4.40 Particle size distributions of RM-w-CLDH

In comparison, the particle sizes of the commercially available Mg-Al LDH before and after calcination are demonstrated in Figure 4.41. Their adsorption performance will be assessed against RM-LDHs in Chapter 5 & 6. The average particle size of the LDH is in the nanometer range of about 180 nm, which is considerably smaller than that of RM-LDHs prepared using Scenario III. However, the particle size distribution for the LDH is much broader than that of RM-LDHs (Figure 4.41). By having calcined, the resulting CLDH shifts to larger particle size (8.71 μm) but over narrower distribution range.

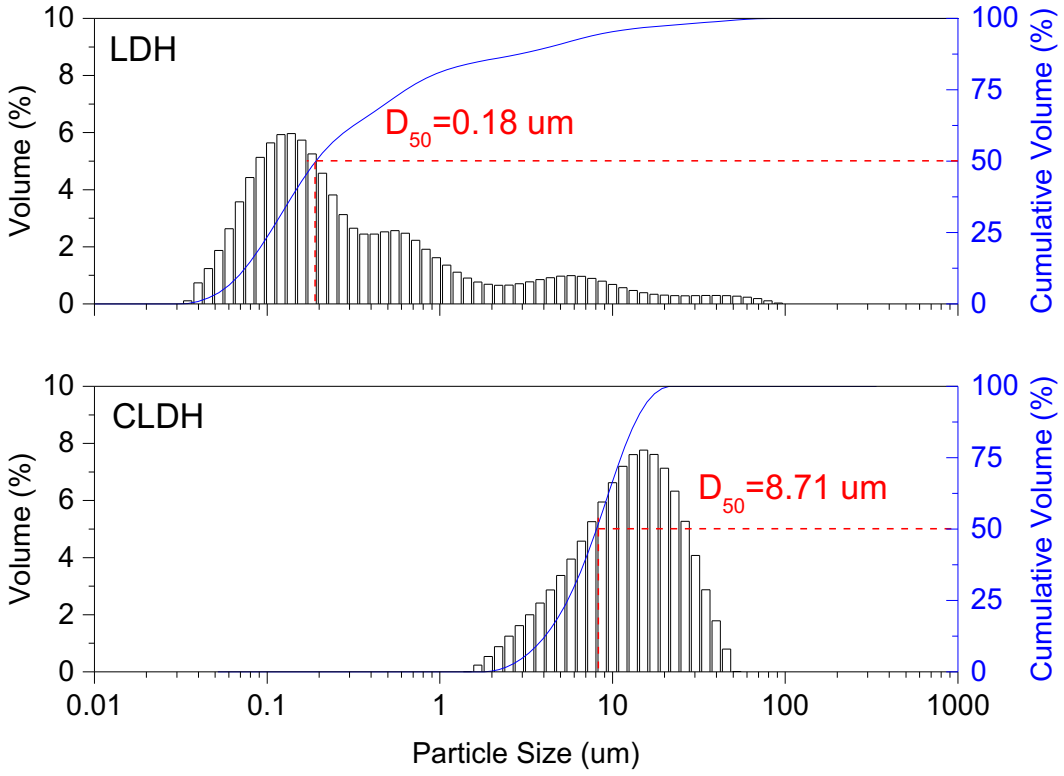

Figure 4.41 Particle size distributions of LDH and CLDH

4.4.2 BET surface area

According to Table 4.11, the BET surface area of RM-w-LDH is 64.0 m^2/g, its average pore size is 8.92 nm and total pore volume is 0.143 cm^3/g; while RM-d-LDH shows larger S_{BET} (74.8 m^2/g), wider pore size (10.9 nm) and larger pore volume (0.204 cm^3/g). Both samples present bimodal size distribution with the small mesopore range (2-5 nm, peak at approximately 3.0 nm) and the large mesopore range (5-50 nm, peak at around 20 nm), as displayed in Figure 4.42. RM-d-LDH possesses larger fraction of bigger mesopores that contributes to its higher surface area. This difference between the surface area of RM-d-LDH and RM-w-LDH could not be clearly distinguished from their TG/DTG analysis, in which RM-d-LDH does not possess larger quantity of physiosorbed and interlayer water as expected, instead less 1st weight loss is found (see Figure 4.36 & 37).

Table 4.11 Surface area and pore size of RM-w-LDH and RM-d-LDH

	BET surface area S_{BET} (m^2/g)	t-plot micropore area (m^2/g)	t-plot external surface area (m^2/g)	Average pore width (nm)	Total pore volume (cm^3/g)
RM-w-LDH	64.0	9.20	54.8	8.92	0.143
RM-d-LDH	74.8	12.8	62.0	10.9	0.204

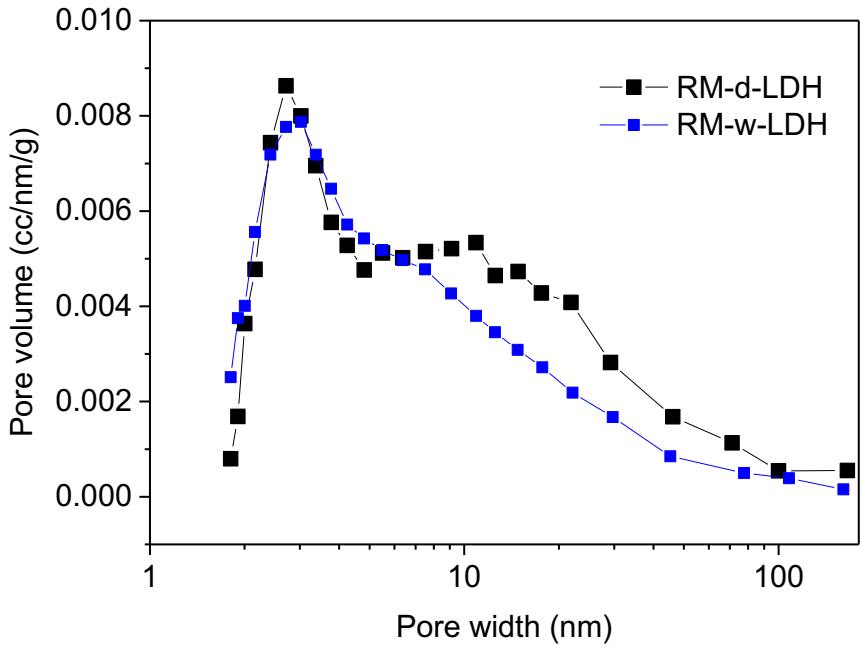

Figure 4.42 Differential pore volume distribution of RM-d-LDH and RM-w-LDH

Vulić, Hadnadjev and Marinković-Nedučin (2008) studied the influence of M(II): M(III) ratio on LDH pore size distribution, as shown in Figure 4.43. The authors discovered that when LDH samples having M(II): M(III) < 5.7, their pore size show bimodal distribution with the fraction of smaller mesopores from 2 to 4 nm and larger mesopores from 10 to 20 nm. Wang *et al.* (2013) suggested the pore size distribution of LDH synthesized by the conventional coprecipitation method (see Figure 4.44), which is also similar to the bimodal shape of distribution in Figure 4.42.

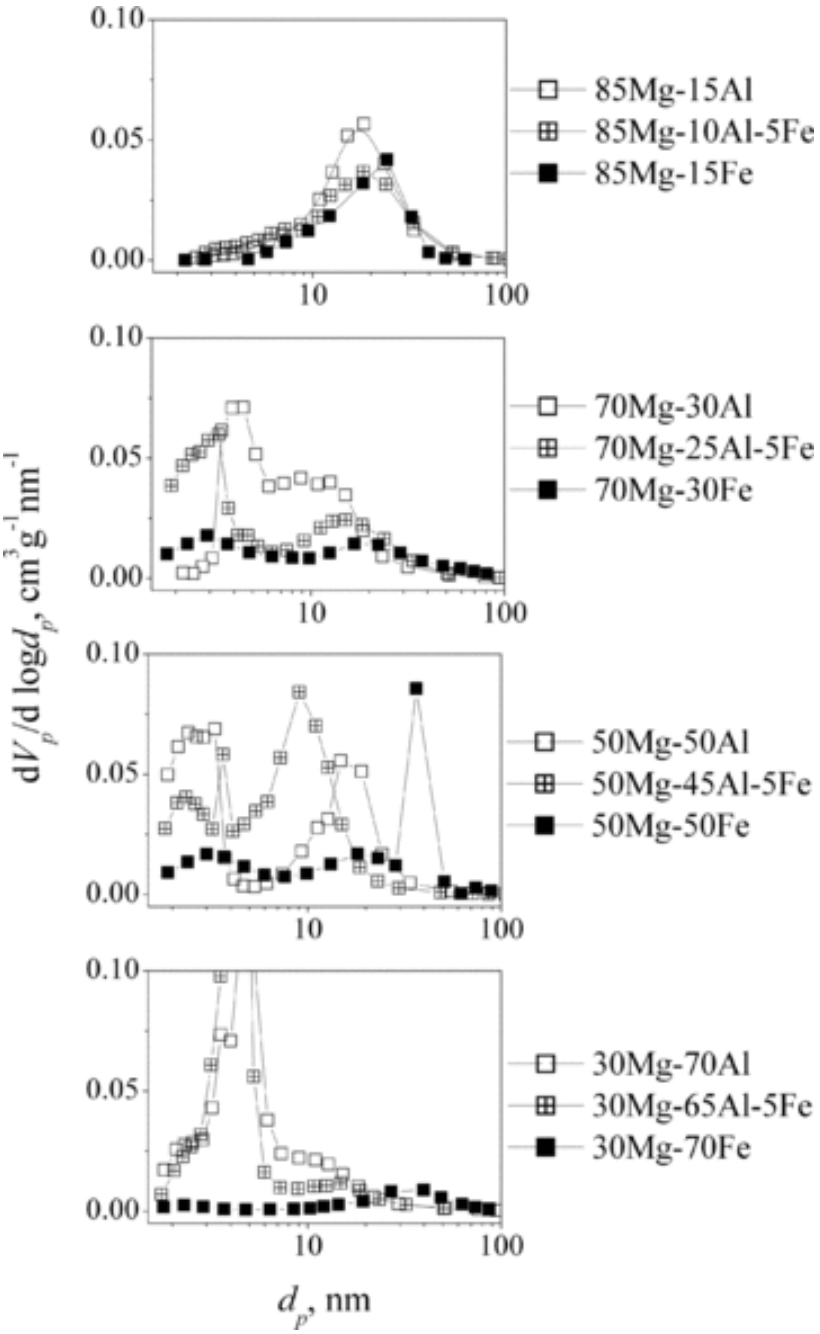

Figure 4.43 Pore size distribution of LDH-derived mixed oxides depending on M(III) ion content, by Vulić, Hadnadjev and Marinković-Nedučin (2008).

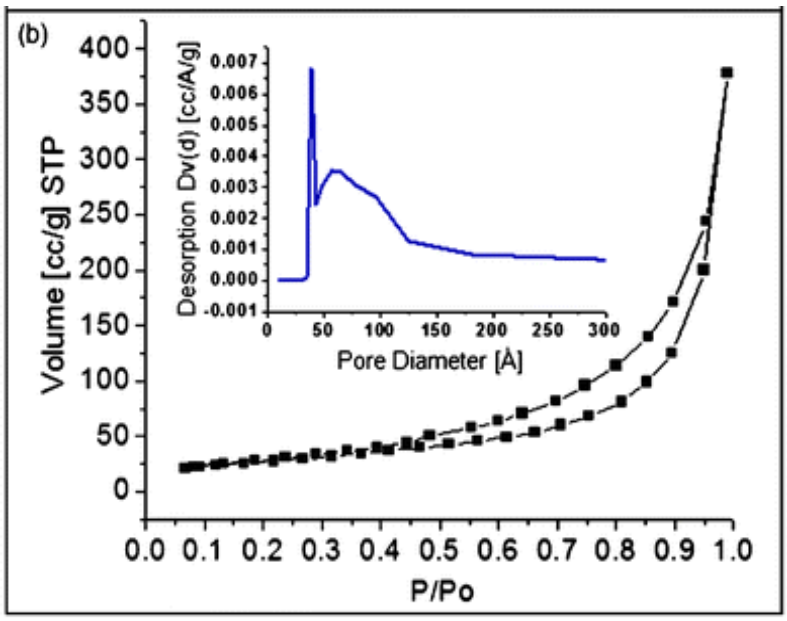

Figure 4.44 BET isotherm patterns of Mg-Al-CO_3 LDH synthesised by conventional co-precipitation method. The inset shows the pore size distributions (Wang *et al.*, 2013)

The surface area and pore size distribution of RM-w-LDH and RM-w-CLDH are shown in Table 4.12 and Figure 4.45 respectively. Upon calcination, the S_{BET} of RM-w-CLDH increased from 64.0 to 79.8 m^2/g, which is very similar to the Mg/Al/Fe-CLDH prepared by Wang *et al.* (2017). This is consistent with the observation of Vulic, Reitzmann and Lázár (2012), the BET specific surface area of synthesised LDH are usually between 70 and 100 m^2/g. They also found that calcination enlarged the S_{BET} of Mg-Fe LDH from 64.0 m^2/g to 126 m^2/g, which are similar to other studies (See Table 4.14). Abou-El-Sherbini et al. (2015) pointed out that the surface area of calcined LDH varies with the kind and loading of transition metal (Cu and/or Co). A low content of transition metal maximises the surface area.

Upon calcination, the average pore diameter of RM-w-CLDH increased from 8.92 to 10.47 nm and the total pore volume also grew from 0.143 to 0.209 cm^3/g. The pore size distribution of RM-w-LDH (Figure 4.45) shows the maximum contribution by pores with a diameter near 3.0 nm and a major contribution by pores in 4.0-10.0 nm; while RM-w-CLDH shows a broader distribution centred at 4.5 nm and larger pore volumes both in mesoporous range 3-11 nm and macroporous range 50-100 nm, which consequently leads to its higher surface area. Evolution of this pore system has been explained by (Ulibarri *et al.*, 2001), suggesting that carbon dioxide escape through holes in the crystal surface which turn to small craters. Table 4.14 lists the changes observed on pore parameters in other literature, indicating that the pore volume and the pore size of LDH are increased upon calcination.

Table 4.12 Surface area and pore size of RM-w-LDH and RM-w-CLDH

	BET surface area S_{BET} (m^2/g)	t-plot micropore area (m^2/g)	t-plot external surface area (m^2/g)	Average pore width (nm)	Total pore volume (cm^3/g)
RM-w-LDH	64.0	9.20	54.8	8.92	0.143
RM-w-CLDH	79.8	10.61	69.2	10.47	0.209

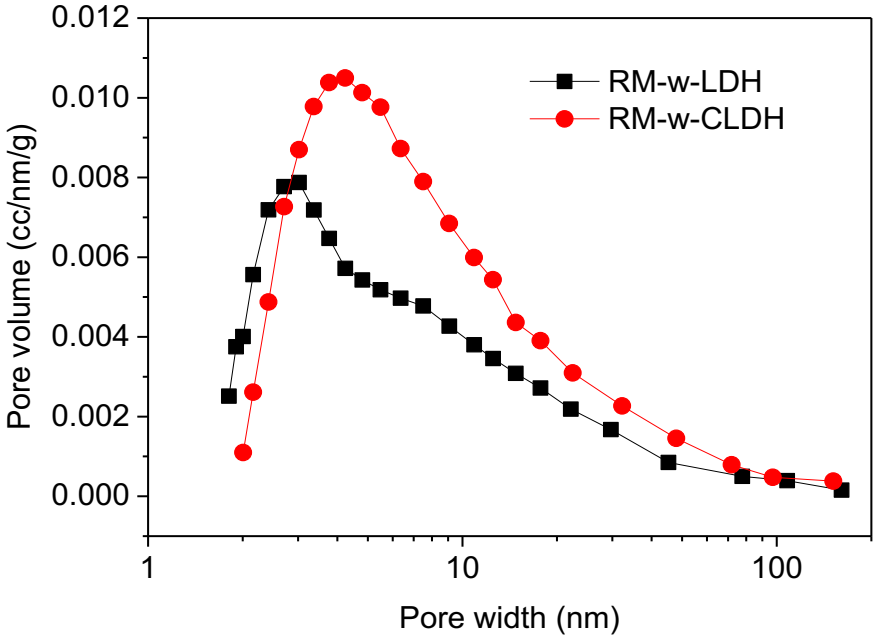

Figure 4.45 Differential pore size distribution of RM-w-LDH and RM-w-CLDH

Table 4.13 presents the relevant physiochemical properties of commercially available Mg-Al LDH. The surface area of CLDH experienced a considerably increase by more than 10 times, reaching to 105.11 m^2/g after calcination. Similar to RM-w-LDH products, the majority of surface areas of LDH and CLDH are contributed by external surface area.

After calcination, the pore size of CLDH (3.81 nm) decreased to half of that of LDH (7.65 nm). Figure 4.46 implies that LDH likely possesses well-packed layered structure with little pore volume in between. On the other hand, the pore size distribution of CLDH shows that almost all the pores fall in the mesopore size range and a very narrow peak centres at 3.0 nm. The total pore volume of CLDH (0.100 cm^3/g) became almost 7 times of the original LDH. That demonstrates the loss of structure water and intercalated ions results in more porous microstructure due to cratering effect. A larger surface area can offer more active adsorption sites, which might potentially induce a higher dye pollutant adsorption capacity.

Table 4.13 Surface area and pore size of LDH and CLDH

	BET surface area S_{BET} (m^2/g)	t-plot micropore area (m^2/g)	t-plot external surface area (m^2/g)	Average pore width (nm)	Total pore volume (cm^3/g)
LDH	8.35	N.A.	11.1	7.65	0.015
CLDH	105.11	N.A.	135.1	3.81	0.100

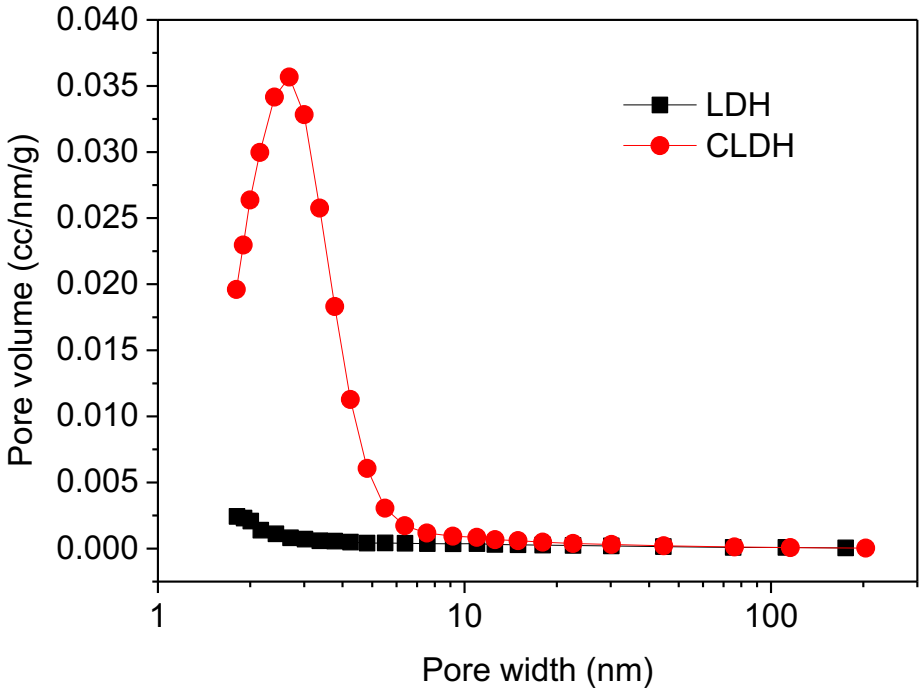

Figure 4.46 Differential pore size distribution of LDH and CLDH

Furthermore, Table 4.14 summaries the BET surface area and the pore parameters of typical LDHs and CLDHs in previous studies (see also Table 2.16). In comparison, RM-LDHs and RM-w-CLDH display very similar physicochemical properties. Therefore, RM-LDHs have the potential to be applied in practical applications, although they are not constituted by pure LDH phases.

Table 4.14 Surface area and pore size of typical LDHs and CLDHs in the literature

LDH Product	BET surface area S_{BET} (m^2/g)	Pore volume (cm^3/g)	Average pore diameter (nm)	Composition molar ratio	Reference
Mg-Al CLDH	254	1.148	3.6; 39.7	Mg: Al = 0.75: 0.248	(Valente *et al.*, 2010)
Mg-Al-Fe CLDH	237	0.623	3.6; 19.2	Mg: Al: Fe = 0.65: 0.286: 0.06	
MgAl–CO_3 LDH	80	0.215	8	Mg: Al = 0.74: 0.26	(Extremera *et al.*, 2012)
MgAl–CO_3 CLDH	94	0.32	11		
MHT-LDHs	83.2	0.21	3.83	Mg: Al: Fe = 9: 1.5: 1.5	(F. Zhang *et al.*, 2014)
Mg–Al–Cu–Fe-CO_3 LDH	48.5	0.361	20.8	Cu: Mg: Al: Fe = 0.63: 0.14: 0.08: 0.15	(Harizi *et al.*, 2018)
Mg–Al–Cu–Fe-CO_3 CLDH	69.67	0.369	32.1		

**CLDH stands for Calcined LDH; MHT stands for Mechano-hydrothermal method.*

4.4.3 Magnetic property

As discussed in Section 2.3.3.2, the magnetic properties of RM and its products are of interests. The possible Fe minerals in RM products are spinel ferrite MFe_2O_4 (M = Mg, Zn, Co, Ni, etc), magnesium-ferrite aluminate, iron oxides Fe_3O_4, maghemite (γ-Fe_2O_3) and α-Fe_2O_3 (Pulford *et al.*, 2012; Heredia *et al.*, 2013). Here, the hysteresis cycles of AOS RM, AOS CRM, RM-I and RM-II products have been investigated using vibrating sample magnetometer (VSM). The magnetic hysteresis displays different features, such as remanence magnetization (Mr), coercivity (Hc), saturation magnetisation (Ms) and shape of non-linear magnetisation curve.

Figure 4.47 and Figure 4.48 display the magnetic behaviour of original AOS RM and CRM, respectively. The magnetizations at the maximum applied magnetic field for AOS RM and CRM are 0.10 and 0.08 emu/g, respectively. The coercivity (Hc) of AOS RM and CRM are approximately 1200 Oe and 2000 Oe respectively, which are comparable to that of α-Fe2O3 nanoparticles (Ma et al., 2010). The presence of wasp-waisting of the hysteresis loops indicates more than one magnetic mineral exist in AOS RM and CRM (Salomé Dominique Schnyder, 2010). Similarly, Belviso *et al.* (2015) states that red mud is dominated by anti-ferromagnetic oxy-hydroxides like hematite and goethite, together with a small portion of ferro(ferri)magnetic oxides. The combination of antiferromagnetic and ferromagnetic components leads to the weak ferromagnetic behaviours. Compared with AOS RM, CRM presents a lower saturation magnetism and a slightly gentle hysteresis.

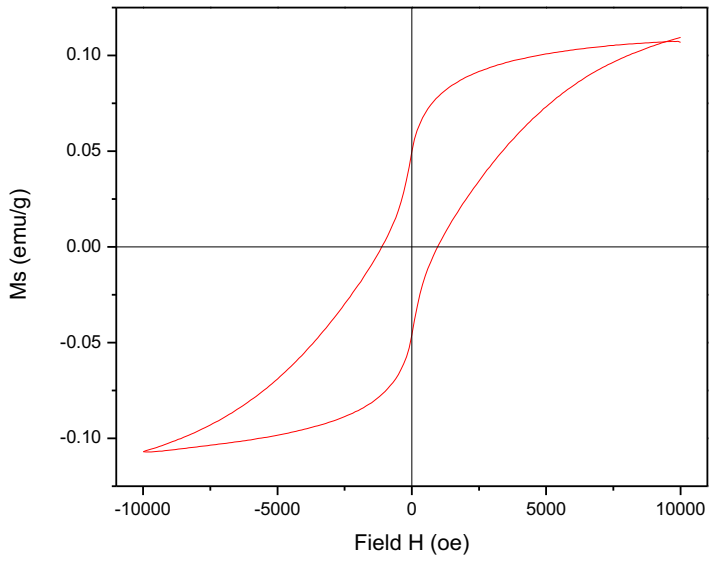

Figure 4.47 Hysteresis loop at room temperature of un-calcined RM

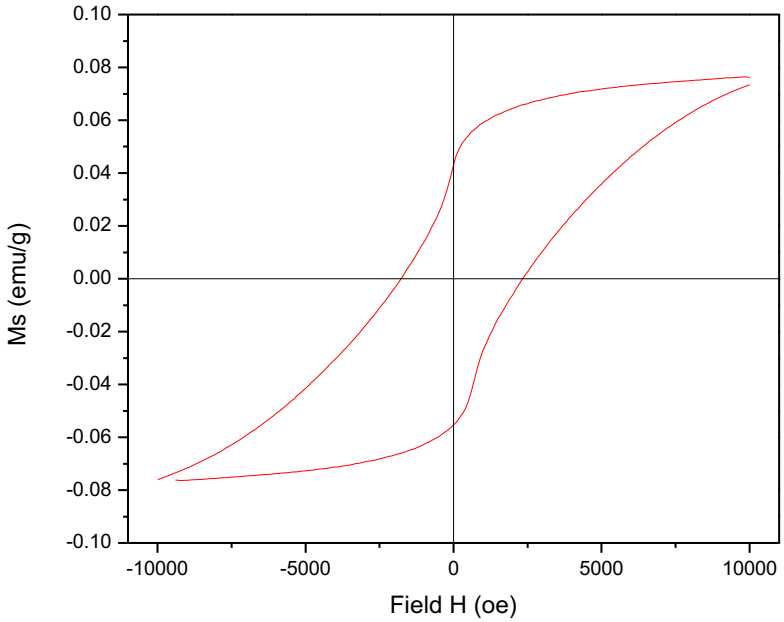

Figure 4.48 Hysteresis loop at room temperature of calcined RM

The magnetic behaviours of the as-synthesised RM-I product ($MgCl_2$: RM = 3:1) and RM-II product (MgO: RM = 3:1) are presented in Figure 4.49 and Figure 4.50. The magnetisation (M) vs. the field (H) is recorded at 299K, from -10 to 10 KOe. The hysteresis cycles of both materials exhibit the characteristics of weak-ferromagnetic solids (Lu, Salabas and Schüth, 2007). Therefore, RM-I and RM-II are still dominated by the oxide-hydroxides from red mud. A small coercivity of around 1000 Oe is observed for both RM-I and RM-II. No actual saturation of the magnetization can be observed up to the maximum applied field. Their magnetizations at M_{max} (10 KOe) are around 0.0015 emu/g and 0.0012 emu/g, respectively. They are remarkably lower than that of original RM materials, implying hematite (α-Fe2O3) may be the predominant contribution to the magnetism of AOS RM and CRM. The newly formed hydroxides phases in RM-I and RM-II weaken the overall magnetism.

It is previously reported that Co-Al LDH and Ni-Al LDH behave as ferromagnets, whereas Mg/Al-LDHs normally exhibit antiferromagnetic behaviour (Pérez-Ramírez *et al.*, 2002). A number of hybrid Fe_3O_4/LDHs have been synthesised via various routes for different purposes (Prasad, Tang and Liu, 2018). For instance, Lu *et al.* (2017) prepared magnetic Fe_3O_4/MgAl-LDH nanomaterial, whose coercive field and saturation magnetization were 35 Oe and 38 emu/g, respectively. From another perspective, the saturation magnetisation of spinel $MgFe_2O_4$ produced from calcined intercalated LDH at 750-1100°C is reported to be

10.6-24.1 emu/g (Meng *et al.*, 2004). Therefore, to enhance the magnetism of the synthesised samples, thermal treatment of RM-LDHs at a much higher temperature than 500°C is an option, so that spinel ferrite could be generated. However, this is beyond the key objectives of the present study.

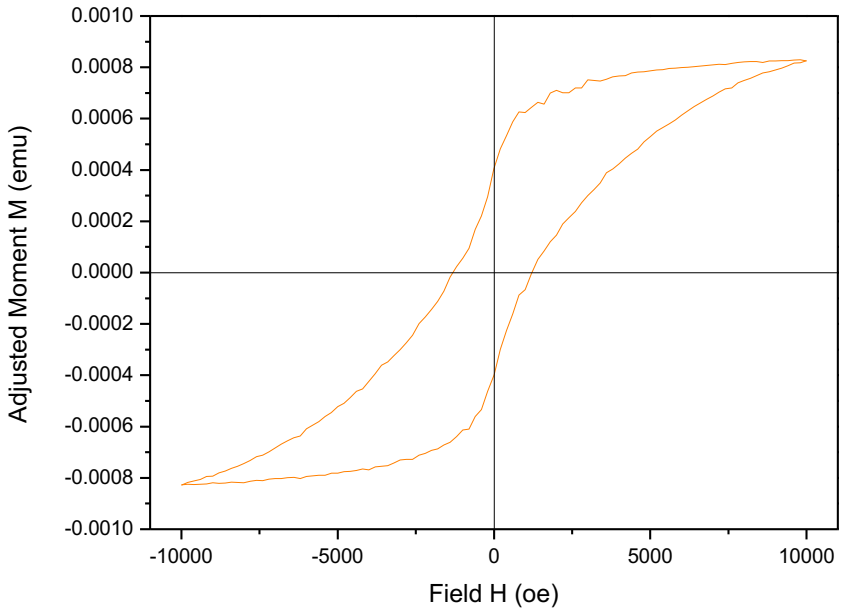

Figure 4.49 Hysteresis loop at room temperature of RM-I product ($MgCl_2$: RM = 3:1)

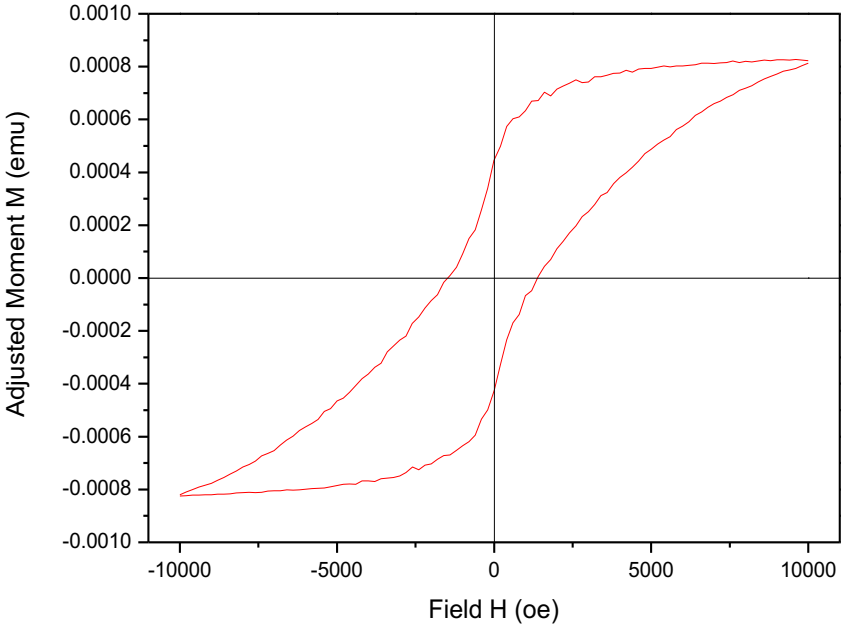

Figure 4.50 Hysteresis loop at room temperature of RM-II product (MgO: RM = 3:1)

Since anisotropy plays a controlling role, the magnetic properties of a material are closely related to its size, shape and morphology (Song and Zhang, 2004). Ma *et al.* (2010) carried out the magnetic hysteresis measurements for three α-Fe_2O_3 nanostructures with different particle sizes and shapes, as shown in Figure 4.51. Up to the maximum applied magnetic field (M_{max}) of 1T, the as-obtained α-Fe_2O_3 samples have not completely reached to their magnetization saturations, which are similar to the results observed in Figure 4.47-50. Amongst different samples, nanoparticles-aggregated α-Fe_2O_3 microcubes exhibited wide-open M-H loops with higher coercivity (Hc, 3756 Oe); while the nanoparticle and nanopolyhedra α-Fe_2O_3 possess smaller coercivity (Hc, 666.3 Oe and 345 Oe, respectively) and weaker hysteresis loop.

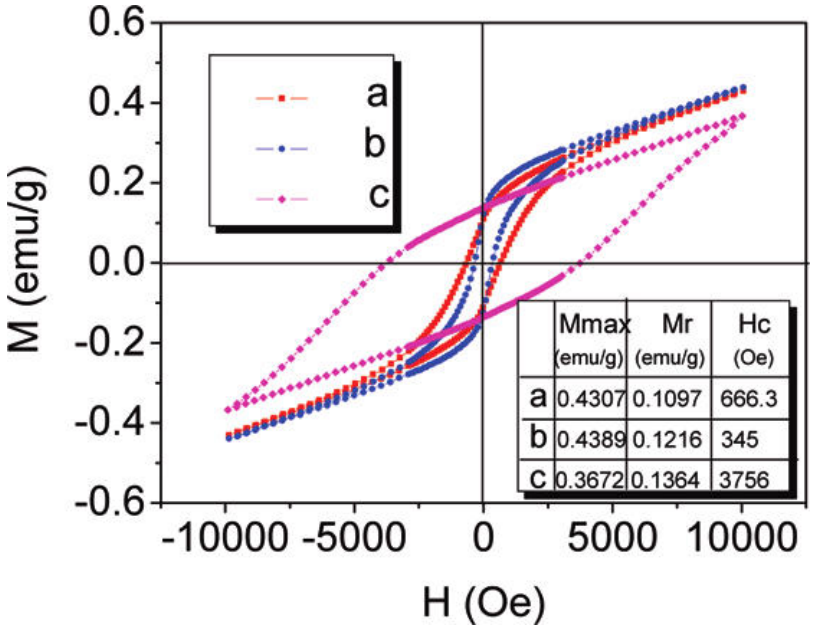

Figure 4.51 Magnetic hysteresis loops of as-prepared samples measured at room temperature by Ma et al. (2010): (a) nanoparticles, (b) nanopolyhedra, and (c) nanoparticles-aggregated α-Fe_2O_3 microcubes

4.5 Discussion and Summary

Chapter 4 has investigated four different routes for synthesising LDHs using AOS RM and Ireland RM. The effects of pre-treatment and process variables have been discussed. Scenario III that employs IRM and MgO, presents the products with the most distinctive characteristics of a typical LDH material. As a result, the main RM-III products have been named as RM-LDHs. The optimum experimental parameters have been summarised in Table 4.10, Section 4.2.5. However, it was not easy to distinguish between the dry-grinding and wet-grinding RM-LDH products.

The mineralogical and morphological features of RM-LDHs have been presented in Section 4.2-4.4. The main characterisation outcomes of RM-LDHs can be summarised as: The XRD, FT-IR and TG-DTA analysis of RM-LDHs and RM-CLDHs agree well with the typical hydrotalcite-like compounds. The average particle sizes of RM-LDHs are between 4.37 to 6.61 μm. The surface areas are ranged from 64.0 to 75.0 m^2/g for fresh samples and around 80.0 m^2/g for calcined sample. Pore size distributions for both RM-LDHs show bimodal shape. The micrographs of both RM-d-LDH and RM-w-LDH reveal well-dispersed platelet structures. In comparison, RM-d-LDH presents higher morphological homogeneity and better dispersed platelets, while RM-w-LDH presents more irregular aggregation of small crystallites. However, the featured hexagonal platelet of LDH phase cannot be detected. Calcination treatment at 500°C is able to destroy the layered structures of RM-LDHs. Overall, the results suggest that both RM-LDHs and RM-CLDHs display similar properties to conventional LDHs and CLDHs.

Section 4.3 confirms that hydrotalcite-like layered structures were successfully synthesised through Scenario III. LDH phases account for at least 20 wt% of the synthesised RM-LDHs. The RM-LDH products are carbonates ion intercalated $Mg^{2+}/(Al^{3+}, Fe^{3+})$-LDH, with a higher substitution of Fe^{3+} than Al^{3+} in the brucite-like hydroxide sheet. The slightly lower Al content than expected could be associated with its lower concentration compared with Fe, as well as the limited solubility of aluminium ions as aluminate species under the synthesis conditions (Klemkaite *et al.*, 2011). Zhang *et al.* (2014) also suggested that Fe^{3+} is favourable for the LDH-phase formation compared with Al^{3+}, owing to a lower ionic radius difference between Mg^{2+}(0.72 Å) and Fe^{3+} (0.645 Å).

The mechanism of forming LDH phases under the designed condition have been explained in detail. The ‘dissociation-deposition-diffusion’ model (see Figure 2.9) is likely to explain for

the LDH synthesis, which previously corresponds to the mechanism of salt-oxide method, as mentioned by several researchers.

The potentials of using RM for LDH synthesis are clearly seen. Meanwhile, the limitations of Scenario III and the drawbacks of its products are also obvious, which have been highlighted in Section 4.2.5. Possible improvements are pointed out for future considerations, such as adjustment on the M^{II}/M^{III} ratio, precise control of the pH and attempts of alternative heating or irradiation sources. The 'role plays' of the synthesised RM-LDHs are studied in Chapter 5 & 6 and their performances will be compared against that of the commercial LDH.

Chapter 5 Synthesised RM-LDHs for Chloride Binding

To better examine whether the as-synthesised products behave like layered double hydrotalcite, the products obtained in Chapter 4 were used as the adsorbents to remove chloride ions from aqueous solution. It is reviewed in the literature review as the 'Role-play I' of LDH materials. Meanwhile, the sorption performances of the original IRM, Cal-IRM, the commercial LDH and CLDH were measured for comparison. This chapter aims to identify the optimal adsorbents for chloride binding. Then, the best performed hydrotalcite-like compounds were characterized by XRD and FT-IR analyses. The conclusions drawn from this chapter aim to further narrow down the materials of focus in Chapter 6.

5.1 Materials Screening Tests

LDHs, which are anion exchangers, have been applied to prevent chloride-induced deterioration, primarily in aqueous solution and simulated concrete pore solution (Yang, Fischer and Polder, 2014). The selectivity of LDHs for chloride is variable and highly sensitive to the composition of the layered structure. This section explores the feasibility of using various RM products to remove chloride from aqueous solution.

The screening tests covered the raw materials that have been used in Section 4.2 including RM, reactive MgO, the red mud products synthesised from different scenarios and the commercial Mg/Al LDH. Table 5.1 lists the materials of interests and their corresponding performances. The competition of OH^- anions in the solution was considered. As specified in Section 3.2.3, two groups of chloride solution were prepared: one was diluted chloride solution of 500 ppm Cl^-, the other was concentrated chloride solution of 0.75 M Cl^- and 0.25 M OH^- ($[Cl^-]/[OH^-] = 3.0$). Then, 0.4 g of adsorbents were added to 40 mL prepared solutions for batch sorption study. A contact time of 7 days was guaranteed to ensure the main sorption equilibrium to be achieved. It is assumed no addition of CO_2 occurred during the sorption. The mixtures were then separated using centrifuge and the supernatant were measured using Ion Chromatography as introduced in Section 3.3.2.3.

Table 5.1 The chloride binding capacities of various raw materials and synthesised products

Initial solution	Adsorbent	Peak Area of the IC chromatogram	Filtrate concentration (ppm)	Adsorbed Cl^- amount (mg)	Removal capacity	
					(mg/g)	(mmol/g)
CH-1 (0.75 M Cl^- & 0.25 M OH^-)	(Cal-IRM+MgO) wet ground	6323	26398.5	9.06	22.65	0.64
	RM-w-LDH	6016	25116.2	60.35	150.88	4.25
	RM-w-CLDH	6112	25513.8	44.45	111.12	3.13
	RM-d-LDH	6527	27250.3	-25.01	-62.53	-1.76
	RM-d-CLDH	6393	26688.9	-2.55	-6.39	-0.18
	RM-IV product (3 day)	6612	27605.0	-39.20	-98.00	-2.76
	Calcined RM-IV product (3 day)	6537	27291.2	-26.65	-66.61	-1.88
	LDH	6167	25747.2	35.11	87.78	2.47
	CLDH	6027	25161.4	58.55	146.46	4.12
Note: the negative values may represent the increase of Cl^- concentration in the filtrate after sorption. They will not be taken as effective values, but only for comparison purpose.						
CH-2 (500 ppm Cl^-)	Original IRM	5928	522.8	0.21	0.53	0.01
	Original MgO	5828	514.0	0.57	1.41	0.04
	(IRM+MgO) dry ground & calcined	5914	521.6	0.26	0.65	0.02
	RM-w-LDH	5846	515.5	0.50	1.26	0.04
	RM-w-CLDH	5143	453.3	3.00	7.49	0.21
	RM-d-LDH	5912	521.4	0.27	0.68	0.02
	RM-d-CLDH	5763	508.2	0.80	1.99	0.06
	CLDH	1794	156.6	14.86	37.16	1.05

Note: the average peak area of the blank chloride solution (500 ppm) either with or without OH^- was 5988.38; hence the adjusted concentration of blank chloride solution is 528.13 ppm.

5.1.1 Concentrated CH-1 solution

In Table 5.1, the best performed materials were highlighted, which are RM-w-LDH, CLDH and RM-w-CLDH for the CH-1 solution. RM-w-LDH demonstrated similar sorption capacity with CLDH. This is close to the reported values in Table 2.13, where the uptake capacity of Mg-Al oxide (Mg/Al molar ratio of 3.0) and CLDH are 102.6 mg/g and 149.5 mg/g, respectively. However, RM-w-CLDH removed less amount of Cl^- than its precursor RM-w-LDH, which is contradictory to the prediction in the literature review -- Section 2.4.2.1. The reason is unclear. One possible explanation is that RM-w-CLDH powder was subject to a state of inhomogeneous distribution after the calcination treatment and the CLDH phases contained in RM-w-CLDH tended to be contaminated by CO_2 in the air during the sample preparation process.

In addition, when exposed to the concentrated CH-1 solution, a few materials exhibited negative sorption capacities, which means the measured concentration of chloride after sorption is larger than the initial concentration. In the present case, the batch adsorption study was carried out in polyethylene tubes, which were fully covered by plastic film during shaking. Besides, no liquid loss was observed in polyethylene tubes after the designated contact duration, therefore moisture evaporation could hardly explain for the increase of chloride concentration.

It is noted that RM-d-LDH, RM-d-CLDH and RM-IV products, which did not experience the wet grinding process, released more Cl- anions into the solution rather than restricting their movement. As for the RM-IV products with nitrate ion intercalated, the chloride loading was the lowest. One explanation is the increase of free chlorides in solution, which is resulted from the decrease of bound chlorides in adsorbents. Chubar *et al.* (2005) has reported the adsorption of fluoride, chloride and bromate ions on double hydrous oxide ($Fe_2O_3 \cdot Al_2O_3 \cdot xH_2O$). The influence of pH on anion sorption is highlighted. Sorption of Cl^- occurs at pH 3-4 and decreases to around zero at pH 5. Referring to studies for the chloride binding of Friedel's salt (i.e. $3CaO \cdot Al_2O_3 \cdot CaCl_2 \cdot 10H_2O$, an anion exchanger mineral belonging to the family of the LDHs), chlorides retained by the cement hydrates are named as ‘bound chlorides’, through either chemical binding (e.g. formation of Friedel’s salt from monosulfoaluminate (AFm)) or physical adsorption (e.g. adsorbed by calcium-silicate-hydrate (C-S-H)) (Goñi and Guerrero, 2003; Yue *et al.*, 2018). However, the bound chloride ions are not stable and can be released to form free chloride ions under certain conditions.

Suryavanshi and Narayan Swamy (1996) pointed out that the stability of bound chlorides is pH dependent. Tritthart (1989) conducted tests on cement pastes immersed in chloride solution with different pH, and the author found the chloride binding increases with the decrease in pH of the host chloride solution. In addition, Geng *et al.* (2016) investigated the effect of carbonation on the release of bound chlorides in chloride-contaminated concretes. It was found that carbonation causes the decomposition of Friedel's salt and C-S-H gel, leading to the release of bound chlorides, which has also been validated by other studies (Anstice, Page and Page, 2005; Galan and Glasser, 2015; Chang *et al.*, 2018). According to Yu *et al.* (2019), the decomposition of Friedel's salt has been demonstrated as Eqn. (5.1). And the interactions between carbon dioxide, chlorides and the solid phase are illustrated in Figure 5.1.

$$3CaO{\cdot}Al_2O_3{\cdot}CaCl_2{\cdot}10H_2O+3CO_2+3H_2O=3CaCO_3+2Al(OH)_3+CaCl_2+10H_2O \quad (5.1)$$

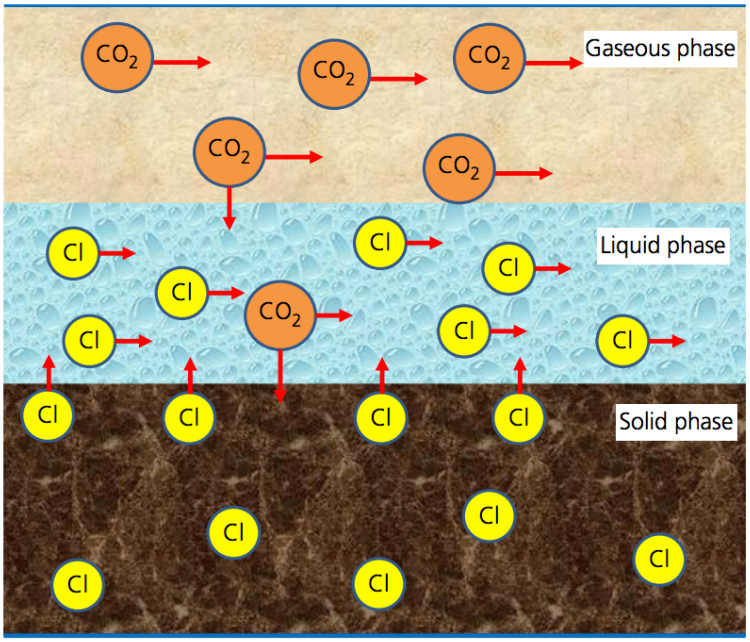

Figure 5.1 One-dimensional transport model proposed for free and bound chlorides in concrete system under carbonation (Geng et al., 2016)

During the ion chromatography measurement of chloride ion, any ion which elutes with the same retention time can interfere with the detection and quantification of target analytes. As previously explained by Pfaff (1993) and Parab *et al.*(2021), the column/ eluent system used in this study was able to separate nitrate and chloride ions effectively. For RM-IV product and calcined RM-IV product, no interference was observed from the nitrate in chloride determination. However, a variety of trace elements that may exist in RM can possibly

interfere with chloride peak. For instance, As (V) may cause interference to the quantification of Cl^- (Chen *et al.*, 2006); bromate (BrO_3^-) is commonly detected in drinking-water and its conductivity peak can overlap with chloride peak (Colombini *et al.*, 1999).

On the other hand, (Cal-IRM+MgO) wet ground raw material, RM-w-LDH and RM-w-CLDH presented positive binding capacities for chloride, implying that wet-grinding treatment positively influences the ability of chloride removal. The Cl removal capacity of RM-w-LDH is more than 6.6 times larger than that of its precursor material -- wet ground (Cal-IRM+MgO) sample, implying the impurities contained in Cal-IRM played a limited role in the binding and retention of chloride anions, while the synthesised phases in RM-w-LDH played a dominating role.

5.1.2 Diluted CH-2 solution

The negative binding phenomenon above is also likely associated with the competition between Cl^- and OH^- ions. As previously highlighted by Miyata (1983), the exchange selectivity of LDH interlayer for monovalent anions is: $OH^- > Cl^-$. Because of its small ionic radius, OH^- ions tend to form hydrogen bonds with H_2O molecules, hence replace Cl^- in the LDH structure (Costa *et al.*, 2012). In this thesis, apart from the added NaOH, it is known that OH^- was triggered naturally during rehydration of the CLDHs (Lv *et al.*, 2006a). With the extensive presence of OH^-, the Cl^- anions initially exist between the interlayer or on the surface of clay materials may be replaced by OH^- anions. Similar phenomenon was presented by Mir *et al.* (2021), at pH >12, ZnAl-NO_2 LDH was partially dissolved and the entrapment of Cl^- significantly decreased. As a consequence, the free Cl^- concentration of supernatant increased after the sorption study. This hypothesis is implicitly confirmed when the sorption environment was switched to the CH-2 solution (with reduced level of OH^-). It is observed that no sample presented negative binding capacities anymore under this less alkaline condition, due to the lower degree of competition offered by the OH^- ions. Similarly, Ke, Bernal and Provis (2017) reported that the chloride uptake of the hydrotalcite-like phases decreases as the $[Cl^-]/[OH^-]$ ratio decreases.

As shown in Table 5.1, the commercial CLDH, RM-w-CLDH and RM-d-CLDH took up the largest amount of chloride, which are 37.16 mg/g, 7.49 mg/g and 1.99 mg/g, respectively. These values are substantially lower than that in the chloride-rich solution, indicating that chloride uptake by hydrotalcite-like materials is sensitive to the chloride concentration.

Furthermore, the CLDH samples display stronger affinity for chloride than their precursors. In the diluted CH-2 solution, RM-w-CLDH adsorbed 7.49 mg/g of Cl^- while RM-w-LDH took up 1.26 mg/g; and RM-d-CLDH loaded 1.99 mg/g of Cl^- while RM-d-LDH adsorbed 0.68 mg/g. As explained in Chapter 4, thermal treatment of RM-LDHs leads to dehydroxylation and decarbonation and increases their specific surface area and porosity. Therefore, both the occupation of interlayer sites and surface adsorption for chloride are favoured for RM-CLDHs.

5.1.3 Summary and suggestion

Through the preliminary sorption tests, two major findings can be deduced as follows:

1) Among the aforementioned materials, RM-w-CLDH, obtained from the wet grinding pre-treatment route of Scenario III (refer to Section 4.2.3.1), exhibits a remarkable ability of binding chloride. Its potential and characteristics are then investigated in detail by comparison with the commercial calcined layered double hydroxides (CLDH) in the following sections.
2) The raw materials for synthesising RM-LDHs, which include the original IRM, reactive MgO, (Cal-IRM+MgO) wet ground sample and the (IRM+MgO) dry ground & calcined sample, exhibit certain binding capacities for chloride but considerably weaker than RM-w-CLDH. Therefore, it is reasonable to infer that the promotion of chloride uptake is attributed to the newly-appeared CLDH phase in RM-w-CLDH.

Accordingly, the formation of LDH phase in RM-w-LDH can be reaffirmed. Calcined layered double hydroxides generally have a greater adsorption capacity for chloride. The initial screening tests have successfully narrow down the scope of the discussion. Section 5.2 therefore draws on a more well-rounded adsorption study for RM-w-CLDH and CLDH.

However, the limitations of the screening tests should also be acknowledged.

1) The effects of OH^- have not been completely separated out from other factors, such as chloride concentration and total ionic strength of the solution. To further discuss the competition between Cl^- and OH^-, $[Cl^-]$ shall be designed as a constant, and $[OH^-]$ is varied to achieve different $[Cl^-]/[OH^-]$ ratios. Then how the anion ratio affects the chloride uptake can be studied, as proposed by Eiby *et al.* (2016) and Ke, Bernal and Provis (2017).

2) Since most of the raw materials for the screening test were produced as trial-and-errors for synthesis routes investigation at different stages of the PhD study, after their consumption for various characterisation analyses, only limited quantities of samples were left. For time-efficiency purpose, parallel comparisons between adsorbents were designed. As a result, the control group was not prepared in the screening test, that is, the background Cl^- concentration of each sample in distilled water was unknown. Therefore, the absolute quantity of sorption may not be accurate, only relative comparisons between different samples are valid.

5.2 Adsorption Process

Following the experimental method introduced in Section 3.2.3, the adsorption equilibrium of chloride removal by RM-w-CLDH and CLDH and the kinetics of chloride uptake by CLDH were studied in batch mode. Considering the limited availability of RM-w-CLDH, CLDH was firstly studied for adsorption kinetics to provide a rudimentary understanding.

5.2.1 Adsorption equilibrium

For the selected RM-w-CLDH and the commercial CLDH, chloride sorption equilibria were studied, and the experimental data was fitted by the Langmuir and Freundlich isotherm models (Eqn. (2.1) & Eqn. (2.3)) respectively. Figure 5.2 describes the adsorption isotherms by plotting the adsorbed amounts versus equilibrium concentration. Table 5.2 presents the parameters calculated from the isotherm models.

The isotherms for chloride sorption are better described by Freundlich model, on the basis of the correlation coefficient $R^2 = 0.941$ for CLDH and $R^2 = 0.975$ for RM-w-CLDH. The '1/n' values obtained are 0.294 and 0.358 receptively for CLDH and RM-w-CLDH, indicating a favourable adsorption process and a certain degree of heterogeneity on the surface of adsorbents (Foo and Hameed, 2010). Meanwhile, Langmuir model also fits the equilibrium data well with R^2 values equal to 0.892 and 0.910 respectively. The values of equilibrium parameter R_L (Eqn. (2.2)) were 0.038 for CLDH and 0.083 for RM-w-CLDH, also suggesting the adsorption of chloride is favourable and reversible under the experimental conditions.

The equilibrium fittings are slightly different from those reported in the literature. For instance, Lv *et al.* (2006b) pointed out that Langmuir model provides a better fit for the adsorption process of chloride ions on the MgAl-CO_3 CLDH in aqueous solution, under N_2 atmosphere. Yoon *et al.* (2014) addressed that Mg/Al CLDH adsorbing chloride ion in cementitious system, is also more suitable to be described by Langmuir model. They both concluded that a monolayer sorption is the principal mechanism for chloride removal by CLDH, which means all binding sites on the outer surface of the adsorbent are equivalent. However, unlike those pure Mg/Al CLDHs in the reference, RM-w-CLDH is composed of multiple mineral phases, its outer sorption sites are supposed to be heterogenous. Furthermore, the inconsistency may also be attributed to the fact that in the present study, the sorption process was not strictly controlled under N_2 condition.

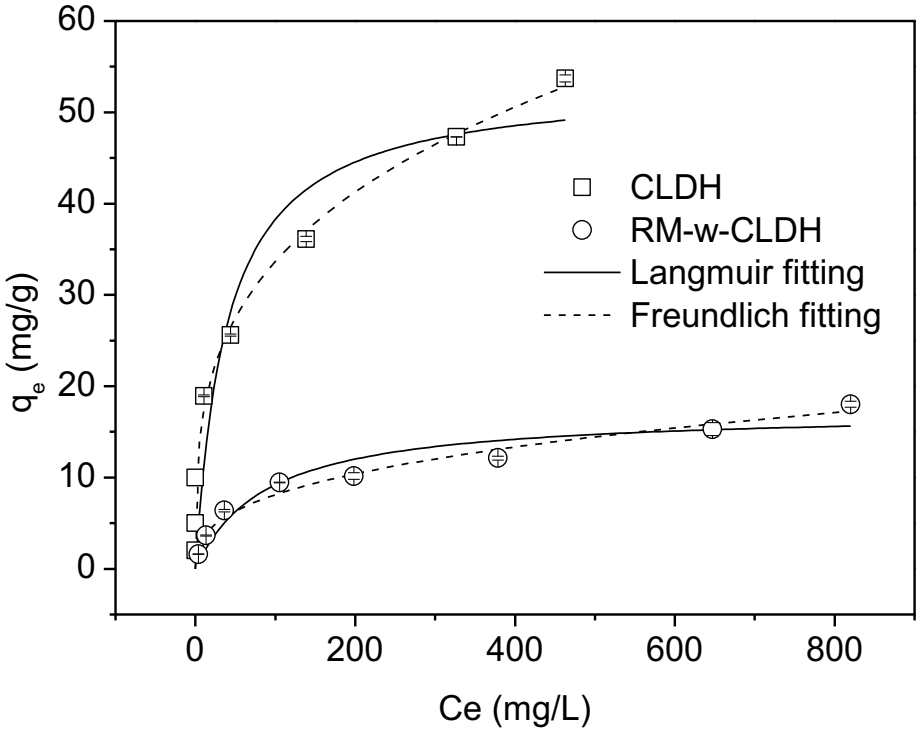

Figure 5.2 Adsorption equilibrium results (q_e – adsorbed amount of adsorbate on adsorbent at equilibrium, Ce – equilibrium solution concentration of adsorbate), 0.4g RM-w-CLDH in 40 mL chloride solution, at temperature = 20 °C; initial pH = 8.0.

Table 5.2 Isotherm model parameters for Cl adsorption on CLDH and RM-w-CLDH (0.4 g adsorbent in 40 mL solution)

Sorbent	Langmuir			Freundlich		
	Q_{max} (mg/g)	b (L/mg)	R^2	K_f (mg/g)	1/n	R^2
CLDH	53.3	0.025	0.892	8.69	0.294	0.941
RM-w-CLDH	17.3	0.011	0.910	1.56	0.358	0.975

The adsorption capacity Q_{max} for chloride are 53.3 mg/g on CLDH and 17.3 mg/g on the as-prepared RM-w-CLDH. As shown in Section 5.1, compared to RM-w-CLDH, the original IRM is only capable to take up less than 10% of chloride in diluted chloride solution, while the (Cal-IRM+MgO) wet ground raw material can take up less than 20% of chloride in concentrated chloride solution. Therefore, the impurities contained within RM-w-CLDH

make minor contribution to the chloride removal, while the newly formed CLDH phase within RM-w-CLDH is responsible for taking up most of the chloride ions. And in this context, the study on pure CLDH is meaningful for a better understanding of the CLDH components in RM-w-CLDH. It is found that CLDH has a larger adsorption capacity, whereas RM-w-CLDH exhibits approximately 30% of CLDH's sorption capacity, which implies LDH components likely constitute up to 30% of the original RM-w-LDH.

As reviewed in Section 2.4.2.1, CLDH sorbents usually have the uptake capacity of 70-150 mg g^{-1} for chloride ions. Recently, Kameda, Oba and Yoshioka (2014) measured that the chloride uptake by Mg-Al metal oxides in seawater (15951 mg/L Cl^-) could reach 280-415 mg g^{-1}. However, it should be noted that their experiment was conducted in a concentrated chloride solution. Since the equilibrium tests in the present study were performed in a diluted chloride environment, CLDH exhibits a much less binding capacity. Actually, the adsorption capacity of CLDH (53.3 mg/g) is very close to the measurement by Lv *et al.* (2006b), which was 53.24 mg/g under the condition of $[Cl^-]$ = 100 mg/L and [CLDH] = 2.0 g/L.

5.2.2 Adsorption kinetics

According to the adsorption equilibrium study in Section 5.2.1, CLDH shows a larger adsorption capacity for chloride. In practical application, the effect of time on its adsorption uptake is crucial. Hence, adsorption kinetics for CLDH is carried out to further evaluate its potential in real application. Meanwhile, intraparticle diffusion study helps to understand the adsorption mechanism. The investigation of CLDH is performed as a prelude to a more comprehensive investigation for materials synthesised in this thesis in the future.

The influence of contact time on the adsorbed amount of chloride is shown in Figure 5.3, at the dosage of 10 g/L and the initial Cl^- concentration of 500 mgL^{-1}. It is seen that most of the Cl^- was removed in the first 12 h and the adsorption process reached its equilibrium at around 20 h, which well accords with the observation of Millange, Walton and O'Hare (2000). To better determine the possible adsorption mechanism, the pseudo-first-order model (Eqn. (2.4)), pseudo-second-order model (Eqn. (2.5)) and the Weber and Morris intraparticle model (Eqn. (2.6)) have been applied to fit the experimental data. Figure 5.3 and Table 5.3 demonstrate the fittings and the fitted parameters of the pseudo kinetic models respectively.

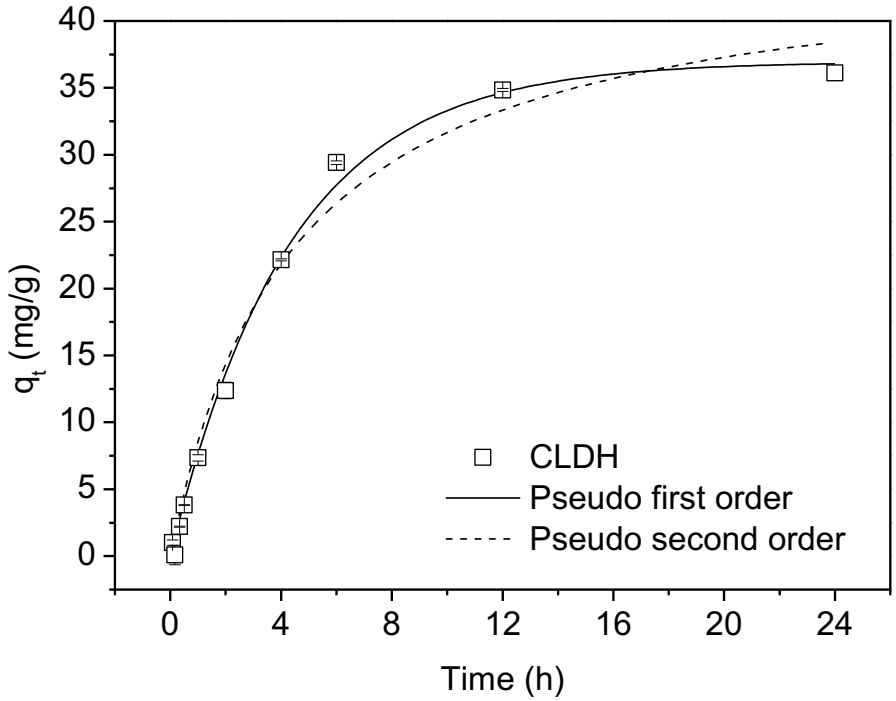

Figure 5.3 Kinetic results for chloride (Cl) adsorption on CLDH (q_t – adsorbed amount of adsorbate on adsorbent at time t) (0.4 g CLDH in 40 mL solution containing 500 mg/L RBB; reaction temperature 25°C; initial solution pH = 8.0).

Table 5.3 Kinetic parameters for Cl adsorption on CLDH

Sorbent	Pseudo first order			Pseudo second order		
	q_e (mg/g)	k_1 (h^{-1})	R^2	q_e (mg/g)	k_2 (g/mg h)	R^2
CLDH	36.9	0.231	0.996	45.3	0.005	0.984

According to the regression coefficients (R^2), the pseudo-first-order model can more accurately describes the adsorption kinetics of CLDH. And the evaluated adsorption capacity q_e (36.9 mg/g) for the first-order kinetic is more approximate to the experimental value. Considering the assumption of the pseudo-first-order kinetics model, the system between the chloride ions and CLDH may not fully reach to equilibrium (Plazinski *et al.*, 2009).

However, Lv *et al.* (2006b) claimed that pseudo-second-order model best describes the adsorption kinetics of chloride ions by CLDH. Hamidi and Kazemi (2015) also found the pseudo-second-order model better represents the Cl adsorption by the Mg/Al-CO_3^{2-} CLDH and pointed out the underlying mechanism is chemisorption. In the present study, the

adsorption kinetics can also be fitted by the pseudo-second-order model with R^2=0.984, implying chemical interaction is also a fundamental mechanism for chloride adsorption by CLDH.

Intraparticle diffusion modelling was implemented to characterise the mass transfer in the sorption process. Figure 5.4 displays the sorption capacity of Cl at specific times against the square root of time $t^{0.5}$. There are three sharp linear parts over the adsorption period, which represent three distinct steps in the sorption process. The first steeper line with slope k_1 represents the external film transfer (Step II), i.e., the sorbate Cl travelled across the external liquid film boundary, overcame the boundary layer resistance and arrived the surface sites of CLDH. The second region starting at 2.5 $h^{0.5}$ marks the beginning of intraparticle diffusion (Step III), from where Cl gradually migrated into the inner pores of CLDH. The slope k_2 of the second linearity is defined as the intraparticle diffusion parameter, which is 5.35. This value is in line with the kinetic parameter reported by Lv *et al.* (2006b), where the intraparticle diffusion k_2 was 5.88 (in the case of [Cl^-] = 100 mg/L, [CLDH] = 2.0 g/L). The third portion from 3.5 $h^{0.5}$ stands for Step IV, at the point intraparticle diffusion reached equilibrium and Cl molecules started to settle at the internal surface sites.

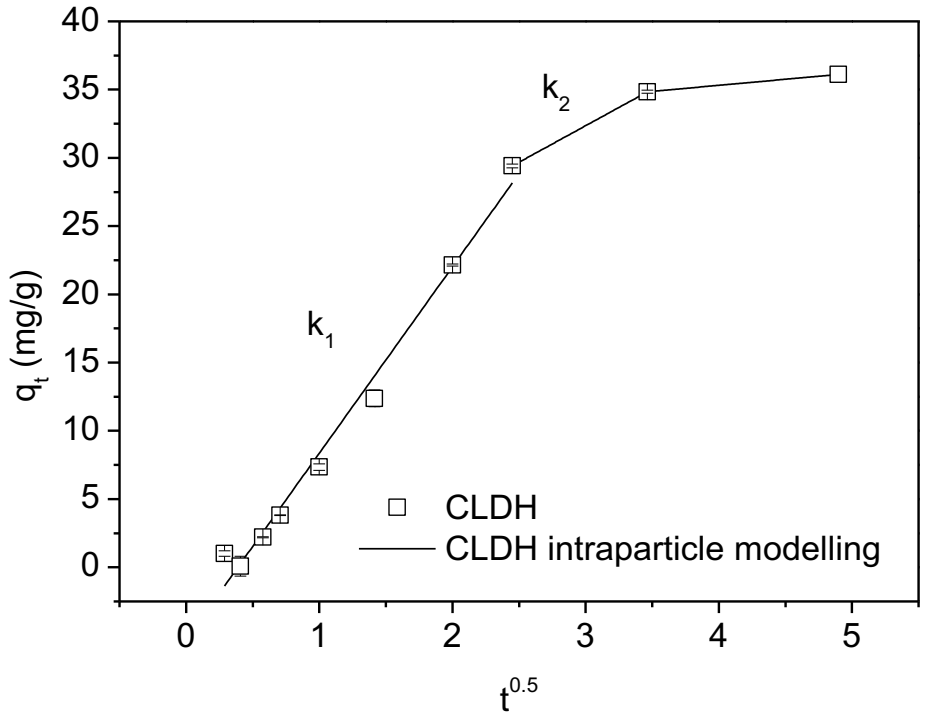

Figure 5.4 Intraparticle diffusion modelling for Cl on CLDH (0.4 g sorbents in 40 mL solution, 500 mg/L Cl^- solution); reaction temperature 20 °C; initial solution pH=9.0)

Table 5.4 Intraparticle parameters for Cl adsorption on CLDH

Sorbent	k_1	C_1 (mg/g)	R_1^2	k_2	C_2 (mg/g)	R_2^2
CLDH	13.7	-5.31	0.984	5.35	16.3	1

As shown in Figure 5.4, the extended plot of the first region with slope k_1 could pass through or very close to the origin. That suggests the transport of sorbate from bulk solution to the exterior film boundaries (Step I) could be neglected. In the present system, the proportion of k_1 region (from 0.4 $h^{0.5}$ to 2.5 $h^{0.5}$, lasted for approximately 6 h) is comparable to the proportion of k_2 region (from 2.5 $h^{0.5}$ to 3.5 $h^{0.5}$, also lasted for approximately 6 h), indicating that external mass transfer and intraparticle diffusion (internal mass transfer) play an equally controlling role in the overall sorption. Choy *et al.* (2004) suggested that the exchange process onto ion exchangers involves external mass transfer and internal diffusion. Therefore, ion exchange is believed to be the main mechanism contributing to this chloride sorption process.

Although the reconstruction of the initial lamellar structures was expected to occur during the sorption, the uptake speed of Cl^- to the sorbent was not that rapid. It implies that either the reconstruction is partial or the competitiveness of Cl^- is restricted by OH^- ions. As discussed in Section 5.1.3, the sorbent CLDH would create an alkaline environment when it was dispersed in water, while the initial chloride concentration was only 500 mg/L.

5.3 Characterisation Studies

This section investigates the microstructure changes in RM-w-CLDH before and after chloride uptake, therefore, to provide a glimpse of the mechanism of chloride binding. To amplify the interaction of chloride with RM-w-CLDH as well as to eliminate the influences of other competing anions, the sorption experiment was conducted in a concentrated chloride solution (1.0 M NaCl) and then shaken for 7 days at room temperature. XRD and FT-IR were employed to study the mineralogy of the adsorbent. The key findings are then compared against the behavior of other CLDH materials in chloride binding, to determine if RM-w-CLDH fulfils the characteristics of 'Role-play I', as outlined in Section 2.4.2.1.

5.3.1 XRD test studies

The XRD patterns of RM-w-CLDH samples before and after adsorption of chloride are plotted in Figure 5.5. Spacing values of (003) and (006) are presented in Table 5.5.

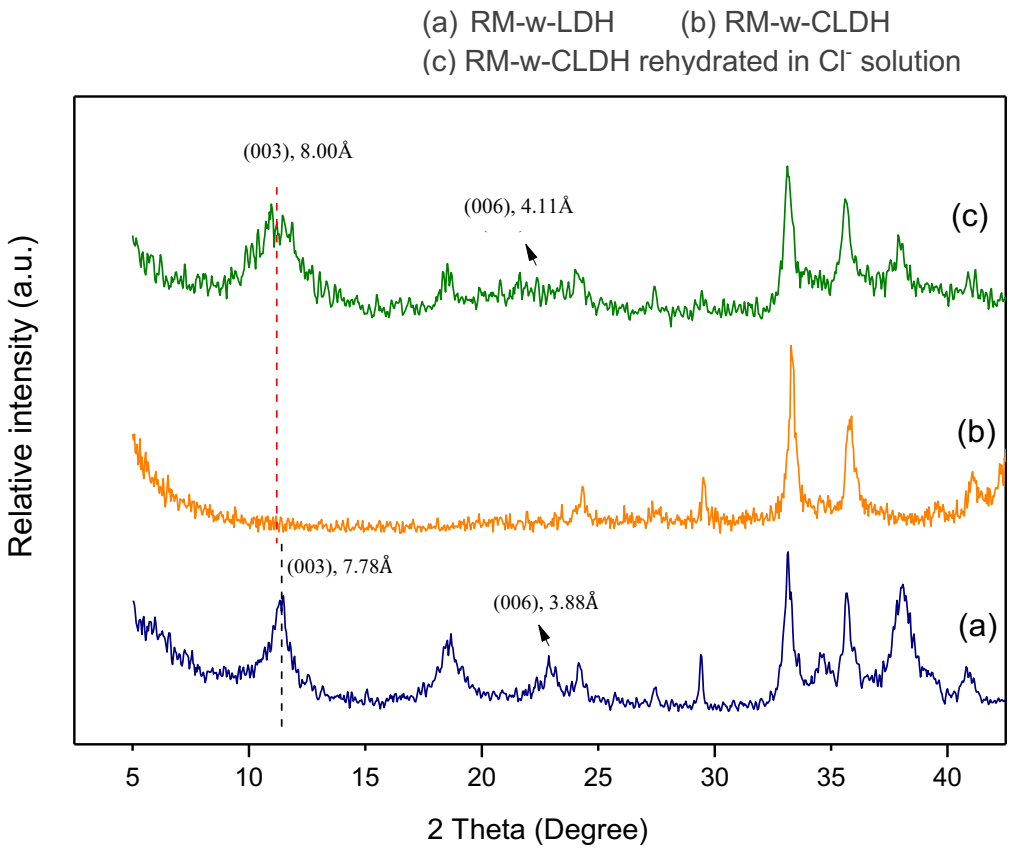

Figure 5.5 Powder XRD patterns of (a) RM-w-LDH, (b) RM-w-CLDH and (c) RM-w-CLDH immersed in Cl^- solution

Table 5.5 Crystallographic data of RM-w-CLDH and RM-w-LDH-Cl

Sample	d_{003} (Å)	d_{006} (Å)	d_{110} (Å)	Cell parameters (Å)		Crystallite size (Å)
				a	c	(003)
RM-w-LDH	7.78	3.88	1.59	3.12	23.37	14
RM-w-CLDH-Cl	8.00	4.11	1.56	3.12	24.33	14

For RM-w-CLDH before the chloride sorption, it can be seen its layered structure was destroyed by heating at 500°C. In the XRD pattern of RM-w-CLDH-Cl, however, the characteristic reflections of LDH phase reappeared, indicating that the layered structure can be regenerated upon immersion in the chloride solution. In fact, the reconstruction is highly complete that its diffractogram is almost the same as the starting phase RM-w-LDH, except for the reduced crystallinity. Compared with RM-w-LDH, the d_{003} peak of RM-w-CLDH-Cl shifted towards smaller angle and the associated basal spacing was raised from 7.78 Å to 8.00 Å after chloride uptake, which is in good agreement with the reported basal spacing of chloride hydrotalcite (Miyata, 1975; Ulibarri *et al.*, 2001; Hibino, 2018). It suggests that chloride ions were intercalated into the reformed interlayer space. This finding agrees with previous studies, which claimed chlorides incorporate into CLDHs in the rehydration process and help to re-construct the lamellar structure (Lv *et al.*, 2006b; Eiby *et al.*, 2016). As discussed in Section 5.1, the OH^- ions in the solution may also enter the reformed interlayer, however, it is hardly detected by the XRD pattern according to Xu *et al.* (2018).

5.3.2 FT-IR test studies

Figure 5.6 demonstrates the FT-IR spectra of RM-w-CLDH before and after the chloride uptake. In the spectra of RM-w-CLDH-Cl, the broadband from 4000 to 2700 cm^{-1} (centred at 3387 cm^{-1}) becomes more intense, originated from the stretching vibration of hydroxyl group and hydrogen bonding of the reconstructed hydroxide layers (Xu *et al.*, 2018). The band at 1643 cm^{-1} is assigned to the OH- bending vibration from the reversibly absorbed H_2O. And the stretching band observed at 1419 cm^{-1} is associated with adsorbed carbonate on the surface of the mixed oxides (Millange, Walton and O'Hare, 2000; Lv *et al.*, 2006a).

Comparing to the spectra of RM-w-LDH (Figure 4.34a), the sharp band of RM-w-CLDH-Cl at 1419 cm^{-1} does not get that strong or moves back to the lower frequency of 1385 cm^{-1}.

From the perspective of electrostatic conservation, that implies the interlayer space of RM-w-CLDH-Cl received little interference from CO_3^{2-} ions during the rehydration process, instead it has been electrostatically bounded to Cl^- ions to some extent. There exists no other obvious change representing Cl^-, since monatomic ion does not have stretching vibration and bending vibration (Eiby *et al.*, 2016; Xu *et al.*, 2018). Furthermore, the deformation at 995 cm^{-1} and 1008 cm^{-1} can be attributed to Si-O and Si(Al)-O vibration (Castaldi *et al.*, 2010). The vibrations recorded between 900-600 cm^{-1} are due to magnesium and aluminium oxides.

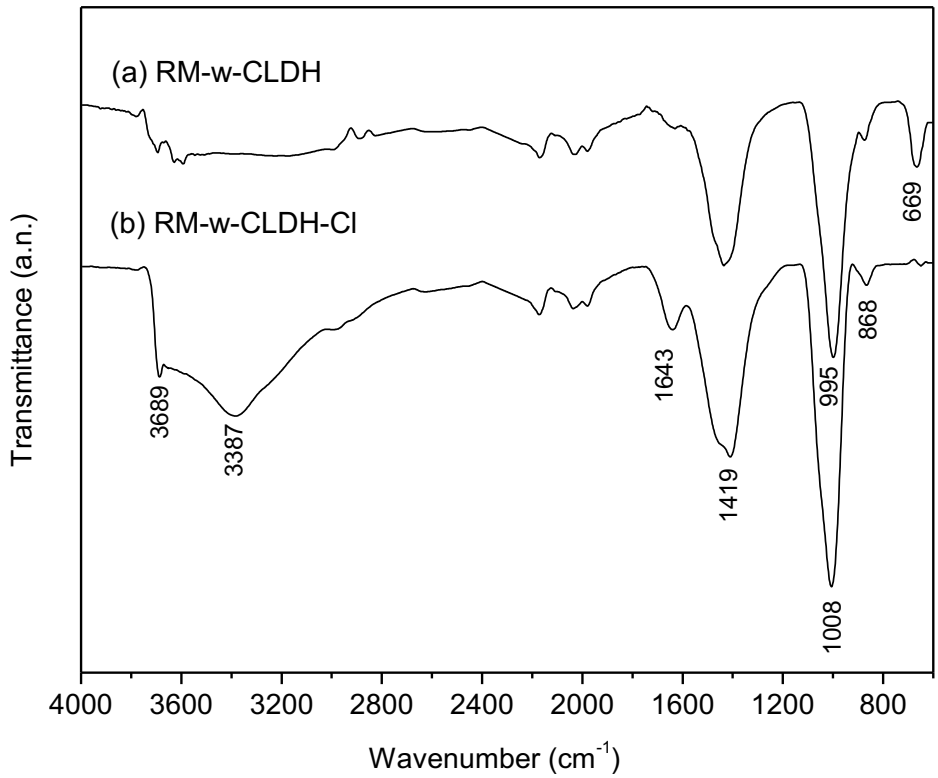

Figure 5.6 FT-IR spectra of RM-w-CLDH before and after chloride adsorption

Based on the results from XRD test and FT-IR analysis, a mechanism of chloride uptake by RM-w-CLDH in aqueous solution is proposed as follows: the calcined product RM-w-CLDH is rehydrated with incorporation of chloride ions while reforming the initial layered structure. This mechanism matches the interpretation drawn by a number of researchers (Châtelet *et al.*, 1996; Lv *et al.*, 2006b; Eiby *et al.*, 2016). Since RM-w-CLDH exhibits similar characteristics as calcined layered hydroxides do in 'Role-play I', the existence of CLDH phase in RM-w-CLDH is further confirmed.

5.4 Discussion and Summary

Chapter 5 has determined the most efficient adsorbents for chloride removal to be CLDH and RM-w-CLDH. It was found that the adsorbents generally presented a larger chloride loading in the concentrated CH-1 solution. Existing studies pointed out that both the chloride concentration and the dosage of adsorbent affect the sorption capacities (Lv *et al.*, 2006b; Yoon, Moon, Bae, Duan, Emmanuel P. Giannelis, *et al.*, 2014). Besides, the co-existing anions in the aqueous solution could also change the chloride-binding capability for CLDHs, such as OH^-, SO_4^{2-} and CO_3^{2-}, which might outcompete Cl^- and adsorb onto CLDHs (Eiby *et al.*, 2016). However, Section 5.1 only provides an incomplete look at the effects of $[Cl^-]/[OH^-]$ anion ratio, more careful analyses are required.

The adsorption features of RM-w-CLDH and CLDH in aqueous media have been investigated in Section 5.2. Their adsorption processes were well interpreted by both Freundlich and Langmuir isotherm model, though the former one provided better fits. The retention of chloride ions by RM-w-CLDH and CLDH were 53.3 mg/g and 17.3 mg/g, respectively. The adsorption kinetics of CLDH was more accurately represented by the pseudo-first-order kinetic model. The results of intraparticle modelling suggest that the chloride binding process is almost equally controlled by film diffusion and intraparticle diffusion. The kinetic and thermodynamic parameters of removing chloride using Mg-Al CLDH were examined by Hamidi and Kazemi (2015), who claimed the uptake process was feasible and endothermic.

As demonstrated in Section 4.2.3.2, the thermal decomposition of RM-w-LDH at 500 °C leads to the collapse of the layered structure. RM-w-CLDH before and after chloride adsorption were characterised by X-ray diffraction analysis and FT-IR spectroscopy analysis, indicating that chloride was intercalated into the interlayer space. Therefore, the uptake of chloride on RM-w-CLDH is a rehydration process with incorporation of Cl^-, accompanied by reformation of the initial layered structure, which could be described by the following equation:

$$Mg_{1-x}AL_xO_{1+x/2} + xCl^- + (m + 1 + x/2)H_2O \rightarrow Mg_{1-x}Al_x(OH)_2Cl_x \cdot mH_2O + x \cdot OH^-$$

That explains why calcination treatment is able to enhance the sorption ability of LDHs. Apart from the so called ‘memory effect’, the chloride binding may also happen on the external surface of the adsorbent (Xu *et al.*, 2018).

Based on the results of this chapter, these key implications can be obtained:

1) RM-w-LDH synthesised from Scenario III process have been the main focus in this chapter, who presents similar features as CLDHs in the literature. Therefore, the successful synthesis of LDH phase in RM-w-LDH can be further reaffirmed. In Chapter 6, RM-w-LDH will also be of particular interests.
2) The overall results shed light on the promising use of CLDH and RM-w-LDH as innovative additives for preventing the chloride-induced deterioration of reinforced concrete. However, the suitability of RM-w-CLDH in practice requires further investigation.

In light of the structural memory effect of the calcined layered double hydroxides, recent studies have investigated the use of CLDHs in concrete as chloride inhibitors. Yoon *et al.* (2014) suggested that CLDHs are not only adsorbed more chloride ions in aqueous solution than the original LDHs, but also exhibit a much higher binding capacity in the cement matrix. Furthermore, one study that has closely investigated the slag chemistry and reaction kinetics of CLDH-blend cements was conducted by Ke, Bernal and Provis (2016), who addressed the addition of CLDH brings other benefits, such as accelerating the reaction, facilitating the hardening process of slag pastes.

Practically, in concrete system, carbonate and other competing ions are omnipresent. If RM-w-CLDH is employed in a cement-based environment, the competitive intercalations of other anions during reformation are inevitable and must always be taken into account. Therefore, the results presented herein are insufficient to quantify the performance of RM-w-CLDH in cement matrix, and the threshold concentration of chloride for intercalation into RM-w-CLDH is still unclear. A good point is, Yoon *et al.* (2014) clarified that pore structure makes little effect on the total binding capacity of CLDHs. Therefore, the effectiveness of RM-w-LDH in preventing chloride-induced corrosion is possible to be estimated if the concrete pore solution is simulated accurately.

Chapter 6 Synthesised RM-LDHs for Dye Removal from Wastewater

6.1 Introduction

Chapter 5 has investigated the potential of RM products for binding chloride as specified in 'Role-play I' and highlighted the high efficiency of RM-LDHs. The occurrence of LDH phases in the as-synthesised RM-LDHs has been re-affirmed. In order to further investigate the properties and potential applications of RM-LDHs, as discussed in Section 2.3.3 and Section 4.2.5, and also aiming to validate their characteristics as 'Role-play II' of typical LDHs as reviewed in Section 2.4.2.2, adsorption studies for acid dye removal in aqueous solution were carried out in this chapter. In addition, it is important to understand the adsorption behaviour of the original Ireland red mud (IRM) materials and commercially available Mg-Al LDH, so that the differences between IRM and RM-LDHs can be observed; the adsorption capacities of LDH and RM-LDHs can be reasonably compared; and the characteristics of the synthesised RM-LDHs can be better understood.

Among a variety of acid dyes, Remazol Brilliant blue R (RBB) is selected as the target acid dye for the adsorption studies, as it is one of the most frequent studied organic anionic pollutants for water contamination (He *et al.*, 2012; Ratnamala, Vidya and Srinikethan, 2015). More importantly, as reviewed in Section 2.3.1, LDHs have received extensive attention as effective adsorbents for the removal of dye and have exhibited relatively high adsorption capacity for RBB. He et al. (2012) reported that the sorption capacity for brilliant blue from wastewater was 166.67 mg/g on LDH powder; and was approximately 26.0 mg/g on red mud.

Therefore, in this chapter, separated adsorption studies were conducted to investigate the adsorption of RBB to several materials: IRM and its calcination product Cal-IRM, two types of RM-LDHs synthesised from Scenario III, their corresponding calcination products RM-CLDHs, and the commercial Mg-Al LDH. The kinetics and the equilibria of RBB adsorbed onto these adsorbents have been investigated.

This chapter aims to (1) assess and compare the adsorption behaviour of RBB on RM-LDHs; (2) investigate the characteristics and properties of RM-LDHs and their associated RM-CLDHs samples; (3) identify the RM-related products which are suitable for future application to water pollution; (4) understand the correlation between the physicochemical properties of hydrotalcite-like materials and their adsorption capacities.

6.2 Synthesised RM-LDHs

6.2.1 Physicochemical properties

As described in Section 4.2.3.1 – Scenario III, different pre-treatment methods have been carried out to prepare RM-LDHs. One was via the path of dry grinding together with MgO then calcination, named as RM-d-LDH; while the other followed the calcination of RM then wet grinding with the MgO path, named as RM-w-LDH. The physicochemical properties of RM-d-LDH, RM-w-LDH and commercial Mg/Al LDH in this study are shown in Table 6.1. Compared with RM-d-LDH and RM-w-LDH (as discussed in Section 4.4), the BET surface area of the commercial LDH is significantly smaller. In parallel, LDH-like compound derived from industrial waste blast furnace slag (BFS) had a surface area of 21.1-25.7 m^2/g, which was lower than that of RM-LDHs in the present study.

Table 6.1 Physicochemical properties of RM-LDHs, calcined RM-LDH and commercial LDH

	BET surface area (m^2/g)	Pore size (nm)	Total pore volume (cm^3/g)	Particle size (μm)
RM-d-LDH	74.8	10.9	0.204	6.61
RM-w-LDH	64.0	8.92	0.143	4.37
RM-w-CLDH	79.8	10.47	0.209	6.61
Commercial Mg/Al LDH	8.35	8.35	0.015	0.18

6.2.2 Kinetics

The influence of contact time on the adsorbed amount of RBB on RM-LDHs is shown in Figure 6.1, at the dosage of 2.5 g/L. The sorption kinetics is an important aspect of the pollutant removal process to predict the involved mechanism. It is noted that 95% and 90% of the RBB were taken up in the first 4 h for the RM-d-LDH and RM-w-LDH adsorbents respectively. When the equilibrium concentrations were approached, the adsorption rates considerably decreased. This effect is resulted from the decreasing abundance of unsaturated sites on the surface of RM-LDHs (Foo and Hameed, 2010), which gradually became occupied with time. At approximately 6 h, the adsorption process reached its equilibrium. Therefore, a contact time of 24 h was sufficient to guarantee that the equilibrium condition can be achieved (Figure 6.1) and the calculated k_2 demonstrated a rapid uptake rate of RBB

from water. RM-w-LDH surpassed RM-d-LDH after 4 hours in regard to the adsorption capacity. Since the surface area and pore size of RM-w-LDH were in fact smaller than that of RM-d-LDH, the physical adsorption could not be the advantage for RM-w-LDH. The main reason is likely to be a higher CEC or a larger amount of crystalline LDH phase contained in RM-w-LDH.

Table 6.2 Kinetics parameters for RBB on RM-d-LDH and RM-w-LDH (400 mg/L)

Sorbent	Pseudo first order			Pseudo second order		
	q_e (mg/g)	k_1 (h^{-1})	R^2	q_e (mg/g)	k_2 (g/mg h)	R^2
RM-w-LDH	110.85	4.31	0.548	120.13	0.05	0.734
RM-d-LDH	95.78	5.10	0.717	100.97	0.08	0.910

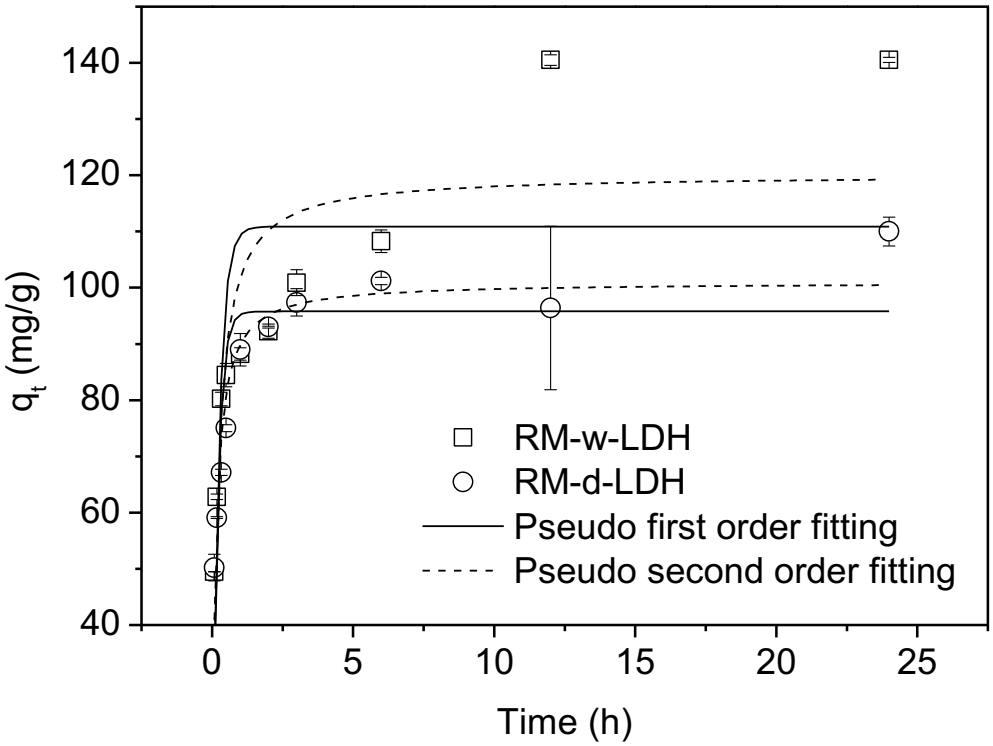

Figure 6.1 Kinetic results and the fit of Pseudo 1st order and 2nd order models for Remazol brilliant blue (RBB) adsorption on RM-d-LDH and RM-w-LDH (q_t – adsorbed amount of adsorbate on adsorbent at time t) (0.1 g RM-d-LDH or RM-w-LDH in 40 mL solution; 400 mg/L RBB).

In order to understand the adsorption mechanism, three kinetic models i.e. pseudo-first-order (Eqn. (2.4)), pseudo-second-order model (Eqn. (2.5)) and the intraparticle diffusion model (Eqn. (2.6)), which are the most frequently used in the literature have been applied to describe the adsorption process. The regression coefficients (R^2) for the RM-d-LDH and RM-w-LDH of the pseudo first order model are low (0.717 and 0.548 respectively), demonstrating a poor fitting with the experimental data (Table 6.2). This indicates that the adsorption of RBB onto RM-LDHs is not an ideal pseudo-first-order reaction.

On the other hand, the kinetic data of RM-d-LDH and RM-w-LDH were fitted relatively well to the pseudo-second order kinetic mode, with the correlation coefficient R^2=0.910 and 0.734 respectively, as shown in Table 6.2. The pseudo-second-order model describes the kinetic data better than the pseudo first model. This finding is consistent with previous results for the adsorption of Orange B onto Mg-Fe LDH by Benselka-Hadj Abdelkader *et al.* (2011). Therefore, the heterogeneous chemisorption mechanism is likely to be responsible for the uptake of RBB on RM-LDHs (Chuang *et al.*, 2008).

However, it should be emphasised that pseudo-first and pseudo-second order kinetic models do not correspond to any specific physical model, but are based on empirical equations (Rudzinski and Plazinski, 2006). They both assume the kinetics is controlled by rate of surface reaction at the liquid/solid interfaces and more precisely, by the number of adsorption sites available on the surface (Plazinski, Rudzinski and Plazinska, 2009). Simonin (2016) examined the data correlation quality of fittings by these two rate laws in the literature. The author found some data was not described well by neither of these two kinetic models, because pseudo-second order model and even more so pseudo-first order model cannot capture the sort-time and the long-time behavior at the same time. Hereby, deviations from the predicted behavior are common to occur in experimental fittings. On the other hand, this may suggest the sorption kinetics is governed by the rate of diffusion, which is usually represented by intraparticle diffusion equation. Choy, Porter and Mckay (2004) suggested that intraparticle diffusion model is more appropriate for the adsorption of acidic dyes.

Intraparticle diffusion model was implemented to examine the mass transfer in the adsorption system. Figure 6.2 and Table 6.3 demonstrate the sorption capacity of RBB at specific times against the square root of time $t^{0.5}$. The plots of both RM-d-LDH and RM-w-LDH demonstrate three linear parts over the adsorption period, which represent three stages in the adsorption process. The first portion of lines with slope k_1 describes that the sorbate RBB

moved across the external liquid film boundary to the external surface sites of RM-LDHs, known as the second stage. After the external sites of sorbent reached saturation, RBB molecules started to migrate into the inner pores of RM-LDHs, i.e. the third stage where intraparticle diffusion happened. The slope k_2 of the second linearity has been recognised as the intraparticle diffusion parameter. The final region stands for the final equilibrium stage, which are after 2.5 $h^{0.5}$ for RM-d-LDH and 3.5 $h^{0.5}$ for RM-w-LDH, respectively. Subsequently, intraparticle diffusion began to slow down and RBB molecules started being attracted to the internal surface sites.

As shown in Figure 6.2, the plot yielded from the region of slope k_1 could pass through or very close to the origin. That suggests that the transport of sorbate from bulk solution to the exterior film boundaries (Step I) could be neglected. In the present system, the appearance of k_1 region is a strong evidence to support that external mass transfer is also a mechanism contributing to the overall sorption before intraparticle diffusion control takes over. Overall, intraparticle diffusion (internal mass transfer) is still the rate-limiting step, especially for RM-w-LDH (from 0.8 $h^{0.5}$ to 3.5 $h^{0.5}$, lasted for approximately 12 h). Meanwhile, it echoes the fact that RM-w-LDH possesses a smaller pore size, as a result, it may require longer intraparticle diffusion time. Ion exchange is believed to be the main mechanism contributing to this sorption process, since the exchange process onto ion exchangers involves external mass transfer and internal diffusion (Choy *et al.*, 2004).

Table 6.3 Intraparticle parameters for GBB on RM-w-LDH and RM-d-LDH (400 mg/L)

Sorbent	k_1	C_1 (mg/g)	R_1^2	k_2	C_2 (mg/g)	R_2^2	k_3	C_3 (mg/g)	R_3^2
RM-w-LDH	86.06	26.61	0.943	19.74	67.02	0.942	0.002	140.50	1.00
RM-d-LDH	53.70	36.07	0.993	8.49	81.14	0.942	3.98	88.21	0.01

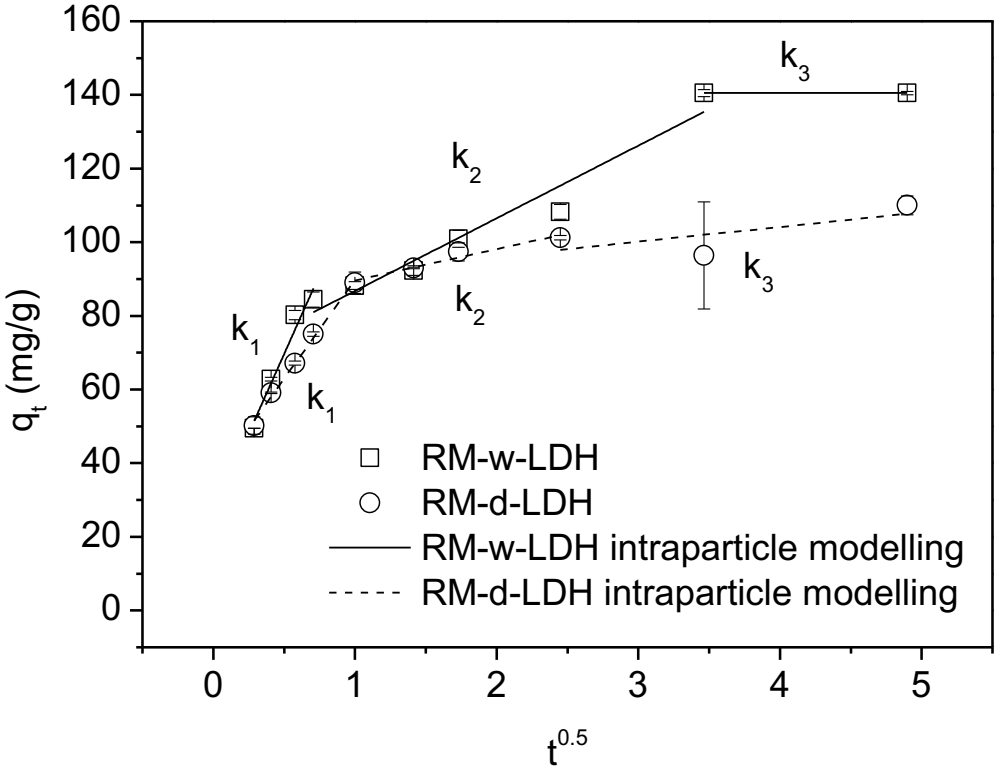

Figure 6.2 Intraparticle diffusion modelling for RBB on RM-d-LDH and RM-w-LDH (0.1 g sorbents in 40 mL solution (400 mg/L RBB solution); reaction temperature 20 °C; initial solution pH 6).

6.2.3 Influence of initial solution pH on adsorption

The pH of a solution is a crucial factor affecting the adsorption of anionic ions onto an adsorbent's surface (see Section 2.5.2.3). In this study, the effect of the initial solution pH was tested in the range of 3-10 and the amounts of RBB removed across the range are shown in Figure 6.3. The adsorption capacity of RBB on RM-d-LDH was significantly reduced as initial solution pH increased from 3 to 4. It then effectively stayed stable at pH 4-9 and slightly decreased from pH 9 to 10. The equilibrium solution pH was at the range of 10.20-10.60, presenting a good buffering ability of RM-d-LDH. The adsorption capacity is related to the equilibrium pH, as its significant drop at 3-4 and slight decrease at 9-10 were both accompanied by an increase of equilibrium solution pH (10.23 to 10.51, and 10.55 to 10.57, respectively).

At low pH values, positive charged sites dominate the RM-d-LDH particles' surface and would potentially strengthen the electrostatic repulsion towards RBB anions in solution.

Therefore, the adsorbed RBB at initial pH of 3 was the highest among the pH values studied. However, increasing the pH also encourages the deprotonation process on the particles' surface, gradually creating more negative sites that would on the contrary reduce the electrostatic adsorption of RBB (see Section 2.5.1). The correlation between the adsorption capacity and the equilibrium solution pH also suggests that the anion exchange may be one of the mechanisms for RBB adsorption on RM-d-LDH, as previous studies reported that the adsorption of RBB through anion exchange can be influenced by the pH of solution.

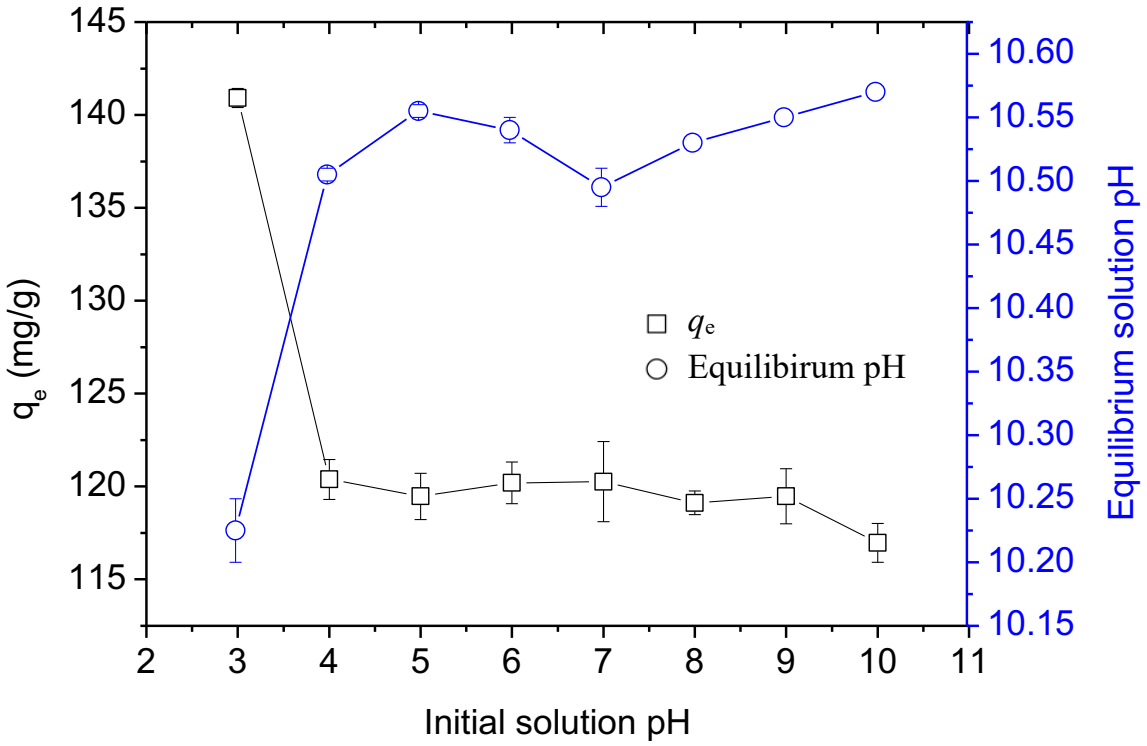

Figure 6.3 Influence of initial solution pH on adsorption of RBB for RM-d-LDH (q_e – adsorbed amount of adsorbate on adsorbent at equilibrium) (0.1 g RM-d-LDH in 40 mL solution containing 400 mg/L RBB)

6.2.4 Adsorption equilibrium

For both RM-d-LDH and RM-w-LDH, RBB dye batch adsorption equilibria were studied, and the experimental data were fitted by the Langmuir and Freundlich isotherm models (Eqn. (2.1) & Eqn. (2.3)) respectively. Figure 6.4 presents the adsorption isotherms that plot the adsorbed amounts versus equilibrium concentration, and Table 6.4 shows the parameters obtained from two isotherm models. The values of equilibrium parameter R_L (Eqn. (2.2))

were 0.018 for RM-d-LDH and 0.014 for RM-w-LDH, indicating the adsorption of RBB is favourable under the experimental conditions.

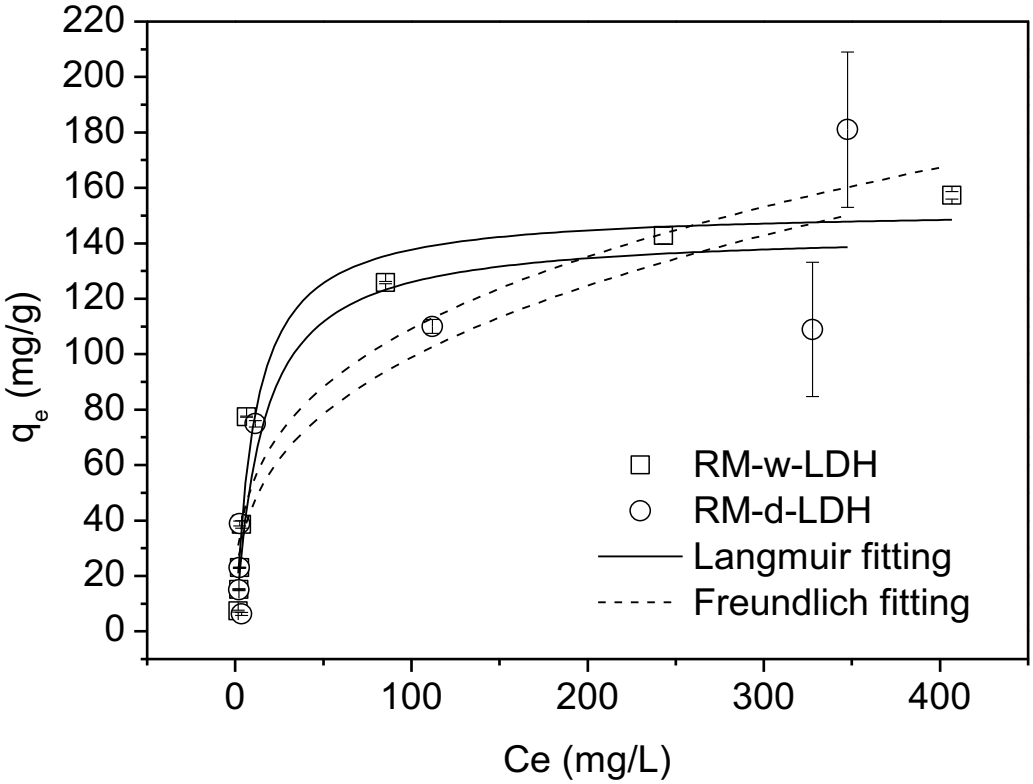

Figure 6.4 Adsorption equilibrium results (q_e – adsorbed amount of adsorbate on adsorbent at equilibrium, C_e – equilibrium solution concentration of adsorbate) (0.1 g RM-d-LDH or RM-w-LDH in 40 mL solution, at temperature = 20°C)

Table 6.4 Isotherm parameters for RBB adsorption on RM-d-LDH and RM-w-LDH

	Langmuir isotherm				Freundlich isotherm		
	Q_{max} (mg/g)	b (L/mg)	R_L	R^2	K_f (mg/g)	1/n	R^2
RM-d-LDH	144.49	0.07	0.018	0.820	21.10	0.34	0.810
RM-w-LDH	152.35	0.09	0.014	0.959	26.39	0.31	0.885

According to Figure 6.4 and Table 6.4, the isotherms for RBB dye on two adsorbents are better described by Langmuir model, with $R^2 = 0.820$ for RM-d-LDH and $R^2 = 0.959$ for RM-w-LDH. The values of equilibrium parameter R_L in Langmuir model (refer to Eqn. (2.2))

were very close to 0 with regard to both samples, suggesting that a favourable sorption of RBB onto the RM-LDHs under the conditions of this study.

Meanwhile, the Freundlich model also fits the experimental data well with R^2 values equal to 0.810 and 0.885 respectively, which were slightly lower than that of Langmuir model. The 1/n values were calculated to be 0.34 and 0.31 for RM-d-LDH and RM-w-LDH samples respectively, indicating that RM-LDHs provides some heterogeneity in the surface adsorption sites but monolayer adsorption is predominant (Huang *et al.*, 2008; Yang *et al.*, 2016).

The adsorption capacity Q_{max} for RBB was found to be 144.49 mg/g on the as-synthesised RM-d-LDH and 152.35 mg/g on RM-w-LDH. This indicates that RM-w-LDH has a higher adsorption capacity of RBB and is more accurately predicted by Langmuir isotherm model. In comparison with RM-d-LDH, therefore, RM-w-LDH provides a slightly more uniform monolayer adsorption, which is also favourable and nearly irreversible.

Overall, the adsorption performances are in good agreement with those reports on the sorption of acid dyes with LDHs material (Guo *et al.*, 2013). For instance, He *et al.* (2012) reported that the adsorption capacity of Mg-Al LDH powder for RBB was 166.7 mg/g; Gidado and Akanyeti (2020) reported Zn-Mg-Al LDH had a adsorption capacity of 164 mg/g for RBB. Although RM-LDHs contain considerable amounts of impurities, they exhibit comparable capacity with Mg-Al LDH and Zn-Mg-Al LDH and present a great potential for removing RBB dye. Referring to Section 2.3.3.2, impacts of Fe have been considered. However, direct reference about RBB sorption by Fe-incorporated LDH was not found. Therefore, whether the adsorption of RBB was enhanced by the presence of Fe in RM-LDHs cannot be deduced from this thesis. The impact of original raw materials (RM and Cal-IRM) will be considered in Section 6.5. Further research is expected to investigate the effects of these impurities, such as brucite and silica in the adsorption performance.

6.3 Calcined RM-LDHs

6.3.1 Physicochemical properties

As discussed in Section 6.2, RM-d-LDH and RM-w-LDH exhibited similarities in various experimental parameters in the batch sorption studies. It is noted that RM-w-LDH presents slightly higher sorption capacity and faster take-up for RBB. Therefore, in the further characterisation, RM-w-LDH has been selected as the main object.

After calcination at 500°C for 3 hours, the obtained materials RM-w-CLDH was granted a change in terms of BET surface area and pore size. According to Table 4.12 and Table 6.1, the BET surface area of the RM-w-CLDH (79.8 m^2/g) was increased from that of RM-w-LDH (64.0 m^2/g). The average pore size of the calcined form has also been enlarged from 8.92 to 10.47 nm.

RM-w-CLDH was also characterised by powder X-ray diffraction, FT-IR spectroscopy and TGA before and after batch adsorptions. And the results have been plotted together and compared with RM-w-LDH in Section 6.3.4, so that their chemical and micro-structural properties as well as the adsorption mechanism could be understood.

6.3.2 Kinetics

The adsorption profile of RBB to RM-w-CLDH over time is shown in Figure 6.5. At the dosage (solid/solution) of 2.5 g/L and the initial concentration of RBB was 400 mgL^{-1}. The sorption reached its equilibrium values within 1.5 hours, which considerably boost in comparison with that of RM-w-LDH (~6 hours). Furthermore, with the same initial dye concentration, RM-w-CLDH exhibits a much higher adsorption capacity than RM-w-LDH. According to the kinetic profile, a contact time of 12 h was sufficient to ensure the sorption equilibrium to be achieved and the calculated k_2 indicates a rapid uptake rate of RBB.

For kinetic modelling, the pseudo-first-order (Eqn. (2.4)), pseudo-second-order model (Eqn. (2.5)) and the Weber and Morris intraparticle diffusion model (Eqn. (2.6)), have been implemented to describe the adsorption process. The calculated parameters were reported in Table 6.5 and Table 6.6 respectively. The regression coefficients (R^2) from pseudo-first-order and pseudo-second-order models for the RM-w-CLDH are both higher than 0.95. However, better correlation is observed between experimental data and the pseudo-second-order model with R^2 close to unity. In addition, little disparity was observed between experimental

sorption capacity for RBB and the calculated equilibrium value (~163 mg/g). This indicates that the adsorption of RBB onto RM-w-CLDH is an ideal pseudo-second-order reaction, which is in line with previous research finding by Benselka-Hadj Abdelkader *et al.* (2011).

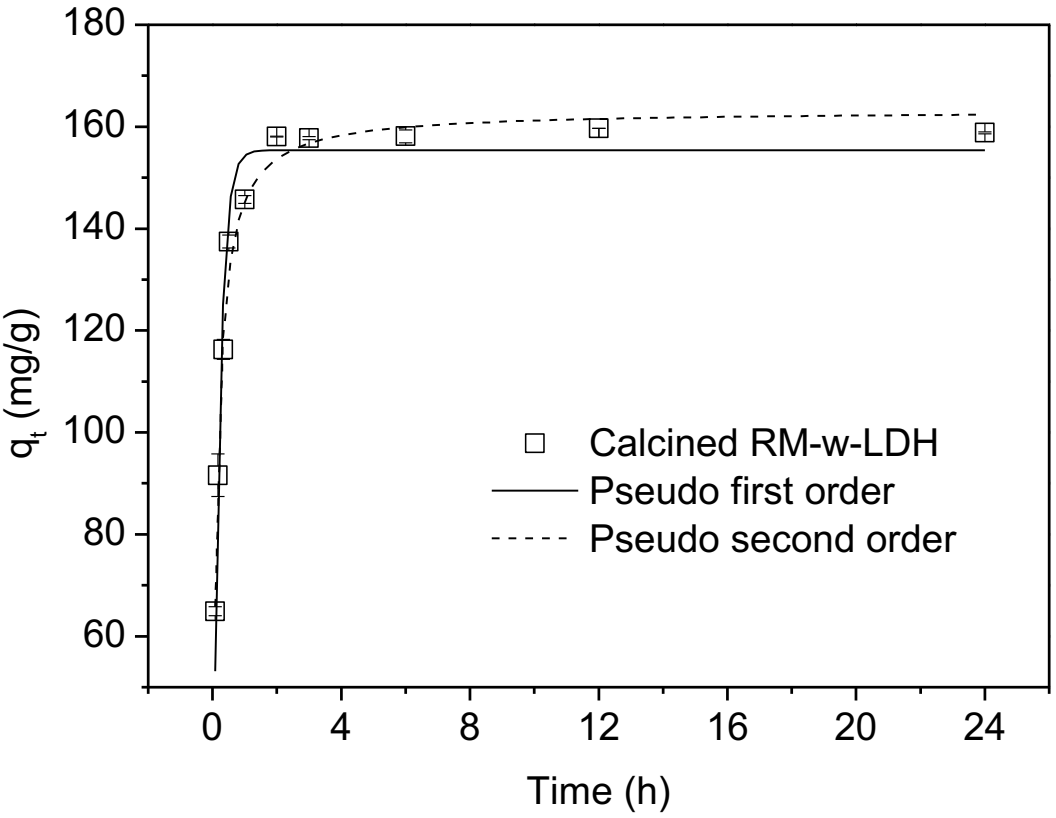

Figure 6.5 Kinetic results for Remazol brilliant blue (RBB) adsorption on RM-w-CLDH (q_t – adsorbed amount of adsorbate on adsorbent at time t) (0.1 g RM-w-CLDH in 40 mL solution containing 400 mg/L RBB; reaction temperature 25°C; initial solution pH = 6.0).

Table 6.5 Kinetic parameters for RBB adsorption on RM-w-CLDH (calcined RM-w-LDH)

Sorbent	Pseudo first order			Pseudo second order		
	q_e (mg/g)	k_1 (h^{-1})	R^2	q_e (mg/g)	k_2 (g/mg h)	R^2
RM-w-CLDH	155.37	5.02	0.955	163.19	0.05	0.989

The equilibrium time difference between RM-w-LDH and RM-w-CLDH could be attributed to different adsorption mechanisms. Dye adsorption on RM-w-LDH mainly depends on exchange mechanism; while on RM-w-CLDH, it may occur by both surface and ion exchange phenomena via layered structure reconstruction (i.e. memory effect). As reviewed in Section 2.5.2.2, there are essentially four steps in the adsorption system, where the mass transfer of sorbate onto and within the sorbent particle directly affects the adsorption rate.

Intraparticle diffusion model was implemented to examine the mass transfer in the adsorption system. Figure 6.6 demonstrates the sorption capacity of RBB at specific times against the square root of time $t^{0.5}$. This plot displays three extremely sharp linear parts over adsorption period, which describe three distinct steps in the adsorption process and are very rare to be captured in other research studies. The first portion of lines with slope k_1 stands for the external film transfer (Step II), i.e. the sorbate RBB moved across the external liquid film boundary, overcame the boundary layer resistance, then reached the surface sites of RM-w-CLDH. Then an exact intersects of the first region and the second region is spotted. The line with slope k_2 marks the beginning of intraparticle diffusion (Step III), from where RBB molecules migrated into the inner pores of RM-w-CLDH. Slope $k_2 = 29.15$ has been defined as the intraparticle diffusion parameter. The final portion represents for Step IV, starting after 1.5 $h^{0.5}$ for RM-w-CLDH, at the point intraparticle diffusion reached the state of equilibrium and RBB molecules started being settled at the internal surface sites. It could be concluded that the adsorption of sorbate at surface sites is very rapid.

As shown in Figure 6.6, the plot yielded from the first region (with slope k_1) would pass through or very close to the origin. That suggests that the transport of sorbate from bulk solution to the exterior film boundaries (Step I) could be neglected as well. The presence of k_1 region demonstrates that external mass transfer is another main controlling mechanism to the sorption process. Since the intraparticle diffusion only contributes to a relatively small amount of time, starting from 0.75 $h^{0.5}$ to 1.5 $h^{0.5}$, it may be attributed to the significant increase of pore size upon the calcination of RM-w-LDH. In consequence, RBB molecules are comparatively easier to move within the internal pores of the sorbent than to transfer from the surface. It could then be deducted that ion exchange is still a contribution to this sorption process, as the exchange process onto ion exchangers involves external mass transfer and internal diffusion (Choy *et al.*, 2004). The notable differences in microstructure raised from the calcination treatment have significantly altered the properties of RM-w-CLDH. Therefore,

a mixture of external mass transfer and intraparticle diffusion through the macrospores/ microspores of LDH may account for the mechanism of dyes sorption, which is consistent with the literature (Yang *et al.*, 2016). Furthermore, the rapid uptake of RBB to the sorbent may also be explained as RBB ions participated the reconstruction of the double layered structures, which would be further investigated in respect of the pore size.

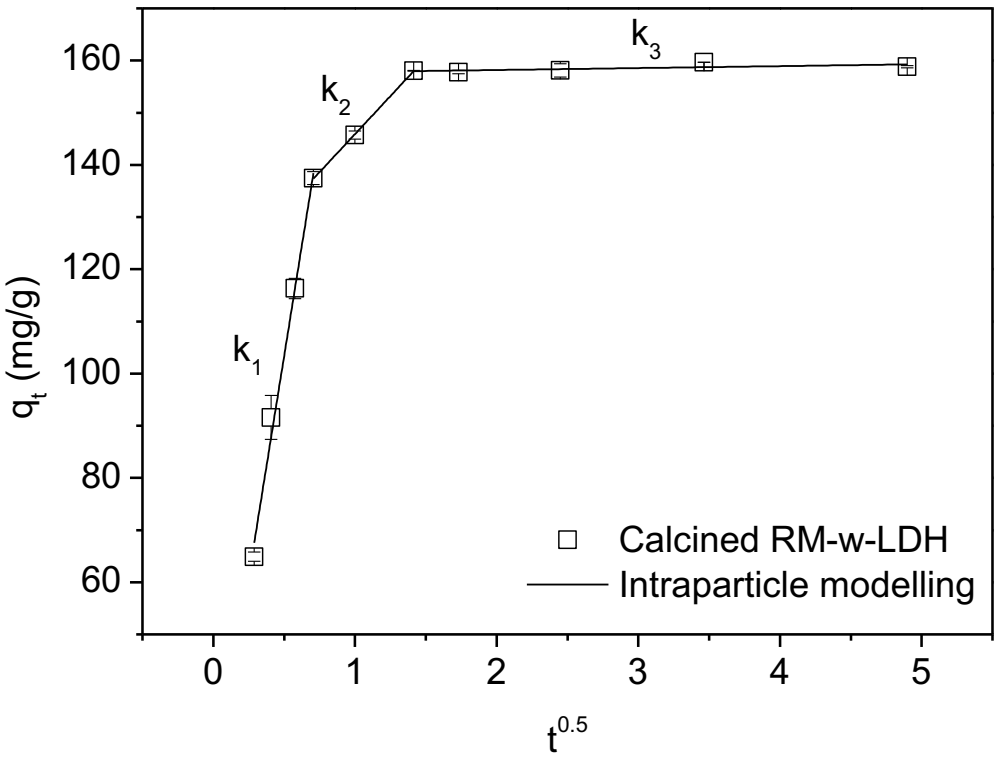

Figure 6.6 Intraparticle diffusion modelling for RBB on RM-w-CLDH (0.1 g sorbents in 40 mL solution with 400 mg/L RBB); reaction temperature 20 °C; initial solution pH = 6.0).

Table 6.6 Intraparticle diffusion parameters for RBB adsorption on RM-w-CLDH

Sorbent	k_1	C_1 (mg/g)	R_1^2	k_2	C_2 (mg/g)	R_2^2	k_3	C_3 (mg/g)	R_3^2
RM-w-CLDH	169.40	18.65	0.989	29.15	116.74	0.9996	0.37	157.45	0.292

6.3.3 Adsorption equilibrium

The experimental equilibrium data of RM-w-CLDH were fitted to the non-linear Langmuir and Freundlich isotherm models as shown in Figure 6.7. In the adsorption study, the solid/solution ratio is 2.5 g/L. 0.1 g RM-w-CLDH was capable of almost completely absorbing 800 mg/L RBB (the maximum solution concentration in the batch adsorption study) from the 40 mL solution. That implies the adsorption capacity of RM-w-CLDH is at least 320 mg/g. In Table 6.7, the Langmuir isotherm regression predicts that Q_{max} for RBB is 2761.68 mg/g. However, Figure 6.7 does not exhibit a typical Langmuir full profile and a dynamic reversible equilibrium has not been reached. The R^2 of Langmuir model and Freundlich model fittings are only around 0.52. It is therefore inadequate to derive a reliable Q_{max}, due to lack of a saturation limit. An adjusted solid/solution ratio (1.0 g/L) shall be employed in a future equilibrium study.

The adsorption isotherm for RM-w-LDH and RM-w-CLDH are both better represented by Langmuir model (R^2 of 0.959 and 0.521 respectively), indicating that the adsorption tends to be predominantly monolayer. Besides, the maximum sorption capacity of RM-w-CLDH was found at least 2.1 times greater than that of its parent material RM-w-LDH (152.35 mg/g). This finding is in line with LDH & CLDH for dye Orange G adsorption (Benselka-Hadj Abdelkader *et al.*, 2011) and various LDHs & CLDHs for dyes wastewater treatments in the review of Yang *et al.* (2016).

Table 6.7 Isotherm parameters for RBB adsorption on RM-w-CLDH (calcined RM-w-LDH)

Sorbent	Langmuir				Freundlich		
	Q_{max} (mg/g)	b (L/mg)	R_L	R^2	K_f (mg/g)	1/n	R^2
RM-w-CLDH	N.A. (2761.68)	0.05	0.024	0.521	129.05	1.05	0.520

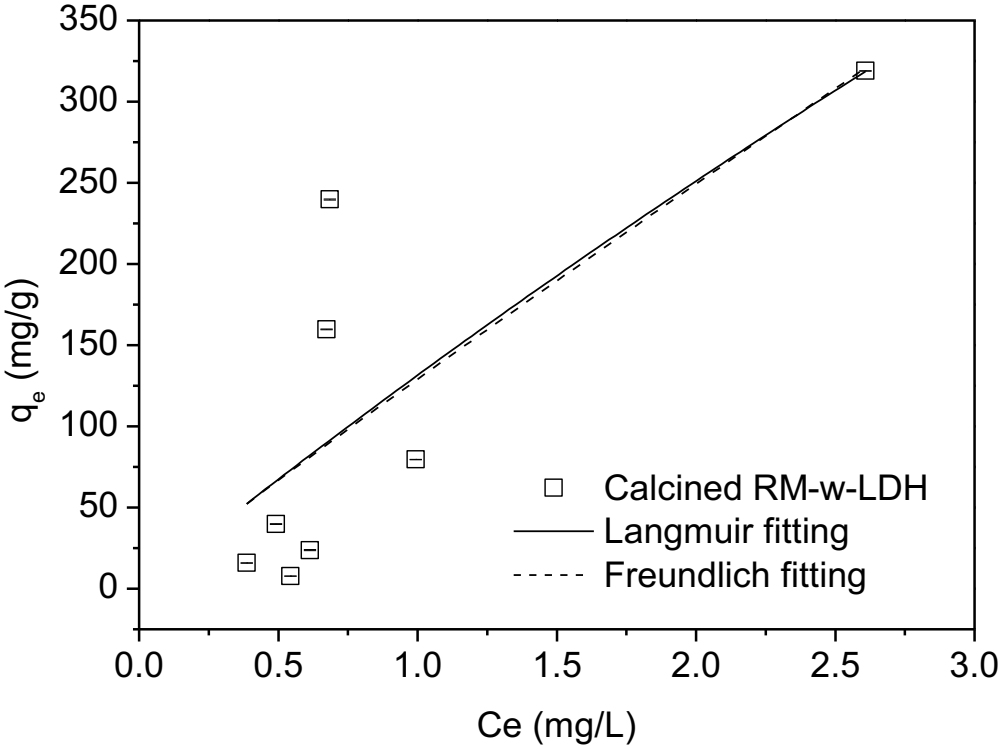

Figure 6.7 Adsorption equilibrium results (q_e – adsorbed amount of adsorbate on adsorbent at equilibrium, C_e – equilibrium solution concentration of adsorbate) (solid / solution (RM-w-CLDH) ratio was 2.5 g/L, initial pH = 6.0).

6.3.4 Regeneration study

In order to test the potential reusability of RM-w-CLDH, after completing equilibrium adsorption experiments, the suspensions were filtrated, washed, dried in the oven and calcined at 500°C again for 4 h. It can be seen that the calcined RM-w-CLDH-RBB turned back to rusty red powder. The recovered adsorbent was re-dispersed in 800 mg/L RBB dye solution with a solid/liquid ratio of 2.5 mg/L. This process was repeated for two cycles and the adsorption capacities of the regenerated RM-w-CLDH are shown in Figure 6.8.

After the first thermal treatment cycles, the removal amount of RBB did not see an obvious decrease, which still maintained at 320 mg/g with a nearly complete elimination percentage of 100%. In the next regeneration round, the sorption capacity of RM-w-CLDH-2 dropped to 278.9 mg/g, at a removal ratio of 87.2% compared with RM-w-CLDH-1. The results are in conformity with the findings reported by Ni *et al.* (2007) with regards to the adsorption of methyl orange on MgFe-LDH and by Alexandrica *et al.* (2015) of the removal of Reactive Blue 19 on MgAl-LDH. Although Zhu *et al.* (2005) reported that the adsorption capacity of

CLDH-1 for Brilliant Blue R decreased 69% after the first cycle of regeneration, compared with the original CLDH. The reduction in adsorption capacity with RM-w-CLDH after the successive cycle may be due to the decrease in the crystallinity of LDH-like materials during continuous reconstruction process (Ahmed and Gasser, 2012). That demonstrates that the reuse of the used RM-w-CLDH via calcination-rehydration pathway is feasible, and RM-w-CLDH presents stable natures in aqueous phase. However, its optimum efficiency is within the first three cycles.

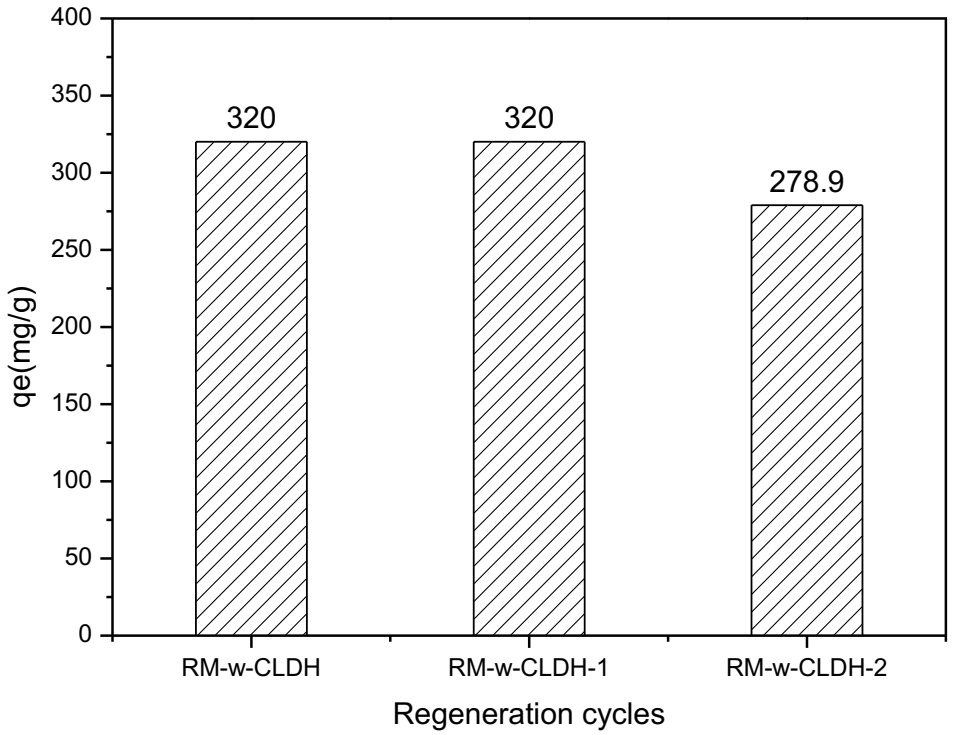

Figure 6.8 Adsorption ability of regenerated RM-w-CLDH after successive cycles; adsorbent dose = 2.5 g/L; RBB concentration = 400 mg/L; pH = 6 at room temperature.

6.4 Commercial Mg-Al LDH

6.4.1 Physicochemical properties

The commercially available Mg-Al LDH has been introduced in Section 4.4.2 and Table 6.1. LDH presents considerably smaller particle size but a broader particle size distribution. The BET surface area of LDH (8.35 m^2/g) is significantly lower than those of RM-w-LDH (64.0 m^2/g) and RM-d-LDH (74.8 m^2/g). The total pore volume of LDH is 0.015 cm^3/g, which is 10 times smaller than that of RM-w-LDH (0.143 cm^3/g).and RM-d-LDH (0.204 cm^3/g).

6.4.2 Kinetics

As observed from Figure 6.9 and Table 6.8, the pseudo-second-order kinetic model fitted the process of RBB adsorbed onto the un-calcined commercial LDH with R^2 of 0.923. The data correlation quality could be further improved by acquiring more kinetic data at the times when the sorption system is reaching to equilibrium (Rudzinski and Plazinski, 2007). The adsorption reached equilibrium after 12 h, which was comparatively longer than RM-LDHs (6 h), as discussed in Section 6.2. And the uptake rate by LDH (k_2= 0.03) is slower than RM-w-LDH and RM-d-LDH (k_2= 0.05 and 0.08, respectively).

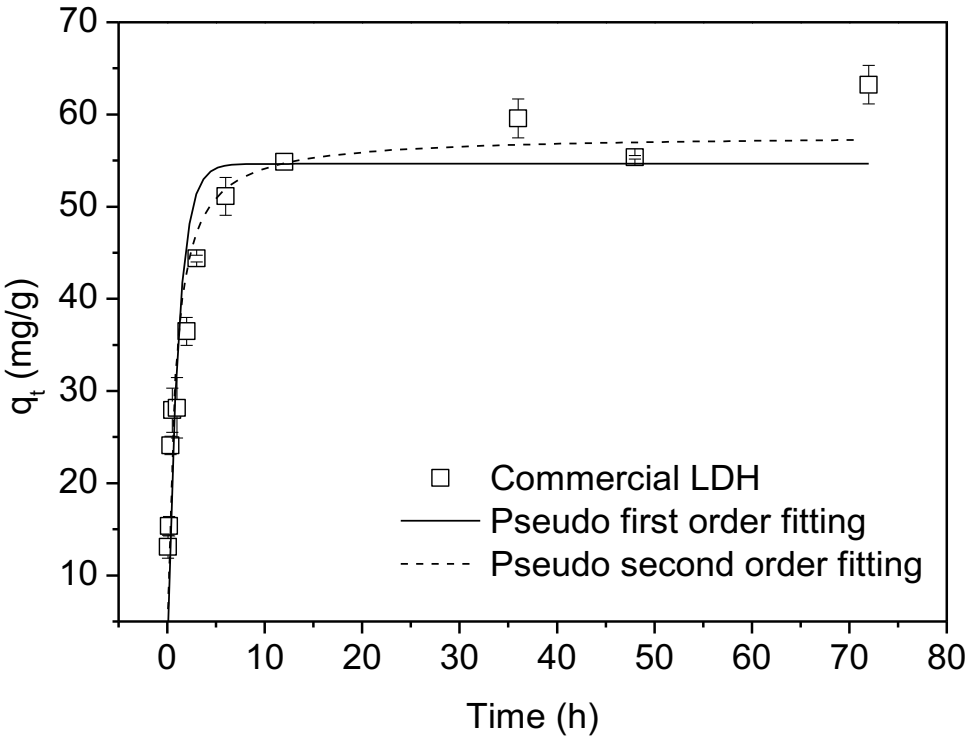

Figure 6.9 Kinetic results for Remazol brilliant blue (RBB) adsorption on commercial LDH (q_t – adsorbed amount of adsorbate on adsorbent at time t) (0.1 g commercial LDH in 40 mL solution containing 400 mg/L RBB; reaction temperature 25°C; initial solution pH = 6.0).

Table 6.8 Kinetic parameters for RBB adsorption on commercial LDH

Sorbent	Pseudo first order			Pseudo second order		
	q_e (mg/g)	k_1 (h^{-1})	R^2	q_e (mg/g)	k_2 (g/mg h)	R^2
Commercial LDH	54.64	0.94	0.819	57.77	0.03	0.923

To determine the transport progress in the adsorption process and which step governs the overall adsorption rate, film diffusion and intraparticle diffusion model were employed. Figure 6.10 displays the mass transfer plot of RBB adsorption on LDH, which consisted of two linear sections. The piecewise linear regression results were listed in Table 6.9. The first, sharper linear section was attributed to the film diffusion from solution to the external surface sites, i.e. Step II. The subsequent process was the slower migration of RBB within the pores by intraparticle diffusion (Step III), which yielded the intraparticle diffusion rate constant k_2 = 1.61 at the initial concentration of 400 mg/L. Such behaviour confirms that intraparticle diffusion is not the sole mechanism operative in the system, but the resistance of intraparticle diffusion plays the key rate-limiting role. Similar trend was observed in the sorption study of dyes on MgZnAl-LDH by Bouraada *et al.* (2009).

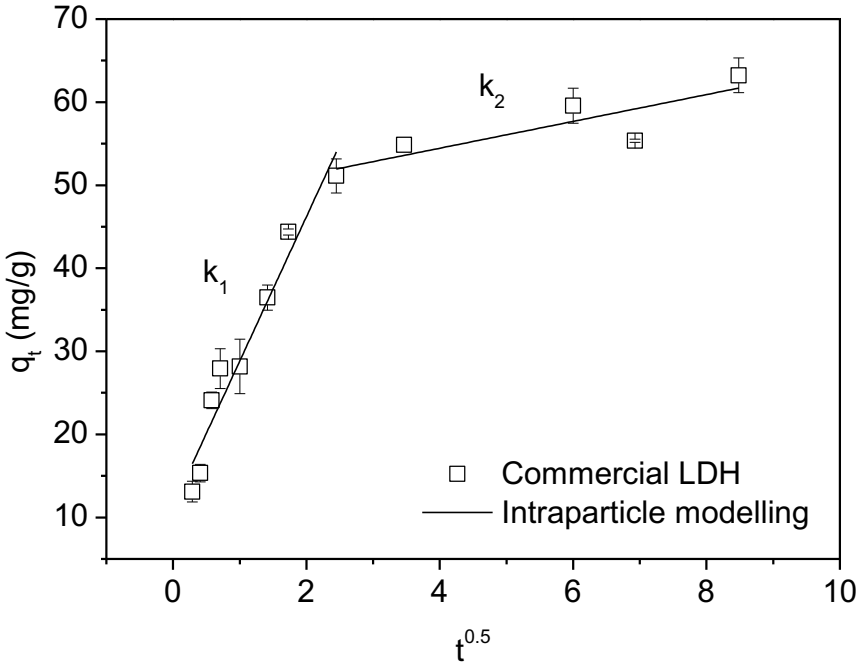

Figure 6.10 Intraparticle modelling for Remazol brilliant blue (RBB) adsorption on commercial LDH (q_t – adsorbed amount of adsorbate on adsorbent at time t) (0.1 g

commercial LDH in 40 mL solution containing 400 mg/L RBB; reaction temperature = 25°C; initial solution pH = 6.0).

Table 6.9 Intraparticle parameters for RBB adsorption on Commercial Mg-Al LDH

Sorbent	k_1	C_1 (mg/g)	R_1^2	k_2	C_2 (mg/g)	R_2^2
Commercial LDH	17.38	11.44	0.941	1.61	48.00	0.651

The kinetic profile in the uptake of RBB by LDH differed with RM-LDHs (Figure 6.2). It was found that RM-LDHs spent less time in film diffusion (external mass transfer) process. In addition, given a much greater intraparticle parameter k_2 (in Table 6.3), both RM-w-LDH and RM-d-LDH exhibit an enhanced diffusion of RBB molecules through porous system. Therefore, it was proved that for RM-LDHs and LDH, intraparticle diffusion is not the sole controlling step, but the variation may be explained by their different pore volume as well as different ionic nature. In addition, the obtained curve of LDH only presents two linear plots, implying Step IV (sorption of sorbate at internal surface sites) could be neglected.

6.4.3 Adsorption equilibrium

The RBB equilibrium data of LDH were analysed with Langmuir and Freundlich isotherm models as shown in Figure 6.11 and Table 6.10. In contrast with RM-LDHs, the equilibrium data of LDH is fitted better by Freundlich model ($R^2 \geq 0.978$), while relatively poorly described by the Langmuir model ($R^2 = 0.815$), indicating a heterogeneous adsorption (Foo and Hameed, 2010). The 1/n value for RBB sorption on LDH suggests a certain degree of heterogeneity on the surface of LDH, which is very similar to RM-LDHs (Table 6.4). However, it can also be found that the values of Q_{max} and K_f were considerably higher for the RM-LDHs than for LDH, indicating RM-LDHs own larger adsorption capacities for RBB.

Table 6.10 Isotherm model parameters (0.1 g commercial LDH in 40 mL solution)

Sorbent	Langmuir isotherm				Freundlich isotherm		
	Q_{max} (mg/g)	b (L/mg)	R_L	R^2	K_f (mg/g)	1/n	R^2
Commercial LDH	49.94	0.02	0.056	0.815	7.00	0.31	0.978

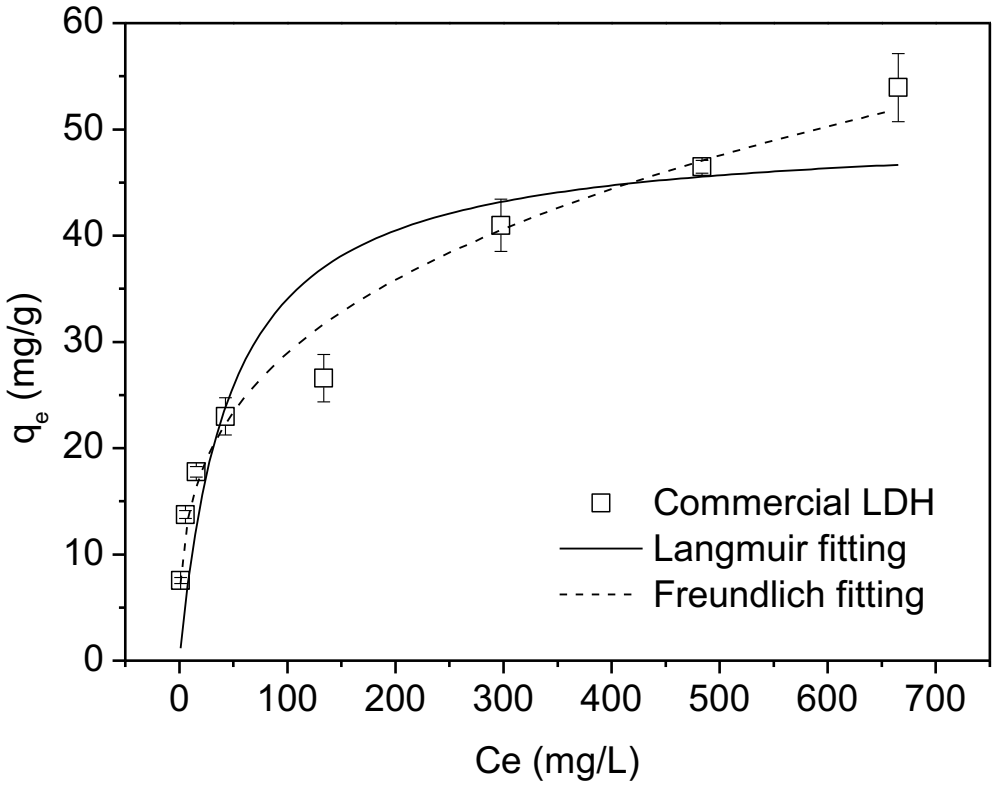

Figure 6.11 Adsorption equilibrium results (q_e – adsorbed amount of adsorbate on adsorbent at equilibrium, Ce – equilibrium solution concentration of adsorbate), 0.1g commercial LDH in 40 mL solution, at temperature = 20 °C; initial pH = 6.0.

6.5 Red mud and Calcined Red mud

6.5.1 Physicochemical properties

The raw materials IRM and Cal-IRM are able to serve as comparisons to the RM-LDHs, since they contain a number of same minerals, such as hematite, cancrinite and/ or sodalite, quartz, and calcite (refer to Figure 4.3). The physicochemical properties of the original IRM and Cal-IRM have been discussed in Chapter 4 – Section 4.1.2. After calcination, the BET surface areas of Cal-IRM increased from 15.8 m^2/g to 24.1 m^2/g, while the pore size dropped slightly from 11.31 nm to 8.98 nm.

6.5.2 Kinetics

Figure 6.12 describes the slow equilibrium for both IRM and Cal-IRM, which suggests that physical sorption is mainly responsible for the RBB uptake. Although left for 72 hours, it is still difficult to affirm that RBB sorption on IRM and Cal-IRM had reached their respective equilibrium. The experimental data shift above the calculated equilibrium values at the longer timescales, as R^2 are slightly away from unity. In comparison, pseudo-second-order model fits the kinetic data better than pseudo-first-order (Table 6.11). According to the kinetic modelling prediction, the adsorption capacities of IRM and Cal-IRM for RBB are both approximately 40 mg/g at the initial RBB concentration of 800 mg/L, where IRM is slightly higher than that of Cal-IRM. Besides, the rate constants k_1 and k_2 of IRM are larger, implying that calcination of red mud does not necessarily improve its capability for RBB adsorption.

However, as suggested by Di Bucchianico (2008), values of $R^2 < 0.5$ indicate a weak relation between the predictor variable(s) and the response variable, while $0.5 < R^2 < 0.8$ indicate that the model is not adequate. Firstly, the solid surfaces of IRM and Cal-IRM are potentially heterogeneous and irregular, the simple equations of pseudo-first-order and pseudo-second-order model may not be able to well correlate the measured kinetic data. More importantly, pseudo-first-order and pseudo-second-order model were derived on the basis of a surface reaction-controlled adsorption, which assume the rate-limiting step is chemical sorption and the adsorption is irreversible (Ho and Mckay, 1999; Rudzinski and Plazinski, 2007; Xiao, Azaiez and Hill, 2018). But for the adsorption of RBB on IRM and Cal-IRM, the effects of transport phenomena and chemical sorption are hardly separable. In addition, the lack of sufficient data points collected in the later stage of the adsorption process may affect the correlation quality ad well.

Table 6.11 Kinetic parameters for RBB adsorption on IRM and Cal-IRM (800 mg/L)

Sorbent	Pseudo first order			Pseudo second order		
	q_e (mg/g)	k_1 (h^{-1})	R^2	q_e (mg/g)	k_2 (g/mg h)	R^2
IRM	38.82	2.90	0.401	42.18	0.08	0.627
Cal-IRM	38.46	1.61	0.356	41.97	0.05	0.592

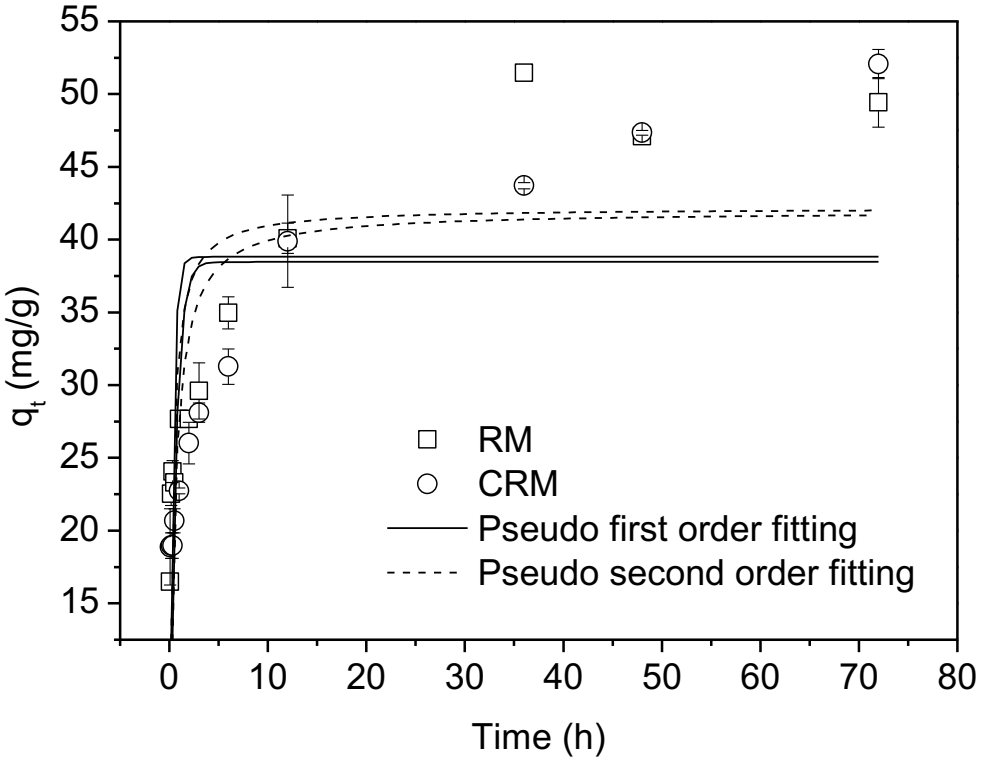

Figure 6.12 Kinetic results for Remazol brilliant blue (RBB) adsorption on IRM & Cal-IRM (q_t – adsorbed amount of adsorbate on adsorbent at time t) (0.1 g sorbent IRM or Cal-IRM in 40 mL solution of 400 mg/L RBB; reaction temperature 25°C; initial solution pH = 6.0)

Figure 6.13 displays the plots of intraparticle diffusion model with double-linear profiles of IRM and Cal-IRM. For IRM, the first linear region (external film transfer - Step II) found at 6 $h^{0.5}$ attributes to the slow adsorption of dye onto the external surface of adsorbent or the weak electrostatic attraction between the dye and IRM particle; while the second linear region shows a downward trend with the value of R^2 below 0 that further confirms the sorption mechanism is film diffusion controlled (Igwe, Mbonu and Abia, 2007). For Cal-IRM, however, the second linear region (intraparticle diffusion – step III) is a gradual adsorption phase, which is the main rate limiting step. It is found that the adsorption kinetics fitted

intraparticle diffusion model better than the pseudo-first-order kinetic model and pseudo-second-order kinetic model. The high value of the regression coefficient (R_2^2) for Cal-IRM indicates that the sorption kinetics is controlled by diffusion rather than by the rate of surface reaction (Rudzinski and Plazinski, 2007). The calcination process has altered the properties of IRM especially in terms of surface area. The increased surface area of Cal-IRM tends to aid the speed of film diffusion as a larger solid-aqueous interface is provided (Choy *et al.*, 2004).

Table 6.12 Intraparticle parameters for RBB adsorption on IRM and Cal-IRM (800 mg/L)

Sorbent	k_1	C_1 (mg/g)	R_1^2	k_2	C_2 (mg/g)	R_2^2
RM	5.55	19.77	0.954	-0.57	53.43	-0.781
CRM	6.69	16.10	0.989	2.41	30.74	0.932

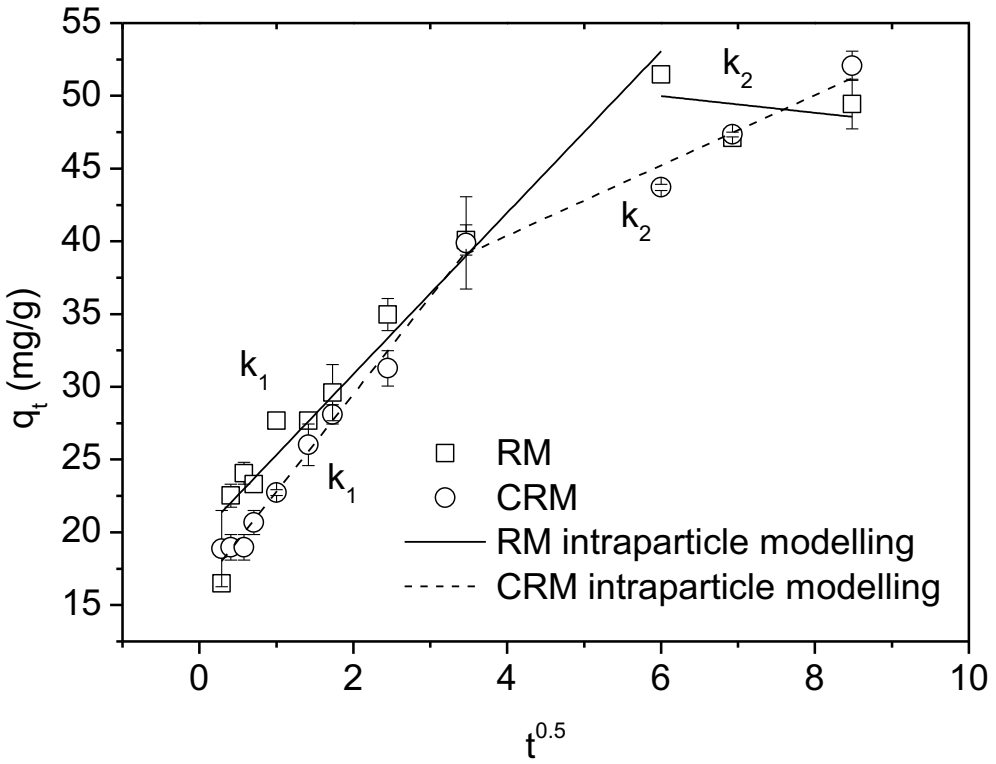

Figure 6.13 Intraparticle modelling for Remazol brilliant blue (RBB) adsorption on raw materials IRM and Cal-IRM (q_t – adsorbed amount of adsorbate on adsorbent at time t) (0.1 g sorbent IRM or Cal-IRM in 40 mL solution containing 800 mg/L RBB; reaction temperature = 25°C; initial solution pH = 6.0).

6.5.3 Adsorption equilibrium

The RBB equilibrium data of IRM and Cal-IRM were fitted to the non-linear Langmuir and Freundlich isotherm models, as shown in Figure 6.14 and Table 6.13. Both isotherms are a close fit by the Langmuir and Freundlich model with all R^2 values > 0.994. However, it should be noted that the Langmuir adsorption model is developed with the assumption as follows: (1) Homogeneous adsorption sites (provided the adsorbate is bound to only one type of site); (2) Each adsorption site binds only one solute molecule; (3) Dynamic reversible equilibrium established in the timeframe of the experiment; (4) No interaction between solutes on the surface to influence their adsorption behavior. If these four requirements for the application of the Langmuir model are not satisfied, the coefficient of determination value (R^2) will be meaningless (Latour, 2015). In the present case, Langmuir model fails to account for the inhomogeneous surface of the adsorbents, which may include multiple types of sites with varying adsorption energy. Additionally, the equilibriums have not been reached according to Figure 6.12, although the batch sorption set was shaken for 7 days. Therefore, the maximum adsorption capacity (Q_{max}) calculated from Langmuir model cannot reveal the actual capacity. Ratnamala, Shetty and Srinikethan (2012) found the RBB adsorption capacity of RM was 27.8 mg/g and the equilibrium was reached within 130 min under diluted RBB concentration.

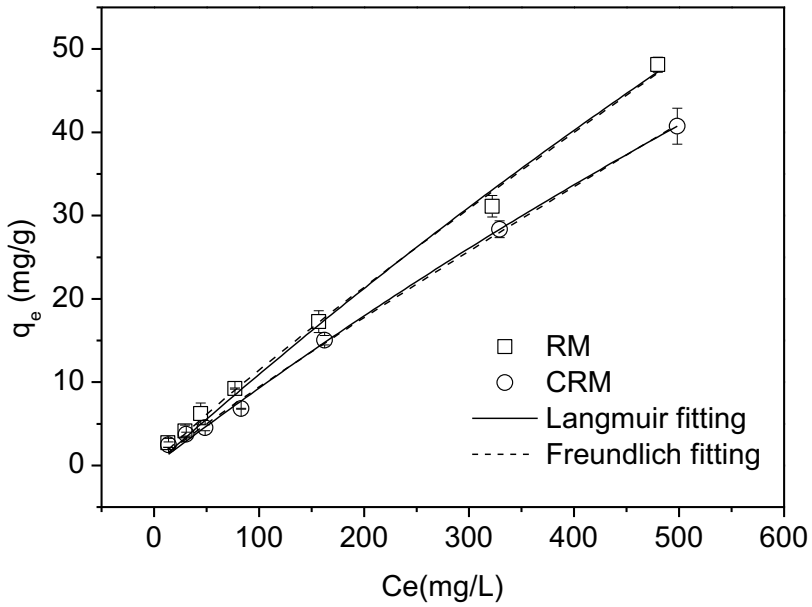

Figure 6.14 Adsorption equilibrium results (q_e – adsorbed amount of adsorbate on adsorbent at equilibrium, Ce – equilibrium solution concentration of adsorbate) (0.1 g IRM or Cal-IRM in 40 mL solution, initial pH = 6.0).

Table 6.13 Isotherm model parameters (0.1 g IRM or Cal-IRM in 40 mL solution)

Sorbent	Langmuir			Freundlich		
	Q_{max} (mg/g)	b (L/mg)	R^2	K_f (mg/g)	1/n	R^2
IRM	N.A. (377.58)	2.98×10^{-4}	0.994	0.18	0.90	0.996
Cal-IRM	N.A. (273.15)	3.52×10^{-4}	0.997	0.14	0.92	0.997

In comparison with RM-w-LDH and RM-d-LDH (see Table 6.2), the adsorption rate constants of IRM and Cal-IRM are much lower, and the equilibrium is much more difficult to be obtained. Apart from the kinetics data, the actual adsorption capacities of RM-LDHs (refer to Table 6.4) are considerably larger than their raw materials, indicating that the synthesis process significantly changes the adsorption characteristics of red mud.

6.6 Characterisation of RM-LDHs and RM-CLDHs

In order to further investigate the adsorption mechanisms of RBB dye on the RM-LDHs synthesised and commercial LDH, the samples before adsorption of RBB, were washed three times, oven dried at 60 °C for 48 h and then analysed. Similarly, after dye adsorption, this process was repeated to form a comparison of before and after RBB adsorption, as well as before and after calcination. Their chemical and micro-structure analyses (as reviewed in Section 2.5.3) are examined and discussed in this section.

6.6.1 XRD test studies

The XRD patterns of RM-w-LDH before & after (RM-w-LDH, RM-w-LDH after RBB sorption, RM-w-CLDH, RM-d-CLDH after RBB sorption respectively) were plotted and compared in Figure 6.15. The characteristic diffractions of LDH-like structure are easily recognized by typical planes of (003) and (006) in the synthesised RM-d-LDH, as discussed previously in Section 4.3.1. After RBB adsorption, the RM-w-LDH-R (Figure 6.15b) did not exhibit a significant difference on the XRD pattern compared with that shown by the original RM-w-LDH, except from the crystallinity of the adsorbent was a bit eliminated (Alexandrica *et al.*, 2015). There is little evidence shows the featured peak of RBB appearing and the basal spacing did not show a notable change either, implying the adsorption mainly happens on the outer surface of the hydroxide layers (Guo *et al.*, 2013). This observation is in well agreement with other research, which are presented in Section 2.5.3. Flores *et al.* (2011) highlighted the chemical affinity between the dipolar groups (e.g. S=O, C=O, and N–H) and the Al-O and Fe-O pairs. And instead of exchanging out CO_3^{2-} contained between the layers, RBB anions may attach to the edge of CO_3^{2-} (Lin, Fang and Chen, 2014). Therefore, it is believed that ion exchange is not the predominant mechanism of removing RBB by RM-w-LDH.

On the other hand, the effect of calcination is visible in Figure 6.15 (b-c). The featured Bragg reflections of LDH-like compounds are absent in the XRD pattern of RM-w-CLDH, which indicates that the layer structure was disappeared after calcination. When the calcination product RM-w-CLDH was in contact with the RBB dye solution again, both the adsorption process and the intercalation of anionic molecule of RBB into the RM-w-CLDH structure occurred, and the layered double structure was mostly reconstructed (Figure 6.15d). A minor enlargement of the interlayer space from $d_{003} = 7.78$ Å to $d_{003} = 8.08$ Å is detected. Since the ion size of anionic RBB is larger than that of CO_3^{2-}, the increasing distance of the

interlayer spacing is attributed to the partial intercalation of RBB^- into the swelled layer structure (sharing this space with the hydroxyl or carbonate anions). However, since the (003) interlayer distance does not exhibit a notable increase, the completed incorporation of RBB^- anions into the interlayers of RM-w-CLDH does not occur. Extremera *et al.* (2012) pointed out that only at high concentrations (10 g/L and 50 g/L), acid orange 10 won the competition with hydroxyl and occupied the interlayer domain of the LDH, d_{003} = 17.7 Å was observed.

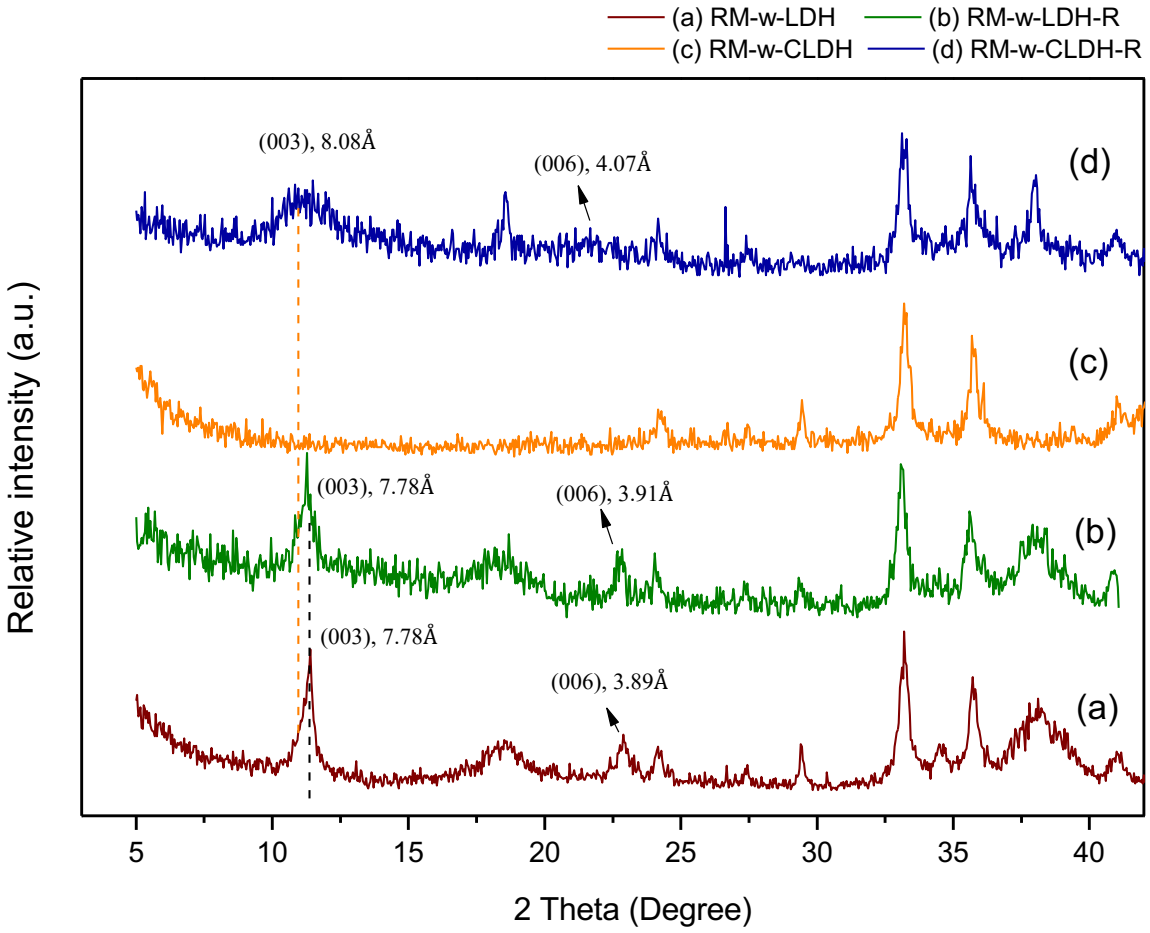

Figure 6.15 XRD patterns of RM-w-LDH synthesised (a) before and (b) after RRB dye removal; and (c) RM-w-CLDH obtained and (d) after RBB adsorption.

The re-appearance of the LDH diffraction peaks is attributed to the ability of RM-w-CLDH to incorporate anions (mainly OH^- and CO_3^{2-}, partially RBB^-) in solution to rebuild its layered structure and compensate the charge, which is the so called 'memory effect'. The $-SO_3^-$ group of the RBB anions may be attracted to the metal ions and hydroxyl from two layers of RM-w-CLDH, which are via electrostatic attraction and hydrogen bonding (Guo *et al.*, 2013). This mechanism explains for the strong uptake ability of RM-w-CLDH (refer to Section 6.3). In addition, the peaks for (003) and (006) are broadened and their intensities are lowered in

comparison to the parental RM-w-LDH (Figure 6.15a), suggesting a reduced crystallinity because of the calcination and regeneration process. The decreased crystallinity of RM-w-CLDH-R probably induces the reduction of its sorption capacity in the next regeneration cycles. The evolution of diffractograms and the corresponding basal space of the RM-w-LDH products during the first (adsorption-calcination-rehydration) cycle, agree well with the observations from Pavlovic *et al.* (2005) and Alexandrica *et al.* (2015). Therefore, it can be concluded that RM-LDHs are capable of being regenerated because of the 'memory effect', the adsorbed pollutants could be eliminated by thermal treatment and the used adsorbents could re-gain their LDH-like structure via rehydration and be prepared for reuse.

6.6.2 FT-IR test studies

The spectra of RM-w-LDH before and after adsorption are included in Figure 6.16. The broad peak located in the 3600-3000 cm^{-1} region corresponds to O-H stretching vibrations of the interlayer surface or interlayer water molecules (Extremera *et al.*, 2012).

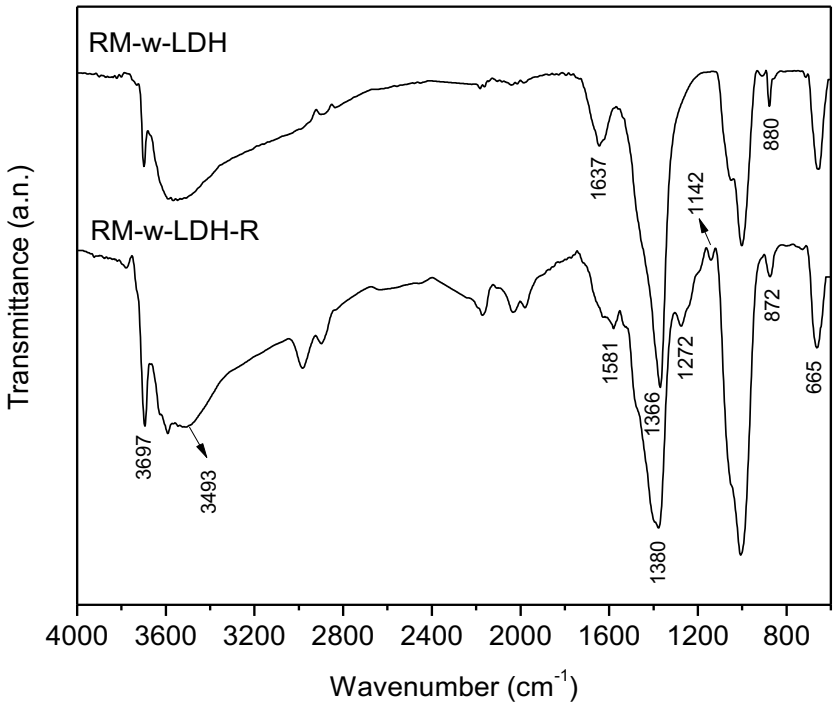

Figure 6.16 FTIR spectra of (a) RM-w-LDH, (b) RM-w-LDH-R

In the spectra of RM-w-LDH-R, the peaks around ~1900 cm^{-1} are assigned to the C-N bond (R. M. M. dos Santos *et al.*, 2017). The band appeared at ~1581 cm^{-1} is likely linked to C=C

vibration in aromatic rings (Li *et al.*, 2018). RM-w-LDH-R reveals the typical peaks of S=O bond from RBB in the 1280-1130 cm^{-1} region (Guo *et al.*, 2013). The band at ~1000 cm^{-1} becomes more intense for RM-w-LDH-R, which can be associated with C-N stretching vibration of RBB (Ahmad, Ahmad Puad and Bello, 2014). Therefore, the connection between the adsorbed RBB anions and the hydroxides layers are via the sulfonate groups and perhaps the aromatic rings (Extremera *et al.*, 2012). The featured band of carbonate ions is still evidenced in RM-w-LDH-R, although it slightly shifted from ~1366 cm^{-1} to ~1380 cm^{-1}. It suggests that the interlayer carbonate anions of RM-w-LDH are not displaced by RBB anions.

Figure 6.17 highlights the differences of RM-w-LDH and RM-w-CLDH after the RBB adsorption. It is observed the stretching vibration located at 3398 cm^{-1} is weakened for RM-w-CLDH-R, indicating less -OH are bonded after the regeneration of layered structure. The C=C vibration belong to aromatic ring accounts for the bands at ~1570 cm^{-1}.

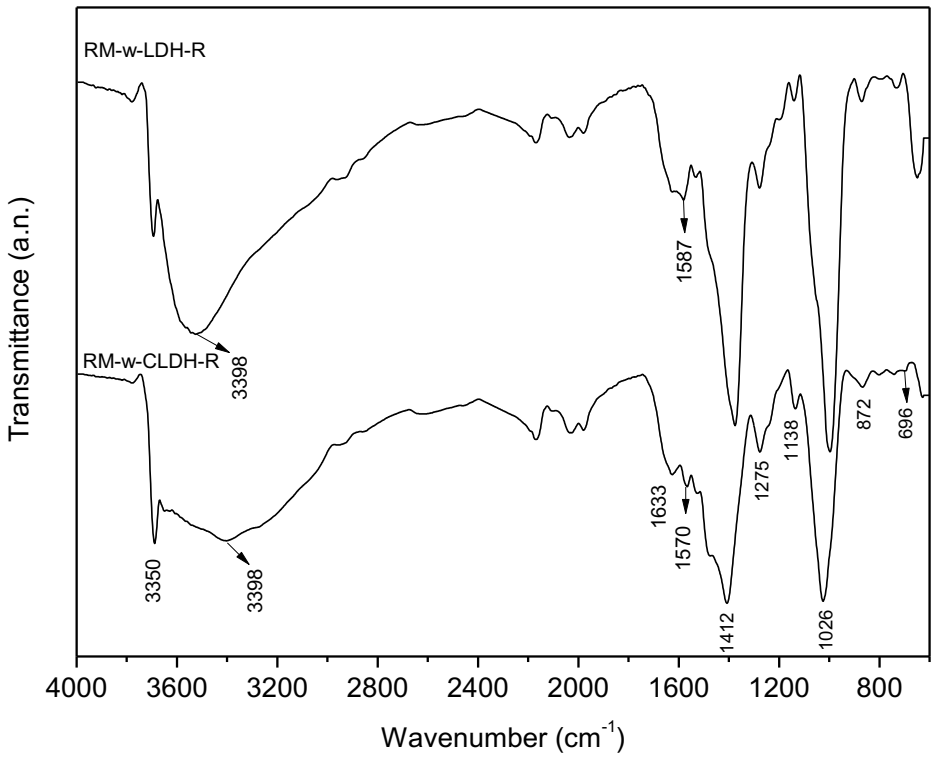

Figure 6.17 FTIR spectra of (a) RM-w-LDH-R, (b) RM-w-CLDH-R

More distinct vibrations appear on RM-w-CLDH-R, due to the higher quantity of RBB dye adsorbed on RM-w-CLDH (Harizi *et al.*, 2018). The asymmetric band close to ~1412 cm^{-1} of RM-w-CLDH-R is related to the axial deformation and bending of the C-H from the RBB dye structure (Alexandrica *et al.*, 2015; R. M. M. dos Santos *et al.*, 2017). The peaks in the

region of 1280-1130 cm^{-1} representing the S=O vibration are stronger in RM-w-CLDH-R. These phenomena may also imply a greater degree of RBB^- intercalation into RM-w-CLDH.

According to Section 6.3.4 and Section 6.6.1, the desorption of RBB upon calcination at 500°C and the regeneration of RM-w-LDH upon contact with aqueous solution can be detected. Figure 6.18 shows the FTIR spectra of RM-w-CLDH-1 and RM-w-CLDH-2. They display almost overlapped patterns with the same main starching vibrations, which are also very similar to RM-w-CLDH (see Figure 4.34). The vibration of interlayer water H-O-H at ~3348 cm^{-1} is weakened after thermal treatment. The band at ~1410 cm^{-1} is attributed to the absorptions of H_2O and CO_2 on oxide surfaces of the calcined products (Lv *et al.*, 2006b). The bands between 1000 cm^{-1} and 600 cm^{-1} could be attributed to the vibration modes of metal oxides MgO, Fe_2O_3 and Al_2O_3 (Geng *et al.*, 2013). However, the characteristic vibrations of RBB dye structure at ~1580 cm^{-1}, ~1275 cm^{-1} and ~1138 cm^{-1}, which can be observed in Figure 6.17, disappear after the calcination of RM-w-CLDH-R. Therefore, the FTIR analyses confirm that RM-w-LDH-R and RM-w-CLDH-R are able to be cleaned up and regenerated via calcination-rehydration pathway.

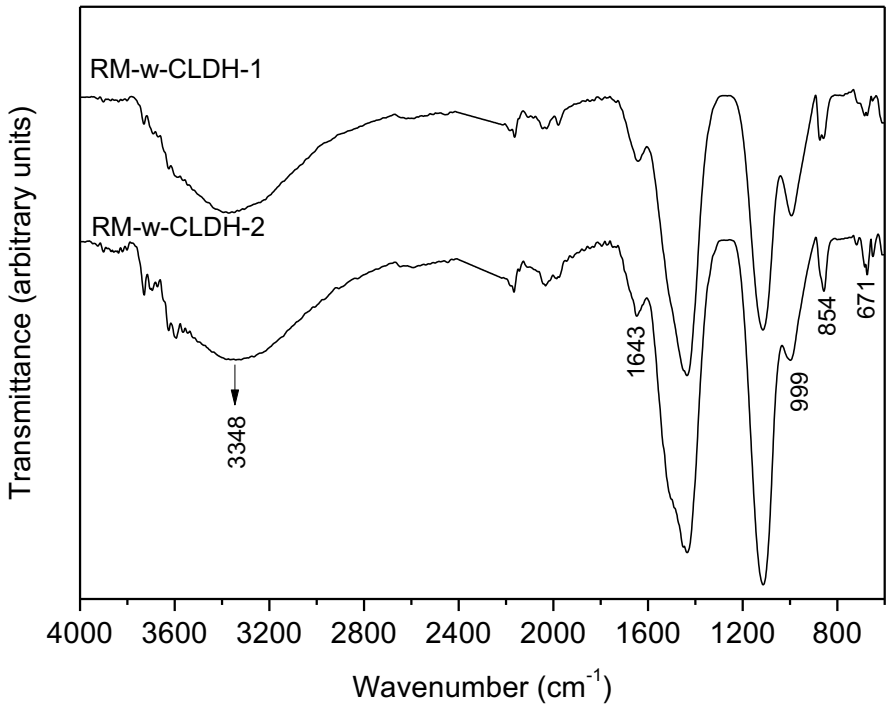

Figure 6.18 FTIR spectra of (a) RM-w-CLDH-1, (b) RM-w-CLDH-2

6.6.3 BET surface area studies

Re-use is a critical factor for assessing an adsorbent in practical wastewater treatment. Regeneration study for RM-w-CLDH was performed, as discussed in Section 6.3.4. By thermally treated at 500°C, RBB adsorbed on RM-w-CLDH can be almost completely removed, and the used RM-w-CLDH can be regenerated. The adsorption capacity of RM-w-CLDH for RBB decreased by 13% after two cycles (Figure 6.8). According to Table 6.14 and Figure 6.19, the S_{BET} and the pore volume decreased in the order of RM-w-CLDH > RM-w-CLDH-1 > RM-w-CLDH-2. It is probably due to the presence of less amount of CO_3^{2-} in the interlayer of regenerated RM-w-LDH and subsequently less craters formed during repeating thermal decomposition. RM-w-CLDH could not gain back to its highest surface area. Figure 6.19 demonstrates that the pore volume of RM-CLDHs was gradually diminished and broader distribution of pores was revealed along with calcination cycles. In contrast, the average pore size continued to be enlarged from 10.47 to 13.9 nm after consecutive calcinations and remained stable around 13.5 nm after the 3rd calcination. The original RM-w-CLDH exhibits the largest surface area as well as the largest pore volume with more micropores and mesopores, which provide more active adsorption sites and may better facilitate the transportation of RBB ions between exterior and interior pore surface. Therefore, the reduced adsorption capacity is likely associated with the progressively decreased surface area and porosity.

However, since regenerated RM-w-CLDH still maintained a relatively high sorption capacity even when the S_{BET} and the pore volume fell to 12.4 m^2/g and 0.041 cm^3/g respectively, surface area and pore volume may not play deciding roles in the RBB adsorption onto the RM-w-CLDH. It is suggested that the loss in adsorption capacity mainly results from the decreasing crystallinity of the LDH-like materials in structural reconstruction (Ulibarri *et al.*, 2001; Ni *et al.*, 2007; Elhalil *et al.*, 2016), as described in Section 6.6.1. Similar observations were reported in other anionic dye sorption studies, for examples, adsorption of methyl orange using regenerated Zn/Al-CLDH (Ni *et al.*, 2007), adsorption of congo red using regenerated Mg/Fe-CO_3 LDH (Ahmed and Gasser, 2012) and removal of acid orange 10 by regenerated Mg/Al-CO_3 LDH (Extremera *et al.*, 2012). In particular, ^{27}Al NMR analysis conducted by Flores *et al.* (2011), showed that CLDH contains a large amount of 4-fold coordinated Al (^{IV}Al), which can serve as better adsorption sites for dye molecules than 6-fold coordinated Al (^{VI}Al), the dominant form in LDH.

Table 6.14 Surface area and pore size of 1st, 2nd and 3rd calcined RM-w-LDH

	BET surface area S_{BET} (m^2/g)	t-plot micropore area (m^2/g)	t-plot external surface area (m^2/g)	Average pore width (nm)	Total pore volume (cm^3/g)
RM-w-CLDH	79.8	10.61	69.2	10.47	0.209
RM-w-CLDH-2	42.1	9.64	32.41	13.9	0.146
RM-w-CLDH-3	12.4	4.20	7.91	13.5	0.041

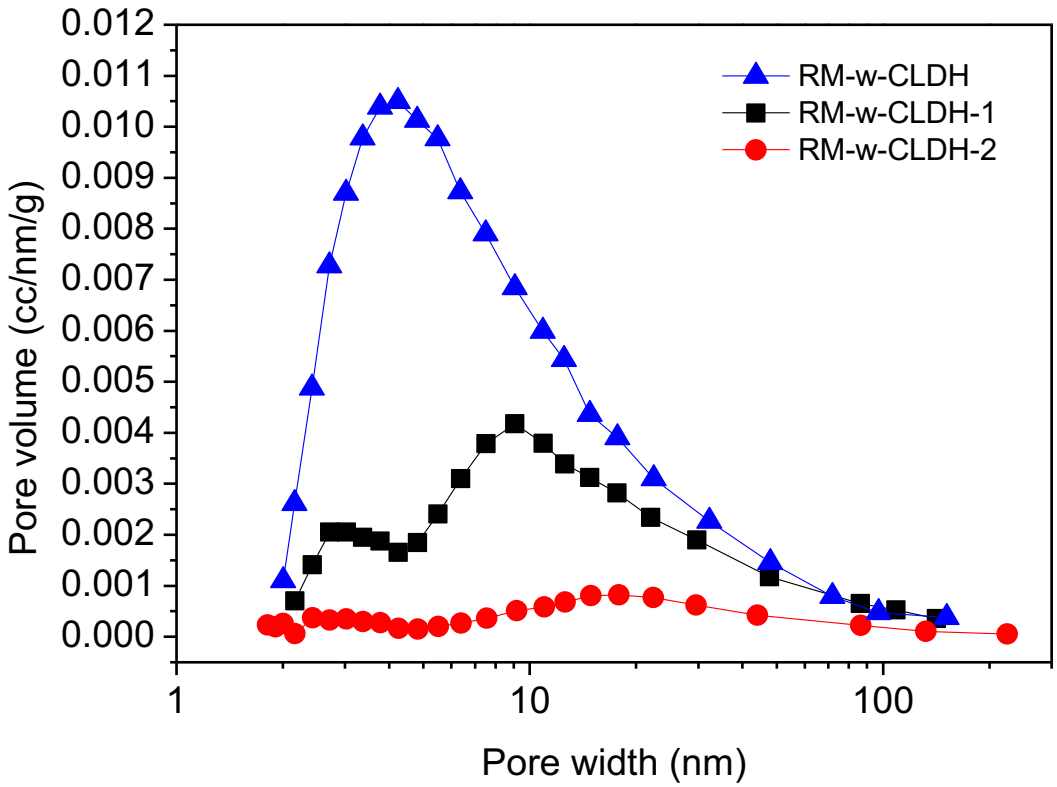

Figure 6.19 Differential pore volume distribution of 1st, 2nd and 3rd calcined RM-w-LDH

6.6.4 SEM test studies

Figure 6.20(a-b) display the SEM images of RM-w-LDH-R after RBB adsorption study. The sheet structure has been preserved, which agrees with the XRD findings. However, Figure 6.20b shows a smoother surface rather than a heterogeneous / rough surface like RM-w-LDH does (see Figure 4.31a). Similar morphology of ZnAl-LDH/$Al(OH)_3$ after the immobilisation of anionic dyes was reported by Guo, Yin and Yang (2018). It is possibly because of the adsorbed RBB dye filling the interconnected pores of the adsorbent. In

Figure 6.20b, the dimensions of aggregates are mostly lower than 2.5 μm, which are smaller than that of RM-w-LDH (Figure 4.31a). This difference on morphology may be resulted from the decrease in crystallinity after RBB adsorption (Elkhattabi *et al.*, 2018).

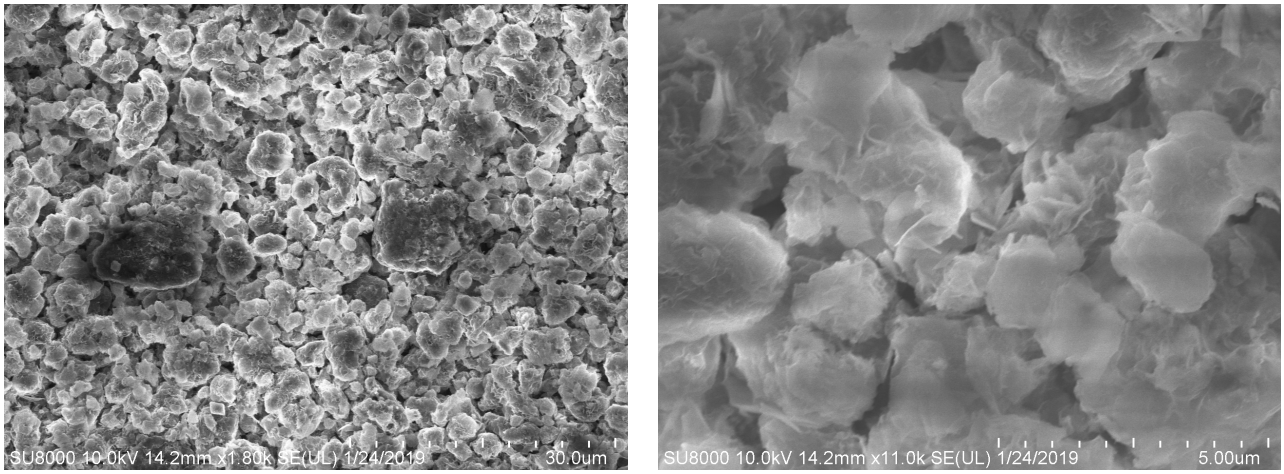

(a) *(b)*

Figure 6.20 Scanning electron microscopy images of (a-b) RM-w-LDH-R with different magnification scales

6.7 Discussion and Summary

6.7.1 Adsorption characteristics of RBB on various adsorbents

The adsorption characteristics of RBB onto the synthesised RM-LDHs and RM-w-CLDH were investigated and compared with the raw materials IRM and Cal-IRM, and the commercial Mg-Al LDH. All adsorbents exhibited certain amount of adsorption for Remazol Brilliant blue R dye. It is observed that IRM and Cal-IRM exhibit limited capacities for RBB and the synthetic process has significantly enhanced their adsorption performances. The key adsorption characteristics and mechanism of various adsorbents for RBB are summarised in Table 6.15. The calculated maximum adsorption capacities for RBB follow the order of RM-w-CLDH > RM-w-LDH > RM-d-LDH > Commercial LDH > RM > CRM, suggesting that the synthesised RM-LDHs, particularly RM-w-CLDH is effective to treat RBB in water.

The kinetic study showed that majority of RBB sorption on RM-LDHs were finished within 3 hours. The kinetic data of the adsorption study was better fitted by the pseudo-second-order model and the equilibrium was reached after 6-12 hours. These observations were consistent with the behavior of commercial LDH. Intraparticle diffusion is the main rate-limiting step in the sorption process of RM-LDHs and LDH. The variations between RM-LDHs and LDH may be explained by their different pore volume as well as different ionic nature.

According to Section 6.2, RM-d-LDH and RM-w-LDH present similar features in the sorption study. Their equilibrium data was well described by the Langmuir model, indicating monolayer adsorption of RM-LDHs for RBB. Ion exchange and external surface adsorption are the dominant mechanisms for their removal of anionic dye. As reported in Section 6.3, the adsorption capacity of RM-w-CLDH increases significantly compared to the uncalcined RM-w-LDH. Apart from electrostatic attraction and hydrogen bonding, partial intercalation plays a main role in removing RBB dye by RM-w-CLDH. In contrast, for the raw material IRM and Cal-IRM, both Langmuir and Freundlich models described their equilibrium data well. Physical adsorption is supposed to be the main mechanism.

Table 6.15 Adsorption characteristics and mechanism of various adsorbents for dye RBB

	Isotherm model		**Kinetic model**		**Possible mechanism**
	Q_{max} (mg/g)	Better fitted to	*t* to equilibrium	Better fitted to	
RM-d-LDH	144.49	Langmuir	~6 h	Pseudo 2nd order	Heterogeneous chemisorption involved but monolayer adsorption is predominant; **intraparticle diffusion** (internal mass transfer) is the rate-limiting step, especially for RM-w-LDH. **Ion exchange** is the main mechanism, as well as **external surface adsorption.**
RM-w-LDH	152.35	Langmuir	~6 h	Pseudo 2nd order	
RM-w-CLDH	N.A. (2761.68) At least 320	neither Langmuir nor Freundlich	< 1.5 h	Pseudo 2nd order	Three distinct steps are captured, i.e. external film transfer -> intraparticle diffusion -> RBB molecules settled at the internal surface sites. **Ion exchange**, partial **intercalation** are the main contributions.
Commercial LDH	49.94	Freundlich	~12 h	Pseudo 2nd order	**Intraparticle diffusion** plays the key rate-limiting role, film diffusion takes longer than RM-LDHs. **Heterogeneous adsorption** dominants.
IRM	< 55	Langmuir & Freundlich	>72 h	Pseudo 2nd order	**Film diffusion** is the main barrier; **physical sorption** is the main mechanism.
Cal-IRM	< 55	Langmuir & Freundlich	>72 h	Pseudo 2nd order	The sorption is **intraparticle diffusion** controlled; **physical sorption** is the main mechanism.

6.7.2 Influence of physicochemical properties on dye adsorption capacity

To further understand the adsorption mechanism, chemical and micro-macrostructural analyses of various adsorbents have been examined in Section 6.6 and the adsorption-desorption cycles of RM-w-CLDH have been investigated in Section 6.3.4.

XRD and FTIR analyses imply that RM-LDHs adsorbed dyes predominantly through ion exchange and external surface adsorption. The minor difference between the adsorption equilibrium data of RM-w-LDH and RM-d-LDH is attributed to their variations in mineralogical composition, surface area, pore size and particle size (see Figure 4.19-20, Table 6.1). Although RM-d-LDH has advantages in surface area and pore volume, which are positive-correlated to the adsorption capacity, RM-w-LDH is narrowly ahead of RM-d-LDH in adsorption ability. It demonstrates that the mineralogical composition of RM-w-LDH, more precisely its surface chemistry and anion exchange capacity allow it to take up more RBB dyes.

As summarised in Section 4.5, the physicochemical properties of RM-LDHs are in consistence with typical Mg-Fe-Al LDHs in the literature. However, the BET surface area of LDH (8.35 m^2/g) is notably smaller than RM-LDHs (64.0-74.8 m^2/g). That is possibly responsible for the remarkably lower adsorption capacity of LDH. In addition, the smaller particle size of LDH results in the longer film diffusion stage. A more heterogeneous adsorption is observed for LDH.

The ability of RM-w-CLDH to retain more dyes and more quickly than RM-w-LDH, is closely related to their physicochemical features, as follows:

- Thermal treatment at 500°C transformed the lamellar structure of RM-w-LDH to metal oxides, leading to a BET surface area of 79.8 m^2/g, a macropore size of 6.62 μm and a porosity of 0.209 cm^3/g. The greater specific surface area and the larger pore size of RM-w-CLDH accelerate the intraparticle diffusion process, meanwhile create more attraction sites for RBB anions.
- The XRD pattern of RM-w-CLDH-R shows minor enlargement in the interlayer space (7.78 Å -> 8.08 Å) after the sorption. That implies partial intercalation of RBB anions occurred during the reconstruction of the layered structure, which also accounts for the higher capacity of RM-w-CLDH.

- A larger number of 4-fold coordinated Al (^{IV}Al) in CLDHs could provide adsorption sites that are more easily for dye molecules to reach than LDHs (Flores *et al.*, 2011).

It is of note that the as-prepared RM-w-LDH shows excellent adsorption ability and recyclable properties. In addition, the collapsed RM-w-CLDH can be reversibly transformed back into the original LDH structure via the 'memory effect' in RBB aqueous solution. The regeneration test confirms that the removal efficiency for RBB maintains at 87.2% even after three cycles. The crystallinity of adsorbent is gradually diminished with repeated cycles, which may affect its surface affinity for RBB anions hence reduce the sorption capacity. Overall, the physiochemical properties presented by RM-w-LDH and RM-w-CLDH in the 'Role-play II' and 'Role-play III' agree well with that of typical LDHs and CLDHs in the literature. The results of Chapter 6 therefore confirm the synthesis of LDH components in RM-w-LDH.

Chapter 7 Conclusions and Recommendations

This thesis aims to investigate the potential of using industrial waste RM for LDH synthesis. The motivations of re-using RM include waste management, development of green materials and pollution remediation. A number of pre-treatment and synthesis methods have been proposed. The mineralogical composition and physiochemical properties of the as-synthesised products were characterised and compared with the 'golden rules' of typical LDHs, confirming the successful synthesis of LDH phases via Scenario III route. The 'role plays', i.e. chloride binding study and dye adsorption study, have been carried out to understand the anion removal capacity and the structural memory effect of RM-LDHs. In order to further investigate the adsorption mechanisms, the samples before and after adsorption were tested using a range of micro-structural analytical methods. Future research is recommended to improve the synthesis process and enhance the performance of RM-LDHs in practical applications.

7.1 Conclusions

This section is structured following the order of the thesis chapters, plus a conclusion of the framework of characterisation and evaluation of as-synthesised products.

7.1.1 Literature review

Chapter 2 firstly provided a comprehensive review of the origin, disposal and utilisation methods of red mud. Red mud is the primary solid waste stream from the caustic Bayer process of bauxite ore digestion, generated at a rate of 1.0-6.0 tonnes per tonne of alumina extraction. Worldwide, there are about 3.4 billion tonnes of RM being stored at active and legacy sites, and over 150 million tonnes being newly produced every year. RM is constituted by more than 30 mineral phases, with a typical elemental order of Fe > Al > Si ~ Ti > Ca > Na. Amongst these minerals, hematite (Fe_2O_3) is the most ubiquitous component, together with goethite (FeOOH), magnetite (Fe_3O_4), gibbsite ($Al(OH)_3$) and desilication products. Due to the nature of fine particles, high alkalinity and trace metal content, RM poses serious landfill issues and leaching risks, which can pollute the soil and groundwater.

Extensive research to date has been conducted to explore options for utilising RM. Many studies have addressed how to modify RM as a whole and use it for various environmental

applications, as low-carbon construction material, catalyst alternative, or adsorbent for wastewater treatment and soil remediation. The modification methods mainly involve thermal treatment, acid activation and mechanical treatment. However, the literature review showed the bulk utilisation of RM is still negligible, due to the low techno-economic viability of available solutions and the uncertainty about their long-term impacts on the environment. Therefore, the development of affordable modification techniques and high added-value materials from RM is of critical importance.

This thesis proposed to employ RM as a whole to synthesise LDH materials. RM presented four key features, implying it would be a feasible starting material for LDH synthesis, which are (1) rich Al, Fe oxides contents, (2) high alkalinity, (3) fine particle size and porous surface, and (4) clay-like behaviour. In addition, the review found that some common approaches to modify RM are very similar to the process of preparing LDH, suggesting the proposal of this thesis has its theoretical basis. Therefore, although only a very few researchers have specifically looked into the synthesis of LDH using RM, this study can still be well supported by existing references.

Layered double hydroxides, also known as anionic clays, consists of positively charged brucite-like host layers $M(OH)_2$ that are partially substituted by trivalent cation M^{3+}, whose general formula is $[M^{2+}_{1-x}M^{3+}_{x}(OH)_2]^{X+}A^{n-}_{x/n} \cdot mH_2O$. Depending on the chemical composition of target LDH, there mainly exist five conventional ways to synthesise LDH, i.e. co-precipitation, urea-based method, salt-oxide method, ion-exchange and calcination-rehydration. Each method and the associated mechanism have been reviewed. The operating parameters of different methods were summarised, including pre-treatment procedure, the M^{3+}/M^{2+} ratio, the liquid-to-solid ratio, pH, aging and drying conditions.

Prior to taking RM as the raw material, it is important to understand the surface chemistry of the RM particles and how these characteristics may influence the synthetic strategy. The review found that the activity of Al species in RM can be enhanced by thermal or mechanochemical pre-treatment, and the solubility of Fe^{III} oxides in RM can be increased at $pH < 4$ or $pH > 10$. The possible impacts of Fe and Ti contents on RM-LDH products were highlighted. According to previous research, a number of Fe-containing LDHs exhibit magnetic behaviour, while Ti-containing LDHs generally have higher anion exchange capacity. In the present thesis, a modified salt-oxide method was proposed to synthesise RM-

LDHs. The pre-treatments taken into account were heat treatment, dry grinding and wet grinding. Dispersion, M^{II}/M^{III} ratio and aging condition were identified as three of the key variables controlling the synthesis process.

In this thesis, the 'golden rules' were defined as a set of micro-structure features of typical LDHs, which can be determined by XRD, SEM, FT-IR and TGA respectively. The as-synthesised products who met the criteria, were then applied in 'role plays', as chloride inhibitor or acidic dye sorbent. The review suggested that CLDHs are capable of removing chloride from aqueous solution via reconstruction of the layered structure. After chloride adsorption, CLDHs usually present noticeable changes in basal spacing, which can be observed from XRD diffraction patterns. The reconstruction ability was another key feature of LDH materials. Based on the literature review, the calcination conditions for RM-LDHs need to be carefully chosen to ensure the collapse of LDH layers but avoid the formation of spinel phases, which would otherwise hinder the regeneration of layered structure.

The adsorption of dyes by LDHs has been a widespread solution for dye treatment. The maximum adsorption capacity and adsorption mechanism of dyes on LDHs were listed. Amongst various acidic dyes, Remazol Brilliant blue R (RBB) dye has been frequently studied. Apart from anion exchange, a range of mechanisms may contribute to the adsorption of dyes to LDHs, including intercalation, electrostatic interaction, hydrogen bonding and physical adsorption. Each of these mechanisms was reviewed. The basics of adsorption studies were introduced, including isotherms, kinetics and pH dependence. A combination of adsorption studies and micro-structural characterisations (XRD, FT-IR, TGA and SEM/EDX) were suggested to be used to understand the adsorption mechanisms of RBB dye on RM-LDHs.

In summary, a number of research gaps and challenges have been pointed out. The most significant ones can be concluded as follows: (1) There lacks economically-feasible technology of re-using RM or transforming RM to high added-value products, therefore only a small portion of RM has been utilised. (2) Limited studies have employed RM as a combined source of Al and Fe oxides for LDH synthesis. An innovative salt-oxide method was proposed in this thesis. The activation of RM in the pre-treatment stage was not fully understood, and the complexity of operation variables in the synthesis stage needs further investigation.; (3) It is difficult to determine whether LDH phases have been synthesised in

the mixed products. A systematic assessment of RM-LDHs was suggested, including micro-structural characterisations, sorption studies for chloride and RBB dye, and calcination-regeneration evaluation of RM-LDHs.

7.1.2 Synthesis routes of RM-LDHs using red mud

Chapter 4 investigated the LDH synthetic methods, focusing on the influences of pre-treatment and process variables. Two kinds of red mud, AOS RM and IRM, were taken as the raw materials. Four different synthesis scenarios have been put forward. AOS RM participated in Scenario I & II process, while IRM participated in Scenario III & IV process. The synthesis processes were illustrated in flow diagrams (see Figure 4.10, 4.14, 4.18 and 4.25).

The mineralogical compositions of the original RM and calcined RM were identified. Hematite [Fe_2O_3], goethite [FeO(OH)], boehmite [AlO(OH)] and gibbsite [$Al(OH)_3$] were the major mineral phases. The common phases presented in both RM were desilication products, quartz [SiO_2] and rutile [TiO_2]. The XRD and TGA analyses tracked the effects of calcination, confirming that the dehydration of gibbsite and goethite occurred between 150-400°C, followed by the transformation to hematite and transition alumina between 400-600°C. The FT-IR spectra of IRM and Cal-IRM supported the findings in the XRD analyses. IRM and Cal-IRM had an average particle size of 0.12 μm and 0.10 μm respectively, which were classified as clay-dominated particles. After thermal treatment at 650°C, the BET surface area of IRM increased from 15.8 to 24.1 m^2/g and the total pore volume increased from 0.045 to 0.054 cm^3/g; while the average pore width decreased from 11.31 to 8.98 nm

The basic mineralogical characteristics of as-synthesised products were firstly identified by X-ray diffraction. In the present work, Scenario III was selected as the most effective method to synthesis LDH using IRM and reactive MgO, whose products were named as RM-LDHs. The optimal experimental parameters were determined, which were L/S ratio = 20, M^{II}/M^{III} ratio =3.0 and aging at 70°C for 72 h. The CO_3^{2-} anion environment was recognised as a favourable environment for producing crystalline LDH structure. Dispersion during aging presented little influence on the final product. The effects of pre-treatment could not be clearly distinguished at this stage. The formation of LDH from reactive MgO and RM roughly follows the 'dissociation-deposition-diffusion' mechanism. The main drawbacks of the salt-oxide based method were recognised as: (1) sensitive to the origin of red mud, (2)

inevitable impurities, including those inherited from RM and brucite formed during the synthesis, (3) being time-energy consuming process. The potential modifications were suggested, which mainly considered more precise controlling of M^{II}/M^{III} ratio and pH, alternative IRM material and alternative hydrothermal or microwave treatment.

The XRD, FT-IR and TG-DTA analyses of RM-LDHs and RM-CLDHs agreed well with the 'golden rules' of typical LDHs. Calcination treatment was able to destroy the layered structures and turn RM-LDHs to Mg, Fe, Al mixed multi-metal oxides. RM-LDHs revealed well-dispersed platelet structures: RM-d-LDH presented higher morphological homogeneity and better dispersed platelets, while RM-w-LDH presented more irregular aggregation of small crystallites. However, the featured hexagonal platelet of typical LDHs cannot be observed in both samples.

The physical properties of the synthesised RM-LDHs and commercial Mg-Al LDH were determined and compared. The average particle sizes of RM-d-LDH and RM-w-LDH were 6.61 μm and 4.37 μm respectively. The calcined product, RM-w-CLDH, had a larger average particle size of 6.61 μm. In comparison, the commercial LDH exhibited a much smaller average particle size of 0.18 μm, and calcination also resulted in increased particle size of 8.71 μm. The surface areas were 75.0 m^2/g for RM-d-LDH and 64.0 m^2/g for RM-w-LDH. After calcination, the S_{BET} of RM-w-CLDH increased to 79.8 m^2/g, which was comparable to the trend of CLDH (from 8.35 to 105.11 m^2/g). Similar to LDH and CLDH, the surface area of RM-LDHs and RM-w-CLDH were mostly contributed by external surface area. With regards to pore size distribution, RM-d-LDH and RM-w-LDH both presented bimodal shape. And the average pore sizes of RM-LDHs and RM-w-CLDH were in the range of 8.92-10.9 nm. The magnetic properties of AOS RM and its products were measured, including AOS RM, CRM, RM-I product ($MgCl_2$: RM = 3:1) and RM-II product (MgO: RM = 3:1). Only weak ferromagnetic behaviours were observed from these four materials, implying RM-I and RM-II were still dominated by the oxide-hydroxides from red mud.

Chapter 4 therefore suggested that the as-prepared RM-LDH products were carbonates ion intercalated $Mg^{2+}/(Al^{3+}, Fe^{3+})$-LDH, with a higher substitution of Fe^{3+} than Al^{3+} in the brucite-like hydroxide sheet. It was deduced that LDH phases accounted for at least 20 wt% of the synthesised RM-LDHs. The potentials of using RM for LDH synthesis were made clear.

7.1.3 Synthesised RM-LDHs for chloride binding

Chapter 5 investigated the chloride sorption of the raw materials and the as-synthesised products. This was defined as 'Role-play I' of LDH materials in the literature review. Materials screening tests were firstly carried out to identify the optimal adsorbents for chloride removal. Batch adsorption studies were then conducted for the selected adsorbent, together with XRD and FT-IR analyses, to better understand the adsorbent and determine the sorption mechanism.

In the screening tests, two groups of chloride solution were employed, which were concentrated chloride solution (0.75 M Cl^- and 0.25 M OH^-) and diluted chloride solution (500 ppm Cl^-). The results revealed that for concentrated Cl^- solution, RM-w-LDH, CLDH and RM-w-CLDH took the leading positions; while for diluted Cl^- solution, CLDH, RM-w-CLDH and RM-d-CLDH were the most efficient adsorbents. It was observed that chloride uptake by hydrotalcite-like materials was sensitive to the concentration of chloride and the competition between Cl^- and OH^-. Two major findings were drawn from the preliminary sorption tests: (1) Wet-grinding treatment promoted the chloride sorption ability of synthesised products. RM-w-CLDH, obtained from the wet grinding route of Scenario III, was selected as the optimal adsorbent. (2) The raw materials for synthesising RM-w-LDH displayed considerably weaker sorption capacities, suggesting chloride binding was mainly contributed by the newly-appeared CLDH phase in RM-w-CLDH.

The initial screening tests have narrowed down the scope of study. More detailed adsorption study focused on RM-w-CLDH and CLDH only. Isotherm study highlighted that both RM-w-CLDH and CLDH were better described by Freundlich model, demonstrating certain degree of heterogeneity on the surface of adsorbents. This was different from the literature, in which CLDH adsorbents were normally better fitted by Langmuir model and a monolayer sorption was suggested. The sorption capacity of RM-w-CLDH and CLDH for chloride were 53.3 mg/g and 17.3 mg/g, implying LDH components likely constituted up to 30% of the original RM-w-LDH. Kinetic study revealed the adsorption of CLDH could be better represented by the pseudo-first-order kinetic model. Intraparticle diffusion modelling demonstrated three distinct stages in the chloride binding process of CLDH and suggested the overall sorption was equally controlled by external mass transfer and intraparticle diffusion.

Characterisation study investigated the mineralogical changes in RM-w-CLDH before and after chloride uptake. X-ray diffraction patterns revealed that chloride was intercalated into the interlayer space of RM-w-CLDH-Cl, accompanied by re-construction of the initial layered structure. FT-IR analysis indicated a decreasing amount of CO_3^{2-} ions in the interlayer space of RM-w-CLDH-Cl, suggesting Cl^- ions has been electrostatically bounded to the layers. These results were largely in line with the observations in previous research, suggesting the uptake of chloride on the calcined product RM-w-CLDH is attributed to the rehydration process with incorporation of Cl^- ions.

To sum up, Chapter 5 highlighted the 'role-play I' of RM-w-LDH and confirmed the successful synthesis of LDH phase in RM-w-LDH. The chloride sorption behaviours of RM-w-CLDH agreed well with the literature in terms of binding capacity and microstructural characteristics. The results suggested that ion exchange and particularly reformation of the LDH structure via 'memory effect' were the main sorption mechanisms. This chapter also demonstrated the potential of CLDH and RM-w-LDH as innovative chloride inhibitors.

7.1.4 Synthesised RM-LDHs for dye removal from wastewater

Chapter 6 focused on the 'Role-play II' of RM-LDHs, IRM and their calcined products, as adsorbents for anionic dye. Remazol Brilliant blue R (RBB) dye was selected because it is frequently studied as target adsorbate for LDH adsorption in the literature. Separated adsorption studies were carried out to investigate the adsorption of RBB to different materials, including the kinetics and the adsorption equilibria. Commercial Mg-Al LDH and CLDH was taken as comparisons. Physicochemical characterisations were conducted so that the properties of RM-LDHs were better understood.

It was found that all adsorbents exhibited certain adsorption ability for RBB dye in aqueous solution. The sequence of adsorption capacity was given in descending order as: RM-w-CLDH > RM-w-LDH > RM-d-LDH > Commercial LDH > RM > CRM. The adsorption characteristics and mechanism of these adsorbents were summarised in Table 6.15. It suggested that the synthesised RM-LDHs and particularly RM-w-CLDH were most effective to treat RBB dye. The calculated adsorption capacities of RM-d-LDH and RM-w-LDH were 144.5 mg/g and 152.35 mg/g, which were larger than commercial LDH (49.94 mg/g) in this study but very close to typical LDH in the literature. The adsorption capacity of RM-w-

CLDH was significantly promoted through calcination treatment, reaching to at least 320 mg/g according to the experimental data.

Kinetic studies indicated that majority of RBB was adsorbed on RM-LDHs within 3 hours and equilibrium was reached after 6-12 hours. The kinetic data of RM-LDHs was better described by the pseudo-second-order model. This agreed well with the behaviour of commercial LDH. While for RM-w-CLDH, the sorption reached equilibrium much rapid, which was within 1.5 hours. The equilibrium time gap between RM-w-LDH and RM-w-CLDH was attributed to different adsorption mechanisms and different physicochemical features. The adsorption of RBB onto RM-w-CLDH was an ideal pseudo-second-order reaction, though both kinetic models provided a good fit.

Intraparticle modelling revealed that for RM-LDHs and commercial LDH, intraparticle diffusion was the main rate-limiting step, but external mass transfer was also a mechanism operative in the sorption process. The transport of sorbate from bulk solution to the exterior film boundaries could be neglected. Compared with commercial LDH, however, RM-LDHs required less time in film diffusion process, confirming RM-LDHs had a larger pore volume. From intraparticle modelling plot of RM-w-CLDH, three distinct steps in adsorption process were observed, which were very rare to be spotted in other research studies. They represented for the external film transfer, intraparticle diffusion and sorbate settling at the internal surface sites, respectively. Due to the increase of pore size upon calcination, intraparticle diffusion became much easier for RM-w-CLDH. Therefore, film transfer and intraparticle diffusion played equally controlling roles.

In the sorption study, RM-d-LDH and RM-w-LDH present very similar features. Their equilibrium data was better fitted by Langmuir model, suggesting monolayer adsorption for RBB dye. Ion exchange and external surface adsorption were the dominant mechanisms for the removal of anionic dye by RM-LDHs. For the raw material IRM and Cal-IRM, the adsorption rate constants were much lower, and the equilibrium was much more difficult to be achieved. Physical adsorption was the main sorption mechanism. It again confirmed the synthesis process profoundly changed the sorption characteristics of red mud. Besides, the influence of initial solution pH for RBB adsorption on RM-d-LDH was studied. The sorption capacity saw a considerable decrease as pH increased from 3 to 4, then it stayed sable

between pH 4-9. The solution pH at equilibrium was between 10.50-10.59, suggesting RM-d-LDH had a good buffering ability between pH 4-10.

The differences between the sorption process of RM-w-LDH and RM-w-CLDH were investigated, which exhibited similar features as LDH and CLDH for dyes removal. The XRD and FTIR analyses implied that RM-LDHs adsorbed dyes predominantly through ion exchange and external surface adsorption. However, the XRD pattern of RM-w-CLDH-R displayed that the layered structure was reconstructed when RM-w-CLDH was in contact with RBB solution. In addition, its interlayer space was enlarged from 7.78 Å to 8.08 Å, implying that RBB^- anions were possibly sharing the swelled layer structure. Therefore, partial intercalation was suggested to be a main mechanism for RM-w-CLDH to remove RBB dye.

7.1.5 Characterisation and evaluation of as-synthesised products

The physicochemical properties of RM-LDHs, RM-w-CLDH and commercial LDH were discussed, including the BET surface area, pore size, total pore volume and particle size. It was concluded that the featured properties of RM-LDHs were in line with typical Mg-Fe-Al LDHs in the literature. According to the kinetic and equilibrium data, the differences of RM-w-LDH and RM-d-LDH on RBB adsorption were minor. Although RM-d-LDH possessed larger surface area, greater pore size and larger pore volume, RM-w-LDH exhibited slightly higher sorption capacity, suggesting that wet grinding brought the product with different surface chemistry and anion exchange capacity. After the calcination, the physicochemical characteristics of RM-w-CLDH were very close to that of RM-d-LDH. However, their sorption behavior remarkably differed, indicating physicochemical properties were not the deciding factors. It further confirmed the main mechanism for RBB adsorption on RM-w-CLDH was through partial intercalation and the 'memory effect' of RM-w-CLDH.

The XRD and FTIR analyses illustrated that the adsorbed RBB can be desorbed from RM-w-LDH and RM-w-CLDH via calcination and the original layered structure were able to be restored upon rehydration. Combined with the regeneration study, it suggested that the contaminated sorbent RM-w-CLDH-R could be cleaned up by calcination treatment and reused in dye sorption. The fresh RM-w-CLDH was able to take up 800 mg/L RBB dye solution at a sorption capacity of at least 320 mg/g. After the 1st regeneration cycle, RM-w-CLDH-1 kept the elimination rate of 100%; while after the 2nd cycle, the removal rate still

maintained at 87.2%. However, according to the findings from the BET measurements, after two regeneration cycles, the S_{BET} decreased significantly from 79.8 to 12.4 m^2/g and the total pore volume fell from 0.209 to 0.041 cm^3/g. It suggested surface area was not playing a controlling role and therefore physical adsorption was not the main mechanism. Instead, the decrease in adsorption capacity after successive cycles was attributed to the gradual demolition in the crystallinity of RM-w-CLDH during repeated reconstruction process.

Overall, in the 'Role-play II', the characteristics presented by RM-LDHs and RM-w-CLDH agreed well with that of typical LDHs and CLDHs in the literature. And RM-w-CLDH continued to be an optimal sorbent in the 'Role-play II' for RBB dye, as it performed well in the 'Role-play I' for chloride removal.

7.2 Future Outlook

This thesis has highlighted the challenges of red mud management, investigated the possibilities of utilising red mud for LDH synthesis, and explored the characteristics of the as-synthesised products in practical applications. Much of the evaluation works on RM-LDHs have been based on a framework of 'golden rules' and 'role plays', followed by the comparisons with previous literature studies. Future studies could focus on direct evaluations, to qualitatively and quantitatively determine the composition and portion of LDHs in RM-LDHs. According to the findings from this PhD work, some future work can be recommended below.

1) Based on various synthesis trials, Scenario III -- using Ireland red mud and reactive MgO, has been identified as the most effective route to synthesise RM-LDHs. Although the preferred experimental conditions have been mostly decided, multi variables are involved and the current conclusions are not definite. Further improvements could look towards the adjustments of M^{II}/M^{III} ratio, a more rigid control of reaction pH and alternative ways of heating or irradiation during aging process, etc. More underlying limitations of Scenario III were recognised, which were its sensitivity to the origin of red mud and the still time-energy consuming process.

2) This study found that RM-LDH products have the ability to bind chloride. However, due to the lack of control groups, the screening tests can only provide the relative sorption amount. While this study has noticed the concentrations of OH^- likely

influenced the chloride uptake, the effects of alkalinity or the total ionic strength have not been clearly understood. Further research is necessary to study the interactions between Cl^- and OH^- ions when they are adsorbed onto RM-LDHs. Moreover, some results of kinetic modelling and isotherm study for RM-w-CLDH and CLDH conflicted with those from other studies, suggesting the sorption studies shall be repeated under strictly controlled N_2 condition. Finally, if RM-LDHs are used as chloride inhibitors in concrete, the long-term effects on material strength need to be validated.

3) Different pre-treatment methods (dry grinding, wet grinding) did not notably affect the mineralogical features of RM-LDHs, however, it is of note that RM-w-LDH gave slightly better performance in chloride binding and dye removal. The predominant drawback of RM-LDH products is the impurities, some derived from the raw material RM and some formed during the synthesis. Despite containing a large amount of impurities, RM-LDHs showed a great potential for removing RBB dye. Further research is expected to clarify the effects of these impurities in the adsorption process, such as brucite and silica. And it is important to assess the leachability of RM-LDHs, which may add rare earth elements or titanium to the treatment system. This study observed that RM-w-CLDH exhibits the fastest uptake for RBB dye and the superior adsorption capacity. However, if RM-w-CLDH is employed in industrial wastewater treatment, the life cycle assessment should be carefully conducted, which considers material handling, time-efficiency, net energy footprint and disposing.

4) The influence of physiochemical properties on RBB dye adsorption have been examined. However, the point of zero charge (pH_{pzc}) of each adsorbent has not been measured, so that the impact of electrostatic adsorption cannot be fully understood. It was found the immobilisation of RBB dye onto RM-d-LDH can be affected by the initial pH of the solution. But the influence of initial solution pH to other adsorbents was unknown. Therefore, more efforts considering the pH_{pzc} and the initial pH are needed in order to obtain a more well-round picture for the adsorption mechanism.

References

Abou-El-Sherbini, K. S. *et al.* (2015) 'Synthesis of novel CO32−/Cl−-bearing 3(Mg+Zn)/(Al+Fe) layered double hydroxides for the removal of anionic hazards', *Journal of Environmental Chemical Engineering*. Elsevier, pp. 2707–2721. doi: 10.1016/j.jece.2015.09.015.

Adachi-Pagano, M., Forano, C. and Besse, J.-P. (2003) 'Synthesis of Al-rich hydrotalcite-like compounds by using the urea hydrolysis reaction—control of size and morphology', *J. Mater. Chem.* Royal Society of Chemistry, 13(8), pp. 1988–1993. doi: 10.1039/B302747N.

Agatzini-Leonardou, S. *et al.* (2008) 'Titanium leaching from red mud by diluted sulfuric acid at atmospheric pressure.', *Journal of hazardous materials*. Elsevier, 157(2–3), pp. 579–86. doi: 10.1016/j.jhazmat.2008.01.054.

Aguiar, J. E. *et al.* (2013) 'Adsorption of Anionic and Cationic Dyes from Aqueous Solution on Non-Calcined Mg-Al Layered Double Hydroxide: Experimental and Theoretical Study', *Separation Science and Technology*, 48(15), pp. 2307–2316. doi: 10.1080/01496395.2013.804837.

Ahmad, M. A., Ahmad Puad, N. A. and Bello, O. S. (2014) 'Kinetic, equilibrium and thermodynamic studies of synthetic dye removal using pomegranate peel activated carbon prepared by microwave-induced KOH activation', *Water Resources and Industry*. Elsevier, 6, pp. 18–35. doi: 10.1016/J.WRI.2014.06.002.

Ahmed, I. M. and Gasser, M. S. (2012) 'Adsorption study of anionic reactive dye from aqueous solution to Mg–Fe–CO3 layered double hydroxide (LDH)', *Applied Surface Science*. North-Holland, 259, pp. 650–656. doi: 10.1016/J.APSUSC.2012.07.092.

Ahmed, M. A., brick, A. A. and Mohamed, A. A. A. (2017) 'An efficient adsorption of indigo carmine dye from aqueous solution on mesoporous Mg/Fe layered double hydroxide nanoparticles prepared by controlled sol-gel route', *Chemosphere*. Elsevier Ltd, 174, pp. 280–288. doi: 10.1016/j.chemosphere.2017.01.147.

Akin, I. *et al.* (2012) 'Arsenic(V) removal from underground water by magnetic nanoparticles synthesized from waste red mud', *Journal of Hazardous Materials*, 235, pp. 62–68. doi: 10.1016/j.jhazmat.2012.06.024.

Akul Mehta (2012) *Ultraviolet-Visible (UV-Vis) Spectroscopy – Limitations and Deviations of Beer-Lambert's Law*, *PharmaXChange.info*. Available at: https://pharmaxchange.info/2012/05/ultraviolet-visible-uv-vis-spectroscopy-–-limitations-and-deviations-of-beer-lambert-law/ (Accessed: 24 June 2017).

Alexandrica, M. C. *et al.* (2015) 'Layered Double Hydroxides As Adsorbents For Anionic Dye Removal From Aqueous Solutions', *Environmental Engineering and Management Journal*, 14(2), pp. 381–388. Available at: http://omicron.ch.tuiasi.ro/EEMJ/ (Accessed: 10 January 2017).

Altundoğan, H. S. and Tümen, F. (2002) 'Removal of phosphates from aqueous solutions by using bauxite. I: Effect of pH on the adsorption of various phosphates', *Journal of Chemical Technology & Biotechnology*. Wiley-Blackwell, 77(1), pp. 77–85. doi: 10.1002/jctb.525.

Altundoğan, H. S. and Tümen, F. (2003) 'Removal of phosphates from aqueous solutions by using bauxite II: the activation study', *Journal of Chemical Technology & Biotechnology*.

Wiley-Blackwell, 78(7), pp. 824–833. doi: 10.1002/jctb.860.

Amutha Rani, D. *et al.* (2008) 'Air pollution control residues from waste incineration: Current UK situation and assessment of alternative technologies', *Waste Management*, 28, pp. 2279–2292. doi: 10.1016/j.wasman.2007.10.007.

Anstice, D. J., Page, C. L. and Page, M. M. (2005) 'The pore solution phase of carbonated cement pastes', *Cement and Concrete Research*. Pergamon, 35(2), pp. 377–383. doi: 10.1016/J.CEMCONRES.2004.06.041.

Antunes, P. *et al.* (2012) 'Red Mud from Brazil: Thermal Behavior and Physical Properties', pp. 775–779.

Aramendía, M. A. *et al.* (2002) 'Comparative Study of Mg/M(III) (M=Al, Ga, In) Layered Double Hydroxides Obtained by Coprecipitation and the Sol–Gel Method', *Journal of Solid State Chemistry*. Academic Press, 168(1), pp. 156–161. doi: 10.1006/JSSC.2002.9655.

Arnold E. Greenberg, L. S. C. and A. D. E. (1992) 'APHA Method 9221: Standard Methods for the Examination of Water and Wastewater. Method 2320', 552.

Aschenbrenner, O. *et al.* (2011) 'Adsorption of carbon dioxide on hydrotalcite-like compounds of different compositions', *Chemical Engineering Research and Design*. Institution of Chemical Engineers, 89(9), pp. 1711–1721. doi: 10.1016/j.cherd.2010.09.019.

Atasoy, A. (2005) 'An investigation on characterization and thermal analysis of the Aughinish red mud', *Journal of Thermal Analysis and Calorimetry*, 81(2), pp. 357–361. doi: 10.1007/s10973-005-0792-5.

Atun, G. and Hisarli, G. (2000) 'A Study of Surface Properties of Red Mud by Potentiometric Method', *Journal of Colloid and Interface Science*, 228, pp. 40–45. doi: 10.1006/jcis.2000.6926.

Ay, A. N., Zümreoglu-Karan, B. and Mafra, L. (2009) 'A Simple Mechanochemical Route to Layered Double Hydroxides: Synthesis of Hydrotalcite-Like Mg-Al-NO3 -LDH by Manual Grinding in a Mortar', *Zeitschrift für anorganische und allgemeine Chemie*. John Wiley & Sons, Ltd, 635(9–10), pp. 1470–1475. doi: 10.1002/zaac.200801287.

Balomenos, E. (2018) *Could "red mud" be the answer to some of Europe's critical-metal supply concerns?* Available at: http://kuleuven.sim2.be/wp-content/uploads/2018/04/REDMUD-Brief-6.5.pdf (Accessed: 20 August 2018).

Barnes, M. C., Addai-Mensah, J. and Gerson, A. R. (1999) 'A methodology for quantifying sodalite and cancrinite phase mixtures and the kinetics of the sodalite to cancrinite phase transformation', *Microporous and Mesoporous Materials*. Elsevier, 31(3), pp. 303–319. doi: 10.1016/S1387-1811(99)00080-3.

Barron, A. (2020) *Physical Methods in Chemistry and Nano Science*, *Midas Green Innovations, Ltd*. Available at: https://chem.libretexts.org/Bookshelves/Analytical_Chemistry/Book%3A_Physical_Methods_in_Chemistry_and_Nano_Science_(Barron)/04%3A_Chemical_Speciation/4.04%3A_UV-Visible_Spectroscopy (Accessed: 24 August 2020).

Basu, P. (1983) 'Reactions of iron minerals in sodium aluminate solutions', *Essential Readings in Light Metals: Alumina and Bauxite, Volume 1*. Wiley Online Library, pp. 176–183.

Bauer, C., Jacques, P. and Kalt, A. (1999) 'Investigation of the interaction between a sulfonated azo dye (AO7) and a TiO2 surface', *Chemical Physics Letters*. North-Holland, 307(5–6), pp. 397–406. doi: 10.1016/S0009-2614(99)00518-7.

Belviso, C. *et al.* (2015) 'Synthesis of magnetic zeolite at low temperature using a waste material mixture: Fly ash and red mud', *Microporous and Mesoporous Materials*, 202, pp. 208–216. doi: 10.1016/j.micromeso.2014.09.059.

Benito, P. *et al.* (2008) 'Microwave-Assisted Homogeneous Precipitation of Hydrotalcites by Urea Hydrolysis', *Inorganic Chemistry*. American Chemical Society, 47(12), pp. 5453–5463. doi: 10.1021/ic7023023.

Benselka-Hadj Abdelkader, N. *et al.* (2011) 'Synthesis and characterization of Mg-Fe layer double hydroxides and its application on adsorption of Orange G from aqueous solution', *Chemical Engineering Journal*, 169, pp. 231–238. doi: 10.1016/j.cej.2011.03.019.

Béres, A. *et al.* (1999) 'Layered double hydroxides and their pillared derivatives – materials for solid base catalysis; synthesis and characterization', *Applied Catalysis A: General*. Elsevier, 182(2), pp. 237–247. doi: 10.1016/S0926-860X(99)00009-5.

Bhagwat, U. O. *et al.* (2019)
'Synthesis of MgTiO3 Nanoparticles for Photocatalytic Applications', *ChemistrySelect*. John Wiley & Sons, Ltd, 4(3), pp. 788–796. doi: 10.1002/SLCT.201803583.

Bharali, D. and Deka, R. C. (2017) 'Preferential adsorption of various anionic and cationic dyes from aqueous solution over ternary CuMgAl layered double hydroxide', *Colloids and Surfaces A: Physicochemical and Engineering Aspects*. doi: 10.1016/j.colsurfa.2017.04.060.

Bhatnagar, A. *et al.* (2011) 'A review of the use of red mud as adsorbent for the removal of toxic pollutants from water and wastewater.', *Environmental technology*, 32(3–4), pp. 231–249. doi: 10.1080/09593330.2011.560615.

Bian, Z. *et al.* (2012) 'The Challenges of Reusing Mining and Mineral-Processing Wastes', *Science*, 337(August), pp. 702–703. doi: 10.1126/science.1224757.

Blengini, G. A. *et al.* (2017) *Methodology for establishing the EU list of critical raw materials guidelines.* Available at: https://eur-lex.europa.eu/legal-content/EN/TXT/HTML/?uri=CELEX:52017DC0490&from=EN (Accessed: 24 August 2018).

Blissett, R. S. and Rowson, N. a. (2012) 'A review of the multi-component utilisation of coal fly ash', *Fuel*. Elsevier Ltd, 97, pp. 1–23. doi: 10.1016/j.fuel.2012.03.024.

Boclair, J. W. and Braterman, P. S. (1999) 'Layered Double Hydroxide Stability. 1. Relative Stabilities of Layered Double Hydroxides and Their Simple Counterparts', *Chemistry of Materials*. American Chemical Society, 11(2), pp. 298–302. doi: 10.1021/CM980523U.

Borra, C. R. *et al.* (2015) 'Leaching of rare earths from bauxite residue (red mud)', *Minerals Engineering*. Elsevier Ltd, 76, pp. 20–27. doi: 10.1016/j.mineng.2015.01.005.

Borra, C. R. *et al.* (2016a) 'Recovery of Rare Earths and Other Valuable Metals From Bauxite Residue (Red Mud): A Review', *Journal of Sustainable Metallurgy*. Springer International Publishing, 2(4), pp. 365–386. doi: 10.1007/s40831-016-0068-2.

Borra, C. R. *et al.* (2016b) 'Smelting of Bauxite Residue (Red Mud) in View of Iron and

Selective Rare Earths Recovery', *Journal of Sustainable Metallurgy*. Springer International Publishing, 2(1), pp. 28–37. doi: 10.1007/s40831-015-0026-4.

Boubakri, S. *et al.* (2018) 'Removal of two anionic reactive textile dyes by adsorption into MgAl-layered double hydroxide in aqueous solutions', *Environmental Science and Pollution Research*. Environmental Science and Pollution Research, 25(24), pp. 23817–23832. doi: 10.1007/s11356-018-2391-6.

Bouraada, M. *et al.* (2009) 'Sorption study of an acid dye from an aqueous solution on modified Mg–Al layered double hydroxides', *Journal of Hazardous Materials*, 163(1), pp. 463–467. doi: 10.1016/j.jhazmat.2008.06.108.

Brindley, G. W. and Kikkawa, S. (1978) 'Formation of mixed Mg Al hydroxides with interlayer nitrate and carbonate ions', *Thermochimica Acta*. Elsevier, 27(1–3), pp. 385–386. doi: 10.1016/0040-6031(78)85056-4.

Brindley, G. W. and Kikkawa, S. (1979) 'A crystal-chemical study of Mg, Al and Ni, N hydroxy-perchlorates and hydroxycarbonates', *American Mineralogist*, 64(7–8), pp. 836–843.

Brinton, T. I., Antweiler, R. C. and Taylor, H. E. (1996) 'Method for the Determination of Dissolved Chloride, Nitrate, and Sulphate in Natural Water using Ion Chromatography', *U.S. Geological Survey*, (95-426A), p. 20. Available at: https://wwwbrr.cr.usgs.gov/projects/SW_inorganic/download/icmethod.pdf (Accessed: 24 June 2019).

Di Bucchianico, A. (2008) 'Coefficient of Determination (R2)', *Encyclopedia of Statistics in Quality and Reliability*. American Cancer Society. doi: 10.1002/9780470061572.EQR173.

Budhysutanto, W. N. *et al.* (2010) 'Pre-treatment of raw materials for the hydrothermal synthesis of hydrotalcite-like compounds', *Chemical Engineering Research and Design*, 88(11), pp. 1445–1449. doi: 10.1016/j.cherd.2009.10.010.

Cao, J. *et al.* (2014) 'Polystyrene microspheres-templated preparation of hierarchical porous modified red mud with high rhodamine B dye adsorption performance', *Micro & Nano Letters*, 9(4), pp. 229–231. doi: 10.1049/mnl.2014.0021.

Carmen, Z. and Daniel, S. (2012) 'Textile Organic Dyes – Characteristics, Polluting Effects and Separation/Elimination Procedures from Industrial Effluents – A Critical Overview', in *Organic Pollutants Ten Years After the Stockholm Convention - Environmental and Analytical Update*.

Castaldi, P. *et al.* (2008) 'XRD, FTIR, and Thermal Analysis of Bauxite Ore-Processing Waste (Red Mud) Exchanged with Heavy Metals', *Clays and Clay Minerals*. GeoScienceWorld, 56(4), pp. 461–469. doi: 10.1346/CCMN.2008.0560407.

Castaldi, P. *et al.* (2010) 'Study of sorption processes and FT-IR analysis of arsenate sorbed onto red muds (a bauxite ore processing waste)', *Journal of Hazardous Materials*. Elsevier, 175(1–3), pp. 172–178. doi: 10.1016/J.JHAZMAT.2009.09.145.

Cavani, F., Trifirò, F. and Vaccari, A. (1991) 'Hydrotalcite-type anionic clays: preparation, properties and applications.', *Catalysis Today*, 11, pp. 173–301.

CEN/TC 292 (2006) *DD CEN/TS 15364:2006 - Characterization of waste. Leaching behaviour tests. Acid and base neutralization capacity test*, *BSI*. Available at: http://shop.bsigroup.com/ProductDetail/?pid=000000000030127714 (Accessed: 16 July

2015).

Chakraborty, P. and Nagarajan, R. (2015) 'Efficient adsorption of malachite green and Congo red dyes by the surfactant (DS) intercalated layered hydroxide containing Zn2+and Y3+-ions', *Applied Clay Science*. Elsevier B.V., 118, pp. 308–315. doi: 10.1016/j.clay.2015.10.011.

Chang, H. *et al.* (2018) 'Chloride maximum phenomenon near the surface of cement paste induced by moisture evaporation and carbonation', *Materials and Structures 2018 51:5*. Springer, 51(5), pp. 1–11. doi: 10.1617/S11527-018-1260-6.

Châtelet, L. *et al.* (1996) 'Competition between monovalent and divalent anions for calcined and uncalcined hydrotalcite: anion exchange and adsorption sites', *Colloids and Surfaces A: Physicochemical and Engineering Aspects*. Elsevier, 111(3), pp. 167–175. doi: 10.1016/0927-7757(96)03542-X.

Chen, L. *et al.* (2016) 'Facile synthesis of mesoporous carbon nanocomposites from natural biomass for efficient dye adsorption and selective heavy metal removal', *RSC Advances*, 6(3), pp. 2259–2269. doi: 10.1039/c5ra19616g.

Chen, Z. *et al.* (2006) 'Speciation of arsenic by ion chromatography inductively coupled plasma mass spectrometry using ammonium eluents', *Journal of Separation Science*. John Wiley & Sons, Ltd, 29(17), pp. 2671–2676. doi: 10.1002/JSSC.200500304.

Cheng, Q. *et al.* (2016) 'Adsorption of Cd by peanut husks and peanut husk biochar from aqueous solutions', *Ecological Engineering*. Elsevier B.V., 87, pp. 240–245. doi: http://dx.doi.org/10.1016/j.ecoleng.2015.11.045.

Chiang, Y. W. *et al.* (2014) 'Towards zero-waste mineral carbon sequestration via two-way valorization of ironmaking slag', *Chemical Engineering Journal*. Elsevier B.V., 249, pp. 260–269. doi: 10.1016/j.cej.2014.03.104.

Chitrakar, R. *et al.* (2007) 'A Solvent-free Synthesis of Zn–Al Layered Double Hydroxides', *Chemistry Letters*, 36(3). Available at: http://www.journal.csj.jp/doi/pdf/10.1246/cl.2007.446 (Accessed: 1 July 2017).

Chitrakar, R. *et al.* (2008) 'A New Method for Synthesis of Mg-Al, Mg-Fe, and Zn-Al Layered Double Hydroxides and Their Uptake Properties of Bromide Ion', *Industrial & Engineering Chemistry Research*, 47(14), pp. 4905–4908. doi: 10.1021/ie0716417.

Chitrakar, R. *et al.* (2011) 'Calcined Mg–Al Layered Double Hydroxides for Uptake of Trace Levels of Bromate from Aqueous Solution', *Industrial & Engineering Chemistry Research*. American Chemical Society, 50(15), pp. 9280–9285. doi: 10.1021/ie1023468.

Chmielarz, L. *et al.* (2002) 'Catalytic activity of Co-Mg-Al, Cu-Mg-Al and Cu-Co-Mg-Al mixed oxides derived from hydrotalcites in SCR of NO with ammonia', *Applied Catalysis B: Environmental*, 35(3), pp. 195–210. doi: 10.1016/S0926-3373(01)00254-5.

Choy, K. K. . *et al.* (2004) 'Film and intraparticle mass transfer during the adsorption of metal ions onto bone char', *Journal of Colloid and Interface Science*. Academic Press, 271(2), pp. 284–295. doi: 10.1016/J.JCIS.2003.12.015.

Choy, K. K. H., Porter, J. F. and Mckay, G. (2004) 'Intraparticle diffusion in single and multicomponent acid dye adsorption from wastewater onto carbon', *Chemical Engineering Journal*, 103(1–3), pp. 133–145. doi: 10.1016/j.cej.2004.05.012.

Chuang, Y. H. *et al.* (2008) 'Removal of 2-Chlorophenol from Aqueous Solution by Mg/Al Layered Double Hydroxide (LDH) and Modified LDH', *Industrial & Engineering Chemistry Research*. American Chemical Society, 47(11), pp. 3813–3819. doi: 10.1021/ie071508e.

Chubar, N. *et al.* (2017) 'Layered double hydroxides as the next generation inorganic anion exchangers: Synthetic methods versus applicability', *Advances in Colloid and Interface Science*, 245(April), pp. 62–80. doi: 10.1016/j.cis.2017.04.013.

Chubar, N. I. *et al.* (2005) 'Adsorption of fluoride, chloride, bromide, and bromate ions on a novel ion exchanger', *Journal of Colloid and Interface Science*. Academic Press, 291(1), pp. 67–74. doi: 10.1016/J.JCIS.2005.04.086.

Chvedov, D., Ostap, S. and Le, T. (2001) 'Surface properties of red mud particles from potentiometric titration', *Colloids and Surfaces A: Physicochemical and Engineering Aspects*, 182(1–3), pp. 131–141. doi: 10.1016/S0927-7757(00)00814-1.

Clark, M. W., Johnston, M. and Reichelt-Brushett, a. J. (2015) 'Comparison of several different neutralisations to a bauxite refinery residue: Potential effectiveness environmental ameliorants', *Applied Geochemistry*. Elsevier Ltd, 56, pp. 1–10. doi: 10.1016/j.apgeochem.2015.01.015.

Collazo, A. *et al.* (2005) 'Evaluation of red mud as surface treatment for carbon steel prior painting', *Progress in Organic Coatings*. Elsevier, 52(4), pp. 351–358. doi: 10.1016/J.PORGCOAT.2004.06.008.

Collins, R. N., Clark, M. W. and Payne, T. E. (2014) 'Solid phases responsible for MnII, CrIII, CoII, Ni, CuII and Zn immobilization by a modified bauxite refinery residue (red mud) at pH 7.5', *Chemical Engineering Journal*, 236, pp. 419–429. doi: 10.1016/j.cej.2013.09.101.

Colombini, S. *et al.* (1999) 'Matrix effects in the determination of bromate in drinking water by ion chromatography', *Journal of chromatography. A*. J Chromatogr A, 847(1–2), pp. 279–284. doi: 10.1016/S0021-9673(99)00035-7.

Constantino, V. R. L. and Pinnavaia, T. J. (1995) 'Basic Properties of Mg2+1-xAl3+x Layered Double Hydroxides Intercalated by Carbonate, Hydroxide, Chloride, and Sulfate Anions', *Inorganic Chemistry*, 34(4), pp. 883–892. doi: 10.1021/ic00108a020.

Cornell, R. M. and Schwertmann, U. (2003) 'The iron oxides : structure, properties, reactions, occurrences, and uses'. Wiley-VCH, p. 664.

Costa, D. G. *et al.* (2012) 'Comparative Structural, thermodynamic and electronic analyses of ZnAlAn− hydrotalcite-like compounds (An −Cl−, F−, Br−, OH−, CO32 − or NO3−): An ab initio study', *Applied Clay Science*. Elsevier, 56, pp. 16–22. doi: 10.1016/J.CLAY.2011.11.014.

Costantino, U. *et al.* (1998) 'New Synthetic Routes to Hydrotalcite-Like Compounds − Characterisation and Properties of the Obtained Materials', *European Journal of Inorganic Chemistry*. John Wiley & Sons, Ltd, 1998(10), pp. 1439–1446. doi: 10.1002/(SICI)1099-0682(199810)1998:10<1439::AID-EJIC1439>3.0.CO;2-1.

Couperthwaite, S. J. *et al.* (2014) 'Minimization of bauxite residue neutralization products using nanofiltered seawater', *Industrial and Engineering Chemistry Research*, 53, pp. 3787–3794. doi: 10.1021/ie403382z.

Curtius, H. *et al.* (2013) 'Preparation and Characterization of Fe-, Co-, and Ni-containing

Mg-Al-Layered Double Hydroxides', *Clays and Clay Minerals*. GeoScienceWorld, 61(5), pp. 424–439. doi: 10.1346/CCMN.2013.0610503.

D2216., A. (1998) 'Standard Test Method for Laboratory Determination of Water (Moisture) Content of Soil and Rock by Mass', in. American Society for Testing and Materials Philadelphia.

D4972., A. (2001) 'Standard Test Method for pH of Soils', in, pp. 1–5. doi: 10.1520/D4972-13.2.

Darmograi, G. *et al.* (2015) 'Study of Adsorption and Intercalation of Orange-Type Dyes into Mg–Al Layered Double Hydroxide', *The Journal of Physical Chemistry C*. American Chemical Society, 119(41), pp. 23388–23397. doi: 10.1021/acs.jpcc.5b05510.

Das, N. N. *et al.* (2009) 'Synthesis, characterization and adsorptive properties of hydrotalcite-like compounds derived from titanium rich bauxite', *Reaction Kinetics, Mechanisms and Catalysis*. Springer Netherlands, 99(1), pp. 167–176. doi: 10.1007/s11144-009-0120-3.

Dentoni, V., Grosso, B. and Massacci, G. (2014) 'Environmental Sustainability of the Alumina Industry in Western Europe', *Sustainability*, 6(12), pp. 9477–9493. doi: 10.3390/su6129477.

Duan, X. and Evans, D. G. (2006) *Layered Double Hydroxides, Volume 119*. Available at: https://books.google.com/books?hl=zh-CN&lr=&id=qujowYGyNagC&pgis=1 (Accessed: 14 July 2015).

Dulger Irdem, S. *et al.* (2014) 'Steam Reforming of Tar Derived from Walnut Shell and Almond Shell Gasification on Red Mud and Iron–Ceria Catalysts', *Energy & Fuels*. American Chemical Society, 28(6), pp. 3808–3813. doi: 10.1021/ef500238f.

Eiby, S. H. J. *et al.* (2016) 'Competition between chloride and sulphate during the reformation of calcined hydrotalcite', *Applied Clay Science*. Elsevier, 132–133, pp. 650–659. doi: 10.1016/J.CLAY.2016.08.017.

Elhalil, A. *et al.* (2016) 'Defluoridation of groundwater by calcined Mg/Al layered double hydroxide', *Emerging Contaminants*. Elsevier, 2(1), pp. 42–48. doi: 10.1016/J.EMCON.2016.03.002.

Elkhattabi, E. H. *et al.* (2018) 'Acid Green 1 removal from wastewater by layered double hydroxides', *Applied Water Science*. Springer Berlin Heidelberg, 8(1), p. 45. doi: 10.1007/s13201-018-0658-1.

Erçağ, E. and Apak, R. (1997) 'Furnace smelting and extractive metallurgy of red mud: recovery of TiO2, Al2O3 and pig iron', *Journal of Chemical Technology & Biotechnology*. John Wiley & Sons, Ltd, 70(3), pp. 241–246. doi: 10.1002/(SICI)1097-4660(199711)70:3<241::AID-JCTB769>3.0.CO;2-X.

Evans, K. (2016) 'The History, Challenges, and New Developments in the Management and Use of Bauxite Residue', *Journal of Sustainable Metallurgy 2016 2:4*. Springer, 2(4), pp. 316–331. doi: 10.1007/S40831-016-0060-X.

Extremera, R. *et al.* (2012) 'Removal of acid orange 10 by calcined Mg/Al layered double hydroxides from water and recovery of the adsorbed dye', *Chemical Engineering Journal*. Elsevier B.V., 213, pp. 392–400. doi: 10.1016/j.cej.2012.10.042.

Feigl, V. *et al.* (2012) 'Red Mud as a Chemical Stabilizer for Soil Contaminated with Toxic Metals', *Water, Air, & Soil Pollution*. Springer Netherlands, 223(3), pp. 1237–1247. doi: 10.1007/s11270-011-0940-4.

Ferna, M. *et al.* (1998) 'The effect of iron on the crystalline phases formed upon thermal decomposition of Mg–Al–Fe hydrotalcites', *Carbon*, 8(11), pp. 2507–2514.

Ferreira, O. P. *et al.* (2004) 'Thermal decomposition and structural reconstruction effect on Mg–Fe-based hydrotalcite compounds', *Journal of Solid State Chemistry*, 177(9), pp. 3058–3069. doi: 10.1016/j.jssc.2004.04.030.

Ferrero, F. (2007) 'Dye removal by low cost adsorbents: Hazelnut shells in comparison with wood sawdust', *Journal of Hazardous Materials*, 142(1), pp. 144–152. doi: 10.1016/j.jhazmat.2006.07.072.

Flores, J. *et al.* (2011) 'Clean-up of wastes from the textile industry using anionic clays', *Clays and Clay Minerals*, 59(3), pp. 240–249. doi: 10.1346/CCMN.2011.0590303.

Fogg, A. M. *et al.* (2004) 'A novel family of layered double hydroxides—[MAl $_4$ (OH) $_{12}$](NO $_3$) $_2$ ·xH $_2$ O (M = Co, Ni, Cu, Zn)', *J. Mater. Chem.* Royal Society of Chemistry, 14(15), pp. 2369–2371. doi: 10.1039/B409027F.

Foo, K. Y. and Hameed, B. H. (2010) 'Insights into the modeling of adsorption isotherm systems', *Chemical Engineering Journal*, 156, pp. 2–10. doi: 10.1016/j.cej.2009.09.013.

Frost, R. L., Palmer, S. J. and Grand, L.-M. (2009) 'Synthesis and thermal analysis of indium-based hydrotalcites of formula Mg6In2(CO3)(OH)16·4H2O', *Journal of Thermal Analysis and Calorimetry*, 101(3), pp. 859–863. doi: 10.1007/s10973-009-0439-z.

Gadepalle, V. P. *et al.* (2007) 'Immobilization of Heavy Metals in Soil Using Natural and Waste Materials for Vegetation Establishment on Contaminated Sites', *Soil and Sediment Contamination: An International Journal*. Taylor & Francis Group , 16(2), pp. 233–251. doi: 10.1080/15320380601169441.

El Gaini, L. *et al.* (2009) 'Removal of indigo carmine dye from water to Mg–Al–CO3-calcined layered double hydroxides', *Journal of Hazardous Materials*. Elsevier, 161(2–3), pp. 627–632. doi: 10.1016/J.JHAZMAT.2008.04.089.

Galan, I. and Glasser, F. P. (2015) 'Chloride in cement', *http://dx.doi.org/10.1680/adcr.13.00067*. Thomas Telford Ltd , 27(2), pp. 63–97. doi: 10.1680/ADCR.13.00067.

Gan, B. K., Madsen, I. C. and Hockridge, J. G. (2009) '*In situ* X-ray diffraction of the transformation of gibbsite to α-alumina through calcination: effect of particle size and heating rate', *Journal of Applied Crystallography*. International Union of Crystallography, 42(4), pp. 697–705. doi: 10.1107/S0021889809021232.

Garau, G. *et al.* (2011) 'Long-term influence of red mud on As mobility and soil physico-chemical and microbial parameters in a polluted sub-acidic soil', *Journal of Hazardous Materials*. Elsevier, 185(2–3), pp. 1241–1248. doi: 10.1016/J.JHAZMAT.2010.10.037.

Genç-Fuhrman, H., Tjell, J. C. and McConchie, D. (2004) 'Adsorption of Arsenic from Water Using Activated Neutralized Red Mud', *Environmental science & technology*. American Chemical Society, 38(8), pp. 2428–2434. doi: 10.1021/ES035207H.

Geng, C. *et al.* (2013) 'Effect of synthesis method on selective adsorption of thiosulfate by calcined MgAl-layered double hydroxides', *Chemical Engineering Journal*, 232, pp. 510–518. doi: 10.1016/j.cej.2013.08.010.

Geng, J. *et al.* (2016) 'Effect of carbonation on release of bound chlorides in chloride-contaminated concrete', *https://doi.org/10.1680/jmacr.15.00234*, 68(7), pp. 353–363. doi: 10.1680/jmacr.15.00234.

Gidado, S. M. and Akanyeti, İ. (2020) 'Comparison of Remazol Brilliant Blue Reactive Adsorption on Pristine and Calcined ZnAl, MgAl, ZnMgAl Layered Double Hydroxides', *Water, Air, and Soil Pollution*. Springer, 231(4), pp. 1–18. doi: 10.1007/S11270-020-04522-0/FIGURES/9.

Gillman, G. (1979) 'A proposed method for the measurement of exchange properties of highly weathered soils', *Australian Journal of Soil Research*, 17(1), p. 129. doi: 10.1071/SR9790129.

Gillman, G. and Sumpter, E. (1986) ' Modification to the compulsive exchange method for measuring exchange characteristics of soils', *Australian Journal of Soil Research*, 24(1), p. 61. doi: 10.1071/SR9860061.

De Gisi, S. *et al.* (2016) 'Characteristics and adsorption capacities of low-cost sorbents for wastewater treatment: A review', *Sustainable Materials and Technologies*. Elsevier B.V., 9, pp. 10–40. doi: 10.1016/j.susmat.2016.06.002.

Goh, K. H., Lim, T. T. and Dong, Z. (2008) 'Application of layered double hydroxides for removal of oxyanions: A review', *Water Research*. Pergamon, 42(6–7), pp. 1343–1368. doi: 10.1016/J.WATRES.2007.10.043.

Goñi, S. and Guerrero, A. (2003) 'Accelerated carbonation of Friedel's salt in calcium aluminate cement paste', *Cement and Concrete Research*. Pergamon, 33(1), pp. 21–26. doi: 10.1016/S0008-8846(02)00910-9.

Grafe, M., Power, G. and Klauber, C. (2009) 'Review of Bauxite Residue Alkalinity and Associated Chemistry', *CSIRO Document DMR-3610. Project ATF-06-3: Management of Bauxite Residues*, (May), p. 51.

Gräfe, M., Power, G. and Klauber, C. (2011) 'Bauxite residue issues: III. Alkalinity and associated chemistry', *Hydrometallurgy*. Elsevier B.V., 108(1–2), pp. 60–79. doi: 10.1016/j.hydromet.2011.02.004.

Gu, K. *et al.* (2014) 'Mechanical and hydration properties of ground granulated blastfurnace slag pastes activated with MgO-CaO mixtures', *Construction and Building Materials*. Elsevier Ltd, 69, pp. 101–108. doi: 10.1016/j.conbuildmat.2014.07.032.

Gu, P. *et al.* (2018) 'Recent advances in layered double hydroxide-based nanomaterials for the removal of radionuclides from aqueous solution', *Environmental Pollution*. Elsevier, 240, pp. 493–505. doi: 10.1016/J.ENVPOL.2018.04.136.

Guo, X., Yin, P. and Yang, H. (2018) 'Superb adsorption of organic dyes from aqueous solution on hierarchically porous composites constructed by ZnAl-LDH/Al(OH)3 nanosheets', *Microporous and Mesoporous Materials*. Elsevier, 259, pp. 123–133. doi: 10.1016/J.MICROMESO.2017.10.003.

Guo, Y. *et al.* (2013) 'Enhanced adsorption of acid brown 14 dye on calcined Mg/Fe layered

double hydroxide with memory effect', *Chemical Engineering Journal*, 219, pp. 69–77. doi: 10.1016/j.cej.2012.12.084.

Gupta, V. K. *et al.* (2004) 'Removal of rhodamine B, fast green, and methylene blue from wastewater using red mud, an aluminum industry waste', *Industrial & engineering chemistry research*. ACS Publications, 43(7), pp. 1740–1747.

Gupta, V. K. and Sharma, S. (2002) 'Removal of cadmium and zinc from aqueous solutions using red mud.', *Environmental science & technology*, 36(16), pp. 3612–7. Available at: http://www.ncbi.nlm.nih.gov/pubmed/12214656 (Accessed: 12 August 2015).

Haha, M. Ben *et al.* (2011) 'Influence of slag chemistry on the hydration of alkali-activated blast-furnace slag — Part I: Effect of MgO', *Cement and Concrete Research*. Pergamon, 41(9), pp. 955–963. doi: 10.1016/J.CEMCONRES.2011.05.002.

Haha, M. Ben *et al.* (2012) 'Influence of slag chemistry on the hydration of alkali-activated blast-furnace slag — Part II: Effect of Al2O3', *Cement and Concrete Research*. Pergamon, 42(1), pp. 74–83. doi: 10.1016/J.CEMCONRES.2011.08.005.

Hamidi, R. and Kazemi, P. (2015) 'Kinetics and mechanism of sorption of chloride ion from sodium carbonate manufacturing wastewater by Mg–Al oxide', *Desalination and Water Treatment*. Taylor & Francis, 54(2), pp. 332–341. doi: 10.1080/19443994.2014.880658.

Hanahan, C. *et al.* (2004) 'Chemistry of Seawater Neutralization of Bauxite Refinery Residues (Red Mud)', *Environmental Engineering Science*. Mary Ann Liebert, Inc., publishers, 21(2), pp. 125–138. doi: 10.1089/109287504773087309.

Harizi, I. *et al.* (2018) 'A New Mg–Al–Cu–Fe-LDH Composite to Enhance the Adsorption of Acid Red 66 Dye: Characterization, Kinetics and Isotherm Analysis', *Arabian Journal for Science and Engineering*. Springer Berlin Heidelberg, pp. 1–17. doi: 10.1007/s13369-018-3526-2.

Hashim, N. *et al.* (2016) 'Layered hydroxide anion exchanger and their applications related to pesticides: a brief review', *http://dx.doi.org/10.1080/14328917.2016.1192717*. Taylor & Francis, 21(3), pp. 129–145. doi: 10.1080/14328917.2016.1192717.

El Hassani, K. *et al.* (2017) 'Effect of morphological properties of layered double hydroxides on adsorption of azo dye Methyl Orange: A comparative study', *Applied Clay Science*. Elsevier B.V., 140, pp. 124–131. doi: 10.1016/j.clay.2017.02.010.

He, J. *et al.* (2006) 'Preparation of layered double hydroxides', *Layered Double Hydroxides*, 119(September 2005), pp. 89–119. doi: 10.1007/430_006.

He, J. *et al.* (2013) 'Synthesis and characterization of red mud and rice husk ash - based geopolymer composites', *Cement and Concrete Composites*, 37, pp. 108–118. doi: 10.1016/j.cemconcomp.2012.11.010.

He, S. *et al.* (2012) 'Fabrication of Hierarchical Layered Double Hydroxide Framework on Aluminum Foam as a Structured Adsorbent for Water Treatment', *Ind. Eng. Chem. Res*, 51, pp. 285–291. doi: 10.1021/ie2015894.

Heredia, A. C. *et al.* (2013) 'Synthesis, characterization and magnetic behavior of Mg–Fe–Al mixed oxides based on layered double hydroxide', *Journal of Magnetism and Magnetic Materials*, 342, pp. 38–46. doi: 10.1016/j.jmmm.2013.04.057.

Hibino, T. (2018) 'Anion Selectivity of Layered Double Hydroxides: Effects of Crystallinity and Charge Density', *European Journal of Inorganic Chemistry*. John Wiley & Sons, Ltd, 2018(6), pp. 722–730. doi: 10.1002/ejic.201701067.

Hibino, T. and Tsunashima, A. (2000) 'Calcination and rehydration behavior of Mg-Fe-CO3 hydrotalcite-like compounds', *Journal of Materials Science Letters*, 19(16), pp. 1403–1405. doi: 10.1023/A:1006754902156.

Hickey, L., Kloprogge, J. T. and Frost, R. L. (2000) 'The effects of various hydrothermal treatments on magnesium-aluminium hydrotalcites', *Journal of Materials Science*. Kluwer Academic Publishers, 35(17), pp. 4347–4355. doi: 10.1023/A:1004800822319.

Hind, A. R., Bhargava, S. K. and Grocott, S. C. (1999) 'The surface chemistry of Bayer process solids: a review', *Colloids and Surfaces A: Physicochemical and Engineering Aspects*. Elsevier, 146(1–3), pp. 359–374. doi: 10.1016/S0927-7757(98)00798-5.

Ho, Y. S. and Mckay, G. (1999) 'Pseudo-second order model for sorption processes', *Process Biochemistry*, 34, pp. 451–465.

Hu, P. *et al.* (2016) 'Preparation of layered double hydroxides using boron mud and red mud industrial wastes and adsorption mechanism to phosphate', *Water and Environment Journal*, 31(2), pp. 145–157. doi: 10.1111/wej.12212.

Hu, Y. *et al.* (2019) 'Role of Fe species in geopolymer synthesized from alkali-thermal pretreated Fe-rich Bayer red mud', *Construction and Building Materials*. Elsevier, 200, pp. 398–407. doi: 10.1016/J.CONBUILDMAT.2018.12.122.

Hua, Y., Heal, K. V. and Friesl-Hanl, W. (2017) 'The use of red mud as an immobiliser for metal/metalloid-contaminated soil: A review', *Journal of Hazardous Materials*. Elsevier, 325, pp. 17–30. doi: 10.1016/J.JHAZMAT.2016.11.073.

Huang, P.-P. *et al.* (2015) 'MgAl layered double hydroxides with chloride and carbonate ions as interlayer anions for removal of arsenic and fluoride ions in water', *RSC Adv.* Royal Society of Chemistry, 5(14), pp. 10412–10417. doi: 10.1039/C4RA15160G.

Huang, W. *et al.* (2008) 'Phosphate removal from wastewater using red mud', *Journal of Hazardous Materials*, 158(1), pp. 35–42. doi: 10.1016/j.jhazmat.2008.01.061.

IAI (2013) *Bauxite Residue Management : Best Practice*.

Igwe, J. C., Mbonu, O. F. and Abia, A. A. (2007) 'Sorption Kinetics, Intraparticle Diffusion and Equilibrium Partitioning of Azo Dyes on Great Millet (Andropogon sorghum) Waste Biomass', *Journal of Applied Sciences*, 7(19), pp. 2840–2847. doi: 10.3923/jas.2007.2840.2847.

Indira, L., Dixit, M. and Kamath, P. V. (1994) 'Electrosynthesis of layered double hydroxides of nickel with trivalent cations', *Journal of Power Sources*. Elsevier, 52(1), pp. 93–97. doi: 10.1016/0378-7753(94)01939-8.

International Aluminium Institue (IAI) (2018) *World Aluminium — Alumina Production*, *26 July*. Available at: http://www.world-aluminium.org/statistics/alumina-production/#linegraph (Accessed: 19 August 2018).

International Aluminium Institute (IAI), Australian Aluminium Council, (AAC) and Brazilian Aluminium Association, (ABAL) (2018) *Sustainable Bauxite Mining Guidelines*

(First Edition). Available at: www.world-aluminium.org (Accessed: 27 August 2018).

Islam, M. and Patel, R. (2009) 'Nitrate sorption by thermally activated Mg/Al chloride hydrotalcite-like compound', *Journal of Hazardous Materials*. Elsevier, 169(1–3), pp. 524–531. doi: 10.1016/J.JHAZMAT.2009.03.128.

Iwasaki, T., Shimizu, K., *et al.* (2012) 'Novel mechanochemical process for facile and rapid synthesis of a Co–Fe layered double hydroxide', *Materials Letters*. North-Holland, 68, pp. 406–408. doi: 10.1016/J.MATLET.2011.11.007.

Iwasaki, T., Yoshii, H., *et al.* (2012) 'Simple and rapid synthesis of Ni–Fe layered double hydroxide by a new mechanochemical method', *Applied Clay Science*. Elsevier, 58, pp. 120–124. doi: 10.1016/J.CLAY.2012.01.024.

Iyer, R. S. and Scott, J. a. (2001) 'Power station fly ash - A review of value-added utilization outside of the construction industry', *Resources, Conservation and Recycling*, 31, pp. 217–228. doi: 10.1016/S0921-3449(00)00084-7.

Jin, F. and Al-Tabbaa, A. (2015) 'Strength and drying shrinkage of slag paste activated by sodium carbonate and reactive MgO', *Construction and Building Materials*, 81, pp. 58–65. doi: 10.1016/j.conbuildmat.2015.01.082.

Johnson, C. a., Brandenberger, S. and Baccini, P. (1995) 'Acid neutralizing capacity of municipal waste incinerator bottom ash', *Environmental science & technology*, 29(1), pp. 142–147. doi: 10.1021/es00001a018.

Johnston, A. L. *et al.* (2021) 'Understanding Layered Double Hydroxide properties as sorbent materials for removing organic pollutants from environmental waters', *Journal of Environmental Chemical Engineering*. Elsevier, 9(4), p. 105197. doi: 10.1016/J.JECE.2021.105197.

Jones, P. T. (2017) *Landfill mining: is this the next big thing in recycling?*, *World Economic Forum*. Available at: https://www.weforum.org/agenda/2017/06/landfill-mining-recycling-eurelco (Accessed: 24 August 2018).

Kameda, T., Oba, J. and Yoshioka, T. (2014) 'Simultaneous removal of Cl− and SO4 2− from seawater using Mg−Al oxide: kinetics and equilibrium studies', *Applied Water Science*. doi: 10.1007/s13201-014-0224-4.

Karaca, O., Cameselle, C. and Reddy, K. R. (2018) 'Mine tailing disposal sites: contamination problems, remedial options and phytocaps for sustainable remediation', *Reviews in Environmental Science and Bio/Technology*. Springer Netherlands, 17(1), pp. 205–228. doi: 10.1007/s11157-017-9453-y.

Ke, X., Bernal, S. A. and Provis, J. L. (2016) 'Controlling the reaction kinetics of sodium carbonate-activated slag cements using calcined layered double hydroxides', *Cement and Concrete Research*. Pergamon, 81, pp. 24–37. doi: 10.1016/J.CEMCONRES.2015.11.012.

Ke, X., Bernal, S. A. and Provis, J. L. (2017) 'Uptake of chloride and carbonate by Mg-Al and Ca-Al layered double hydroxides in simulated pore solutions of alkali-activated slag cement', *Cement and Concrete Research*. Pergamon, 100, pp. 1–13. doi: 10.1016/J.CEMCONRES.2017.05.015.

Khairul, M. A., Zanganeh, J. and Moghtaderi, B. (2019) 'The composition, recycling and utilisation of Bayer red mud', *Resources, Conservation and Recycling*. Elsevier, 141, pp.

483–498. doi: 10.1016/J.RESCONREC.2018.11.006.

Khaitan, S. *et al.* (2010) 'Field Evaluation of Bauxite Residue Neutralization by Carbon Dioxide, Vegetation, and Organic Amendments', *Journal of Environmental Engineering*, 136(10), pp. 1045–1053. doi: 10.1061/(ASCE)EE.1943-7870.0000230.

Khaitan, S., Dzombak, D. A. and Lowry, G. V. (2009) 'Chemistry of the Acid Neutralization Capacity of Bauxite Residue', *Environmental Engineering Science*, 26(5), pp. 873–881. doi: 10.1089/ees.2007.0228.

Khan, M. S. H., Kayali, O. and Troitzsch, U. (2016) 'Chloride binding capacity of hydrotalcite and the competition with carbonates in ground granulated blast furnace slag concrete', *Materials and Structures*. Springer Netherlands. doi: 10.1617/s11527-016-0810-z.

Khusnutdinov, V. R. and Isupov, V. P. (2007) 'Mechanochemical synthesis of layered double Mg–Al hydroxides', *Chem. Sustain. Dev*, 15, pp. 367–372.

Kirwan, L. J. *et al.* (2013) 'Chemistry of bauxite residue neutralisation and aspects to implementation', *International Journal of Mineral Processing*. Elsevier B.V., 119, pp. 40–50. doi: 10.1016/j.minpro.2013.01.001.

Klauber, C., Gräfe, M. and Power, G. (2011) 'Bauxite residue issues: II. options for residue utilization', *Hydrometallurgy*. Elsevier B.V., 108(1–2), pp. 11–32. doi: 10.1016/j.hydromet.2011.02.007.

Klemkaite, K. *et al.* (2011) 'Synthesis and characterization of layered double hydroxides with different cations (Mg, Co, Ni, Al), decomposition and reformation of mixed metal oxides to layered structures', *Central European Journal of Chemistry*, 9(2), pp. 275–282. doi: 10.2478/s11532-011-0007-9.

Koumanova, B., Drame, M. and Popangelova, M. (1997) 'Phosphate removal from aqueous solutions using red mud wasted in bauxite Bayer's process', *Resources, Conservation and Recycling*, 19(1), pp. 11–20. doi: 10.1016/S0921-3449(96)01158-5.

Kounalakis, P., Aravossis, K. and Karayianni, C. (2016) 'Feasibility study for an innovative industrial red mud utilisation method.', *Waste management & research : the journal of the International Solid Wastes and Public Cleansing Association, ISWA*, 34(2), pp. 171–5. doi: 10.1177/0734242X15615423.

Kuwahara, Y. *et al.* (2010) 'A novel conversion process for waste slag: synthesis of a hydrotalcite-like compound and zeolite from blast furnace slag and evaluation of adsorption capacities', *Journal of Materials Chemistry*, 20, p. 5052. doi: 10.1039/c0jm00518e.

Labajos, F. M., Rives, V. and Ulibarri, M. A. (1992) 'Effect of hydrothermal and thermal treatments on the physicochemical properties of Mg-Al hydrotalcite-like materials', *Journal of Materials Science*, 27(6), pp. 1546–1552. doi: 10.1007/BF00542916.

Labuschagné, F. J. W. J. *et al.* (2018) 'Green synthesis of hydrotalcite from untreated magnesium oxide and aluminum hydroxide', *Green Chemistry Letters and Reviews*, 11(1), pp. 18–28. doi: 10.1080/17518253.2018.1426791.

Lafi, R. *et al.* (2016) 'Adsorption study of Congo red dye from aqueous solution to Mg-Al-layered double hydroxide', *Advanced Powder Technology*. The Society of Powder Technology Japan, 27(1), pp. 232–237. doi: 10.1016/j.apt.2015.12.004.

Laskou, M., Margomenou-Leonidopoulou, G. and Balek, V. (2006) 'Thermal characterization of bauxite samples', *Journal of Thermal Analysis and Calorimetry*. Kluwer Academic Publishers, 84(1), pp. 141–146. doi: 10.1007/s10973-005-7126-5.

Latour, R. A. (2015) 'The langmuir isotherm: A commonly applied but misleading approach for the analysis of protein adsorption behavior', *Journal of Biomedical Materials Research Part A*. John Wiley & Sons, Ltd, 103(3), pp. 949–958. doi: 10.1002/JBM.A.35235.

Lawrence, Mike *et al.* (2017) 'Chapter 2 Porosity, Pore Size Distribution, Micro-structure', *RILEM State-of-the-Art Reports*, 23. doi: 10.1007/978-94-024-1031-0_2.

Li, E. *et al.* (2018) 'The Interactions Between Three Typical PPCPs and LDH', *Frontiers in Chemistry*. Frontiers, 6, p. 16. doi: 10.3389/fchem.2018.00016.

Li, F. *et al.* (2004) 'Stoichiometric Synthesis of Pure MFe2O4 (M) Mg, Co, and Ni) Spinel Ferrites from Tailored Layered Double Hydroxide (Hydrotalcite-Like) Precursors', *Chemistry of Materials*, 16(8), pp. 1597–1602. doi: 10.1021/cm035248c.

Lin, Y., Fang, Q. and Chen, B. (2014) 'Perchlorate uptake and molecular mechanisms by magnesium/aluminum carbonate layered double hydroxides and the calcined layered double hydroxides', *Chemical Engineering Journal*. Elsevier, 237, pp. 38–46. doi: 10.1016/J.CEJ.2013.10.004.

Ling, F. *et al.* (2016) 'A novel CoFe layered double hydroxides adsorbent: High adsorption amount for methyl orange dye and fast removal of Cr(VI)', *Microporous and Mesoporous Materials*, 234, pp. 230–238. doi: 10.1016/j.micromeso.2016.07.015.

Liu, W., Yang, J. and Xiao, B. (2009) 'Application of Bayer red mud for iron recovery and building material production from alumosilicate residues', *Journal of Hazardous Materials*. Elsevier, 161(1), pp. 474–478. doi: 10.1016/J.JHAZMAT.2008.03.122.

Liu, Y. *et al.* (2016) 'Effects of thermal treatments on the characterisation and utilisation of red mud with sawdust additive', *Waste Management & Research*. SAGE PublicationsSage UK: London, England, 34(6), pp. 518–526. doi: 10.1177/0734242X16634197.

Liu, Y. and Naidu, R. (2014) 'Hidden values in bauxite residue (red mud): Recovery of metals', *Waste Management*. Elsevier Ltd, 34(12), pp. 2662–2673. doi: 10.1016/j.wasman.2014.09.003.

Liu, Z. *et al.* (2006) 'Synthesis, anion exchange, and delamination of Co-Al layered double hydroxide: Assembly of the exfoliated nanosheet/polyanion composite films and magneto-optical studies', *Journal of the American Chemical Society*, 128(14), pp. 4872–4880. doi: 10.1021/ja0584471.

Lombi, E. *et al.* (2002) 'In situ fixation of metals in soils using bauxite residue: chemical assessment', *Environmental Pollution*. Elsevier, 118(3), pp. 435–443. doi: 10.1016/S0269-7491(01)00294-9.

Lonkar, S. P., Raquez, J.-M. and Dubois, P. (2015) 'One-Pot Microwave-Assisted Synthesis of Graphene/Layered Double Hydroxide (LDH) Nanohybrids', *Nano-Micro Letters*, 7(4), pp. 332–340. doi: 10.1007/s40820-015-0047-3.

Lopez, T. *et al.* (1996) 'Synthesis and characterization of sol-gel hydrotalcites. Structure and texture', *Langmuir*, 12(1), pp. 189–192. doi: 10.1021/la940703s.

Lu, A.-H., Salabas, E. L. and Schüth, F. (2007) 'Magnetic nanoparticles: synthesis, protection, functionalization, and application.', *Angewandte Chemie (International ed. in English)*, 46(8), pp. 1222–44. doi: 10.1002/anie.200602866.

Lu, L. *et al.* (2016) 'A hierarchically porous MgFe2O4/γ-Fe2O3 magnetic microspheres for efficient removals of dye and pharmaceutical from water', *Chemical Engineering Journal*, 283, pp. 524–534. doi: 10.1016/j.cej.2015.07.081.

Lu, L. *et al.* (2017) 'Synthesis of novel hierarchically porous Fe3O4@MgAl–LDH magnetic microspheres and its superb adsorption properties of dye from water', *Journal of Industrial and Engineering Chemistry*. Elsevier, 46, pp. 315–323. doi: 10.1016/J.JIEC.2016.10.045.

Lu, Y. *et al.* (2016) 'High performance NiFe layered double hydroxide for methyl orange dye and Cr(VI) adsorption', *Chemosphere*, 152, pp. 415–422. doi: 10.1016/j.chemosphere.2016.03.015.

Lutpi, N. A. and Zhu, J. (2010) 'Carbonation of Bauxite Residue : a Solution for Carbon Dioxide Capture in Alumina Industry', in *Proceeding of ICSTIE*.

Lv, L. *et al.* (2006a) 'Factors influencing the removal of fluoride from aqueous solution by calcined Mg–Al–CO3 layered double hydroxides', *Journal of Hazardous Materials*. Elsevier, 133(1–3), pp. 119–128. doi: 10.1016/J.JHAZMAT.2005.10.012.

Lv, L. *et al.* (2006b) 'Uptake of chloride ion from aqueous solution by calcined layered double hydroxides: Equilibrium and kinetic studies', *Water Research*. Pergamon, 40(4), pp. 735–743. doi: 10.1016/J.WATRES.2005.11.043.

Ma, J. *et al.* (2010) 'α-Fe 2 O 3 : Hydrothermal Synthesis, Magnetic and Electrochemical Properties', *The Journal of Physical Chemistry C*. American Chemical Society, 114(24), pp. 10671–10676. doi: 10.1021/jp102243g.

Ma, W. *et al.* (2011) 'Removal of fluoride ions from aqueous solution by the calcination product of Mg–Al–Fe hydrotalcite-like compound', *Desalination*, 268(1), pp. 20–26. doi: 10.1016/j.desal.2010.09.045.

Mandal, S. *et al.* (2009) 'Azoic Dye Hosted in Layered Double Hydroxide: Physicochemical Characterization of the Intercalated Materials', *Langmuir*. American Chemical Society, 25(18), pp. 10980–10986. doi: 10.1021/LA901201S.

Manfroi, E. P., Cheriaf, M. and Rocha, J. C. (2014) 'Microstructure, mineralogy and environmental evaluation of cementitious composites produced with red mud waste', *Construction and Building Materials*. Elsevier, 67, pp. 29–36. doi: 10.1016/J.CONBUILDMAT.2013.10.031.

Marcelin, G. *et al.* (1989) 'Dynamics and ordering of intercalated water in layered metal hydroxides', *The Journal of Physical Chemistry*. American Chemical Society, 93(11), pp. 4646–4650. doi: 10.1021/j100348a048.

Marchi, A. J. and Apesteguıa, C. R. (1998) 'Impregnation-induced memory effect of thermally activated layered double hydroxides', *Applied Clay Science*. Elsevier, 13(1), pp. 35–48.

Mascolo, G. and Marino, O. (1980) 'A new synthesis and characterization of magnesium-aluminium hydroxides 1', *Mineralogical Magazine*, 43(March), pp. 619–21. Available at: http://www.minersoc.org/pages/Archive-MM/Volume_43/43-329-619.pdf (Accessed: 29

June 2017).

Mcconchie, D. *et al.* (2006) 'Processes for the treatment of a waste material having a high ph and/or alkalinity'. Google Patents. Available at: https://www.google.com.ar/patents/WO2004005202A1?cl=en.

McConchie, D., Clark, M. and Davies-McConchie, F. (2002) 'New strategies for the management of bauxite refinery residues (red mud)', in *The 6th International Alumina Quality Workshop*. Available at: https://www.researchgate.net/publication/230751909 (Accessed: 21 May 2019).

McConchie, D. M., Clark, M. W. and Davies-McConchie, F. G. (2006) 'Processes for water treatment'. Google Patents. Available at: http://www.google.com/patents/US7077963.

McLaughlin, W. J., White, J. L. and Hem, S. L. (1994) 'Influence of Heterocoagulation on the Formation of Hydrotalcite in Mixed Suspensions of Magnesium Hydroxide and Aluminum Hydroxycarbonate', *Journal of Colloid and Interface Science*. Academic Press, 165(1), pp. 41–52. doi: 10.1006/JCIS.1994.1203.

Meng, W. *et al.* (2004) 'Preparation of magnetic material containing MgFe2O4 spinel ferrite from a Mg–Fe(III) layered double hydroxide intercalated by hexacyanoferrate(III) ions', *Materials Chemistry and Physics*. Elsevier, 86(1), pp. 1–4. doi: 10.1016/J.MATCHEMPHYS.2004.03.011.

Meyn, M., Beneke, K. and Lagaly, G. (1990) 'Anion-exchange reactions of layered double hydroxides', *Inorganic Chemistry*. American Chemical Society, 29(26), pp. 5201–5207. doi: 10.1021/ic00351a013.

Millange, F., Walton, R. I. and O'Hare, D. (2000) 'Time-resolved in situ X-ray diffraction study of the liquid-phase reconstruction of Mg–Al–carbonate hydrotalcite-like compounds', *Journal of Materials Chemistry*, 10(7), pp. 1713–1720. doi: 10.1039/b002827o.

Mir, Z. M. *et al.* (2021) 'The Stability and Chloride Entrapping Capacity of ZnAl-NO2 LDH in High-Alkaline/Cementitious Environment', *Corrosion and Materials Degradation 2021, Vol. 2, Pages 78-99*. Multidisciplinary Digital Publishing Institute, 2(1), pp. 78–99. doi: 10.3390/CMD2010005.

Mishra, G., Dash, B. and Pandey, S. (2018) 'Layered double hydroxides: A brief review from fundamentals to application as evolving biomaterials', *Applied Clay Science*. Elsevier, 153, pp. 172–186. doi: 10.1016/J.CLAY.2017.12.021.

Misra, C. (1992) 'Composition and Properties of Synthetic Hydrotalcites', *Clays and Clay Minerals*, 40(2), pp. 145–150. doi: 10.1346/CCMN.1992.0400202.

Miyata, S. (1975) 'The Syntheses of Hydrotalcite-Like Compounds and Their Structures and Physico-Chemical Properties—I':, *Clays and Clay Minerals*, 23(5), pp. 369–375.

Miyata, S. (1980) 'Physico-Chemical Properties of Synthetic Hydrotalcites in Relation to Composition', *Clays and Clay Minerals*, 28(1), pp. 50–56. doi: 10.1346/CCMN.1980.0280107.

Miyata, S. (1983) 'Anion-exchange properties of hydrotalcite-like compounds.', *Clays Clay Miner*, 31(4), pp. 305–311. Available at: http://www.clays.org/journal/archive/volume 31/31-4-305.pdf (Accessed: 28 July 2015).

Mo, L. *et al.* (2015) 'Deformation and mechanical properties of the expansive cements produced by inter-grinding cement clinker and MgOs with various reactivities', *Construction and Building Materials*, 80, pp. 1–8. doi: 10.1016/j.conbuildmat.2015.01.066.

Murayama, N. *et al.* (2012) 'Synthesis of various layered double hydroxides using aluminum dross generated in aluminum recycling process', *International Journal of Mineral Processing*. Elsevier B.V., 110–111, pp. 46–52. doi: 10.1016/j.minpro.2012.03.011.

Namasivayam, C. and Arasi, D. J. S. E. (1997) 'Removal of congo red from wastewater by adsorption onto waste red mud', *Chemosphere*. Pergamon, 34(2), pp. 401–417. doi: 10.1016/S0045-6535(96)00385-2.

Namasivayam, C., Yamuna, R. and Arasi, D. (2001) 'Removal of acid violet from wastewater by adsorption on waste red mud', *Environmental Geology*. Springer, 41(3–4), pp. 269–273.

Namasivayam, C., Yamuna, R. T. and Arasi, D. J. S. E. (2002) 'Removal of procion orange from wastewater by adsorption on waste red mud', *Separation Science and Technology*. Taylor & Francis Group , 37(10), pp. 2421–2431. doi: 10.1081/SS-120003521.

Nasri, N. S. *et al.* (2014) 'Assessment of porous carbons derived from sustainable palm solid waste for carbon dioxide capture', *Journal of Cleaner Production*. Elsevier Ltd, 71, pp. 148–157. doi: 10.1016/j.jclepro.2013.11.053.

Nejati, K. *et al.* (2011) 'Adsorption of metanil yellow azoic dye from aqueous solution onto Mg-Fe-NO3 layered double hydroxide', *Zeitschrift fur Anorganische und Allgemeine Chemie*, 637(11), pp. 1573–1579. doi: 10.1002/zaac.201100132.

Ni, Z.-M. *et al.* (2007) 'Treatment of methyl orange by calcined layered double hydroxides in aqueous solution: Adsorption property and kinetic studies', *Journal of Colloid and Interface Science*. Academic Press, 316(2), pp. 284–291. doi: 10.1016/J.JCIS.2007.07.045.

Nikbin, I. M. *et al.* (2018) 'Environmental impacts and mechanical properties of lightweight concrete containing bauxite residue (red mud)', *Journal of Cleaner Production*. Elsevier, 172, pp. 2683–2694. doi: 10.1016/J.JCLEPRO.2017.11.143.

Ning, W. *et al.* (2009) 'Preparation of modified red mud with aluminum and its adsorption characteristics on fluoride removal'. Available at: https://scholar.google.co.uk/scholar?hl=en&as_sdt=0%2C5&q=Preparation+of+modified+red+mud+with+aluminum+and+its+adsorption+characteristics+on+fluoride+removal&btnG= (Accessed: 12 December 2018).

Nishimura, S., Takagaki, A. and Ebitani, K. (2013) 'Characterization, synthesis and catalysis of hydrotalcite-related materials for highly efficient materials transformations', *Green Chemistry*, 15, pp. 2026–2042. doi: 10.1039/C3GC40405F.

Novais, R. M. *et al.* (2018) 'Innovative application for bauxite residue: Red mud-based inorganic polymer spheres as pH regulators', *Journal of Hazardous Materials*. Elsevier, 358, pp. 69–81. doi: 10.1016/J.JHAZMAT.2018.06.047.

Ochsenkühn-Petropoulou, M. T. *et al.* (2002) 'Pilot-Plant Investigation of the Leaching Process for the Recovery of Scandium from Red Mud'. American Chemical Society. doi: 10.1021/IE011047B.

Oehman, L. O. (1988) 'Equilibrium and structural studies of silicon(IV) and aluminum(III) in aqueous solution. 17. Stable and metastable complexes in the system hydrogen (+)-

aluminum(3+)-citric acid', *Inorganic Chemistry*. American Chemical Society, 27(15), pp. 2565–2570. doi: 10.1021/ic00288a003.

Olanrewaju, J. *et al.* (2000) 'Simplified synthesis of nitrate form of layered double hydroxide', *Materials Letters*. North-Holland, 45(6), pp. 307–310. doi: 10.1016/S0167-577X(00)00123-3.

Othman, M. R. *et al.* (2009) 'Synthetic hydrotalcites from different routes and their application as catalysts and gas adsorbents: A review', *Applied Organometallic Chemistry*, 23(9), pp. 235–246. doi: 10.1002/aoc.1517.

Paikaray, S. *et al.* (2014) 'Formation Mechanism of Layered Double Hydroxides in Mg2+-, Al3+-, and Fe3+-rich Aqueous Media: Implications for Neutralization in Acid Leach Ore Milling', *Journal of Materials Chemistry A*, 101, pp. 579–590. doi: 10.1016/j.clay.2014.09.022.

Paikaray, S. and Hendry, M. J. (2012) 'The role of trivalent cations and interlayer anions on the formation of layered double hydroxides in an oxic-CO2 medium', *Applied Surface Science*, 263, pp. 633–639. doi: 10.1016/j.apsusc.2012.09.125.

Paikaray, S. and Hendry, M. J. (2014) 'Formation and crystallization of Mg2+–Fe3+–SO42−–CO32−-type anionic clays', *Applied Clay Science*. Elsevier B.V., 88–89, pp. 111–122. doi: 10.1016/j.clay.2013.11.034.

Palmer, S. J. and Frost, R. L. (2009) 'The Effect of Synthesis Temperature on the Formation of Hydrotalcites in Bayer Liquor: A Vibrational Spectroscopic Analysis', *Applied Spectroscopy*. SAGE PublicationsSage UK: London, England, 63(7), pp. 748–752. doi: 10.1366/000370209788701152.

Palmer, S. J. and Frost, R. L. (2011) 'Characterization of bayer hydrotalcites formed from bauxite refinery residue liquor', *Industrial and Engineering Chemistry Research*, 50(9), pp. 5346–5351. doi: 10.1021/ie1018194.

Palmer, S. J., Frost, R. L. and Nguyen, T. (2009) 'Hydrotalcites and their role in coordination of anions in Bayer liquors: Anion binding in layered double hydroxides', *Coordination Chemistry Reviews*, 253(1–2), pp. 250–267. doi: 10.1016/j.ccr.2008.01.012.

Pang, H. *et al.* (2011) 'Direct synthesis of hexagonal Mg(OH)2 nanoplates from natural brucite without dissolution procedure', *Chemical Communications*. The Royal Society of Chemistry, 47(22), p. 6317. doi: 10.1039/c1cc10279f.

Parab, H. *et al.* (2021) 'Overview of ion chromatographic applications for the analysis of nuclear materials: Case studies', *Reviews in Analytical Chemistry*. De Gruyter, 40(1), pp. 204–219. doi: 10.1515/REVAC-2021-0135.

Paranavithana, G. N. *et al.* (2016) 'Adsorption of Cd2+ and Pb2+ onto coconut shell biochar and biochar-mixed soil', *Environmental Earth Sciences*. Springer Berlin Heidelberg, 75(6), p. 484. doi: 10.1007/s12665-015-5167-z.

Paredes, J. . *et al.* (2004) 'Catalytic combustion of methane over red mud-based catalysts', *Applied Catalysis B: Environmental*. Elsevier, 47(1), pp. 37–45. doi: 10.1016/S0926-3373(03)00325-4.

Parks, G. A. (1965) 'The Isoelectric Points of Solid Oxides, Solid Hydroxides, and Aqueous Hydroxo Complex Systems', *Chemical Reviews*. American Chemical Society, 65(2), pp.

177–198. doi: 10.1021/cr60234a002.

Pascual, J. *et al.* (2009) 'Thermal characterization of a Spanish red mud', *Journal of Thermal Analysis and Calorimetry*. Springer Netherlands, 96(2), pp. 407–412. doi: 10.1007/s10973-008-9230-9.

Pavlovic, I. *et al.* (2005) 'Adsorption of acidic pesticides 2,4-D, Clopyralid and Picloram on calcined hydrotalcite', *Applied Clay Science*. Elsevier, 30(2), pp. 125–133. doi: 10.1016/J.CLAY.2005.04.004.

Payán, M. C. *et al.* (2012) 'Potential influence of CO2 release from a carbon capture storage site on release of trace metals from marine sediment.', *Environmental pollution (Barking, Essex : 1987)*, 162, pp. 29–39. doi: 10.1016/j.envpol.2011.10.015.

Peng, F. *et al.* (2005) 'Nano-crystal glass-ceramics obtained by crystallization of vitrified red mud', *Chemosphere*. Pergamon, 59(6), pp. 899–903. doi: 10.1016/J.CHEMOSPHERE.2004.11.002.

Pérez-Ramírez, J. *et al.* (2001) 'In situ investigation of the thermal decomposition of Co–Al hydrotalcite in different atmospheres', *Journal of Materials Chemistry*. Royal Society of Chemistry, 11(3), pp. 821–830. doi: 10.1039/b009320n.

Pérez-Ramírez, J. *et al.* (2002) 'Magnetic properties of Co–Al, Ni–Al, and Mg–Al hydrotalcites and the oxides formed upon their thermal decomposition', *Journal of Materials Chemistry*, 12(8), pp. 2370–2375. doi: 10.1039/b110314h.

Pfaff, J. D. (1993) *EPA Method 300.0 - Determination of inorganic anions by ion chromatography* .

Plazinski, W., Rudzinski, W. and Plazinska, A. (2009) 'Theoretical models of sorption kinetics including a surface reaction mechanism: A review', *Advances in Colloid and Interface Science*. Elsevier B.V., 152(1–2), pp. 2–13. doi: 10.1016/j.cis.2009.07.009.

Pourfaraj, R. *et al.* (2017) 'Synthesis of hexagonal mesoporous MgAl LDH nanoplatelets adsorbent for the effective adsorption of Brilliant Yellow', *Journal of Colloid and Interface Science*. Academic Press, 508, pp. 65–74. doi: 10.1016/J.JCIS.2017.07.101.

Power, G., Gräfe, M. and Klauber, C. (2011) 'Bauxite residue issues: I. Current management, disposal and storage practices', *Hydrometallurgy*. Elsevier B.V., 108(1–2), pp. 33–45. doi: 10.1016/j.hydromet.2011.02.006.

Prasad, C., Tang, H. and Liu, W. (2018) 'Magnetic Fe3O4 based layered double hydroxides (LDHs) nanocomposites (Fe3O4/LDHs): recent review of progress in synthesis, properties and applications', *Journal of Nanostructure in Chemistry*, 8(4), pp. 393–412. doi: 10.1007/s40097-018-0289-y.

Pratapa, S. *et al.* (2015) 'A simple dissolved metals mixing method to produce high-purity MgTiO3 nanocrystals', *AIP Conference Proceedings*. American Institute of PhysicsAIP, 1586(1), p. 39. doi: 10.1063/1.4866726.

Pratt, K. C. and Christoverson, V. (1982) 'Hydrogenation of a model hydrogen-donor system using activated red mud catalyst', *Fuel*. Elsevier, 61(5), pp. 460–462. doi: 10.1016/0016-2361(82)90072-2.

Provis, J. L., Palomo, A. and Shi, C. (2015) 'Advances in understanding alkali-activated

materials', *Cement and Concrete Research*. Elsevier B.V. doi: 10.1016/j.cemconres.2015.04.013.

Pulford, I. D. *et al.* (2012) 'Carbonised red mud - A new water treatment product made from a waste material', *Journal of Environmental Management*, 100, pp. 59–64. doi: 10.1016/j.jenvman.2011.11.016.

Qian, Y., Li, S. and Chen, X. (2015) 'Synthesis and characterization of LDHs using Bayer red mud and its flame-retardant properties in EVA/LDHs composites', *Journal of Material Cycles and Waste Management*. Springer Japan. doi: 10.1007/s10163-015-0409-4.

Qiu, G. *et al.* (1995) 'Influence of coal sort on the direct reduction of high-iron-content red mud', *Journal of Central South University of Technology*, 2(2), pp. 27–31. doi: 10.1007/BF02652003.

Qu, J. *et al.* (2016) 'Mechanochemical approaches to synthesize layered double hydroxides: a review', *Applied Clay Science*. Elsevier, 119, pp. 185–192. doi: 10.1016/J.CLAY.2015.10.018.

Rai, S. *et al.* (2012) 'Neutralization and utilization of red mud for its better waste management', *Arch. Environ. Sci.*, 6, pp. 13–33.

Rai, S. *et al.* (2013) 'Feasibility of red mud neutralization with seawater using Taguchi's methodology', *International Journal of Environmental Science and Technology*, 10, pp. 305–314. doi: 10.1007/s13762-012-0118-7.

Rajamathi, M. *et al.* (2000) 'Reversible thermal behavior of the layered double hydroxide of Mg with Al: mechanistic studies', *Journal of Materials Chemistry*. The Royal Society of Chemistry, 10(12), pp. 2754–2753. doi: 10.1039/b006610i.

Raman, C. V. and Nedungadi, T. M. K. (1940) 'The α-β Transformation of Quartz', *Nature*. Nature Publishing Group, 145(3665), pp. 147–147. doi: 10.1038/145147a0.

Ratnamala, G. M., Shetty, K. V. and Srinikethan, G. (2012) 'Removal of Remazol Brilliant Blue Dye from Dye-Contaminated Water by Adsorption Using Red Mud: Equilibrium, Kinetic, and Thermodynamic Studies', *Water, Air, & Soil Pollution*. Springer Netherlands, 223(9), pp. 6187–6199. doi: 10.1007/s11270-012-1349-4.

Ratnamala, G. M., Vidya, S. K. and Srinikethan, G. (2015) 'Isotherm, kinetics, and process optimization for removal of Remazol Brilliant Blue dye from contaminated water using adsorption on acid-treated red mud', *Desalination and Water Treatment*, 57(July 2015), pp. 1–14. doi: 10.1080/19443994.2015.1055311.

Raut, S. P., Ralegaonkar, R. V. and Mandavgane, S. a. (2011) 'Development of sustainable construction material using industrial and agricultural solid waste: A review of waste-create bricks', *Construction and Building Materials*. Elsevier Ltd, 25(10), pp. 4037–4042. doi: 10.1016/j.conbuildmat.2011.04.038.

Ribeiro, D. V., Labrincha, J. A. and Morelli, M. R. (2011) 'Chloride diffusivity in red mud-ordinary portland cement concrete determined by migration tests', *Materials Research*. Materials Research, 14(2), pp. 227–234. doi: 10.1590/S1516-14392011005000026.

Rivas Mercury, J. M. *et al.* (2011) 'Thermal behavior and evolution of the mineral phases of Brazilian red mud', *Journal of Thermal Analysis and Calorimetry*. Springer Netherlands, 104(2), pp. 635–643. doi: 10.1007/s10973-010-1039-7.

Rives, V. (2001) *Layered Double Hydroxides: Present and Future*. Nova Publishers. Available at: https://books.google.co.uk/books/about/Layered_Double_Hydroxides.html?id=U5c5zzqjthgC&pgis=1 (Accessed: 28 July 2015).

Rozov, K. *et al.* (2010) 'Synthesis and characterization of the LDH hydrotalcite-pyroaurite solid-solution series', *Cement and Concrete Research journal*, pp. 1248–1254. doi: 10.1016/j.cemconres.2009.08.031.

Rubinos, D. A. *et al.* (2005) 'Speciation of adsorbed arsenic(V) on red mud using a sequential extraction procedure', *Mineralogical Magazine*, 5 October, pp. 591–600. doi: 10.1180/0026461056950273.

Rubinos, D. A. and Barral, M. T. (2013) 'Fractionation and mobility of metals in bauxite red mud', *Environmental Science and Pollution Research*. Springer Berlin Heidelberg, 20(11), pp. 7787–7802. doi: 10.1007/s11356-013-1477-4.

Rudzinski, W. and Plazinski, W. (2006) 'Kinetics of Solute Adsorption at Solid/Solution Interfaces: A Theoretical Development of the Empirical Pseudo-First and Pseudo-Second Order Kinetic Rate Equations, Based on Applying the Statistical Rate Theory of Interfacial Transport', *The Journal of Physical Chemistry B*, 110(33), pp. 16514–16525. doi: 10.1021/jp061779n.

Rudzinski, W. and Plazinski, W. (2007) 'Theoretical description of the kinetics of solute adsorption at heterogeneous solid/solution interfaces: On the possibility of distinguishing between the diffusional and the surface reaction kinetics models', *Applied Surface Science*. North-Holland, 253(13), pp. 5827–5840. doi: 10.1016/J.APSUSC.2006.12.038.

De Sá, F. P., Cunha, B. N. and Nunes, L. M. (2013) 'Effect of pH on the adsorption of Sunset Yellow FCF food dye into a layered double hydroxide (CaAl-LDH-NO3)', *Chemical Engineering Journal*. Elsevier B.V., 215–216, pp. 122–127. doi: 10.1016/j.cej.2012.11.024.

Sahu, R. C., Patel, R. K. and Ray, B. C. (2010) 'Neutralization of red mud using CO2 sequestration cycle', *Journal of Hazardous Materials*. Elsevier B.V., 179(1–3), pp. 28–34. doi: 10.1016/j.jhazmat.2010.02.052.

Sahu, R. C., Patel, R. and Ray, B. C. (2010) 'Utilization of activated CO2-neutralized red mud for removal of arsenate from aqueous solutions', *Journal of Hazardous Materials*. Elsevier, 179(1–3), pp. 1007–1013. doi: 10.1016/J.JHAZMAT.2010.03.105.

Salomão, R. *et al.* (2011) 'Hydrotalcite synthesis via co-precipitation reactions using MgO and Al(OH)3 precursors', *Ceramics International*, 37(8), pp. 3063–3070. doi: 10.1016/j.ceramint.2011.05.034.

Salomé Dominique Schnyder, J. (2010) *Magnetic Characterization of Iron Oxide Nanoparticles*. ETH Zurich.

Sánchez-Cantú, M. *et al.* (2014) 'MgZnAl hydrotalcite-like compounds preparation by a green method: effect of zinc content', *Chemical Papers*, 68(5), pp. 638–649. doi: 10.2478/s11696-013-0491-9.

Santona, L., Castakdi, P. and Melis, P. (2006) 'Evaluation of the interaction mechanisms between red muds and heavy metals', *Journal of Hazardous Materials*, 136(2), pp. 324–329. doi: 10.1016/j.jhazmat.2005.12.022.

Santos, R. M. M. *et al.* (2017) 'Thermal decomposition and recovery properties of ZnAl-CO3layered double hydroxide for anionic dye adsorption: Insight into the aggregative nucleation and growth mechanism of the LDH memory effect.', *Journal of Materials Chemistry A*. Royal Society of Chemistry, 5(20), pp. 9998–10009. doi: 10.1039/c7ta00834a.

Santos, R. M. M. dos *et al.* (2017) 'Adsorption of Acid Yellow 42 dye on calcined layered double hydroxide: Effect of time, concentration, pH and temperature', *Applied Clay Science*, 140, pp. 132–139. doi: 10.1016/j.clay.2017.02.005.

Sato, T. *et al.* (1988) 'Synthesis of hydrotalcite-like compounds and their physico-chemical properties', *Reactivity of Solids*. Elsevier, 5(2–3), pp. 219–228. doi: 10.1016/0168-7336(88)80089-5.

Schwertfeger, D. M. and Hendershot, W. H. (2009) 'Determination of Effective Cation Exchange Capacity and Exchange Acidity by a One-Step BaCl Method', *Soil Science Society of America Journal*. Soil Science Society, 73(3), p. 737. doi: 10.2136/sssaj2008.0009.

Senff, L. *et al.* (2014) 'Influence of red mud addition on rheological behavior and hardened properties of mortars', *Construction and Building Materials*. Elsevier, 65, pp. 84–91. doi: 10.1016/J.CONBUILDMAT.2014.04.104.

Senff, L., Hotza, D. and Labrincha, J. A. (2011) 'Effect of red mud addition on the rheological behaviour and on hardened state characteristics of cement mortars', *Construction and Building Materials*. Elsevier, 25(1), pp. 163–170. doi: 10.1016/J.CONBUILDMAT.2010.06.043.

Series, A. C. S. S., Chemical, A. and Washington, S. (1987) 'Distinguishing A d s o r p t i o n f r o m Surface Precipitation Garrison Sposito Department of Soil and Environmental Sciences , University of California , Riverside , Measurements of the chemical composition of an aqueous solution phase are interpreted '.

Shan, R. ran *et al.* (2015) 'Highly efficient removal of three red dyes by adsorption onto Mg-Al-layered double hydroxide', *Journal of Industrial and Engineering Chemistry*. The Korean Society of Industrial and Engineering Chemistry, 21, pp. 561–568. doi: 10.1016/j.jiec.2014.03.019.

Shanmuganathan, K. and Ellison, C. J. (2014) 'Layered Double Hydroxides: An Emerging Class of Flame Retardants', *Polymer Green Flame Retardants*. Elsevier, pp. 675–707. doi: 10.1016/B978-0-444-53808-6.00020-2.

Sharma, S. K. *et al.* (2007) 'Effect of Hydrothermal Conditions on Structural and Textural Properties of Synthetic Hydrotalcites of Varying Mg/Al Ratio'. American Chemical Society. doi: 10.1021/IE061438W.

Shaw, W. H. R. and Bordeaux, J. J. (1955) 'The Decomposition of Urea in Aqueous Media', *Journal of the American Chemical Society*. American Chemical Society, 77(18), pp. 4729–4733. doi: 10.1021/ja01623a011.

Shekoohi, K. *et al.* (2017) 'Synthesis of some Mg/Co-Al type nano hydrotalcites and characterization', *MethodsX*. Elsevier, 4, pp. 86–94. doi: 10.1016/J.MEX.2017.01.003.

Shen, Z. *et al.* (2017) 'Qualitative and quantitative characterisation of adsorption mechanisms of lead on four biochars', *Science of the Total Environment*. Elsevier B.V., 609, pp. 1401–1410. doi: 10.1016/j.scitotenv.2017.08.008.

Shen, Z. *et al.* (2018) 'Comparison of nickel adsorption on biochars produced from mixed softwood and Miscanthus straw', *Environmental Science and Pollution Research*. Springer Berlin Heidelberg, 25(15), pp. 14626–14635. doi: 10.1007/s11356-018-1674-2.

Si, C., Ma, Y. and Lin, C. (2013) 'Red mud as a carbon sink: Variability, affecting factors and environmental significance', *Journal of Hazardous Materials*. Elsevier B.V., 244–245, pp. 54–59. doi: 10.1016/j.jhazmat.2012.11.024.

Simonin, J.-P. (2016) 'On the comparison of pseudo-first order and pseudo-second order rate laws in the modeling of adsorption kinetics', *Chemical Engineering Journal*, 300, pp. 254–263. doi: 10.1016/j.cej.2016.04.079.

Six, J. *et al.* (2000) 'Soil Structure and Organic Matter', *Soil Science Society of America Journal*. Soil Science Society, 64(2), p. 681. doi: 10.2136/sssaj2000.642681x.

Soner Altundoğan, H. *et al.* (2000) 'Arsenic removal from aqueous solutions by adsorption on red mud', *Waste Management*. Pergamon, 20(8), pp. 761–767. doi: 10.1016/S0956-053X(00)00031-3.

Song, Q. and Zhang, Z. J. (2004) 'Shape control and associated magnetic properties of spinel cobalt ferrite nanocrystals', *Journal of the American Chemical Society*. ACS Publications, 126(19), pp. 6164–6168.

Speakman, S. A. (2011) *Fundamentals of Rietveld Refinement I. XRD Pattern Simulation An Introduction to Rietveld Refinement using PANalytical X'Pert HighScore Plus v3.0d*. Available at: http://prism.mit.edu/xray/Fundamentals of Rietveld Refinement XRD Simulation 2011.pdf (Accessed: 12 May 2019).

Stanimirova, T. and Kirov, G. (2003) 'Cation composition during recrystallization of layered double hydroxides from mixed (Mg, Al) oxides', *Applied Clay Science*. Elsevier, 22(6), pp. 295–301. doi: 10.1016/S0169-1317(03)00122-4.

Summers, R. N., Bolland, M. D. A. and Clarke, M. F. (2001) 'Effect of application of bauxite residue (red mud) to very sandy soils on subterranean clover yield and P response', *Soil Research*. CSIRO PUBLISHING, 39(5), p. 979. doi: 10.1071/SR97095.

Sundararajan, M. D. *et al.* (1984) 'Mossbauer investigation of magnesium ferrite-aluminate', *Journal of Physics C: Solid State Physics*. IOP Publishing, 17(16), pp. 2953–2965. doi: 10.1088/0022-3719/17/16/014.

Suryavanshi, A. K. and Narayan Swamy, R. (1996) 'Stability of Friedel's salt in carbonated concrete structural elements', *Cement and Concrete Research*. Pergamon, 26(5), pp. 729–741. doi: 10.1016/S0008-8846(96)85010-1.

Sutar, H. *et al.* (2014) 'Progress of Red Mud Utilization : An Overview', *American Chemical Science Journal*, 4(3), pp. 255–279.

Tamura, H. *et al.* (2006) 'Formation of hydrotalcite in aqueous solutions and intercalation of ATP by anion exchange', *Journal of Colloid and Interface Science*. Academic Press, 300(2), pp. 648–654. doi: 10.1016/J.JCIS.2006.04.007.

Tao, Q. *et al.* (2006) 'Synthesis and characterization of layered double hydroxides with a high aspect ratio', *Journal of Solid State Chemistry*, 179(3), pp. 708–715. doi: 10.1016/j.jssc.2005.11.023.

Teixeira, T. P. F. *et al.* (2014) 'Use of calcined layered double hydroxides for the removal of color and organic matter from textile effluents: kinetic, equilibrium and recycling studies', *Brazilian Journal of Chemical Engineering*. Associação Brasileira de Engenharia Química, 31(1), pp. 19–26. doi: 10.1590/S0104-66322014000100003.

Theiss, F. L., Ayoko, G. A. and Frost, R. L. (2016) 'Synthesis of layered double hydroxides containing Mg2+, Zn2+, Ca2+ and Al3+ layer cations by co-precipitation methods—A review', *Applied Surface Science*. North-Holland, 383, pp. 200–213. doi: 10.1016/J.APSUSC.2016.04.150.

Tichit, D. and Coq, B. (2003) 'Catalysis by hydrotalcites and related materials', *Cattech*, 7(6), pp. 206–217. doi: 10.1023/B:CATT.0000007166.65577.34.

Tongamp, W., Zhang, Q. and Saito, F. (2007) 'Preparation of meixnerite (Mg–Al–OH) type layered double hydroxide by a mechanochemical route', *Journal of Materials Science*. Springer US, 42(22), pp. 9210–9215. doi: 10.1007/s10853-007-1866-5.

Tor, A. and Cengeloglu, Y. (2006) 'Removal of congo red from aqueous solution by adsorption onto acid activated red mud', *Journal of hazardous materials*. Elsevier, 138(2), pp. 409–415. doi: 10.1016/J.JHAZMAT.2006.04.063.

Tritthart, J. (1989) 'Chloride binding in cement II. The influence of the hydroxide concentration in the pore solution of hardened cement paste on chloride binding', *Cement and Concrete Research*. Pergamon, 19(5), pp. 683–691. doi: 10.1016/0008-8846(89)90039-2.

Tsyganok, A. (2003) 'Dry reforming of methane over catalysts derived from nickel-containing Mg–Al layered double hydroxides', *Journal of Catalysis*, 213(2), pp. 191–203. doi: 10.1016/S0021-9517(02)00047-7.

Turner, R. C. and Brydon, J. E. (1962) 'Formation of Double Hydroxides and the Titration of Clays', *Science*, 136(3521). Available at: http://science.sciencemag.org/content/136/3521/1052 (Accessed: 29 June 2017).

Ujaczki, É. *et al.* (2016) 'Red mud as acidic sandy soil ameliorant: a microcosm incubation study', *Journal of Chemical Technology & Biotechnology*. Wiley-Blackwell, 91(6), pp. 1596–1606. doi: 10.1002/jctb.4898.

Ujaczki, É. *et al.* (2018) 'Re-using bauxite residues: benefits beyond (critical raw) material recovery', *Journal of Chemical Technology & Biotechnology*. Wiley-Blackwell, 93(9), pp. 2498–2510. doi: 10.1002/jctb.5687.

Ulibarri, M. A. *et al.* (2001) 'Adsorption of anionic species on hydrotalcite-like compounds: effect of interlayer anion and crystallinity', *Applied Clay Science*. Elsevier, 18(1–2), pp. 17–27. doi: 10.1016/S0169-1317(00)00026-0.

Uzun, D. and Gülfen, M. (2007) 'Dissolution kinetics of iron and aluminium from red mud in sulphuric acid solution', *Indian Journal of Chemical Technology*, 14, pp. 263–268. Available at: http://nopr.niscair.res.in/bitstream/123456789/1119/1/IJCT 14(3) (2007) 263-268.pdf (Accessed: 3 January 2019).

Vaccari, A. (1998) 'Preparation and catalytic properties of cationic and anionic clays', *Catalysis Today*. Elsevier, 41(1–3), pp. 53–71. doi: 10.1016/S0920-5861(98)00038-8.

Vachon, P. *et al.* (1994) *Chemical and Biological Leaching of Aluminum from Red Mud*, *Environ. Sol. Techno!* Available at: https://pubs.acs.org/sharingguidelines (Accessed: 9

December 2018).

Valcheva-Traykova, M. L., Davidova, N. P. and Weiss, A. H. (1993) 'Thermal decomposition of Mg, Al-hydrotalcite material', *Journal of Materials Science*, 28(8), pp. 2157–2162. doi: 10.1007/BF00367577.

Valente, J. S. *et al.* (2009) 'Method for Large-Scale Production of Multimetallic Layered Double Hydroxides: Formation Mechanism Discernment', *Chemistry of Materials*. American Chemical Society, 21(24), pp. 5809–5818. doi: 10.1021/cm902377p.

Valente, J. S. *et al.* (2010) 'Calcined layered double hydroxides Mg–Me–Al (Me: Cu, Fe, Ni, Zn) as bifunctional catalysts', *Catalysis Today*, 150(3–4), pp. 340–345. doi: 10.1016/j.cattod.2009.08.020.

Valente, J. S., Cantu, M. S. and Figueras, F. (2008) 'A Simple Environmentally Friendly Method to Prepare Versatile Hydrotalcite-like Compounds', *Chemistry of Materials*. American Chemical Society, 20(4), pp. 1230–1232. doi: 10.1021/cm7031306.

Verma, A. S., Suri, N. M. and Kant, S. (2017) 'Applications of bauxite residue: A mini-review', *Waste Management & Research*. SAGE PublicationsSage UK: London, England, 35(10), pp. 999–1012. doi: 10.1177/0734242X17720290.

Vulić, T., Hadnadjev, M. and Marinković-Nedučin, R. (2008) 'Structure and morphology of Mg-Al-Fe-mixed oxides derived from layered double hydroxides', *Journal of Microscopy*. Blackwell Publishing Ltd, 232(3), pp. 634–638. doi: 10.1111/j.1365-2818.2008.02130.x.

Vulic, T. J., Reitzmann, A. F. K. and Lázár, K. (2012) 'Thermally activated iron containing layered double hydroxides as potential catalyst for N2O abatement', *Chemical Engineering Journal*, 207–208, pp. 913–922. doi: 10.1016/j.cej.2012.06.152.

Wang, Q. *et al.* (2009) 'The color removal of dye wastewater by magnesium chloride/red mud (MRM) from aqueous solution', *Journal of Hazardous Materials*, 170(2), pp. 690–698. doi: 10.1016/j.jhazmat.2009.05.011.

Wang, Q. *et al.* (2013) 'Synthesis of nano-sized spherical Mg3Al–CO3 layered double hydroxide as a high-temperature CO2 adsorbent', *RSC Advances*. The Royal Society of Chemistry, 3(10), p. 3414. doi: 10.1039/c2ra22607c.

Wang, S. *et al.* (2005) 'Removal of dyes from aqueous solution using fly ash and red mud', *Water Research*. Pergamon, 39(1), pp. 129–138. doi: 10.1016/J.WATRES.2004.09.011.

Wang, S., Ang, H. M. M. and Tadé, M. O. O. (2008) 'Novel applications of red mud as coagulant, adsorbent and catalyst for environmentally benign processes', *Chemosphere*. Pergamon, 72(11), pp. 1621–1635. doi: 10.1016/j.chemosphere.2008.05.013.

Wang, X. *et al.* (2017) 'Preparation of a Mg/Al/Fe layered supramolecular compound and application for removal of Cr(vi) from laboratory wastewater', *RSC Adv.* The Royal Society of Chemistry, 7(56), pp. 34984–34993. doi: 10.1039/C7RA04646D.

Wang, Y. *et al.* (2018) 'Recovery of alkali and alumina from bauxite residue (red mud) and complete reuse of the treated residue', *Journal of Cleaner Production*. Elsevier, 188, pp. 456–465. doi: 10.1016/J.JCLEPRO.2018.04.009.

Whittington, B. and Ilievski, D. (2004) 'Determination of the gibbsite dehydration reaction pathway at conditions relevant to Bayer refineries', *Chemical Engineering Journal*, 98(1–2),

pp. 89–97. doi: 10.1016/S1385-8947(03)00207-9.

Wu, P. *et al.* (2011) 'Removal of reactive brilliant orange X-GN from aqueous solutions by Mg-Al layered double hydroxides', *Clays and Clay Minerals*, 59(5), pp. 438–445. doi: 10.1346/CCMN.2011.0590501.

Xiao, Y., Azaiez, J. and Hill, J. M. (2018) 'Erroneous Application of Pseudo-Second-Order Adsorption Kinetics Model: Ignored Assumptions and Spurious Correlations', *Industrial and Engineering Chemistry Research*. American Chemical Society, 57(7), pp. 2705–2709. doi: 10.1021/ACS.IECR.7B04724.

Xu, J. *et al.* (2017) 'Chloride absorption by nitrate, nitrite and aminobenzoate intercalated layered double hydroxides', *Journal of Materials Science*. Springer US, 52(10), pp. 5908–5916. doi: 10.1007/s10853-017-0826-y.

Xu, J. *et al.* (2018) 'Chloride removal and corrosion inhibitions of nitrate, nitrite-intercalated MgAl layered double hydroxides on steel in saturated calcium hydroxide solution', *Applied Clay Science*. Elsevier, 163, pp. 129–136. doi: 10.1016/J.CLAY.2018.07.023.

Xu, Z. P. and Lu, G. Q. (2005) 'Hydrothermal synthesis of layered double hydroxides (LDHs) from mixed MgO and Al2O3: LDH formation mechanism', *Chemistry of Materials*, 17(5), pp. 1055–1062. doi: 10.1021/cm048085g.

Yan, Q. *et al.* (2015) 'Hierarchical Fe3O4 Core-Shell Layered Double Hydroxide Composites as Magnetic Adsorbents for Anionic Dye Removal from Wastewater', *European Journal of Inorganic Chemistry*, 2015(25), pp. 4182–4191. doi: 10.1002/ejic.201500650.

Yang, J. *et al.* (2008) 'Preparation of glass-ceramics from red mud in the aluminium industries', *Ceramics International*. Elsevier, 34(1), pp. 125–130. doi: 10.1016/J.CERAMINT.2006.08.013.

Yang, S. *et al.* (2015) 'Enhanced adsorption of Congo red dye by functionalized carbon nanotube/mixed metal oxides nanocomposites derived from layered double hydroxide precursor', *Chemical Engineering Journal*. Elsevier B.V., 275, pp. 315–321. doi: 10.1016/j.cej.2015.04.049.

Yang, Yiqiong *et al.* (2012) 'Adsorption of perchlorate from aqueous solution by the calcination product of Mg/(Al–Fe) hydrotalcite-like compounds', *Journal of Hazardous Materials*. Elsevier, 209–210, pp. 318–325. doi: 10.1016/J.JHAZMAT.2012.01.026.

Yang, Yanmin *et al.* (2012) 'Transformation mechanism of magnesium and aluminum precursor solution into crystallites of layered double hydroxide', *Chemistry of Materials*, 24(1), pp. 81–87. doi: 10.1021/cm201936b.

Yang, Z. *et al.* (2016) 'Utilization of LDH-based materials as potential adsorbents and photocatalysts for the decontamination of dyes wastewater: a review', *RSC Adv.* Royal Society of Chemistry, 6(83), pp. 79415–79436. doi: 10.1039/C6RA12727D.

Yang, Z., Fischer, H. and Polder, R. (2013) 'Modified hydrotalcites as a new emerging class of smart additive of reinforced concrete for anticorrosion applications: A literature review', *Materials and Corrosion*, 64(12), pp. 1066–1074. doi: 10.1002/maco.201206915.

Yang, Z., Fischer, H. and Polder, R. (2014) 'Synthesis and characterization of modified hydrotalcites and their ion exchange characteristics in chloride-rich simulated concrete pore solution', *Cement and Concrete Composites*. Elsevier Ltd, 47, pp. 87–93. doi:

10.1016/j.cemconcomp.2013.03.008.

Yanik, J. *et al.* (2008) 'Biomass gasification in supercritical water: II. Effect of catalyst', *International Journal of Hydrogen Energy*. Pergamon, 33(17), pp. 4520–4526. doi: 10.1016/J.IJHYDENE.2008.06.024.

Ye, N. *et al.* (2017) 'Transformations of Na, Al, Si and Fe species in red mud during synthesis of one-part geopolymers', *Cement and Concrete Research*. Pergamon, 101, pp. 123–130. doi: 10.1016/J.CEMCONRES.2017.08.027.

Yokoyama, S. *et al.* (1989) 'Catalytic activity of sulphate for hydroliquefaction of coal by using diphenylether and diphenylmethane', *Fuel*. Elsevier, 68(4), pp. 531–533. doi: 10.1016/0016-2361(89)90278-0.

Yoon, S., Moon, J., Bae, S., Duan, X., Giannelis, Emmanuel P, *et al.* (2014) 'Chloride adsorption by calcined layered double hydroxides in hardened Portland cement paste', *Materials Chemistry and Physics*, 145, pp. 376–386. doi: 10.1016/j.matchemphys.2014.02.026.

Yoon, S., Moon, J., Bae, S., Duan, X., Giannelis, Emmanuel P., *et al.* (2014) 'Chloride adsorption by calcined layered double hydroxides in hardened Portland cement paste', *Materials Chemistry and Physics*. Elsevier B.V, 145(3), pp. 376–386. doi: 10.1016/j.matchemphys.2014.02.026.

Yu, L. B. *et al.* (2019) 'Effect of electrochemical chloride removal and ground granulated blast furnace slag on the chloride binding of cement paste subjected to NaCl and Na2SO4 attack', *Construction and Building Materials*. Elsevier, 220, pp. 538–546. doi: 10.1016/J.CONBUILDMAT.2019.06.033.

Yue, X. *et al.* (2017) 'Simultaneous removal of Cu(II) and Cr(VI) by Mg–Al–Cl layered double hydroxide and mechanism insight', *Journal of Environmental Sciences*. Elsevier, 53, pp. 16–26. doi: 10.1016/J.JES.2016.01.015.

Yue, Y. *et al.* (2018) 'Raman spectroscopic investigation of Friedel's salt', *Cement and Concrete Composites*, 86, pp. 306–314. doi: 10.1016/j.cemconcomp.2017.11.023.

Yun Zhao *et al.* (2002) 'Preparation of Layered Double-Hydroxide Nanomaterials with a Uniform Crystallite Size Using a New Method Involving Separate Nucleation and Aging Steps', *Chemistry of Materials*. American Chemical Society, 14(10), pp. 4286–4291. doi: 10.1021/CM020370H.

Yunessnia lehi, A. and Akbari, A. (2017) 'Membrane capsules with hierarchical Mg(OH)2 nanostructures as novel adsorbents for dyeing wastewater treatment in carpet industries', *Journal of the Taiwan Institute of Chemical Engineers*. Elsevier, 70, pp. 391–400. doi: 10.1016/J.JTICE.2016.10.041.

Zhang, B. *et al.* (2017) 'Enhanced adsorption capacity of dyes by surfactant-modified layered double hydroxides from aqueous solution', *Journal of Industrial and Engineering Chemistry*. The Korean Society of Industrial and Engineering Chemistry, 49, pp. 208–218. doi: 10.1016/j.jiec.2017.01.029.

Zhang, F. *et al.* (2013) 'Mechano-hydrothermal synthesis of Mg2Al–NO3 layered double hydroxides', *Journal of Solid State Chemistry*. Academic Press, 206, pp. 45–50. doi: 10.1016/J.JSSC.2013.07.030.

Zhang, F. *et al.* (2014) 'Synthesis of Mg-Al-Fe-NO3 layered double hydroxides via a mechano-hydrothermal route', *Solid State Sciences*, 32, pp. 41–47. doi: 10.1016/j.solidstatesciences.2014.03.012.

Zhang, G., He, J. and Gambrell, R. P. (2010) 'Synthesis, Characterization, and Mechanical Properties of Red Mud–Based Geopolymers', *Transportation Research Record: Journal of the Transportation Research Board*. SAGE PublicationsSage CA: Los Angeles, CA, 2167(1), pp. 1–9. doi: 10.3141/2167-01.

Zhang, P. *et al.* (2012) 'Mechanism of interaction of hydrocalumites (Ca/Al-LDH) with methyl orange and acidic scarlet GR', *Journal of Colloid and Interface Science*. Academic Press, 365(1), pp. 110–116. doi: 10.1016/J.JCIS.2011.08.064.

Zhang, Y. X. *et al.* (2014) 'MnOx -modified ZnAl-LDOs as high-performance adsorbent for the removal of methyl orange', *Dalton Trans.* Royal Society of Chemistry, 43(18), pp. 6667–6676. doi: 10.1039/C3DT53597E.

Zhao, H. *et al.* (2004) 'Alteration of Kaolinite to Cancrinite and Sodalite by Simulated Hanford Tank Waste and its Impact on Cesium Retention', *Clays and Clay Minerals*. GeoScienceWorld, 52(1), pp. 1–13. doi: 10.1346/CCMN.2004.0520101.

Zhao, J. *et al.* (2017) 'Synthesis of functionalized MgAl-layered double hydroxides via modified mussel inspired chemistry and their application in organic dye adsorption', *Journal of Colloid and Interface Science*. Academic Press, 505, pp. 168–177. doi: 10.1016/J.JCIS.2017.05.087.

Zhu, M.-X. *et al.* (2005) 'Sorption of an anionic dye by uncalcined and calcined layered double hydroxides: a case study', *Journal of Hazardous Materials*, 120(1–3), pp. 163–171. doi: 10.1016/j.jhazmat.2004.12.029.

Zimmer, E., Nafissi, A. and Winkhaus, G. (1978) 'Reclamation treatment of red mud', *US Patent*. Available at: https://patents.google.com/patent/US4119698A/en (Accessed: 8 December 2018).

Zubair, M. *et al.* (2017) 'Recent progress in layered double hydroxides (LDH)-containing hybrids as adsorbents for water remediation', *Applied Clay Science*. doi: 10.1016/j.clay.2017.04.002.